Towards understanding how lymph nodes process nanoparticle vaccines for humoral immunity

by

Yinan Zhang

A thesis submitted in conformity with the requirements
for the degree of Doctor of Philosophy
Institute of Biomaterials and Biomedical Engineering
University of Toronto

Towards understanding how lymph nodes process nanoparticle vaccines for humoral immunity

Yinan Zhang
Doctor of Philosophy
Institute of Biomaterials & Biomedical Engineering
University of Toronto
2020

Abstract

Vaccines are essential to induce the pathogen specific immune responses against infectious disease. Antigens derived from pathogens needs to be delivered to and retained in the immune organs (especially lymph nodes) for efficient immune responses and production of neutralized antibodies. A strategy is to use engineered nanoparticles as delivery carriers to help antigen delivery inside lymph nodes. We do not know how lymph nodes process nanoparticle-based vaccines for immune responses. In this thesis, we first found that follicular dendritic cell (FDC) networks determine the intra-lymph node follicle fate of nanoparticles based on nanoparticle size. The FDCs clear smaller nanoparticles (5-15 nm) and retain larger nanoparticles (50-100 nm) on their dendrites. These retained larger nanoparticles are then presented to B cells to induce humoral immune responses. Next, we assessed the role of immune cell population on nanoparticle delivery inside lymph nodes and found subcapsular sinus macrophage prevent the nanoparticle delivery to FDCs. Suppressing the subcapsular sinus macrophage results in enhancement of nanoparticle delivery to lymph node follicles and up to 60 times more antigen specific antibody production. Lastly, removal of liver macrophages promotes nanoparticle delivery to lymph nodes and tumours after systemic administration. These studies reveal the mechanism of how our immune system process nanoparticles. This knowledge enables us to rationally engineer nanoparticle vaccines and develop strategies of altering immune cell populations to generate effective immune responses.

Acknowledgements

I would like to thank my supervisor Dr. Warren Chan for his continuous support and help. I thank him for his patient and open mind to let me try lots of crazy experiments and eventually focus on the current thesis. I appreciate him for training my thinking process and sharpening my ideas. I thank my committee members Dr. David Sinton and Dr. Gang Zheng for their support and advice during committee meetings. I thank Dr. Fayi Song for his consistent help and assistant in Chan lab. I would like to thank my colleagues and friends in Chan lab for providing endless support and advice during these years. I enjoy the memories of when they gave me hard times on objective group meetings. Special thanks to my co-authors, Anthony Tavares, Wilson Poon, Ben Ouyang and James Lazarovits. They not only contribute to my research, more importantly they influence my thinking and daily life. Anthony taught me how to write a good NSERC proposal from the first day I joined Chan lab. He is the chemistry boss and taught me most of the chemical reactions and nanoparticle synthesis. Wilson joined the lab at the same time of myself. He is the biology boss and taught me how to do mice necropsy and biological studies. He also provided me with lots of good restaurant and place to visit. Ben is the tumour macrophage boss and one of smartest people I have ever seen. His questions were sometimes crazy, but I liked them. James is the protein boss and taught me a lot of nanoparticle and nanoparticle vaccine characterization. He taught me how to rationalize the ideas, criticize the research plans, and prioritize the tasks. I would like to thank my other co-authors, Luan Nguyen, Benjamin Kingston, Elana Sefton, Qin Dai, Ding Ding. Without their support and pushing, I will not able to finish these projects. I thank Kim Tsoi for introducing the lymph node to me the first time. She also taught me how to isolate lymph nodes from a mouse. I thank David Zhang, Alexander Vlahos, Shrey Sindhwani and Abdullah Syed for being real models as the greatest scientist in Chan and Sefton labs.

I would like to thank our collaborators Rickvinder Besla, Angela Li, and Clinton Robbins for assisting with a model of polymicrobial sepsis to evaluate the systemic toxicity of macrophage depletion. I thank Juan Chen, Jiachuan Bu, Lili Ding, and Gang Zheng for fruitful discussion of elemental analysis using ICP-MS. I would like to acknowledge Prof. Michael Carroll at Harvard Medical School for valuable discussion and comments on 2D and 3D images of nanoparticle interaction with follicular dendritic cells and complement knockout mice studies. I thank Prof. Jason Cyster at University of California, San Francisco for discussion on nanoparticle interaction with follicular dendritic cells. I acknowledge Dr. Zhenyue Hao at The Donnelly Centre for Cellular and Biomolecular Research of University of Toronto for valuable suggestions and discussions on humoral function tests. I thank Prof. Darrell Irvine at Massachusetts Institute of Technology for fruitful discussions on nanoparticle interactions with lymph nodes. I thank Dr. Rino Rappuoli at GSK vaccines for the recommendation of our Nano Letters paper on F1000Prime and the discussion on transforming vaccinology. I thank Dionne White and Joanna Warzyszynska at Faculty of Medicine Flow Cytometry Facility of Univeristy of Toronto and Olga Rojas at the Department of Immunology Faculty of Medicine of University of Toronto for their expertise in flow cytometry. I thank Doug Holmyard and Ali Darbandi at The Hospital for Sick Children Nanoscale Biomedical Imaging Facility for TEM sample preparation and their expertise in TEM operation. I thank Vivian Bradaschia, Milan Ganguly, Qiang Xu at the Toronto Centre for Phenogenomics for their expertise in histology and immunostaining.

I thank my previous Bachelor, Master, and post-master supervisors, Profs. Yufeng Wu and Wenbo Du at Beijing University and Technology, Mamoun Medraj at Concordia University, Xinjin Cao at NRC aerospace, Zaven Altounian at Mcgill University. With their continuous support, I was

able to pursue my PhD at University of Toronto and obtain multiple scholarships and awards. I give my special thanks to my previous supervisors, Profs. Ali Khademhosseini and Nasim Annabi at Harvard Medical School and University of California, Los Angeles. They gave me the chance to change from my previous background of metallurgy and mechanical engineering to biomedical engineering before pursing my PhD. I also learnt from them to push things forwards. I thank Prof. Jiang Zhu at Scripps Research Institute for providing me the postdoctoral research opportunity to gain more knowledge of structural and computational biology for better antigen design. This will help me better design vaccines against infectious diseases. Last but not least, I thank my family for their continuous supports, to my grandma Fangpei Zhu, father Qing Zhang, mother Ming Guan, father-in-law Yuhua Gao, mother-in-law Huizhen Zhang, two kids Ian Zhang and Ivy Zhang, and especially to my wife Bo Gao. Finally, I thank my old friends, Bailaoshi, Falaomen, Indian brother, Oboe king, Philippine leader, and Jeffrey, Gabriel, Alexandra, Mr. LN and Mr. Woo in easy.

Table of Contents

List of Tables

List of Figures

List of Abbreviations

ALP	Alkaline phosphatase
ALT	Alanine aminotransferase
ANOVA	Analysis of variance
AST	Aspartate aminotransferase
BA	Basophils
BSA	Bovine serum albumin
BSPP	Bis(p-sulfonatophenyl)phenylphosphine dihydrate dipotassium salt
CL	Clodronate
CLP	Cecal ligation and puncture
CR	Complement receptor
DiD	1,1'-dioctadecyl-3,3,3',3'-tetramethylindodicarbocyanine,4-chlorobenzenesulfonate salt
DLS	Dynamic light scattering
DMEM	Dulbecco's modified eagle medium
ELISA	Enzyme-linked immunosorbent assay
EO	Eosinophils
FDC	Follicular dendritic cell
GC	Germinal center
H&E	Hematoxylin and eosin
HCT	Hematocrit
HEPES	4-(2-hydroxyethyl)-1-piperazineethanesulfonic acid
HGB	Hemoglobin
HPI	Hours post injection
HR	Heart
HRP	Horseradish peroxidase
I.D. or ID	Injected dose
i.v. or IV	Intravenous
ICP-MS	Inductively coupled plasma – mass spectrometry

IN	Intestine(s)
KC	Kupffer cell
KD	Kidney(s)
LEC	Lymphatic endothelial cell
LN	Lymph node(s)
LU	Lungs
LV	Lymphatic vessel
LY	Lymphocytes
Mal	Maleimide
MCH	Mean corpuscular hemoglobin
MCHC	Mean corpuscular hemoglobin concentration
MCV	Mean corpuscular volume
MO	Monocytes
MPV	Mean platelet volume
MZ	Marginal zone
NE	Neutrophils
NP	Nanoparticle
OVA	Ovalbumin
PBS	Phosphate buffered saline
PEG	Poly(ethylene) glycol
PK	Pharmacokinetics
PLT	Platelet count
RBC	Red blood cell
RDW	Red blood cell distribution width
RES	Reticuloendothelial system
RPMI	Roswell Park Memorial Institute
RPZ	Red pulp zone
SC or s.c.	Subcutaneous

SCS	Subcapsular sinus
SD	Standard deviation
SK	Skin
SP	Spleen
ST	Stomach
TBIL	Total bilirubin
TCP	Toronto Centre for Phenogenomics
TEM	Transmission electron microscopy
TM	Tumour
TLR	Toll-like receptor
UV	Ultraviolet
WBC	White blood cells
WPZ	White pulp zone

Overview of chapters & author contributions

Chapter 1 presents an overview of vaccines, lymph nodes and nanoparticle-based vaccines.

Y.-N.Z. and W.C.W.C. conceived the idea. Y.-N.Z. wrote the section.

Chapter 2 studies how nanoparticle size impacts antigen retention and presentation in lymph node follicles. This chapter provides the fundamental understanding of how lymph node cellular components process different nanoparticle designs for stimulation of humoral immune responses. This chapter shows that we can tune humoral immunity by simply manipulating the carrier size design for effective vaccination.

Y.N. Zhang, *J. Lazarovits, *W. Poon, *B. Ouyang, L.N.M. Nguyen, B.R. Kingston, W.C.W. Chan, "Nanoparticle Size Influences Antigen Retention and Presentation in Lymph Node Follicles for Humoral Immunity", *Nano letters*, Vol. 19, 7226-7235 (2019). *Equal contribution

Author contributions: Y.-N.Z. and W.C.W.C. conceptualized the project. Y.-N.Z., J.L. and L.N.M.N. designed, synthesized, and characterized nanoparticles and nanoparticle vaccines. Y.-N.Z., J.L., W.P., B.O. and B.R.K. designed, performed, and analyzed experiments. Y.-N.Z. and W.C.W.C. wrote the initial manuscript draft. All authors contributed to review and editing of the manuscript.

Chapter 3 investigates how subcapsular sinus macrophage influences nanoparticle intra-lymph node transport. This chapter shows that removing or functionally altering the subcapsular sinus macrophages enhances nanoparticle delivery to lymph node follicles. This chapter suggests that altering immune cell population in the lymph node is a valid strategy to boost effective vaccination.

Y.N. Zhang, W. Poon, E. Sefton, W.C.W. Chan, "Suppressing subcapsular sinus macrophages enhance transport of nanovaccines to lymph node follicles for robust humoral immunity", *ACS Nano* (2020).

Author contributions: Y.-N.Z. and W.C.W.C. conceptualized the project. Y.-N.Z., E.S. designed, synthesized, and characterized nanoparticles and nanovaccines. Y.-N.Z., W.P., and E.S designed, performed and analyzed experiments. Y.-N.Z. and W.C.W.C. wrote the initial manuscript draft. All authors contributed to review and editing of the manuscript.

Chapter 4 studies how liver macrophages impact nanoparticle sequestration in the liver and other organs. This chapter shows that removal of liver macrophage causes limited systemic toxicity and nanoparticle redistribution to lymph nodes and tumour. This provides the strategy to manipulate biological components for more efficient targeted delivery.

*A.J. Tavares, *W. Poon, ***Y.N. Zhang**, Q. Dai, R. Besla, D. Ding, B. Ouyang, A. Li, J. Chen, G. Zheng, C. Robbins, W.C.W. Chan, "Effect of removing Kupffer cells on nanoparticle tumor delivery", *Proceedings of the National Academy of Sciences*, Vol. 114, E10871-E10880 (2017).

*Equal contribution

Author contributions: A.J.T., W.P., Y.-N.Z., B.O., C.R., and W.C.W.C. designed research; A.J.T., W.P., Y.-N.Z., Q.D., R.B., D.D., B.O., and A.L. performed research; J.C. and G.Z. contributed new reagents/analytic tools; A.J.T., W.P., Y.-N.Z., and W.C.W.C. analyzed data; and A.J.T., W.P., Y.-N.Z., Q.D., B.O., and W.C.W.C. wrote the paper.

Chapter 1 - Introduction

Vaccines

Vaccines are considered the most successful and cost-effective medical invention in the world by protecting humans against pathogens and infectious diseases[1]. Vaccines have tremendous impacts on global public health[2,3]. The life expectancy was almost doubled in the past 100 years due to vaccination[4]. Successful vaccine development remains a challenge against several life-threatening infectious diseases, such as HIV/AIDS, tuberculosis, malaria, influenza, respiratory syncytial virus, and coronavirus[1,2].

Efficient vaccinations require pathogen derived antigen to transport into local lymph nodes and induce the production of effective neutralized antibodies[5,6]. Vaccines are commonly injected through a needle underneath the skin. The route of immunization (intramuscular vs. subcutaneous administrations) may access different lymph nodes but makes no different on innate or adaptive immune responses[7]. These vaccines can stimulate a local immune response and transport through the lymphatic system into sentinel lymph nodes to induce B cell mediated humoral immune responses and elicit antigen specific neutralized antibodies[8–11]. However, it is unclear how lymph nodes process antigens/pathogens and induce robust humoral immunity. The lack of fundamental understanding prevents the development of next generation vaccines against remaining and novel infectious diseases[2].

Lymphatic system

The lymphatic system consists of lymph fluid, lymphatic vessels, and lymphoid organs[12]. The lymphatic system is a parallel system of the blood circulatory system. Blood pumps out from the heart and goes through the arteries, interstitial tissue, lymphatic system, the veins and eventually

flows back to heart (Fig. 1.1)[12]. The detailed pathway is summarized here: heart → blood vessel → interstitial tissue → lymphatic capillary → lymphatic vessel → lymph node → lymphatic vessel → lymphatic trunk → collecting duct → subclavian vein → superior vena cava → heart. The lymphatic pathway is non-symmetric: ¼ drainage of right lymphatic duct → right subclavian vein, ¾ drainage of thoracic duct → left subclavian vein). The main functions of lymphatic system include: (1) balancing the body fluid; (2) transportation of lymph/body fluid back to the blood circulation; (3) scanning pathogens; and (4) modulating innate and adaptive immunity[12–16].

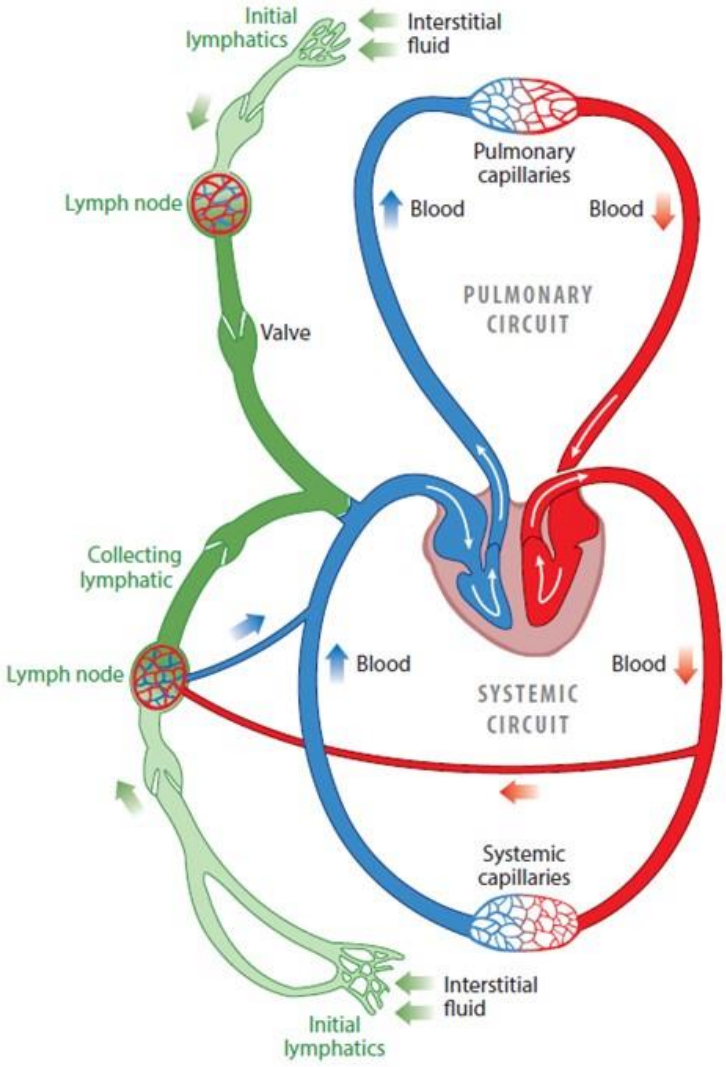

Fig. 1. 1. Schematic of the lymphatic system and blood circulation[12].

Lymphocytes and lymphoid organs

Lymphocytes are born and matured in the primary lymphoid organs, including the bone marrow and thymus. Once these lymphocytes are trained and matured, they will migrate to the peripheral lymphoid organs such as the secondary lymphoid organs and skin (Fig. 1.2). Secondary lymphoid organs are the organs that contain myeloid and lymphoid cell populations that play an important role to stimulate adaptive immune responses[13]. There are about 500-600 lymph nodes through our body. Lymph nodes drain and filter pathogens through the lymphatic system[16,17]. The major lymph node cellular components are T and B lymphocytes. Lymphocytes enter lymph nodes through two pathways: (1) high endothelial venule from blood circulatory system; and (2) afferent lymphatic vessels from lymphatic system.

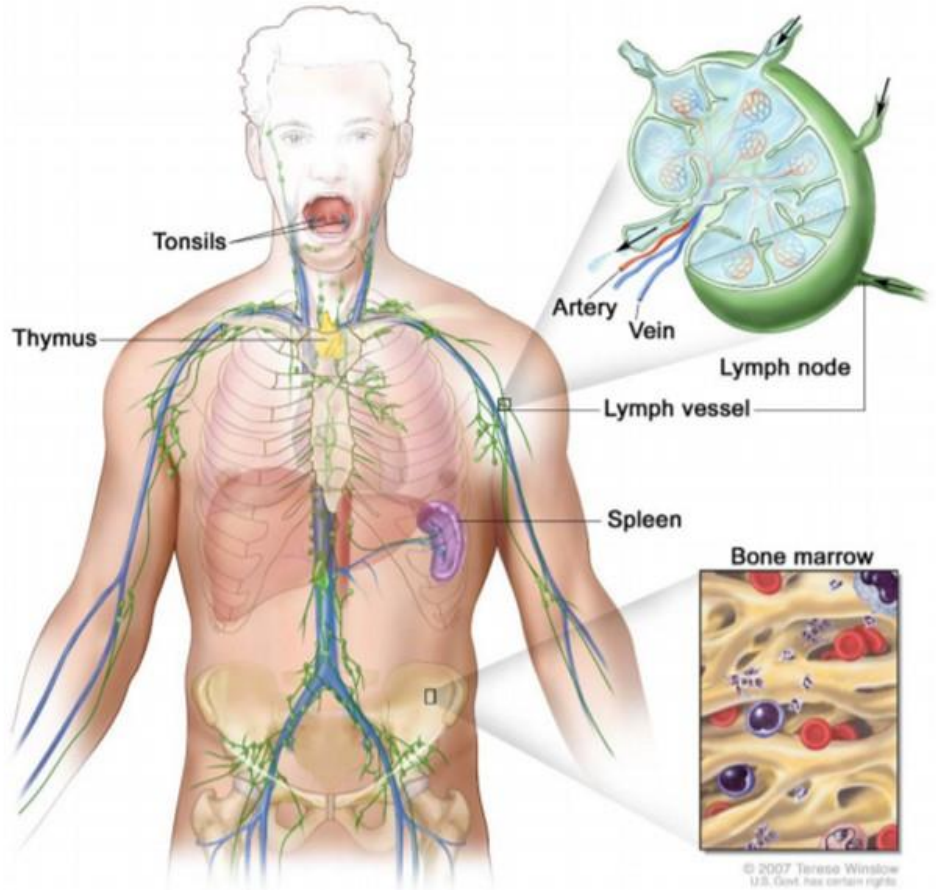

Fig. 1. 2. Lymphoid organs. Primary lymphoid organs include bone marrow and thymus. Secondary lymphoid organs include spleen, tonsils, Peyers' patches and lymph nodes[12].

Lymph node anatomy and function

Lymph nodes are highly organized structural organs with multiple functions[17–20]. The structure of the lymph node consists of four specific areas: subcapsular sinus, cortex (follicle), paracortex, and medullary cord (Fig. 1.3). The lymph fluid flow pathway is summarized here: afferent lymph vessels → subcapsular sinus → cortical sinuses (trabecular sinuses) → medullary sinuses → efferent lymph vessels. Multiple afferent lymphatic vessels connect to the subcapsular sinus, and only one efferent lymphatic vessel clears the lymph fluid from the medullary cord (Fig. 1.3). Antigen presenting cells and T cells are mainly resided in the paracortex area. T cells migrate through high endothelial venules or lymphatics vessels and interact with antigen presenting cells to stimulate T cell mediate immune responses[21]. B cells are mainly located in the cortex (follicles) area. Antigens are required to pass through the subcapsular sinus and interact with B cells in lymph node follicles to generate B cell mediated humoral immune responses[5,9]. The main functions of the lymph nodes include: (1) draining and filtering lymphatic fluids; (2) collecting T and B lymphocytes; (3) scanning for the pathogen derived antigen; (4) retaining and presenting antigens; (5) maturing and proliferating lymphocytes; and (6) generating germinal center and eliciting antigen specific antibody production[20].

In this thesis, I will focus on understanding B cell mediated humoral immunity and how nanoparticle interaction with cell populations in lymph node follicles for humoral immune responses (Fig. 1.4).

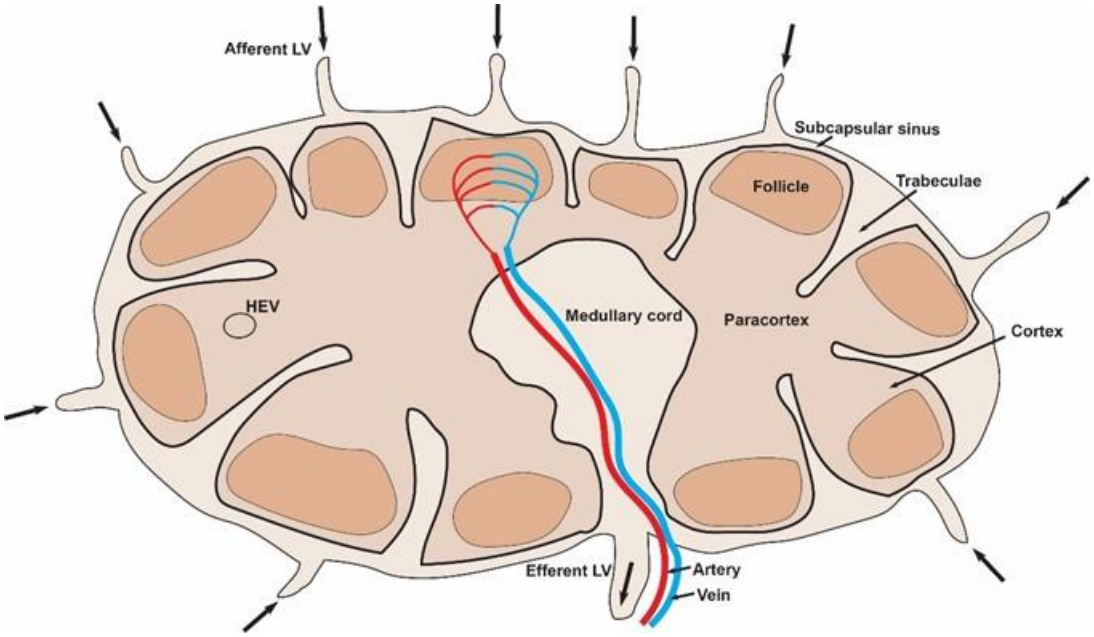

Fig. 1. 3. Lymph node anatomy. The Lymph node consists of four specific areas, including the subcapsular sinus, cortex (follicles), paracortex and medullary cord.

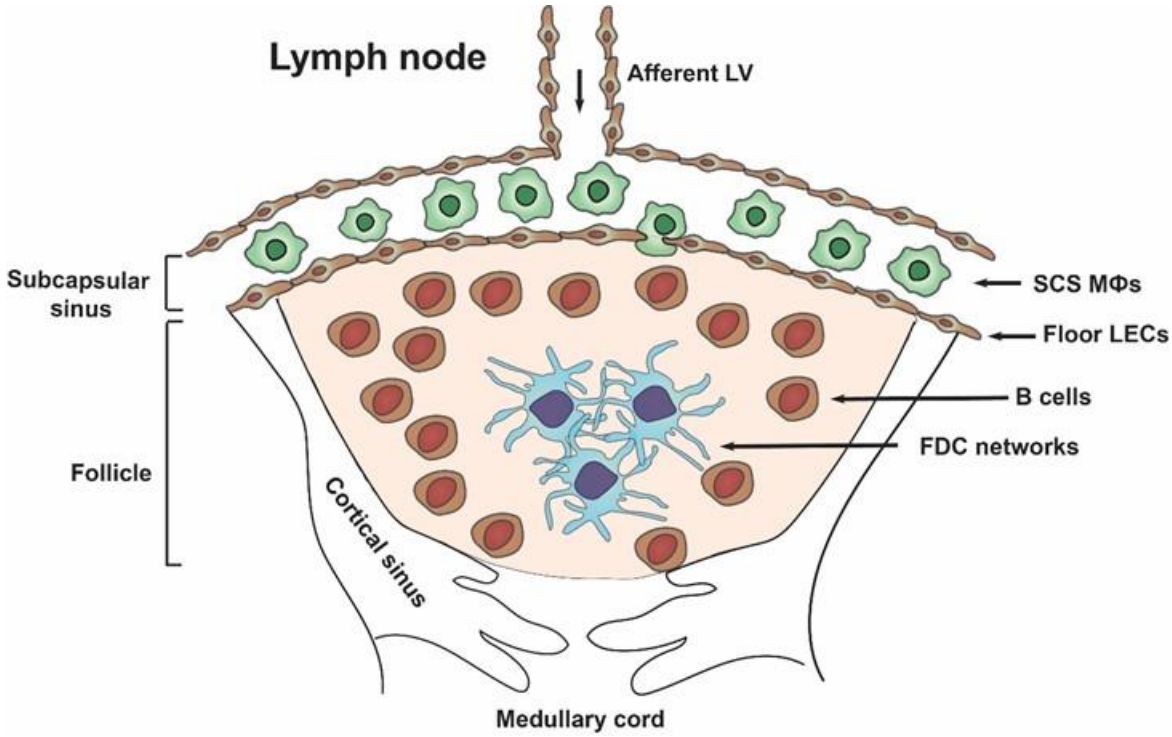

Fig. 1. 4. Schematic of cellular components in lymph node follicles that mediate humoral immune responses. SCS MΦ stands for subcapsular sinus macrophages, LEC stands for lymphatic endothelial cells, FDC stands for follicular dendritic cells. LV stands for lymphatic vessel.

Lymph node follicle cellular components and B cell mediated humoral immunity

Subcapsular sinus macrophages

Antigens are required to be transported into lymph node follicles to interact with B cells and induce efficient humoral immune responses. Antigens diffuse from the injected site through the lymphatic system into the sentinel lymph nodes. Antigens enter lymph nodes via afferent lymphatic vessels and flow in subcapsular sinus (Fig. 1.4). The subcapsular sinus has a tube-like structure and is lined by lymphatic endothelial cells (LECs). These subcapsular sinus lymphatic vessel structures only allow lymphatic fluid or smaller sized antigens (< 15 nm) to leak out of the vessels[22–24]. Larger sized particles, such as viruses, bacteria, and immune complexes are accumulated in the subcapsular sinus and have greater interactions with subcapsular sinus cell populations. The key cell populations in the subcapsular sinus are macrophages. These subcapsular sinus (SCS) macrophages are the first layer of defense once pathogen drain into the lymph node[25,26]. SCS macrophages are highly phagocytic cells that are involved in sequestration and clearance of pathogens[10,27–32]. SCS macrophages can function in two ways: (1) they serve as antigen presenting cells and process the antigen to activate T cells for T cell mediated adaptive immunity[33]; and (2) they capture the antigen and hand over the antigen to migrating B cells in lymph node follicles for B cell mediated humoral immunity[10,34,35].

B cells

Once antigens are transported to B cell follicles, they can interact with B cells and stimulate humoral immune responses. B cell stimulation is the key in the humoral immune responses of the adaptive immune system by secreting antigen specific neutralized antibodies. The essential steps of B cell encountering antigens, B cell activation, differentiation and antibody production are briefly summarized in Fig. 1.5[9,36]. B cells express B cell receptors on their cell surface that can bind on viral antigens which are essential to initiate B cell activation. Antigen derived from

pathogen have a repetitive organized pattern on the pathogen surface[36]. These repetitive organized patterns facilitated antigen binding and recognition by B cell receptors. Clustering of B cell receptors is a strong activation signal for B cells. With the help of CD4+ T cells, B cells differentiate into plasma cells and memory B cells. These plasma cells then produce IgG against specific pathogens[5]. Here, the formation of the repetitive antigen recognition patterns is essential for B cell stimulation and production of antigen specific antibodies. It has been suggested that other supporting cells, such as follicular dendritic cells in the lymph node follicle, can facilitate antigen retention and presentation and mediate B cell activation[10,35].

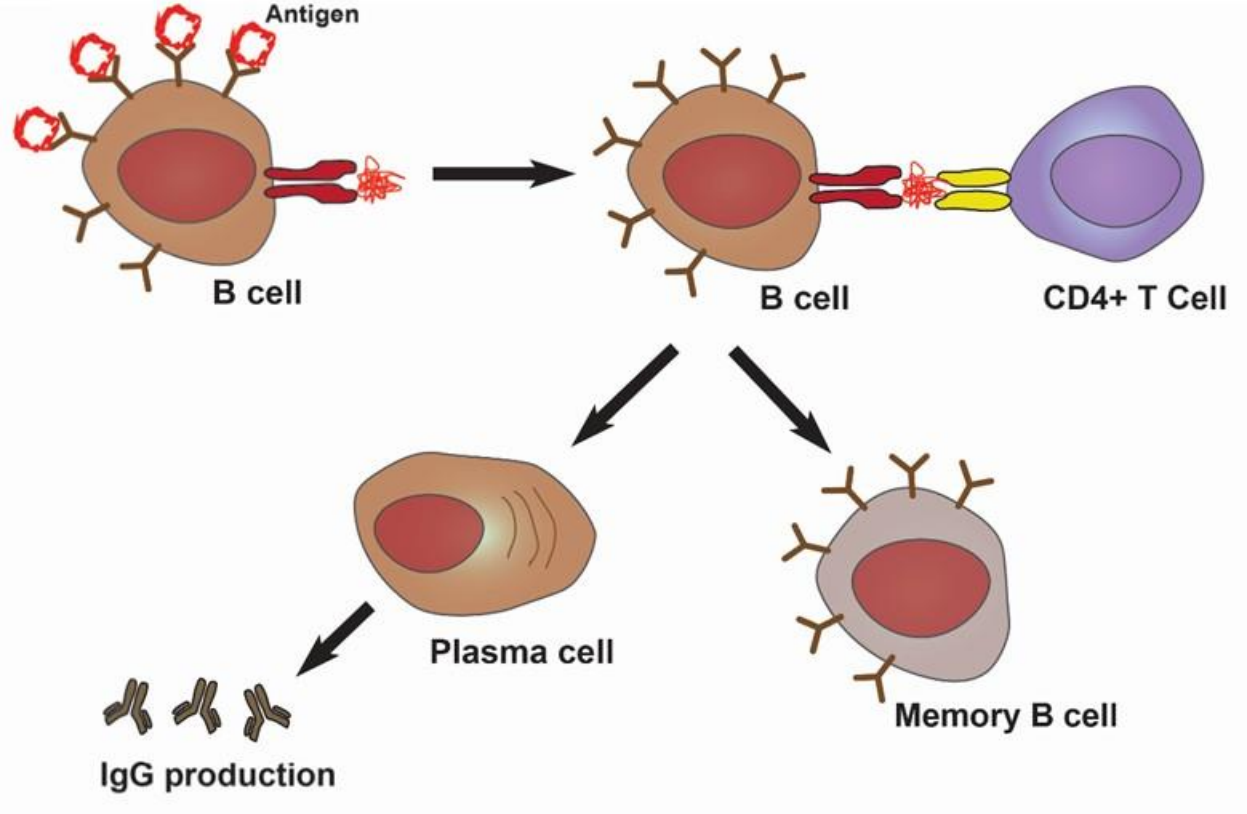

Fig. 1. 5. Key steps of B cell mediated humoral immune responses[36].

Follicular dendritic cells

Follicular dendritic cells (FDCs) form networks and are located in the center of the B cell follicle. Unlike the conventional dendritic cells that are derived from the hematopoietic stem cells in the

bone marrow, FDCs are the resident stromal cells and are derived from mesenchymal cells[37]. FDCs maintain the lymph node follicle structure in a CXCR5-CXCL13-depednent manner[10]. FDCs produce chemokine CXCL13 to attract B cells via chemokine receptor CXCR5 in the lymph node follicle. Depletion of FDCs fails to form the lymph node B cell follicles[35].

Once the antigen is transported into the follicles and are sequestered by FDCs. FDCs can prevent the antigen internalization by other phagocytic cells, such as conventional dendritic cells and macrophages. This is due to the unique location of FDCs in the center of B cell follicles. TEM images show ^{125}I-labelled *Salmonella* flagellar antigen binds on the surface and dendrites of FDCs in lymph nodes (Fig. 1.6)[38]. FDCs express the high amounts of complement receptors Cr1 and Cr2 (also known as CD35 and CD21 respectively), which is critical for antigen retention. Opsonized antigens, such as viruses, bacteria, and immune complexes can bind to FDC dendrites through receptor-ligand interaction, where complement receptor Cr1/2 binds with opsonized complement C3. In the Cr1/Cr2-deficient or complement C3-deficient mice, FDC fails to retain an immune complexes[39]. This function enables FDCs to retain the naïve antigen and present the antigen on their surfaces or dendrites for over months[35,37,40–42]. The alignment of antigen on FDC dendrites in a repetitive organized pattern facilitates antigen binding and crosslinking of B cell receptors[8,9,11,43–45].

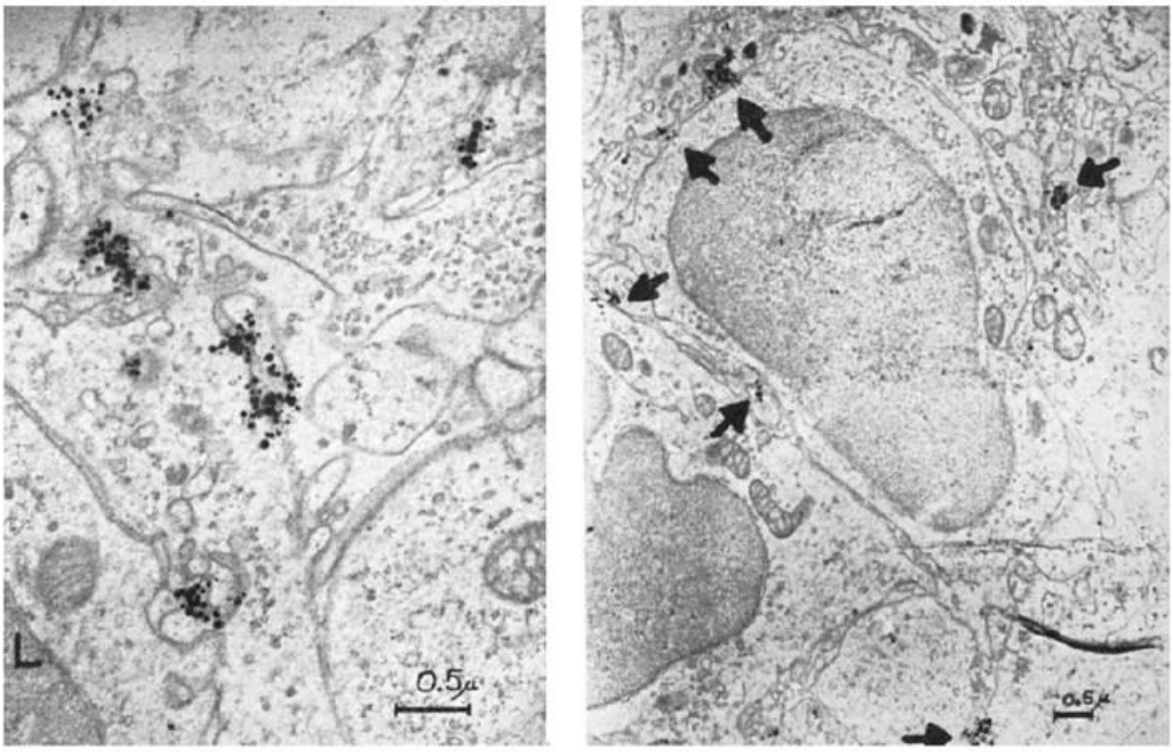

Fig. 1. 6. TEM images of FDC ultrastructure. Arrows point to ^{125}I-labelled Salmonella flagellar antigens on FDC surface and dendrites[38].

Germinal center reaction

Antigen retention and presentation on FDC dendrites in lymph node follicle promotes long-term humoral immune responses, including B cell activation, somatic hypermutation, affinity maturation, and germinal center reactions[5,9,37]. This leads to production of high-affinity neutralized antibodies and memory B cells[9]. The process of the germinal center reactions is shown in Fig. 1.7[35,46]. B cells present antigen and are co-stimulated by T helper cells. Activated B cells enter to the dark zone of germinal centers and undergo somatic hypermutation. Proliferated B cells migrate to the light zone of the germinal centers. These B cell receptors are exposed to antigens that are presented on FDC dendrites. If the affinity of these B cell receptors is low, FDCs will not give the survival signals to B cells and those B cells will undergo apoptosis. If the affinity of these B cell receptors is high, these B cells can re-enter the dark zone and go through these cycles multiple

times to further improve the affinity of B cell receptors. This affinity maturation process takes one to several weeks. The affinity matured B cells undergo the class switching induced by follicular T helper cells and exit germinal centers as plasma cells or B memory cells[5,46]. FDCs are essential for long term maintenance of germinal center reaction for humoral immunity[5,35,37].

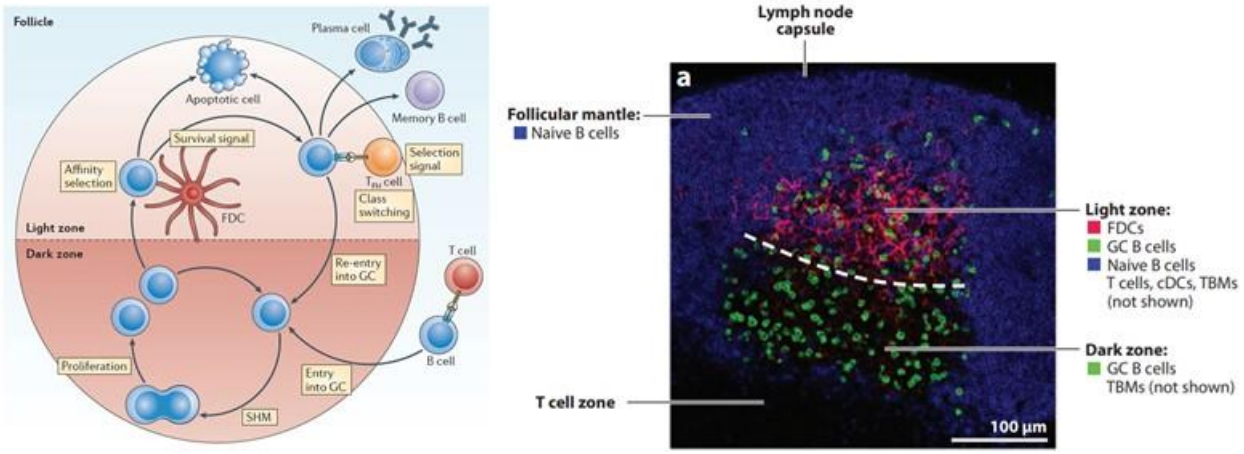

Fig. 1. 7. Germinal center reaction. B cell activation, somatic hypermutation, affinity maturation, and differentiation are processed in germinal centers to stimulate long-term humoral immune responses[35,46].

Antigen delivery to FDC networks

FDC networks in lymph node follicles are central to inducing robust humoral immune responses. How antigen transport occurs in FDC networks is an essential question. The opsonized antigen size impacts the antigen transport pathways. Antigens with sizes smaller than 15 nm flow directly to FDCs through conduit networks in the lymph nodes. Antigens with sizes larger than 15 nm, such as viruses, bacteria, and immune complexes require cell-mediated transport to FDCs[24,27–32,47–49]. It has been widely accepted that SCS macrophages bind the opsonized antigen (C3d) via complement receptor 3 (Cr3) on their surface. SCS macrophages hand over the opsonized antigens to migrating B cells (Cr2) and these organized antigens eventually deposit on FDC dendrites (Cr2) (Fig. 1.8)[10,35]. The crystal structures of the Cr2-C3d complex and Cr3-C3d complex were studied

and opposite binding sites on C3d opsonized antigen investigated[35,50]. SCS macrophages were used as a target to efficiently transport antigens to FDCs[10,51,52]. Besides accumulation in the subcapsular sinus, viruses can accumulate at the medullary cord. Medullary dendritic cells capture viruses via the SIGN-R1 receptor, and shuttle viruses to B cells for transport to FDCs[47]. Endocytosis and recycling of antigen immune complexes by FDCs can enhance B cell binding with these antigens[53]. The antigens are eventually presented on FDC dendrites to stimulate B cell responses.

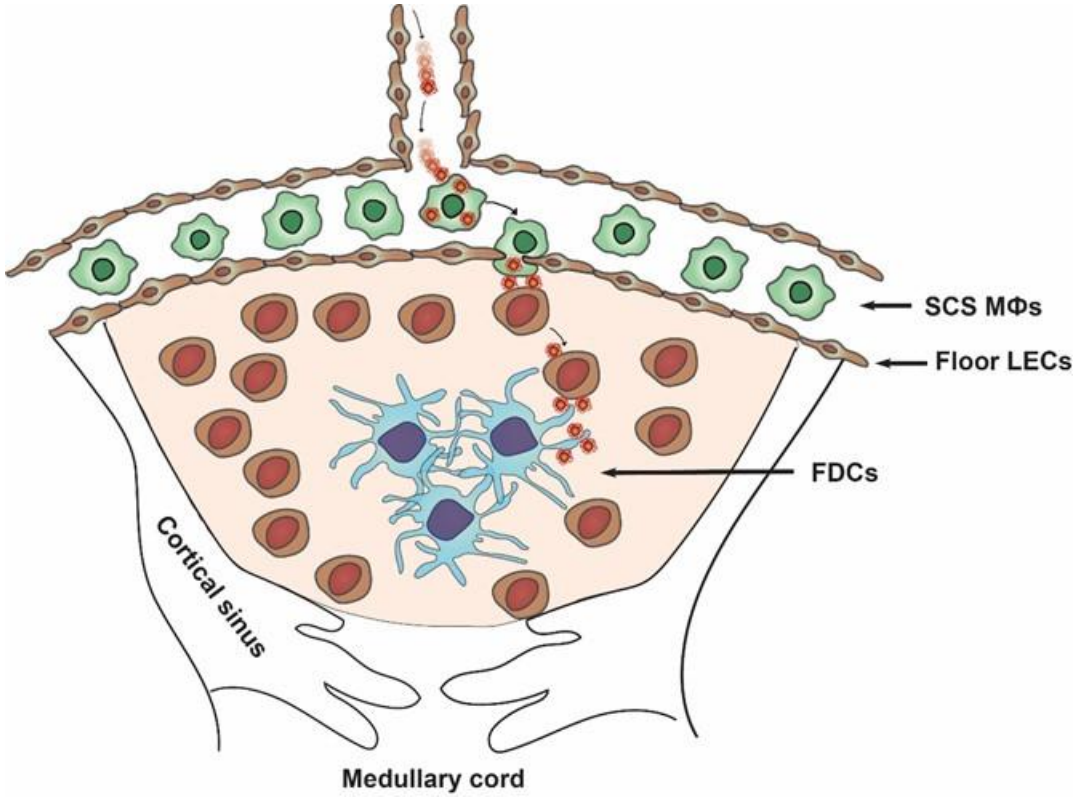

Fig. 1. 8. Antigen transport to FDC networks through SCS macrophages, migrating B cells and eventually depositing on FDCs[10,35].

Nanoparticle conjugated antigen-based vaccines

Efficient transport of antigens to FDCs in lymph node follicles is the prerequisite to inducing robust germinal centers and neutralized antibodies. Free antigen proteins isolated from pathogens

have poor lymph node retention. They cannot induce efficient clustering of B cell receptors, germinal center reactions and effective neutralized antibody production. Antigens conjugated to synthetic nanoparticles are designed for codelivery into follicles to elicit greater humoral immune responses than antigen alone[8,49,54–57]. The rationale of using nanoparticles include: (1) ease of synthesis using biocompatible materials; (2) ease of manipulating antigen conjugation on nanoparticle surface or encapsulation inside the nanoparticle; (3) precise control of the size and shape of nanoparticle to mimic immune complex and virus; (4) incorporation of imaging agents; and (5) ability to alter organ and cellular distribution. Nanoparticles conjugated to antigen show advantages such as interactions with lymph node cellular components and the stimulation of humoral immune responses compared to antigen alone[58–61], as summarized in Fig. 1.9 and Table 1.1. Nanoparticles can serve as scaffolds or templates to improve antigens integration, antigens alignment and display on nanoparticles[59]. Nanoparticles can also act as delivery carriers to alter antigens trafficking to lymph nodes, intra-lymph node distribution, antigens retention and presentation, and eventually elicit germinal center reaction and production of antigen specific neutralized antibodies.

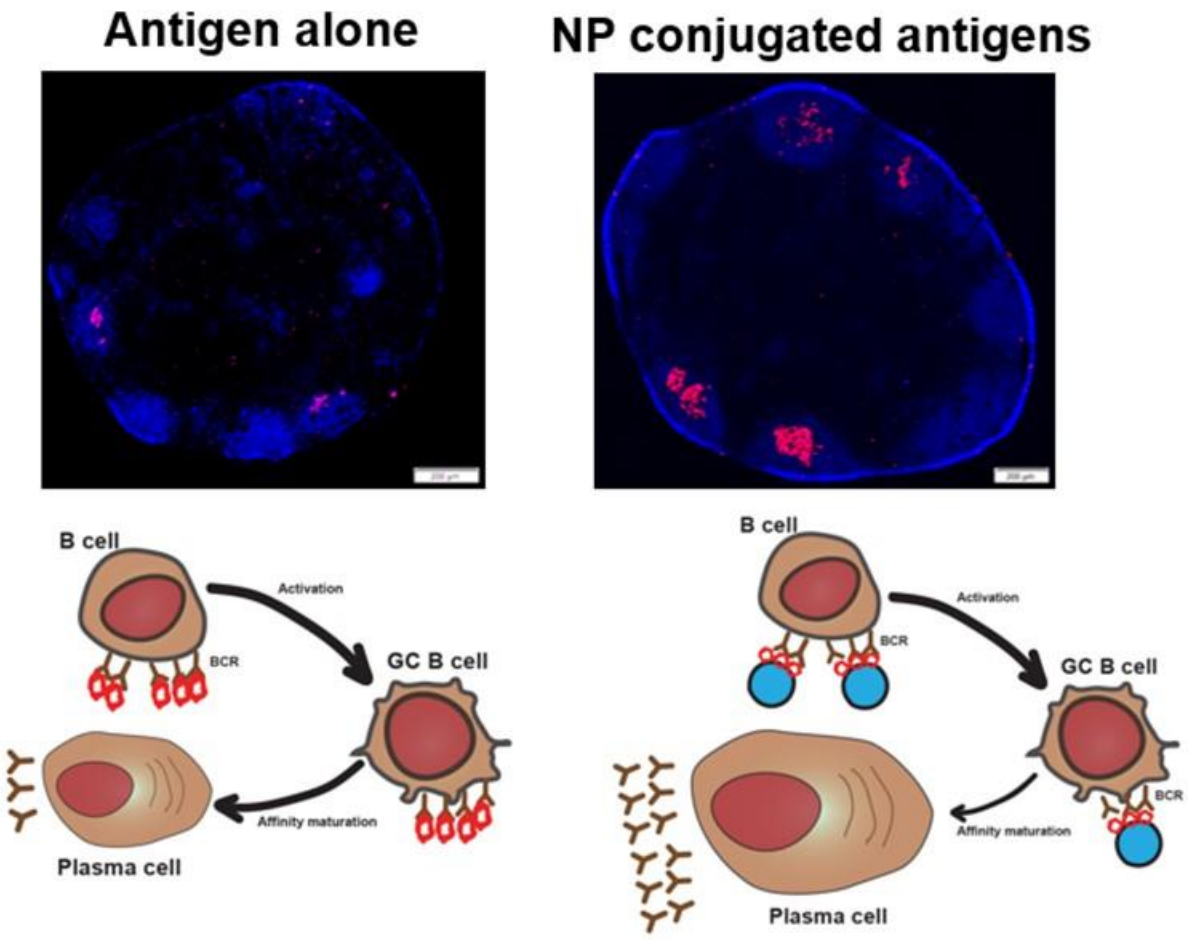

Fig. 1. 9. Nanoparticles conjugated with antigens induce greater humoral immune responses than antigen alone. Blue color represents B cell follicles, red color represents germinal centers.

Table 1.1. Nanoparticle conjugated antigen is superior than free antigen to elicit greater humoral immune responses

Biological components	Antigen alone	Nanoparticle conjugated antigen
Lymph node delivery	high	high
Lymph node retention	low	high
Follicle retention	low	high
FDC interaction	low	high
Crosslinking B cell receptors	low	high
Germinal center reaction	low	high
Neutralized antibody production	low	high

Nanoparticle size impacts lymph node delivery and intra-lymph node interaction

Size impacts the pathways of nanoparticle transport into lymph nodes. Sub-100 nm nanoparticles are small enough to freely enter lymphatic vessels from the injection site (Fig. 1.10 and 11). These nanoparticles directly drain through lymphatics and transport into the lymph node through afferent lymphatic vessels[62]. Viruses follow the same pathway to transport to the lymph nodes[63]. Nanoparticles larger than 100 nm are internalized by resident dendritic cells underneath the skin. These dendritic cells migrate into the lymphatic vessels and transport the nanoparticles into the lymph nodes[16,20,36,64,65] (Fig. 1.10 and 11). It is unclear how these migrating dendritic cells transport nanoparticles to other cells inside lymph nodes. Once nanoparticles enter the lymph node, their size mediates the binding, internalization and other interactions with cells and biological environment. 10-1000 nm nanoparticles can be sequestered by antigen presenting cells (Fig. 1.11)[36]. Nanoparticles smaller than 15 nm can enter lymph node follicles though the subcapsular sinus floor formed by lymphatic endothelial cells[22–24]. Nanoparticles larger than 50 nm are captured by SCS macrophages and transported to migrating B cells in the lymph node follicles[24,27–

[32,47–49]. Once nanoparticles conjugated with antigens transported to FDCs in lymph node follicles, it enables the generation of B cell mediated humoral immune responses. Nanoparticles conjugated with HIV antigens (30-50 nm) can retain in lymph node follicles for over 2 week and interact with FDCs[55]. This leads to generation of robust germinal centers and HIV specific antibody production[55]. It has been known that size mediates nanoparticle transport into lymph node follicles, we do not know how nanoparticle size impacts antigen retention and presentation on FDC dendrites and eventually drive germinal center reactions and antigen specific antibody production.

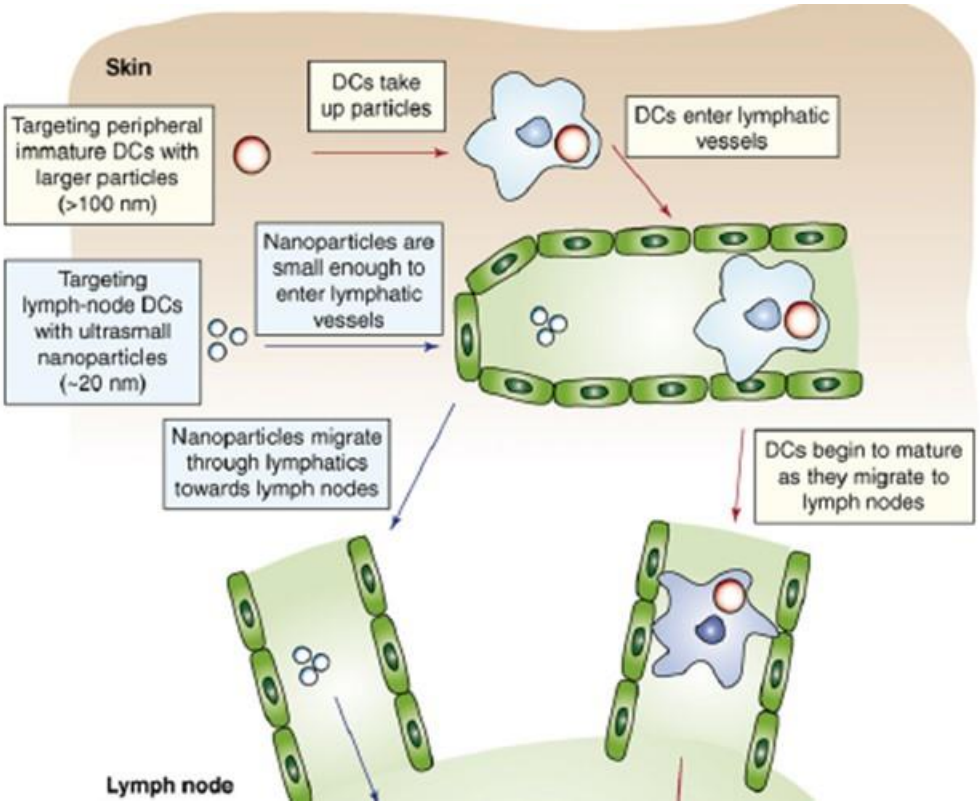

Fig. 1. 10. Size impacts nanoparticle transport into lymph nodes. Nanoparticle smaller than 100 nm freely drain into the lymphatic system and flow into local lymph nodes. Nanoparticle larger than 100 nm requires dendritic cell-mediated transport to local lymph nodes[65].

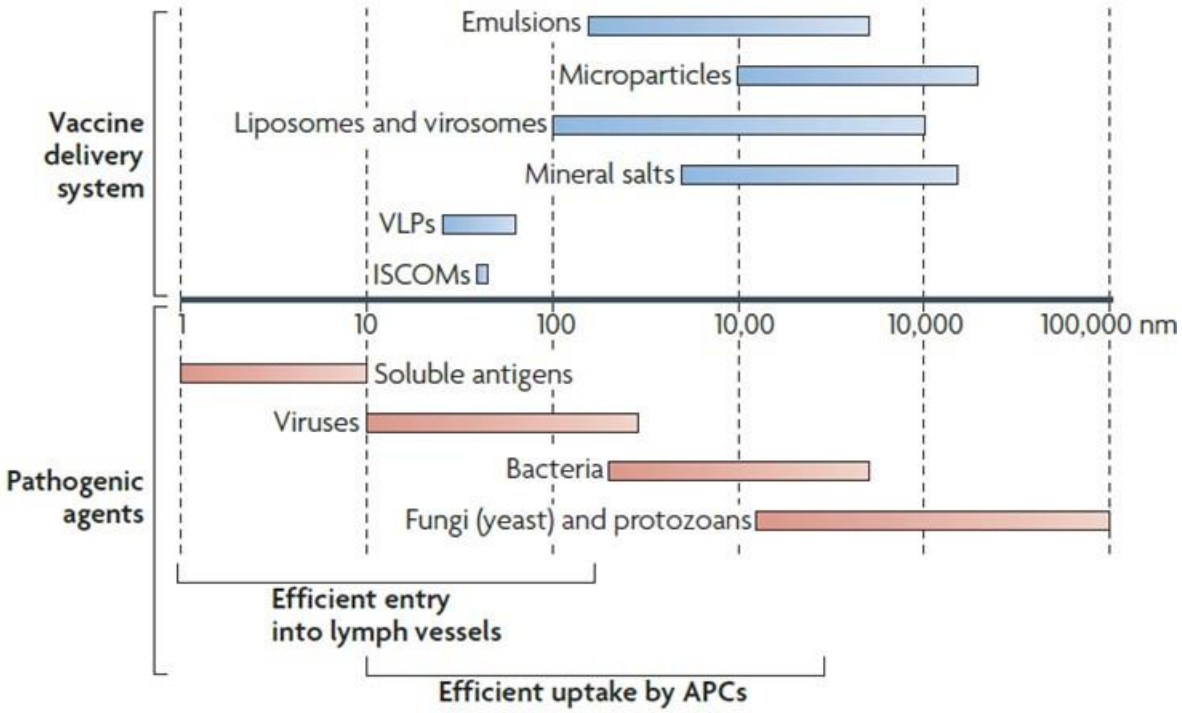

Fig. 1. 11. The size of nanoparticle delivery system and pathogenic agents. Nanoparticles smaller than 100 nm efficiently enter lymph vessels and directly flow into lymph nodes. Nanoparticles with size between 10 and 1000 nm are efficiently taken up by antigen presenting cells[36].

Complement protein adsorption on nanoparticle facilitates FDC retention

To induce germinal centers and acquired humoral immunity, larger particulate antigens of immune complexes, viruses and bacteria require opsonization by complement C3 and retention on FDC surface through complement receptor 2 (Cr2)[10,11,35,56,66,67]. Nanoparticles conjugated with HIV antigens were reported to stimulate humoral immune responses through this innate immune recognition[55]. These nanoparticles that accumulated in the FDC networks and the generated germinal centers were dependent on complement, mannose-binding lectin[55]. Loss of complement (either C3 or Cr2) prevented nanoparticle retention in lymph node follicles. Loss of mannose-binding lectin disrupted nanoparticle interaction with FDCs. This resulted in significant reduction of humoral immune responses (germinal center B cells, follicular T helper cells, antigen-specific antibody production) compared to wild type mice[55]. Complements were also suggested to mediate

humoral immune response of targeted adjuvant and polymer-based nanoadjuvants[49,68–72]. Nanoparticle surface chemistry can induce complement activation and opsonization of complement proteins *in vivo*[73,74]. The relationship between the designed nanoparticle surface chemistry and complement protein absorption *in vivo* is currently unclear. Future work should be focused on how to design nanoparticle surface chemistry to maximize the complement opsonization. This will enable maximizing nanoparticle transport to lymph node follicles and the interaction with FDCs for more efficient humoral immune responses.

Challenge of nanoparticle conjugated antigen-based vaccine

Although there are significant merits of using nanoparticles as antigen delivery vehicles, several challenges remain: (1) How can the nanoparticle and antigen be tracked? (2) How can we ensure the nanoparticle conjugated antigens are incorporated during transport at organ, intra-organ, and cellular levels? (3) How can we make sure nanoparticles do not degrade in vivo so they can bind to FDC dendrites for weeks? (4) How do lymph nodes clear nanoparticles over time? and (5) How can we ensure the antigen structure displayed on the nanoparticle performs with the same presentation and accessibility compared to antigen alone? Addressing these questions will enable us to better understand nanoparticle platform to delivery antigen. It will also provide us with the foundation to further design multifunctional nanoparticle-based vaccines for effective vaccination.

Thesis rationale

A better understanding of nanoparticle designs and their interactions with lymph nodes can guide the rational engineering of nanoparticle vaccines for efficient humoral immune responses.

Thesis hypothesis

Nanoparticle design and the role of immune cell populations mediate nanoparticle delivery and retention in lymph nodes for humoral immune responses.

Thesis objective

Understand how lymph nodes process nanoparticle vaccines for humoral immunity.

Specific aims:

1. understand how nanoparticle design influences antigen retention and presentation in lymph node follicles
2. understand the role of the immune cell populations inside lymph nodes for nanoparticle delivery into lymph node follicle
3. understand the role of the immune cell populations in the liver for nanoparticle delivery into lymph nodes after systemic administration

Chapter 2 - Nanoparticle size influences antigen retention and presentation in lymph node follicles for humoral immunity

Introduction

Efficient vaccination requires long-lived germinal center reactions to drive antibody-mediated humoral immunity [5,6,46,75]. Antigens must be retained and presented to B cells in lymph node follicles to generate an effective humoral immune response [8–10,76]. A proposed strategy is to use engineered nanoparticles to deliver antigens into follicles [8,49,54–57]. Tuning the size of nanoparticle alters its transport to the lymph node follicle [10,11,36]. 5 nm nanoparticles such as toll-like receptor agonists flow directly to lymph node follicles, whereas 100 nm nanoparticle such as viruses require cell-mediated transport into follicles [24,27–32,47–49]. Although it is generally known that lymph node physiology mediates nanoparticle transport to follicles in a size-dependent matter, it is unclear how different sizes of nanoparticles interact with cells inside follicles to influence: (1) follicular retention, (2) antigen presentation, (3) germinal center formation and (4) antigen-specific antibody production. A better understanding of the interaction of nanoparticle design with the lymph node system can guide the rational/optimal engineering nanoparticles to drive germinal center reactions that generate antibody-mediated humoral immunity for efficient vaccination.

Materials and methods

Synthesis of gold nanoparticles

5 nm gold nanoparticles (AuNPs) were synthesized according to previously developed methods [77]. In brief, 50 µL of 10% HAuCl4 (Sigma-Aldrich S4641) was diluted in 40mL of deionized H_2O. The solution was stirred and heated to 60^{o} C for 50 minutes. Meanwhile, reducing solution containing 3 mL 1% sodium citrate tribasic (Sigma-Aldrich S4641), 1.125 mL 1% (w/v) tannic

acid (Sigma-Aldrich 1401554), and 1.125 mL 25 mM potassium carbonate (Sigma-Aldrich 367877) diluted in 9.5 mL deionized H_2O was heated in a water bath at 60° C for 50 minutes. Then, 10 mL of the reducing solution was added into the $HAuCl_4$ containing flask. The reaction was maintained at 60° C for 30 minutes, followed by 100° C for 10 minutes. The solution was then cooled on ice to room temperature. 1 mL of 40 mg/mL bis(p-sulfonatophenyl)phenylphosphine dihydrate dipotassium salt (Sigma-Aldrich 698539) was added to the reaction flask and allowed to stir overnight. The next day, AuNPs were washed three times by ultracentrifugation (Beckman Coulter's Optima MAX-XP) and resuspension of the pellet in 0.02% sodium citrate tribasic, 0.02% Tween-20 (BioShop TWN510). The centrifugation speed was 150,000 g. AuNPs were then stored at 4° C before use.

15 nm AuNPs were synthesized using a method adapted from Frens [78]. In brief, 1 mL of 3% (w/v) sodium citrate tribasic was diluted in 100 mL deionized water and heated to a boil. 100 µL of 10% (w/v) aqueous $HAuCl_4$ was then added under vigorous stirring. The reaction was maintained for 10 minutes and immediately cooled on ice to room temperature. 15 nm AuNPs were then used to seed the growth of larger AuNP sizes. The synthesis of 50 nm and 100 nm AuNPs were described previously by our group [79]. Briefly, molar equivalents of sodium citrate tribasic (1.5×10^{-2} M), aqueous $HAuCl_4$ (2.5×10^{-2} M), and 15 nm AuNPs ($2\text{-}4 \times 10^{-9}$ M) were diluted in 100-500 mL deionized water at room temperature. The appropriate molar equivalent of hydroquinone (Sigma-Aldrich H17902) (2.5×10^{-2} M) was rapidly added to the solution under vigorous stirring. The reaction was maintained overnight. In the following day, 1-5 mL of 5% (w/v) Tween-20 was added to the solution and stirred for 10 minutes. AuNPs were washed two times by centrifugation and resuspension of the pellet in 0.02% sodium citrate tribasic and 0.05% Tween-20. The

centrifugation speeds ranged from 500-10000 g depending on the AuNP size. AuNPs were then stored at 4^{o} C before use.

Synthesis of nanoparticle conjugated vaccines

Nanoparticle conjugated vaccines were synthesized using different sizes of spherical AuNPs conjugated to ovalbumin (OVA) (Sigma-Aldrich A5503) antigen. Before protein conjugation, nanoparticle stock was washed once in 0.02% sodium citrate tribasic for 35 minutes. 100 mM sodium citrate tribasic solution and HCl was mixed and pH was adjusted to 2.3. This solution was then diluted to 20 mM of sodium citrate tribasic (pH 3) and mixed with 10 mg/mL pre-solubilized OVA in PBS. After that, OVA in 20 mM of sodium citrate tribasic (pH 3) was rotated for 2 hours and filtered using a 0.22 µm PES filter. AuNPs with 1.6×10^{16} nm^2 total surface area was added to 250 µL OVA solution and incubated at 37^{o} C for 1 hour. The solution was topped up to 1.2 mL with 500 µL of 1× PBS + 0.05% Tween-20 (PBST). The 5 nm AuNPs conjugated to OVA was purified using 100 kDa Amicon tube with the centrifugation speed of 4000 g for 5 minutes. The other sizes (15, 50, and 100 nm) of AuNPs conjugated to OVA was purified in 1.5 mL Eppendorf tube with centrifugation speeds of 5000, 600, and 200 g respectively for 60 minutes. OVA-AuNPs were washed three times by centrifugation using PBST buffer. OVA-AuNPs were finally resuspended in sterile PBS. OVA-AuNP vaccine was filtered using a 0.22 µm PES filter and the concentration was re-adjusted before footpad intradermal administration.

PEGylation of gold nanoparticles

AuNPs suspended in 0.02% sodium citrate tribasic, 0.02% Tween-20 were mixed with 2 kDa thiol-methoxyl heterobifunctionalized PEG (CH_3O-PEG_{2kDa}-SH) (Laysan Bio, Inc MPEG-SH-2000) and 5 kDa amine-thiol heterobifunctioanlized PEG (NH_2-PEG_{5kDa}-SH) (Rapp Polymere

135000-40-20) at a 4:1 molar ratio with a total poly(ethylene) glycol (PEG) density of 5 PEG/nm^2. The reaction was allowed to proceed in a 60^o C water bath for 1 hour. The 5 nm PEGylated AuNPs were purified in 0.1 M sodium bicarbonate (pH 8.4) and 0.05% Tween-20 buffer using ultra-centrifugation at the speed of 220,000 g for 45 minutes. 50 nm PEGylated AuNPs were purified with centrifugation speed of 2000 g for 35 minutes. The purified PEGylated AuNPs were then mixed with Cy5 NHS Ester (Click Chemistry Tools 1076-100) in a 2:1 ratio between the amounts of the 5 kDa mPEG-SH and NHS-Cy5. The reaction proceeded on a rotator overnight protected from light. Cy5 conjugated to PEG-AuNPs were purified using PBST for four times by centrifugation. Pellets were resuspended in sterile PBS before injection. PEGylated AuNPs were stored at 4^o C and protected from ambient light before use.

Physicochemical characterization of gold nanoparticles and nanoparticle vaccines

The core size of AuNPs, OVA-AuNPs, and PEG-AuNPs were characterized by transmission electron microscopy (TEM) (Fig. 2S1 and Table. 2S.1). 5 µL of nanoparticle stock was added on the plasma treated copper grids (Ted Pella 01813-F). After 3 minutes, the samples were blotted and left undisturbed for 10 minutes to be completely air-dried. To visualize the protein conjugated layer on the AuNP core, OVA-AuNP sample on the TEM grid were washed one time with 5 µL deionized water before negatively stained with 3 µL of 1% uranyl acetate (Ted Pella 19481). The stained samples were blotted after 1 minutes of staining and air dried for another 10 minutes. All samples were tested using TEM at 200 kV (Tecnai 20, FEI, Hillsboro, OR, USA) and imaged using an AMT 16000 camera. The average nanoparticle core sizes were determined by measuring over 100 particles using ImageJ (NIH, Maryland) [80]. The hydrodynamic diameters were characterized using dynamic light scattering (DLS) (Malvern Instruments Ltd., Worcestershire, UK) and UV-visible absorbance spectroscopy (UV-Vis) (Shimadzu Scientific Instruments). The surface change

was measured using Zetasizer Nano-ZS (Malvern Instruments Ltd.). The concentrations of nanoparticles were measured using UV-Vis. The conjugated OVA amount was determined by bicinchoninic acid (BCA) assay (ThermoFisher Scientific 23235).

OVA protein extraction and quantification using bicinchoninic acid assay

OVA-AuNPs (with 2 x 10^{14} nm^2 total surface area) resuspended in 25 µL PBS were added to 8 µL of 4% NuPAGE LDS buffer (ThermoFisher Scientific NP0007) and 4 µL of 500 mM dithiothreitol (DTT) (BioShop DTT001.5). This solution was incubated at 70°C for 1 hour. After 1 hour, the particles were centrifuged at 18,000 g for 15 minutes. The supernatant was retrieved and solubilized in 25 µL of 2% (w/v) sodium dodecyl sulfate (SDS) (ThermoFisher Scientific NP0001). To remove the SDS and DTT from protein isolates, 950 µL of 10% (w/v) trichloroacetic acid (TCA) (Sigam-Aldrich T6399) in acetone was added into the Eppendorf with protein isolates and incubated at -80˚C for 12 hours. The samples were centrifuged down at 18,000 g at 4˚C for 15 minutes to pellet the protein. The supernatant was discarded, and the protein pellet was resuspended in 500 µL of 0.03% (w/v) deoxychol (Sigma-Aldrich 30970) and vortexed thoroughly. 100 µL of 72% (w/v) TCA was added and incubated on ice for 30 minutes to allow protein precipitation. Samples were centrifuged again at 18,000 g at 4˚C for 15 minutes. The washed pellet was then topped up with 950 µl of acetone at -30˚C. Samples were vortexed thoroughly and incubated at -80˚C for 1 hour. The precipitated protein was centrifuged to the bottom at 18,000 g at 4˚C for 15 minutes. The supernatant was discarded and the purified protein pellet was air dried. These purified protein samples were dissolved in a 2% (w/v) SDS solution in PBS. At the same time, OVA was dissolved in the same SDS solution and diluted stepwise for the standard curve. The OVA standards and purified protein samples were incubated again at 70˚C for 1 hour. 200 µL of the bicinchoninic acid (BCA) (ThermoFisher Scientific 23235) working reagent provided in the

kit was added to samples, standards and controls. They were incubated at 60˚C for 30 minutes until a purple colour developed. The samples were cooled to room temperature and scanned on an absorbance plate reader at 562 nm (Tecan Sunrise). The estimated total protein content was calculated based on the standard curve. The final footpad injection dose was normalized based on the same total amount of OVA antigen (10 μg) for each size as determined by the BCA assay described here (Fig. 2S3).

Animal care

All animal experiments were performed according to the protocols approved by the University of Toronto Division of Comparative Medicine and Animal Care Committee (protocol numbers: 20011620, 20011910, 20012102). 6 to 10-week old wild type C57BL/6 mice were purchased form Charles River Laboratories (Montreal, Canada) and The Jackson Laboratory (Maine, USA). The genetically modified female C57BL/6 C3 (Jax stock #003641), Cr2 (Jax stock #008225) and CD19 (Jax stock #006785) knockout (KO) mice were purchased from The Jackson Laboratory. Mice were anesthetized using isoflurane (3%) carried with oxygen during injection. OVA-AuNP vaccines and PEG-AuNPs were injected into the intradermal footpads of mice using a 29-gauge insulin needle (Fig. 2S2). The injection dose was normalized to the same conjugated OVA amount (10 μg) and the injection volume was 20 μL for each footpad. 4 footpads were injected, and sentinel lymph nodes were further studied.

Histology, immunostaining and imaging

The mice were sacrificed after different injection times (from 2 hours to 8 weeks). The sentinel (axillary, brachial and popliteal) lymph nodes were collected for histological analysis. To preserve the antigens on cell membrane and on nanoparticles, the isolated fresh lymph nodes were directly

placed into frozen section compound (VWR® International, LLC 95057-838) in a plastic cryomold (Tissue-Tek® at VWR® 4565) and frozen with liquid nitrogen. The frozen samples were taken to the Toronto Centre for Phenogenomics (TCP) on dry ice for further sample processing. 8 μm tissue sections were cut on Cryostar NX70 and placed on charged slides. Tissue sections were stained using silver enhancement kits (Ted Pella, Inc. 15718) to enhance gold nanoparticle signal. For immunostaining, tissue sections were stained for follicular dendritic cells (FDCs) using anti-CD21 antibody (Abcam 75985) and/or anti-FDC-M1 antibody (BD Biosciences 551320), for B cells using anti-B220 antibody (eBioscience 14-0452-82), and for subcapsular sinus macrophages using anti-sialoadhesin (CD169) antibody (Abcam 53443). To verify if OVA antigen is still intact with gold nanoparticles, tissue sections were stained with anti-ovalbumin antibody (FITC) (Abcam 85584) to visualize OVA antigens location. To verify germinal center formation, tissue sections were stained with anti-GL7 antibody (FITC) (BioLegend 144604). Tissue sections were then counter stained with DAPI.

The stained tissue sections were scanned using an Olympus VS-120 slide scanner and imaged using a Hamamatsu ORCA-R2 C10600 digital camera for all bright-field, fluorescent and dark-field images. The bright-field images of silver stained nanoparticles in lymph node follicles were quantified using ImageJ (NIH) [80]. The threshold of all silver stained images was set up the same value for each. The total area of the silver stained area was then determined and compared across all conditions. To colocalize gold nanoparticle signal and immunostaining, dark-field images were used based on the scattering intensity from gold nanoparticles. Dark-field images [81] of gold nanoparticle signal were used to colocalize the distribution of FDC networks, and OVA antigens in lymph node follicles.

Tissue clearing

Lymph node tissues were processed for tissue clearing as previously described [82]. Briefly, lymph nodes were extracted and placed into hydrogel monomer solution containing 4% formaldehyde (Bioshop Canada Inc. FOR201.500), 2% w/v acrylamide (Bioshop Canada Inc AB1032), and 0.25% w/v VA-044 azo initiator (Wako Chemicals VA-044) in 1× PBS. The lymph nodes were incubated in the hydrogel monomer solution for 7 days at 4°C. To crosslink the hydrogel monomer within the tissues, fresh hydrogel monomer solution was added to the samples, and then samples were degassed and purged with argon gas. The samples were incubated at 37°C for 3 hours. The hydrogel embedded lymph nodes were rinsed with PBS and then incubated in clearing solution containing 4% w/v SDS in 200 mM sodium borate solution (pH 8.5 with 0.1% Triton-X 100 (Sigma-Aldrich X100) and 0.01% sodium azide (Bio Basic DB0613)) for 5 days at 50°C. Samples were then placed in borate solution for storage at 4°C.

Immunostaining of cleared tissues and three-dimensional light-sheet imaging

Immunostaining of cleared tissue was performed by blocking lymph node tissues with blocking buffer containing 5% w/v bovine serum albumin (BSA) (Sigma-Aldrich A9418) in PBS, 0.1% Triton X-100, 0.01% sodium azide. Lymph nodes were left in blocking solution at room temperature overnight. Next, primary CD21 antibody (Abcam 75985) was added to lymph nodes at a 1:100 dilution in 1 mL of PBS with 2% v/v goat serum, 0.1% Triton X-100, and 0.01% sodium azide solution and incubated at room temperature for 2 days. Tissues were then washed for 24 hours with PBS, 0.1% Triton X-100, 0.01% sodium azide solution to remove excess primary antibody. Cy5 conjugated secondary antibody was then incubated with the lymph nodes at a 1:200 dilution as well as with DAPI (Sigma-Aldrich D9542) at a final concentration of 10 μM in 2% v/v goat serum, PBS, 0.1% Triton-X 100, 0.01% sodium azide for 2 days at room temperature. The

stained tissues were then washed with PBS, 0.1% Triton-X 100, 0.01% sodium azide solution for 24 hours to remove excess stain. Tissues are placed in 67% 2'2-thiodiethanol (TDE) solution in 200 mM sodium borate, 0.1% Triton-X, 0.01% sodium azide solution for refractive index matching prior to light-sheet imaging. 3D light-sheet imaging of the cleared and stained lymph nodes was performed using the Zeiss Light-sheet Z.1 microscope using the CLARITY Plan-Neofluar Objective, 20X, NA 1.0, refractive index of 1.45 in 67% TDE solution. Standard emission and filter lines were used for DAPI and CD21 detection. Dark-field imaging of gold nanoparticles was done as previously described by detecting scattering intensity from the metallic nanoparticles [81]. The 3D images were visualized using Bitplane IMARIS version 8.1.

TEM study on lymph node tissues

TEM was used to visualize the localization of nanoparticle distribution around FDCs in lymph node follicles at the subcellular level. The mice were sacrificed after different injection times (from 2 hours to 8 weeks). The sentinel lymph nodes were collected and directly fixed with 0.5% formaldehyde and 4% glutaraldehyde (Sigma-Aldrich 340855) in PBS at room temperature for 1 hour. The samples were then stored at 4°C. Fixed lymph node samples were sent to the Nanoscale Biomedical Imaging Facility at The Hospital for Sick Children for further processing. The lymph node samples were mounted and sectioned, then placed on copper grids. Samples were then negative stained with 2% uranyl acetate (Ted Pella 19481). The morphology of FDCs and nanoparticle localization of lymph node sections were imaged using TEM at 200 kV. The numbers of nanoparticles on FDC dendrites were quantified using TEM images. In brief, the area (um^2) of FDC dendrites were measured using ImageJ (NIH) [80]. The total numbers of gold nanoparticle within the area of FDC dendrites were calculated using ImageJ by setting up the same threshold value. The numbers of OVA protein conjugated on different sizes of AuNPs were previously

quantified using BCA (Fig. 2S3). The total amount of conjugated antigen on FDC dendrites for each size was then calculated.

Lymph node disaggregation and cell staining and flow cytometry

Total number of GL7+B220+ germinal center B cells were quantified using flow cytometry. The mice were immunized using different sizes of OVA-AuNP vaccines and sacrificed at 5 weeks. The sentinel lymph nodes were isolated and mechanically disaggregated using a razor blade. After that, these lymph nodes were enzyme disaggregated into single cell suspension using 4790 µL of Hanks' Balanced Salt Solution (HBSS) buffer (ThermoFisher Scientific 14185052) with 200 µL of 10 mg/ml collagenase IV (Sigma-Aldrich C5138) and 10 µL of 10 mg/mL of DNase (Roche 10104159001) in an Eppendorf tube. These samples were incubated and rotated at 37°C for 30 minutes. The disaggregated lymph node cells were passed through a 70 µm cell strainer and centrifuged at 300 g at 4°C for 10 minutes. The supernatant was discarded, and cell pellet was resuspended in HBSS blocking buffer supplemented with 0.5% (w/v) bovine serum albumin and 2 mM EDTA. Cell suspension was stained with fluorescent labelled antibodies. Anti-CD16/32 antibody (BioLegend 101302) was used for Fc receptor blocking. Antibodies stained for germinal center B cells including: Zombie NIR Live/Dead stain (BioLegend 423106), BV510 anti-B220 (RA3-6B2) (BioLegend 103247), and Alexa Fluor® 647 anti-GL7 (BioLegend 144606). Cells were stained on ice for 30 minutes and followed by 2 washes using HBSS blocking buffer. Cells were then fixed using 1.6% paraformaldehyde (Thermo Fisher Scientific 28906) in HBSS on ice for 30 minutes. Cells were resuspended in blocking buffer for flow cytometry. Cell stain events were acquired using a 5-laser BD LSR FORTESSA X-20 flow cytometer. Cell stain events were analyzed using FlowJo V10 software.

ELISA of OVA-specific antibody production

OVA-specific antibody production was measured in the sera using enzyme-linked immunosorbent assay (ELISA) after immunization of different sizes of OVA-AuNP vaccines at 5 weeks. 100 µL of OVA with a concentration of 20 µg/mL was pre-coated on MaxiSorp 96-well plate (Thermo Fisher Scientific 442404) at 4°C overnight. The solution was discarded, and the wells was washed one time with 400 µL of PBST. After discarding the washing PBST, 200 µL of 1× casein buffer (Sigma-Aldrich B6429-500ML) was added to block the wells at room temperature for 2 hours. The solution was discarded and washed one time with PBST. To perform serial dilution of the sera, 100 µL of 0.5× casein buffer was added into the lanes except the 1st one. The serum samples were first diluted 100 times with 0.5× Casein buffer and then added into the 1st lane of the plate (200 µL). The samples were then serially diluted until the second final lane. The last lane was kept as a control without serum samples. Samples were then incubated at room temperature for 1 hour. The wells were washed two times using PBST. Goat anti-mouse IgG secondary antibody, horseradish peroxidase (HRP) (Thermo Fisher Scientific 31430) was diluted 5000 times. The diluted HRP solution (100 µL) was then added into wells and incubated at room temperature for 1 hour. The wells were washed two times using PBST. 100 µL TMB (3,3',5,5;-tetramethylbenzidine) chromogen solution (Thermo Fisher Scientific 002023) was added into each well and incubated at room temperature for 20 minutes. The blue color was developed, and the reaction was terminated by adding 1 M sulfuric acid (100 µL). The absorbance was measured using an absorbance plate reader at 450 nm (Tecan Sunrise). The reference was setup at 570 nm. All titers reported are inverse dilutions where $A_{450\ nm}$ - $A_{570\ nm}$ equals 0.1.

Modified ELISA of C3 protein absorbed on nanoparticles

C3 absorption on nanoparticles were measured using a modified ELISA [55]. 5 nm and 50 nm OVA-AuNP vaccines were pre-coated onto MaxiSorp 96-well plate overnight at 4°C. The pre-coated concentration was normalized by 5 μg/mL of OVA in 50 μL of PBS. The solution was discarded, and the wells were washed one time with PBST. 1× casein buffer was used to block the wells at room temperature for 2 hours. The wells were washed one time with PBST. 30% serum from wild type mice was added to each well and allowed to incubate at 37°C for 1 hour. Plates were washed two times. 1× HRP-conjugated anti-mouse complement C3 antibodies (Abcam 157711) were added into the wells and incubated at room temperature for 1 hour. The wells were then washed two more times using PBST. TMB was added into the wells and incubated at room temperature for 20 minutes. The reaction was stopped by adding sulfuric acid. The absorbance was then measured using a plate reader at 450 nm with the reference of 570 nm. The optical density (OD) at 450 nm was determined.

To verify the C3 absorption on nanoparticles in vivo, OVA-AuNP vaccines were injected intradermally into the footpads of mice. The mice were sacrificed, and sentinel lymph nodes were isolated after 1 and 6 hours post-injection for 5 and 50 nm OVA-AuNP vaccines. These sentinel lymph nodes were mechanically disaggregated using a razor blade and passed through a 70 μm cell strainer and centrifuged at 300 g at 4°C for 10 minutes. The supernatant was collected and washed three times using HBSS buffer. To isolate the nanoparticles, samples of 5 and 50 nm OVA-AuNPs were centrifugated with the speeds of 80,000 g and 600 g respectively for 60 minutes. The supernatant was discarded and nanoparticles were purified using PBST 3 times. The concentration of OVA-AuNPs was measured using UV-Vis and 5 μg/mL of OVA normalized nanoparticles in 50 μL of PBS was coated on MaxiSorp 96-well plate at room temperature for 12 hours. Using the

same protocol of in vitro modified ELISA, 1× Casein buffer was used to block the wells at room temperature for 2 hours. Plates were washed two times. 1× HRP-conjugated anti-mouse complement C3 antibody was added into wells and incubated at room temperature for 1 hour. After washing using PBST, TMB was added to establish the reaction for 20 minutes. The reaction was terminated by adding sulfuric acid. The OD was measured at 450 nm using a plate reader.

Statistical analyses

Data was collected from 4-8 mice per group. All statistical analyses and graphing were performed using GraphPad Prism 6.0. Data were analyzed using one-way ANOVA followed by Tukey's multiple comparisons test or an unpaired t test. Data are presented as mean ± SD. $P < 0.05$ is defined as significant: $*P < 0.05$; $**P < 0.01$; $***P < 0.001$; $****P < 0.0001$.

Results and discussion

We first studied the relationship between nanoparticle size and follicle retention in the lymph node. We synthesized a model nanoparticle vaccine composed of different sizes of spherical gold nanoparticles (AuNPs) conjugated to ovalbumin (OVA) antigen. The full characterization of the nanoparticle physicochemical properties is described in Fig. 2S1 and Table 2S.1. We chose AuNPs because: (1) they can be easily synthesized with broad and precise sizes in the 2 to 100 nm size range, (2) they are non-degradable that allows long-term tracking at the organ and cellular levels, and (3) they can be coated with multiple molecules which enables them to be used as an adjuvant and delivery vehicle for antigen peptides or proteins [83–87]. These sub-100 nm nanoparticles should transport from the injection site to sentinel lymph nodes through the lymphatics[16,20,36,64] (Fig. 2.1A). We expect the size of the nanoparticles mediates their kinetics, binding, and other interactions with cells and biological structures in the lymph nodes. Once nanoparticles enter the afferent lymphatic

vessel of a lymph node, they need to pass a two-layer filter system [22,23], subcapsular sinus macrophages and lymphatic sinus endothelial cells, before entering lymph node follicles and interacting with B cells (Fig. 2.1B). We administered our model OVA-AuNP vaccine through intradermal footpad injections into C57BL/6 mice (Fig. 2.1A). The injection dose was normalized based on the same total amount of OVA (10 μg) for each size (Fig. 2.S1 and S2). The normalizing of dosing in our study enable us to test the impact size of nanoparticles on their lymph node interaction. We sacrificed the mice after different injection times (from 2 hours to 8 weeks) and collected the axillary, brachial and popliteal as sentinel lymph nodes for histological analysis (Fig.2.1B). We stained the sample with silver to enhance the AuNP signal on the tissue. We observed a clear difference between different nanoparticle sizes and their intra-lymph node transport and retention in follicles (Fig. 2.1C, S3). The smaller OVA-AuNPs (5-15 nm) appeared in the follicles within 2 hours but were cleared in the next 48 hours. The larger OVA-AuNPs (50-100 nm) accumulated in subcapsular sinus at 2 hours. They required a longer time to accumulate in follicles and were retained for over 5 weeks (Fig. 2.1D). The 50-100 nm OVA-AuNPs showed greater retention than the 5-15 nm ones after 48 hours of injection. 50 nm OVA-AuNPs shows 19-fold and 4-fold greater amounts of nanoparticles accumulated in lymph node follicles than 5 nm and 15 nm OVA-AuNPs at 48 hours (Fig. 2.1E). These results confirmed a clear relationship between nanoparticle size and lymph node follicle retention.

We determined the lymph node cells involved with the retention of nanoparticles. We know from previous studies that follicular dendritic cells (FDCs) are resident stromal cells that form networks located in the follicle centers and are the only known cell type that acquire and retain naïve antigens for months [35,37,40–42]. FDC networks reserve these naïve antigens and present to B cells for B cell

activation and generate germinal center reactions [8,9,11,43–45]. Therefore, FDCs were a logical candidate to mediate both the sequestration and retention of OVA-AuNPs inside lymph node follicles. The mice were sacrificed at the peak OVA-AuNP accumulation times in lymph node follicles (2 hours for 5 and 15 nm OVA-AuNPs, and 48 hours for 50 and 100 nm OVA-AuNPs). To preserve the antigens on cell membrane, the isolated fresh lymph nodes were directly placed into frozen solution in a plastic cryomold and frozen with liquid nitrogen. 8 μm tissue sections were cut and placed on charged slides. Tissue sections were stained using silver enhance kits to enhance gold nanoparticle signal and antibody immunostaining for FDCs and other cell types. We found the AuNP signal (silver staining) colocalized with the networks of CD21+ FDCs in the 5-15 nm (Fig. 2.2A, and Fig. 2S4A) and the 50-100 nm OVA-AuNP (Fig. 2.2B, and Fig. 2S4B) tissue samples. This cell is highlighted by the green colour staining in Fig. 2.2A-B and Fig. 2S4. To verify the histology stain for FDCs, we co-stained this cell type using another FDC-M1 antibody (Fig. 2.2C). FDC-M1 (red colour) and CD21 (green colour) stains are colocalized on FDCs. We also show that T cells (CD3+), tingible body macrophages (CD68+), and dendritic cells (CD11c+) are not the major cell types involved in sequestration of the OVA-AuNPs (Fig. 2.2D). This is because these stained immune cells (brown colours) are not corresponding to the area of OVA-AuNP signals (Silver staining). We confirmed this conclusion using 3D images of lymph nodes after CLARITY processing [81,82]. The results show that FDCs formed network clusters (green colour) and OVA-AuNPs (red colour) were colocalized in these FDC networks (Fig. 2S5). Our results confirmed the role of FDCs in mediating the retention of nanoparticles inside of the lymph node follicle.

We further analyzed whether the nanoparticles are inside the FDCs or on their dendrites. The mice were sacrificed after the peak OVA-AuNP accumulation times in lymph node follicles. The sentinel lymph nodes were collected and directly fixed with 0.5% formaldehyde and 4% glutaraldehyde in PBS. The fixed samples were mounted and sectioned, then placed on copper grids. The sample sections were negative stained with 2% uranyl acetate. The morphology of FDCs and nanoparticle localization of lymph node sections were imaged using transmission electron microscopy (TEM) at 200 kV. TEM analysis showed that the residence of OVA-AuNPs in or out of the FDCs is size-dependent (Fig. 2.3A-B). The 5 nm OVA-AuNPs are internalized in the endolysosome-like structures of FDCs while the 50-100 OVA-AuNPs are aligned on the FDC surfaces or dendrites (Fig. 2.3C). The 15 nm OVA-AuNPs can inside the FDC or on the FDC surface. While the 5 nm OVA-AuNPs were trapped in endolysosome-like structures (Fig. 2.3A), interestingly, we observed instances where the endolysosomal membrane were disrupted and 5 nm OVA-AuNPs were found in the cytoplasm (Fig. 2.4A). This is shown by the green arrow. We also found extracellular vesicles containing 5 nm OVA-AuNPs (red circles) attached to the FDC surface (Fig. 2.4A). These results suggest that 5 nm OVA-AuNPs can be cleared by FDCs through endolysosomal escape or extracellular vesicles within 48 hours. These cleared 5 nm OVA-AuNPs by FDCs were further eliminated from lymph node follicles (Fig. 2.1C). In contrast, the 50-100 nm OVA-AuNPs remained on the surface of the FDCs, with most of them residing on the dendrites (Fig. 2.4B). They were retained on the dendrites for a few weeks. We conclude that the size of the nanoparticles determines when they are taken up by the FDCs or resided on the cell surface and dendrites.

Next, we tested how nanoparticle size mediates antigen presentation on FDC dendrites. We administered different sizes of OVA-AuNPs through intradermal footpad injections into C57BL/6 mice and sacrificed the mice at 48 hours. The sentinel lymph nodes were isolated and fixed. We sectioned the lymph node tissues and placed on copper grids for TEM study. TEM revealed that B cells were surrounded by FDC dendrites containing the OVA-AuNPs (Fig. 2.5A-B). The FDC dendrites deposited with OVA-AuNPs grip B cells that facilitates the interaction of conjugated-antigen and B cell receptors. There were significantly more 50 and 100 nm OVA-AuNPs on FDC dendrites than 5 nm OVA-AuNPs at 48 hours (Fig. 2.5C-E). In addition, 100 nm AuNPs can conjugate 317-fold and 100-fold more OVA than the 5 and 15 nm AuNPs, respectively (Fig. 2S2). This leads to 175-fold more OVA bound to the FDC dendrites by the 100 nm AuNPs in comparison to the 15 nm AuNPs (Fig. 2.5F). This result suggests 50-100 nm OVA-AuNPs can present more antigen on FDC dendrites to B cells.

This allowed us to test if the 50-100 nm OVA-AuNPs would induce more humoral immune responses over the smaller 5-15 nm OVA-AuNPs. We immunized the mice using different sizes of OVA-AuNP vaccine and sacrificed the mice at 5 weeks. The isolated lymph nodes were frozen in a plastic cryomold. The lymph node tissue sections were cut and stained with anti-OVA antibody for OVA and other antibodies for immunostaining. Our result shows that 100 nm AuNPs were still colocalized with OVA in the follicles, confirming that the OVA remained conjugated to the AuNPs after 5 weeks of injection (Fig. 2.6A). We first observed germinal center generation as a measurement of humoral immune response. We performed histological analysis for germinal centers using an anti-GL7 stain. We observed that 100 nm OVA-AuNPs can induce germinal centers (red colour) that attach FDC networks (green colour) and 100 nm OVA-AuNPs are still

colocalized with FDC networks after 5 weeks of immunization (Fig. 2.6B). We performed histology for all sizes. The 50 and 100 nm OVA-AuNPs could induce germinal centers (red colour), whereas the 5 nm OVA-AuNPs failed to generate robust germinal center reactions (Fig. 2.6C-D). We further quantified the total number of GL7+B220+ germinal center B cells by disaggregation of the lymph node into single cells for flow cytometry (Fig. 2.6E-F, 2S6). We found that the 100 nm OVA-AuNPs generated 5-fold more germinal center B cells than 5 nm OVA-AuNPs (Fig. 2.6F). These findings confirm that the retained 50 and 100 nm OVA-AuNPs on FDC dendrites can induce greater stimulation of germinal center reactions, and proliferation of germinal center B cells. Next, we quantified the amount of OVA-specific antibody in the sera using enzyme-linked immunosorbent assay (ELISA) to determine if the 100 nm OVA-AuNPs elicited greater antigen-specific antibody production. 5-fold more OVA-specific antibody was produced in response to 100 nm OVA-AuNPs than the 5 nm OVA-AuNPs (Fig. 2.6G). We conclude that the conjugation of OVA to the 50-100 nm nanoparticle can induce greater humoral immune responses than the 5-15 nm nanoparticles because more conjugated antigens are bound and presented on FDC dendrites to stimulate B cells.

While OVA is involved in generating an antigen-specific immune response, we were curious to know why the nanoparticles are bound to receptors on the FDCs. Our recent study showed that nanoparticles opsonize serum proteins when they are administered into the animal[74]. Previously, we used mass spectrometry to identify the adsorbed proteins. Thus, we have a list of candidates that can be tested to identify the specific proteins that may be responsible for the receptor-ligand interaction. We hypothesize that complement C3 was opsonized on the nanoparticle surface and this ligand is responsible for its interaction with the FDC through complement receptor 2 (Cr2)

(Fig. 2S7). This hypothesis is built on previous findings that virus and bacteria require opsonization by complement C3 [10,11,35,66,67]. We performed experiments with C3 and Cr2 knockout mice, and used CD19 knockout mice as a negative control. It has been shown previously that inhibition of CD19 receptors disables B cell stimulation and germinal center formation [88,89]. Here, we expected that even OVA-AuNPs retained and presented on FDC dendrites, OVA-AuNPs should not induce humoral immune responses in CD19 knockout mice. We injected the C3, Cr2 and CD19 receptor knockout mice with 50 nm OVA-AuNP vaccines and sacrificed the mice after 48 hours and 5 weeks, respectively (Fig. 2.7A-F). We determined a loss of complement (either C3 or Cr2) prevented OVA-AuNP retention in follicles (Fig. 2.7A and 7D) and OVA-AuNP presentation on FDC dendrites (Fig. 2.7B and 7E) at 48 hours. We determine that a loss of C3 protein failed to induce germinal centers at 5 weeks (Fig. 2.7C). Both complement knockout mice (C3 protein and Cr2) produced significantly lower numbers of germinal center B cells than wild types and showed no significant difference compared to CD19 knockout mice at 5 weeks (Fig. 2.7F). These results show that C3-Cr2 ligand-receptor pair assists the retention and presentation of OVA-AuNPs on the FDCs, leading to germinal center reactions. We then tested for OVA-specific antibody production using ELISA. Surprisingly, we found loss of complements did not limit OVA-specific antibody production (Fig. 2S8). The mechanism is unknown and will be explored later. To test if nanoparticle opsonization by C3 is based on nanoparticle size, we designed a modified ELISA experiment where different sizes of OVA-AuNPs were pre-coated onto plates and incubated with wild type mice sera. Our results show that 50 nm OVA-AuNPs have greater C3 deposition than 5 nm ones *in vitro* (Fig. 2S9). To verify that OVA-AuNPs follow the same principle *in vivo*, we performed the same ELISA experiment on 5 nm and 50 nm OVA-AuNPs isolated from lymph nodes *in vivo* at 1 and 6 hours post-injection. Similarly, we found

more C3 adsorbed onto 50 nm OVA-AuNPs than 5 nm ones (Fig. 2.7G). These results suggest that larger OVA-AuNPs are opsonized by complements more than smaller ones, leading to enhanced nanoparticle retention, antigen presentation on FDC dendrites and more robust germinal center reactions.

Conclusion

In this study, we discovered that the physiology of the lymph node determines the kinetics and cellular interaction of the nanoparticles. Sub-100 nm nanoparticles can transport through the lymph node. However, the intra-lymph node fate is determined by the size. The 5-15 nm nanoparticles can enter the FDCs while the 50-100 nm remained on the surface. The binding of the nanoparticles to the dendrites were greater with the 50-100 nm. Our study reveals the mechanism of how lymph node follicles process different nanoparticle sizes. This provides us with fundamental knowledge on how biological selection of antigens occurs and functions. Our report provides results for gold nanoparticles with OVA only. The role of organic or inorganic synthetic nanoparticles with other antigens on how to shape the acquired immune responses should be fully assessed in the future as well. The results of these findings will guide the rational design of antigen-conjugated synthetic nanoparticles in mediating FDC interaction for more effective vaccine development.

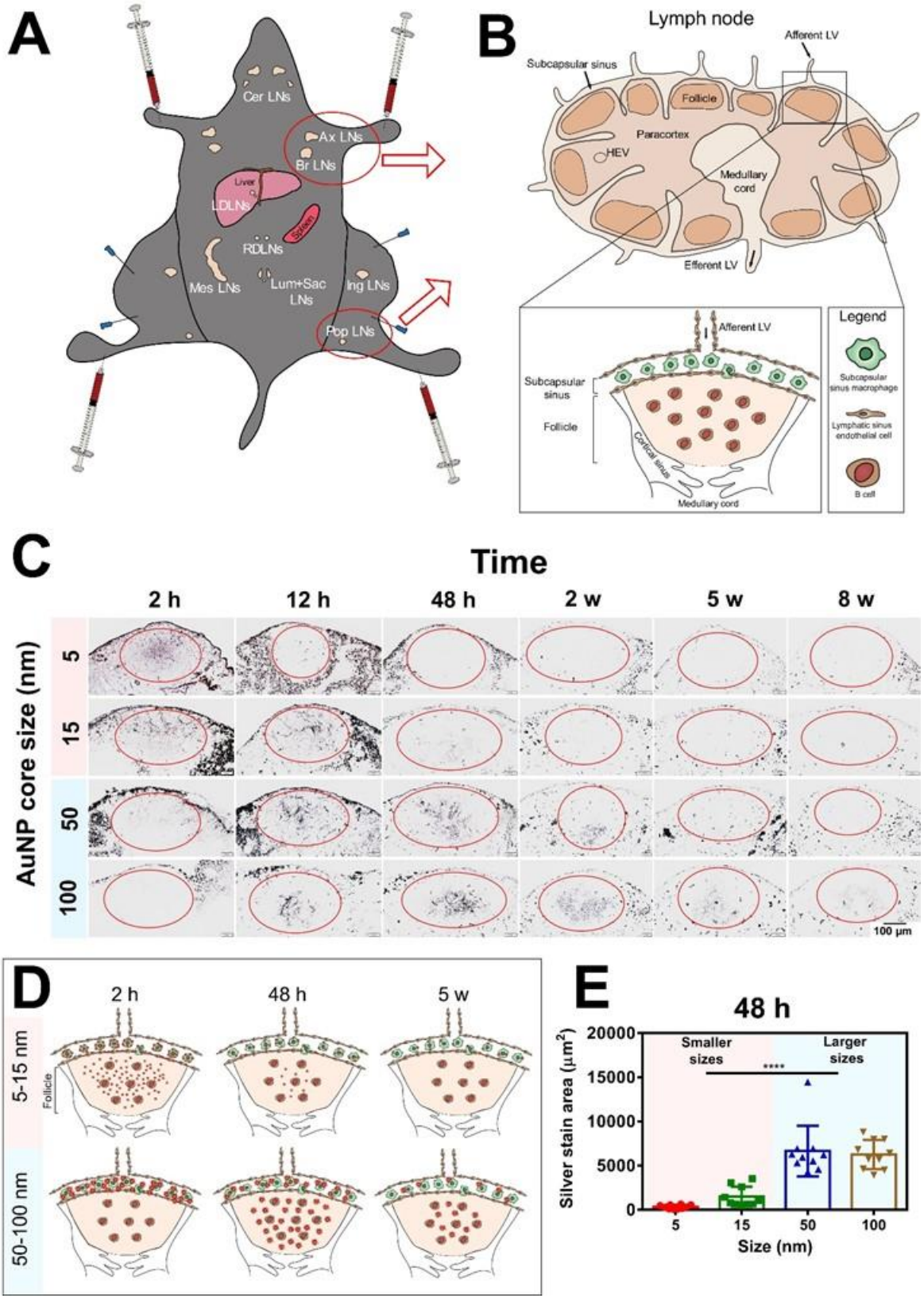
A
Cer LNs
Ax LNs
Br LNs
Liver
LDLNs
Spleen
RDLNs
Mes LNs
Lum+Sac LNs
Ing LNs
Pop LNs
B
Lymph node
Afferent LV
Subcapsular sinus
Follicle
Paracortex
HEV
Medullary cord
Efferent LV
Legend
Subcapsular sinus macrophage
Lymphatic sinus endothelial cell
B cell
Cortical sinus
C
Time
2 h
12 h
48 h
2 w
5 w
8 w
AuNP core size (nm)
5
15
50
100
100 µm
D
2 h
48 h
5 w
5-15 nm
50-100 nm
Follicle
E
48 h
Smaller sizes
Larger sizes
****
Silver stain area (µm²)
20000
15000
10000
5000
0
5
15
50
100
Size (nm)

Fig. 2. 1. Lymph node follicles clear smaller nanoparticles and retain larger ones. (**A**) Schematic of lymph node distribution. OVA-AuNPs were injection into C57BL/6 mice through intradermal footpad administration. Axillary (Ax), brachial (Br) and popliteal (Pop) lymph nodes are defined as sentinel lymph nodes. (**B**) Schematics of a lymph node that are made of subcapsular sinus, follicle, paracortex and medullary cord areas. Lymph nodes are considered as a two-layer size-selective filter system that comprised of subcapsular sinus macrophages and lymphatic sinus endothelial cells before entering B cell follicle. (**C**) Histological images of different OVA-AuNP sizes cleared or retained in lymph node follicles after 2 hours to 8 weeks post intradermal footpad injection into C57BL/6 mice (n = 4 mice/group). Lymph node follicles of sentinel lymph nodes were collected. Data collected from 10 lymph node follicles (n = 4). The injection dose was normalized based on the same OVA antigen amount (10 μg) for each size. (**D**) Schematic of the size-dependent OVA-AuNP transport kinetics. The 5-15 nm OVA-AuNPs appeared in the follicles within 2 hours but are cleared in the next 48 hours. The 50-100 nm OVA-AuNPs accumulated at subcapsular sinus at 2 hours. They had the delayed follicle accumulation and were retained for over 5 weeks. (**E**) Quantification of different sizes of OVA-AuNP accumulation in follicles at 48 hours post-injection. Graphs represent mean ± SD; ****P < 0.0001. All P values from one-way ANOVA followed by Tukey's multiple comparisons test.

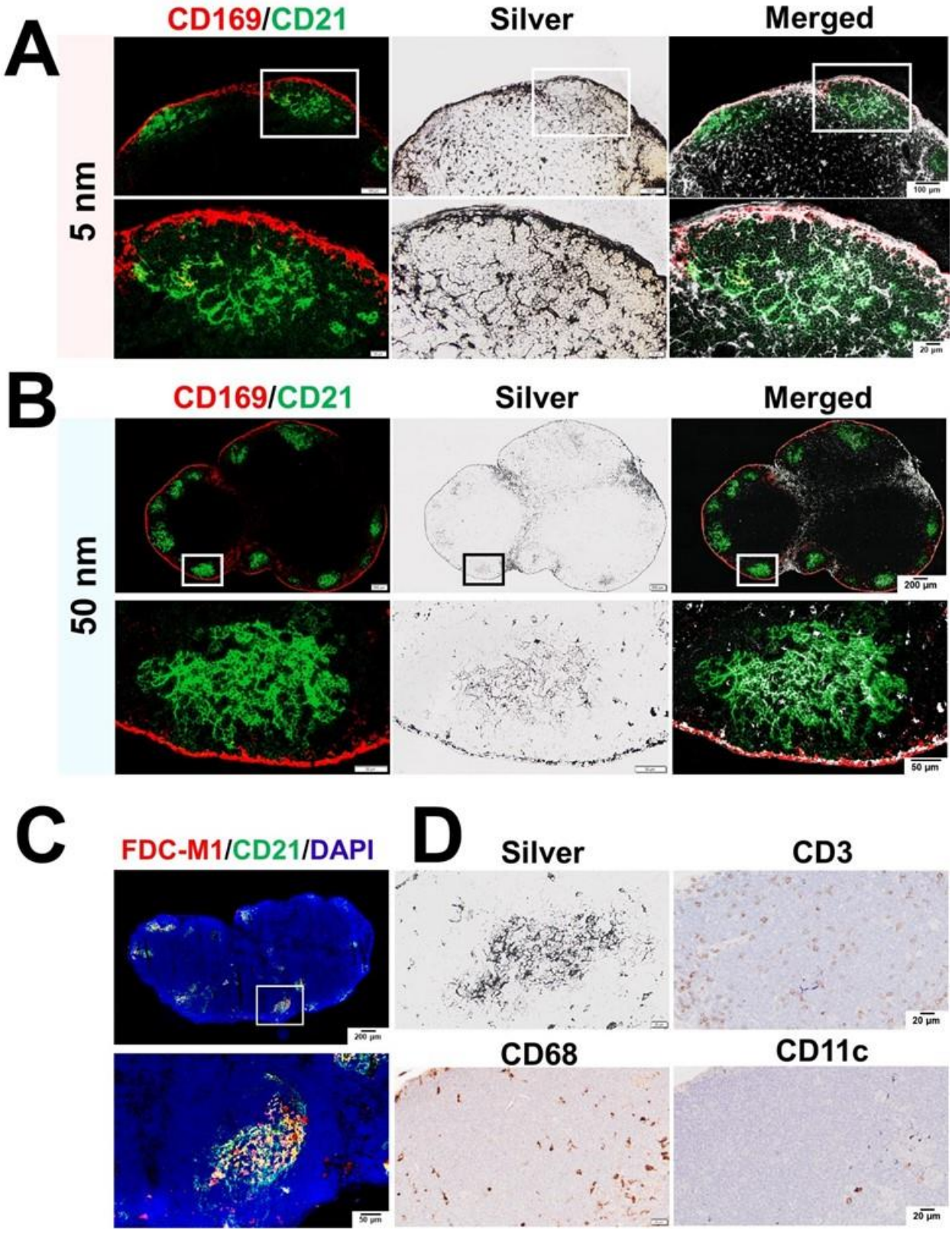
A
CD169/CD21
Silver
Merged
5 nm
100 μm
20 μm
B
CD169/CD21
Silver
Merged
50 nm
200 μm
50 μm
C
FDC-M1/CD21/DAPI
200 μm
50 μm
D
Silver
CD3
20 μm
CD68
CD11c
20 μm

Fig. 2. 2. FDC networks involved in nanoparticle sequestration in lymph node follicles. Histology of (**A**) 5 nm and (**B**) 50 nm OVA-AuNP sequestration in lymph node follicles associated with FDC networks at 2 hours and 48 hours post intradermal footpad injection. Gold nanoparticle signals colocalized in the area of FDC networks (CD21 green; CD169 red; Silver black). (**C**) Validation of antibody staining for FDCs in lymph node follicles. FDC-M1 (red) and CD21 (green) stains colocalized on FDCs. (**D**) OVA-AuNP signals are not colocalized with T cells (CD3) (brown), tingible body macrophages (CD68) (brown), and dendritic cells (CD11c) (brown), indicating that they are not majorly involved in sequestration of OVA-AuNPs in lymph node follicles.

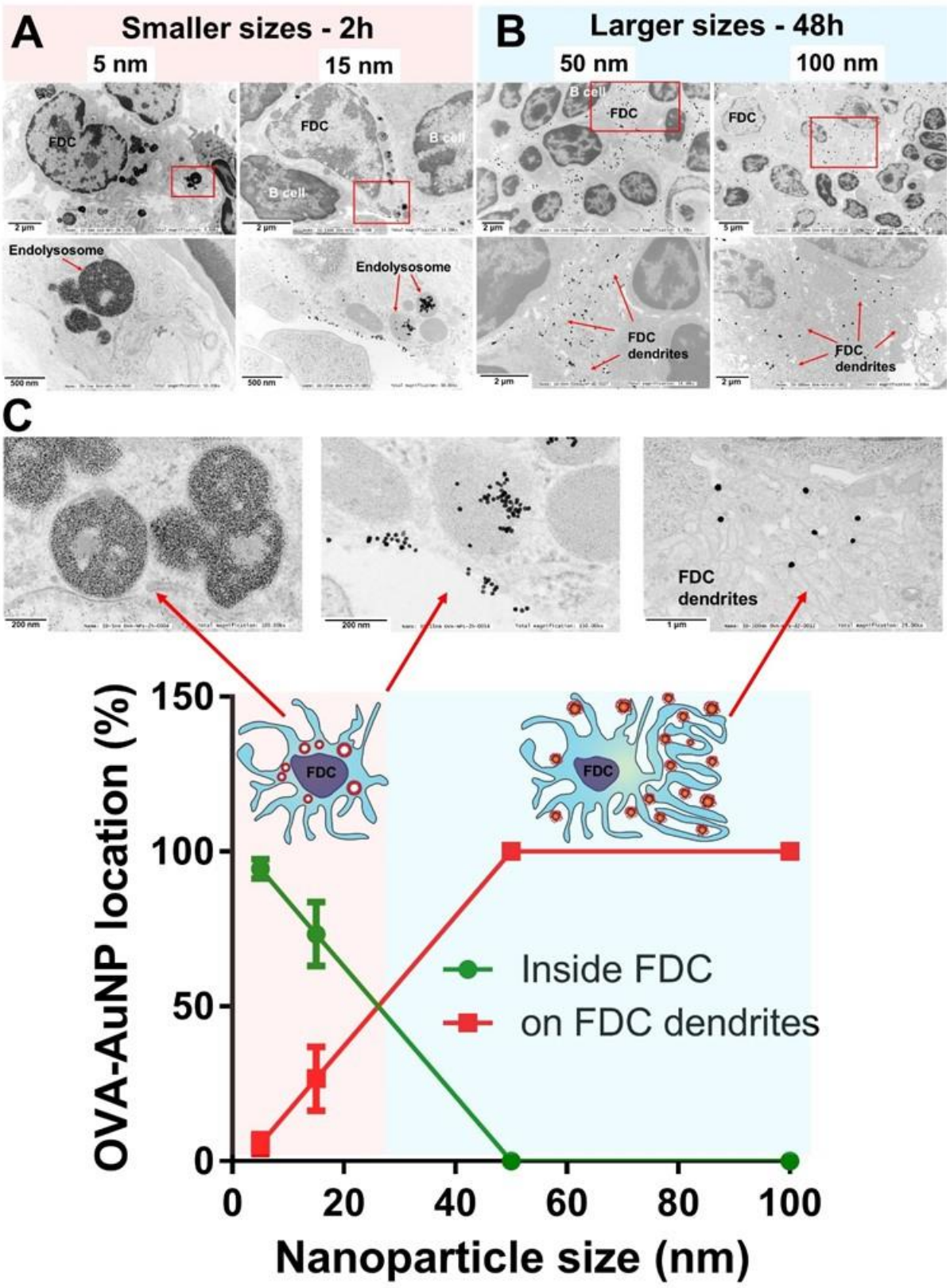
A
Smaller sizes - 2h
5 nm
15 nm
B
Larger sizes - 48h
50 nm
100 nm
FDC
B cell
Endolysosome
FDC dendrites
C
OVA-AuNP location (%)
Nanoparticle size (nm)
Inside FDC
on FDC dendrites
0
50
100
150
0
20
40
60
80
100

Fig. 2. 3. FDCs internalize smaller nanoparticles and align larger nanoparticles on their surfaces and dendrites. (**A**-**B**) Representative TEM images of nanoparticle location associated with FDCs in a size-dependent manner. TEM study was performed at different times of post-intradermal footpad injection (the 5-15 OVA-AuNPs at 2 hours; the 50-100 nm OVA-AuNPs at 48 hours). (**A**) The 5 nm OVA-AuNPs preferred to be internalized by FDCs (red arrows point to endolysosomes), and (**B**) The 50-100 nm OVA-AuNPs preferred to be aligned on FDC surfaces and dendrites (red arrows point to FDC dendrites). (**C**) Quantification of nanoparticle location either inside the FDC or on FDC dendrites. TEM images and schematics of 5 nm OVA-AuNPs internalized by FDCs while 50-100 nm OVA-AuNPs retained on FDC surface or dendrites. 15 nm OVA-AuNPs can be both inside the FDC or on FDC surface. Data collected from 3 sentinel lymph nodes for each size (n = 3-4 mice/group).

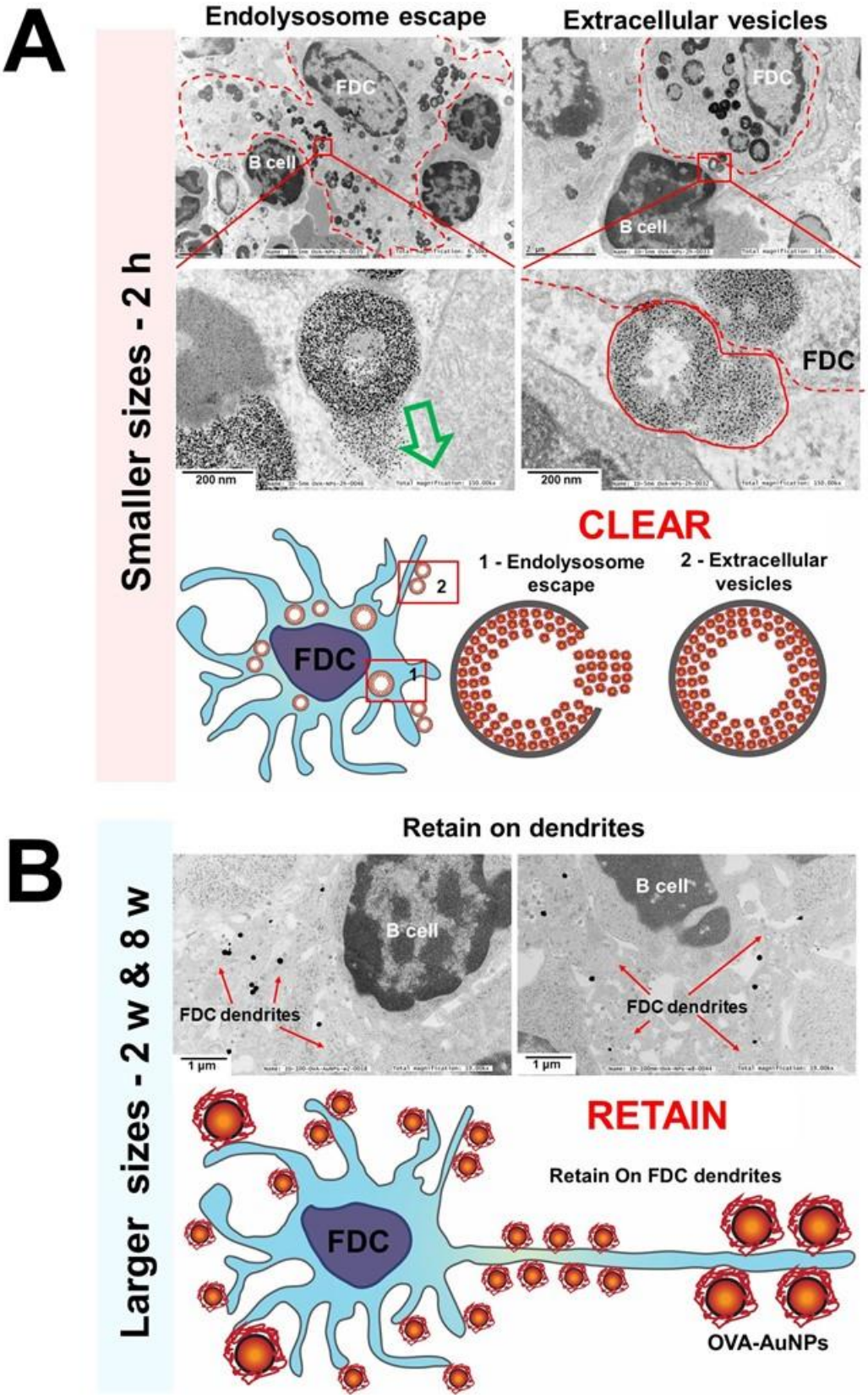
A
Endolysosome escape
Extracellular vesicles
Smaller sizes - 2 h
FDC
B cell
FDC
B cell
200 nm
200 nm
FDC
CLEAR
1 - Endolysosome escape
2 - Extracellular vesicles
2
FDC
1
B
Retain on dendrites
Larger sizes - 2 w & 8 w
B cell
FDC dendrites
1 µm
B cell
FDC dendrites
1 µm
RETAIN
Retain On FDC dendrites
FDC
OVA-AuNPs

Fig. 2. 4. FDCs clear smaller nanoparticles by endolysosomal escape and extracellular vesicles, and retain larger ones on their dendrites. (**A**) TEM images and schematics of 5 nm OVA-AuNPs cleared through endolysosomal escape or exosomes. (**B**) TEM images and schematics of 100 nm OVA-AuNPs retained on FDC dendrites over a few weeks. Data collected from 3 sentinel lymph nodes for each size (n = 3-4 mice/group).

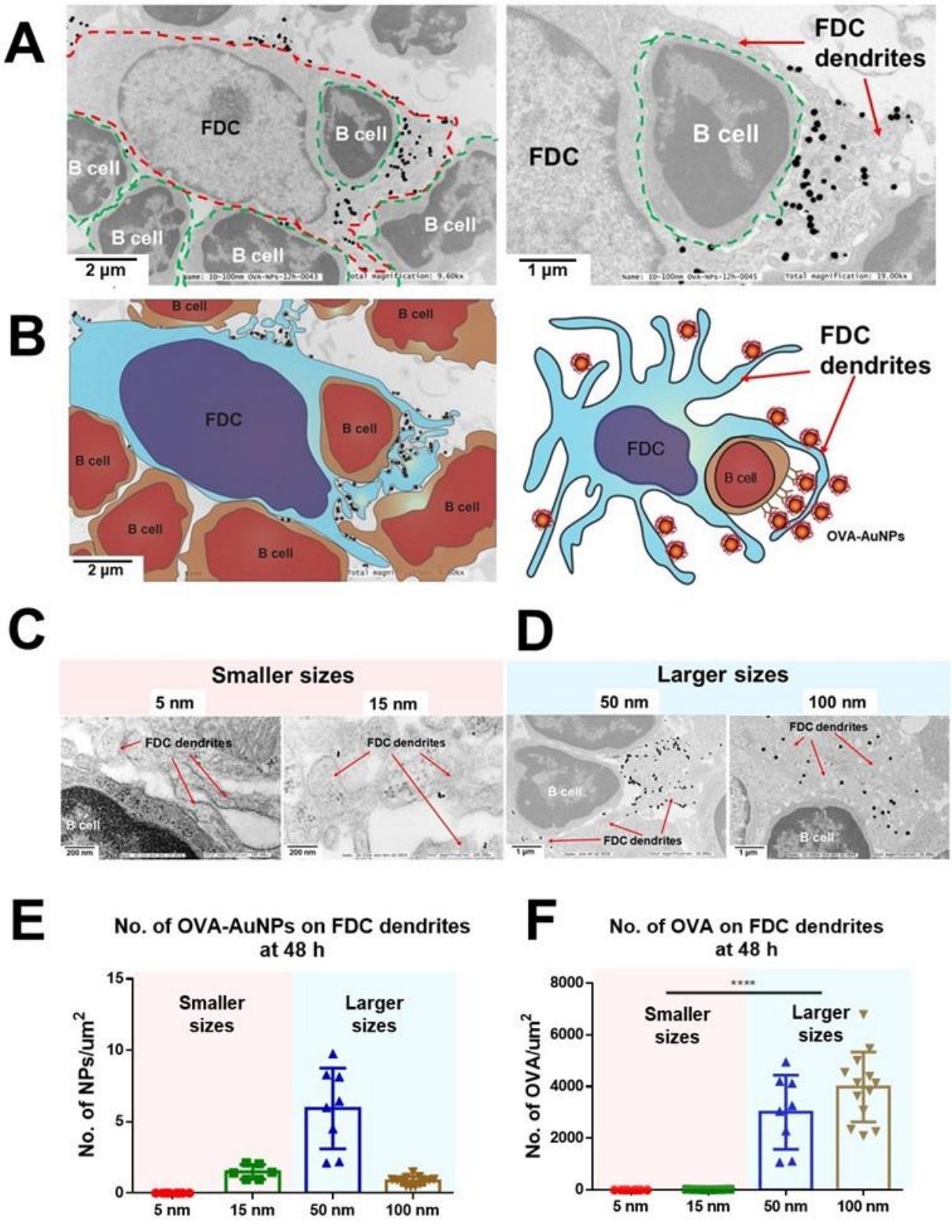
A
FDC
B cell
B cell
B cell
B cell
B cell
2 μm
FDC dendrites
B cell
FDC
1 μm
B
B cell
B cell
FDC
B cell
B cell
B cell
B cell
B cell
2 μm
FDC dendrites
FDC
B cell
OVA-AuNPs
C
Smaller sizes
5 nm
15 nm
FDC dendrites
B cell
FDC dendrites
D
Larger sizes
50 nm
100 nm
B cell
FDC dendrites
FDC dendrites
B cell
E
No. of OVA-AuNPs on FDC dendrites at 48 h
No. of NPs/um2
15
10
5
0
Smaller sizes
Larger sizes
5 nm
15 nm
50 nm
100 nm
F
No. of OVA on FDC dendrites at 48 h
****
No. of OVA/um2
8000
6000
4000
2000
0
Smaller sizes
Larger sizes
5 nm
15 nm
50 nm
100 nm

Fig. 2. 5. Larger nanoparticles have greater deposition on FDC dendrites leading to more conjugated antigens presentation on FDC to stimulate B cells. (**A**) Representative TEM images of FDC dendrites surrounding B cells containing OVA-AuNPs (red arrows point to FDC dendrites). (**B**) Schematics of (**A**) that OVA-AuNPs are deposited on FDC surfaces and dendrites. FDC dendrites surrounding B cells with OVA-AuNPs that facilitates the interaction of conjugated-antigen and B cell receptors. (**C-D**) TEM images of different sizes of OVA-AuNPs depositing and presenting conjugated-antigen on FDC dendrites at 48 hours post intradermal footpad injection. Red arrows point to the FDC dendrites. Quantifying (**E**) numbers of OVA-AuNPs and (**F**) numbers of conjugated OVA on FDC dendrites at 48 hours. Data collected from 3 sentinel lymph nodes for each size (n = 3-4 mice/group). Data shown as mean ± SD; ****$P < 0.0001$. All P values from one-way ANOVA followed by Tukey's multiple comparisons tests.

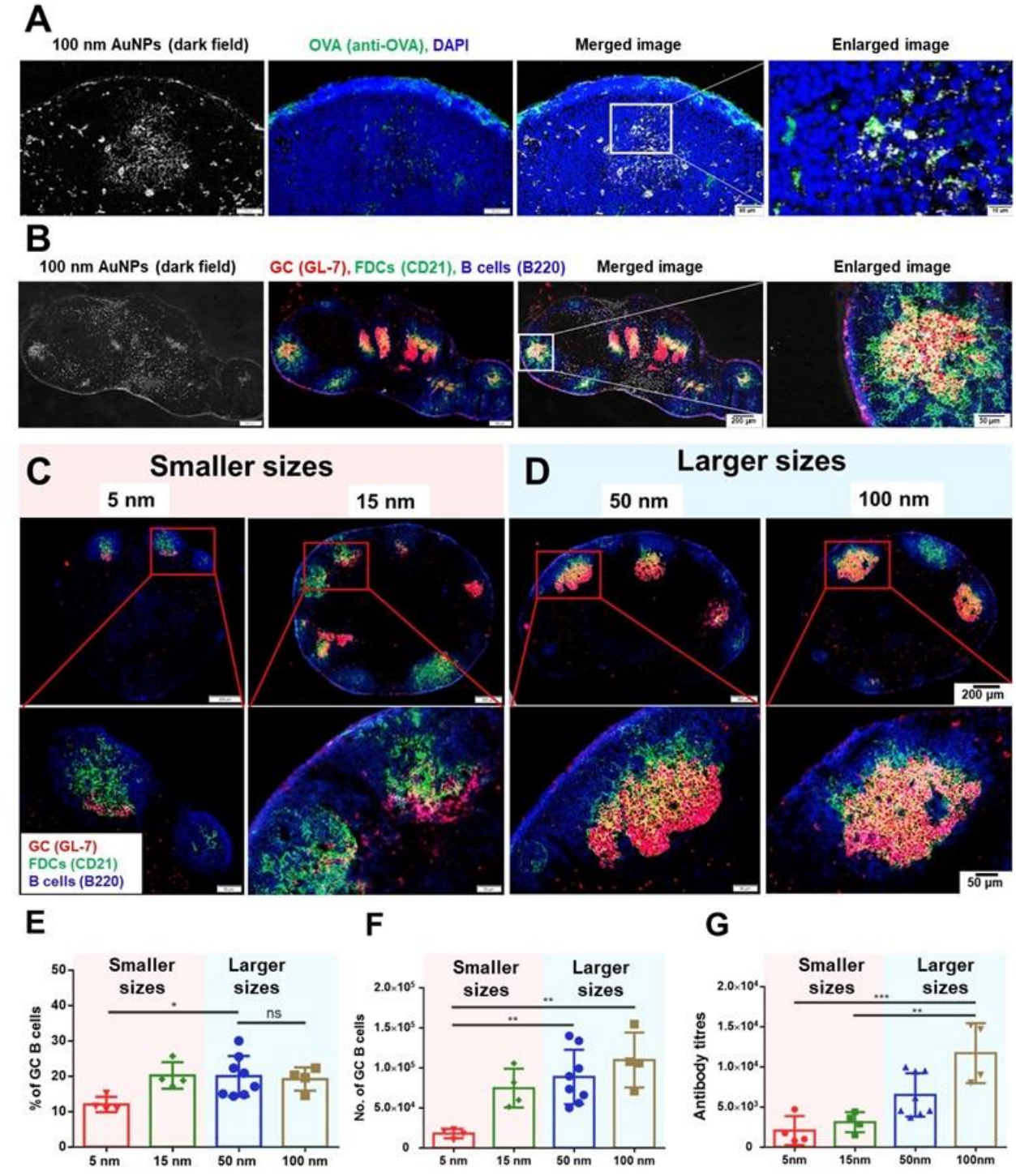

Fig. 2. 6. Larger nanoparticle vaccines induce greater humoral immune responses. (A) Colocalization of 100 nm AuNPs with OVA antigen in follicles after 5 weeks of injection. Anti-OVA stain colocalized with AuNP signal generated by dark field microscopy, indicating that the OVA remained conjugated to the AuNPs. (**B**) Colocalization of 100 nm OVA-AuNPs with FDCs in germinal centers after 5 weeks of immunization. FDC colocalized with AuNP signal generated

by dark field microscopy. Assessment of (**C and D**) germinal center formation (GL7 red; CD21 green; B220 blue), (**E**) percentage of germinal center B cells (GL7+ B220+), (**F**) numbers of germinal center B cells (GL7+ B220+), and (**G**) antigen-specific antibody production in sera after intradermal footpad injection with different sizes of OVA-AuNP vaccine at 5 weeks (n = 4-8 mice/group). The injection dose is normalized based on the same amount of OVA antigen (10 μg) for each size. Data shown as mean ± SD; **P < 0.01; ***P < 0.001; ****P < 0.0001. All P values from one-way ANOVA followed by Tukey's multiple comparisons tests.

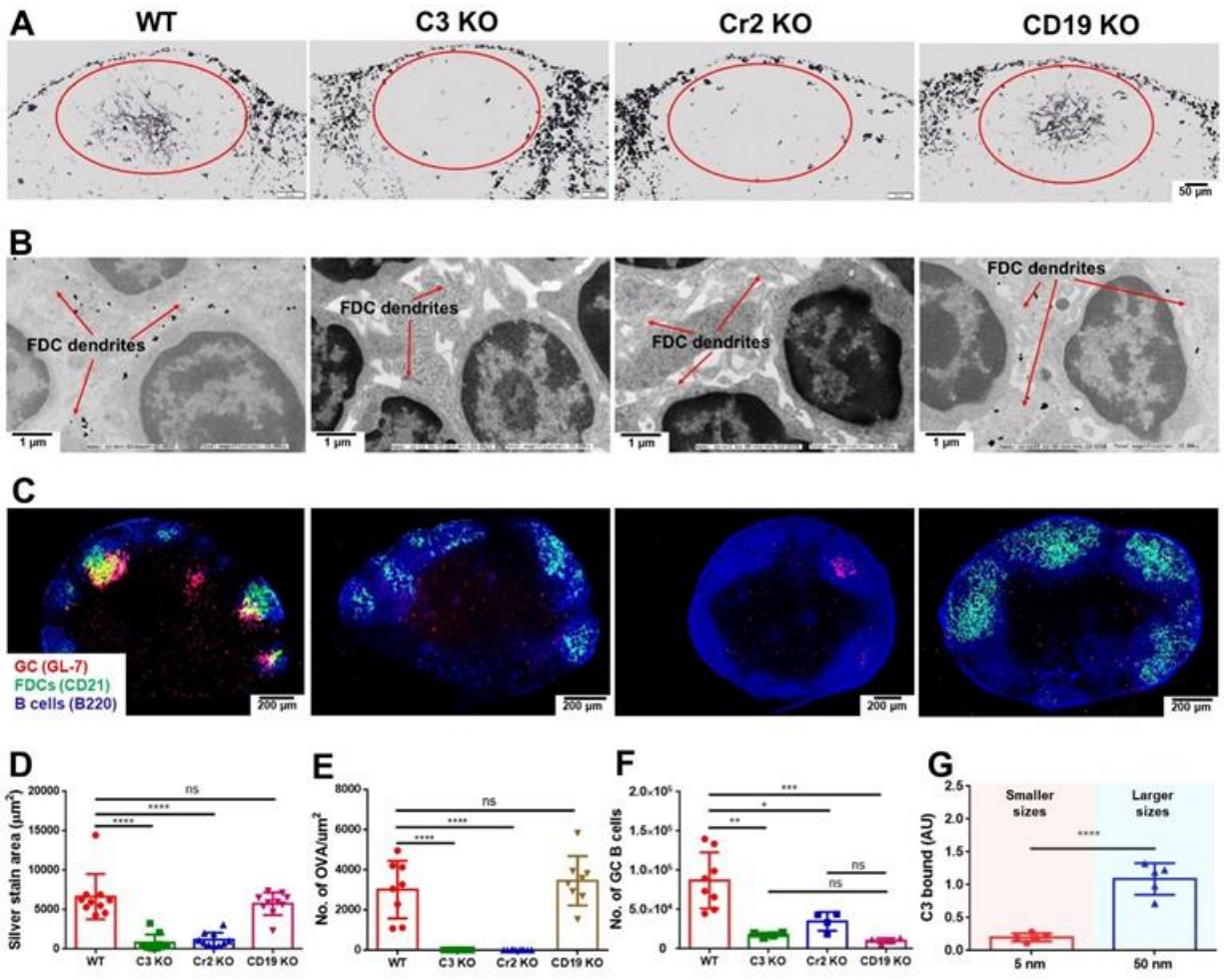

Fig. 2. 7. Larger nanoparticle vaccines induce greater complement opsonization resulting in enhanced nanoparticle retention, antigen presentation on FDC dendrites and germinal center reactions. (A-F) Study of nanoparticle retention, antigen presentation and germinal center reactions in wild type and C3, Cr2 and CD19 receptor knockout mice after intradermal footpad injection with 50 nm OVA-AuNP vaccines. (**A and D**) Histology of OVA-AuNP sequestration in lymph node follicles at 48 hours (n = 4 mice/group in C57BL/6 background) (**B and E**) Representative TEM images of AuNP conjugated antigen presentation on FDC dendrites at 48 hours. Data collected from 3 sentinel lymph nodes for each condition (n = 3-4 mice/group). Assessment of (**C**) germinal center formation (B220 blue; CD21 green; GL7 red) and (**F**) numbers of germinal center B cells (GL7+ B220+) after intradermal footpad injection with 50 nm OVA-AuNP vaccine at 5 weeks (n = 4-8 mice/group). (**G**) Quantification of the complement C3 adsorbed on OVA-AuNP surfaces using ELISA (AU standards for arbitrary units, n = 5). Graphs represent mean ± SD; *P < 0.05; **P < 0.01; ***P < 0.001; ****P < 0.0001. All P values from one-way ANOVA followed by Tukey's multiple comparisons tests or an unpaired t test.

Supplementary figures and table

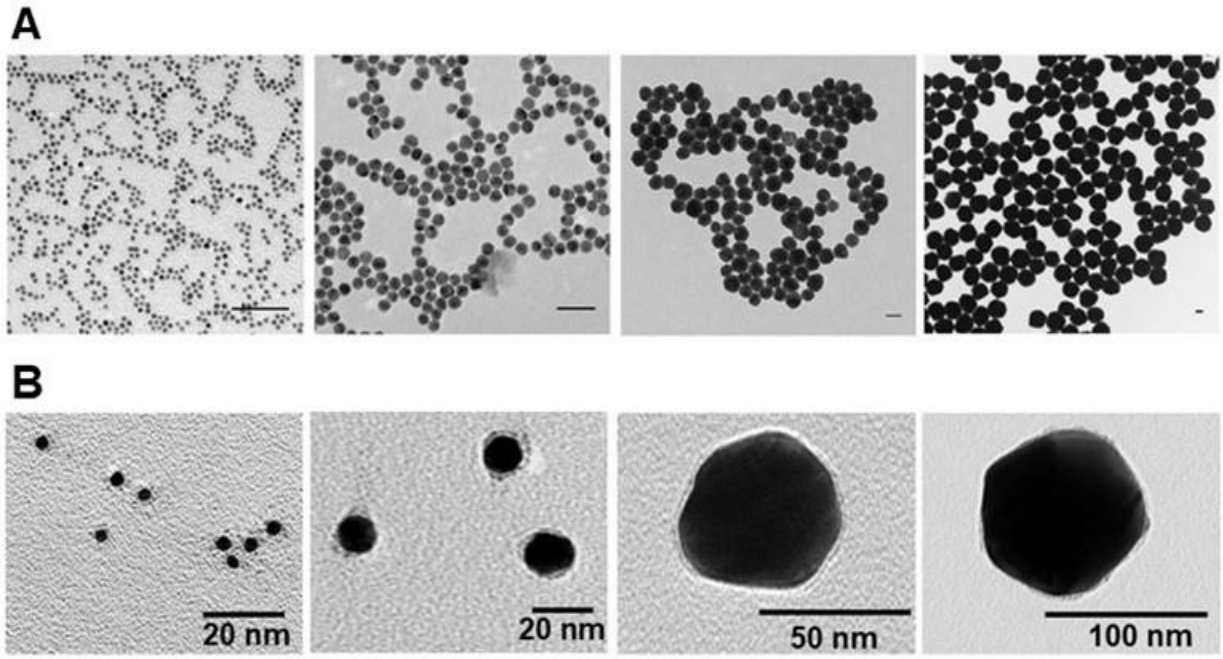

Fig. 2S. 1. Nanoparticle vaccine characterization. (A) TEM images of 5, 15, 50, and 100 nm (left to right) Citrate-coated gold nanoparticles (citrate-AuNPs). The scale bars in each figure is 50 nm. **(B)** TEM images of ovalbumin-coated gold nanoparticles (OVA-AuNPs) with core sizes of 5, 15, 50, and 100 nm (left to right).

Table 2S.1. Physicochemical properties of nanoparticle vaccines

Nanoparticle		Physicochemical Properties			
Size	Surface Ligands	Inorganic Diameter (nm)	Hydrodynamic Diameter (nm)	ζ Potential (mV)	λ_{LSPR} (nm)
5	Citrate	4.6 ± 0.1	8.9 ± 0.9	-9.9 ± 2.0	515
	OVA		18.7 ± 2.6	-12.6 ± 0.3	520
15	Citrate	15.1 ± 0.6	21.8 ± 2.4	-8.0 ± 0.8	521
	OVA		82.2 ± 9.3	-20.4 ± 0.2	528
50	Citrate	48.2 ± 2.0	60.8 ± 1.5	-22.9 ± 0.5	531
	OVA		125.3 ± 7.9	-23.0 ± 0.2	548
100	Citrate	112.0 ± 3.7	112.5 ± 3.7	-25.7 ± 3.1	570
	OVA		167.5 ± 5.9	-20.2 ± 0.2	585

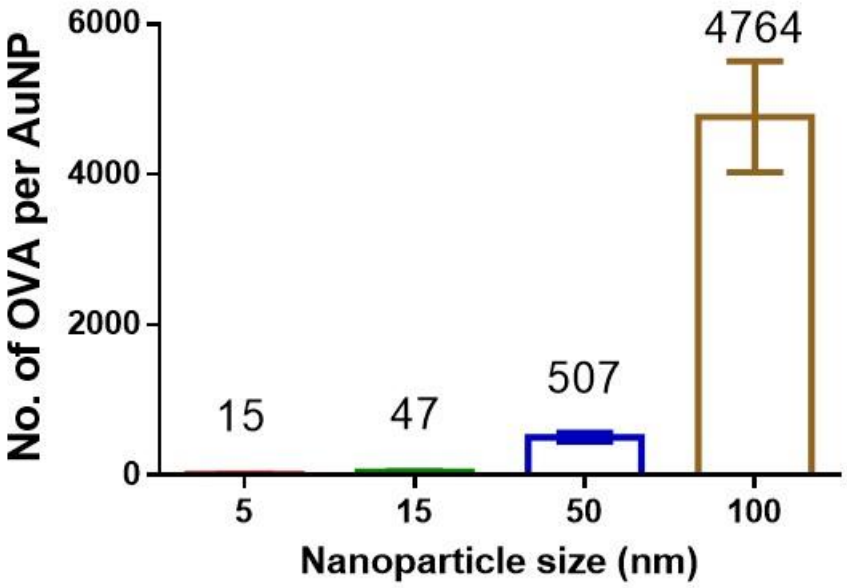

Fig. 2S. 2. Quantification of numbers of OVA protein on AuNPs using bicinchoninic acid (BCA) assay. The injection dose is normalized based on the same total amount of OVA antigen (10 μg) for each injection.

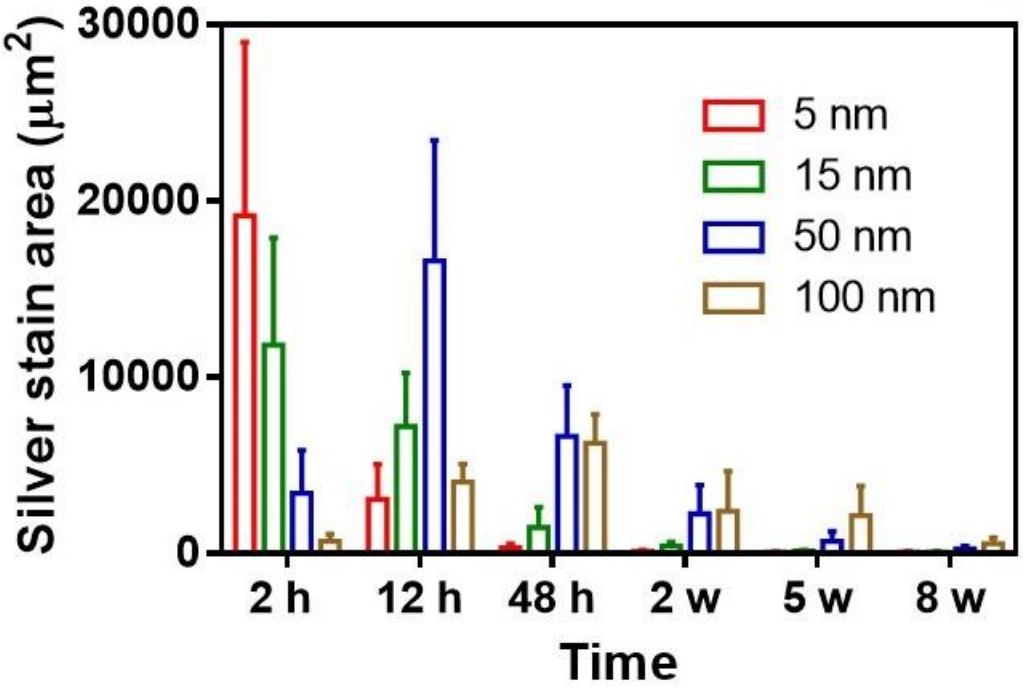

Fig. 2S. 3. **Quantification of silver stained area in histology images of different sizes of OVA-AuNP retention in lymph node follicles over 8 weeks.** Histology images of different OVA-AuNP vaccine sizes cleared or retained in lymph node follicles after various times (from 2 hours to 8 weeks) post intradermal footpad injection into C57BL/6 mice (n = 4 mice/group). Lymph node follicles of sentinel (axillary, brachial and popliteal) lymph nodes were collected. Data collected from 10 lymph node follicles (n = 4). The injection dose was normalized based on the same OVA antigen amount (10 μg) for each size.

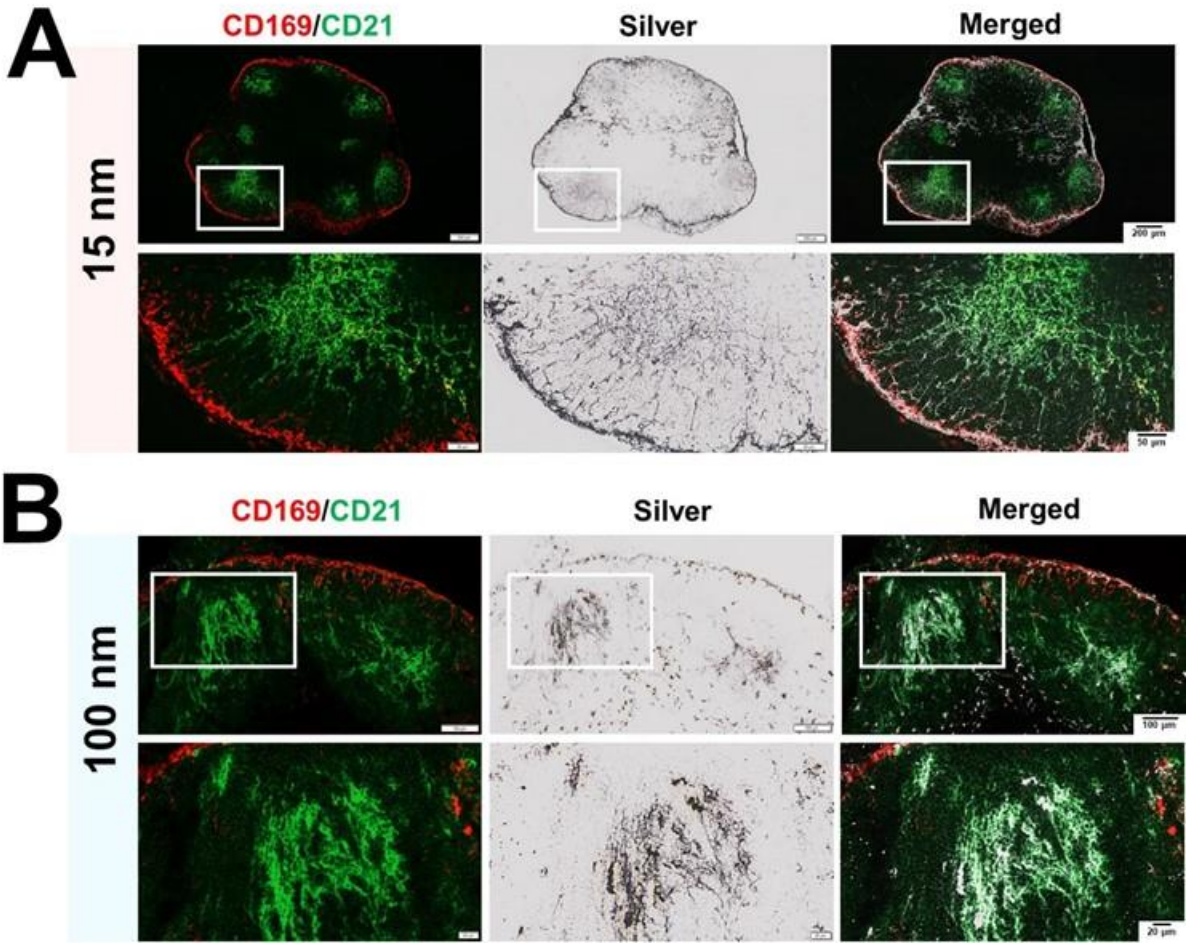

Fig. 2S. 4. FDC networks involved in nanoparticle sequestration in lymph node follicles. Histology study of (**A**) 15 nm and (**B**) 100 nm OVA-AuNP sequestration in lymph node follicles associated with FDC networks at 2 hours and 48 hours post intradermal footpad injection. Gold nanoparticle signals colocalized in the area of FDC networks (CD21 green; CD169 red; Silver black).

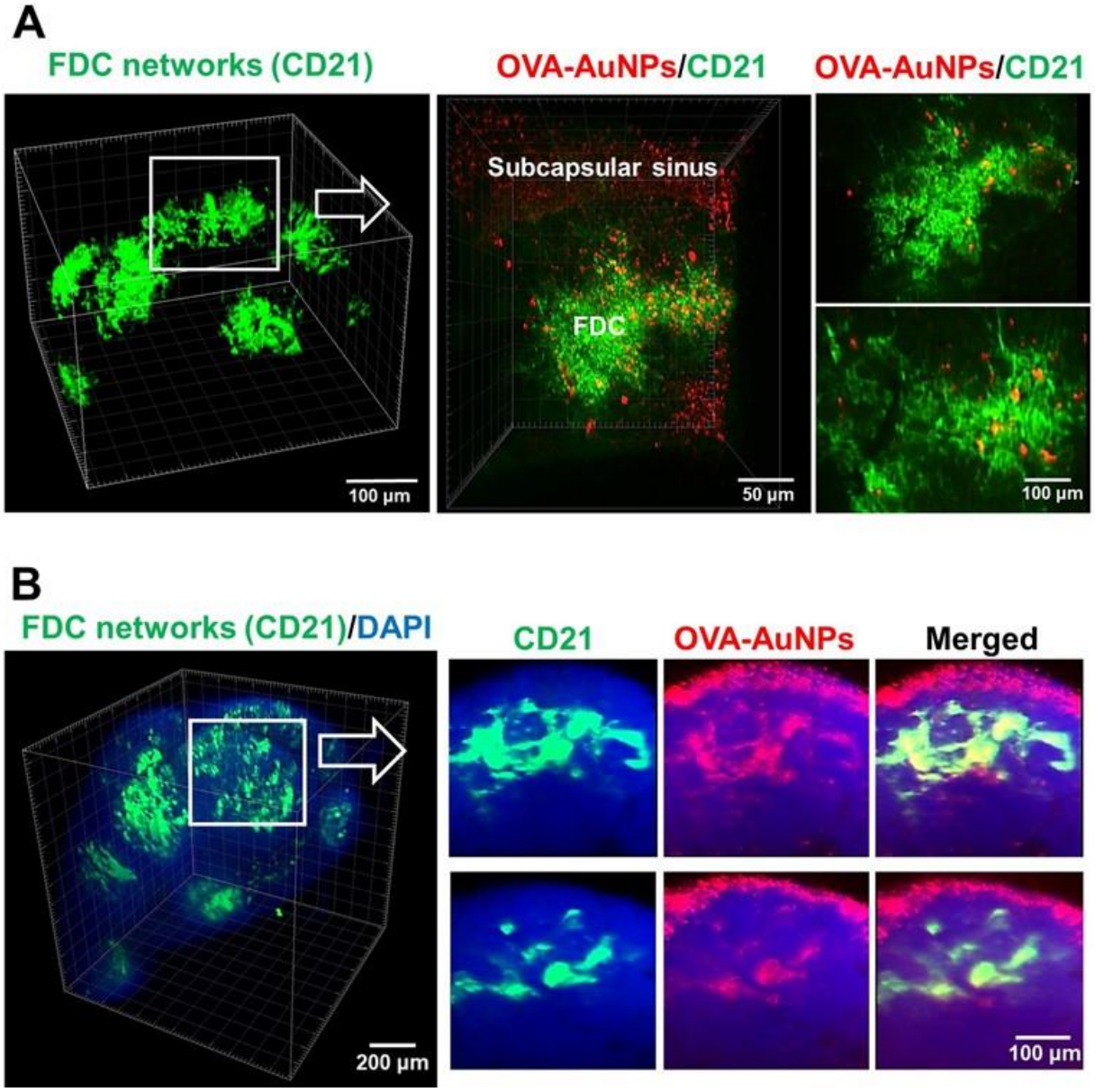

Fig. 2S. 5. 3D images of 50 nm OVA-AuNPs associated with FDC networks in lymph node follicles after CLARITY processing. Sentinel lymph nodes were isolated and cleared after 48 hours post intradermal footpad injection into C57BL/6 mice (n = 4 mice/group). (**A**) OVA-AuNPs deposited on FDC (CD21+) networks. (CD21 green; OVA-AuNP red). (**B**) Colocalization of OVA-AuNPs with FDC networks in lymph node follicles (CD21 green; OVA-AuNP red).

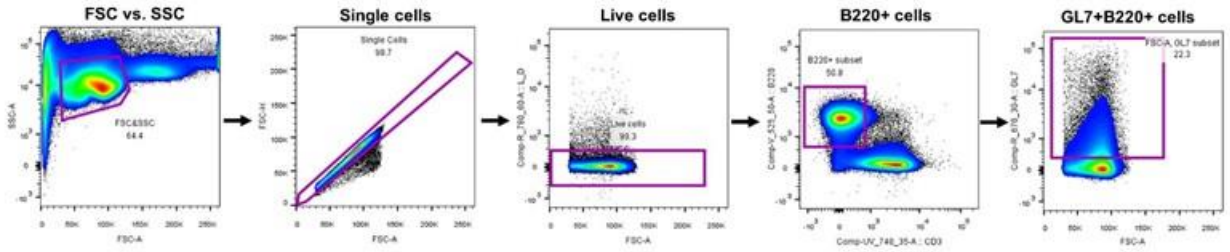

Fig. 2S. 6. Gating strategy for analyzing germinal center B cells after 5 weeks of immunization.

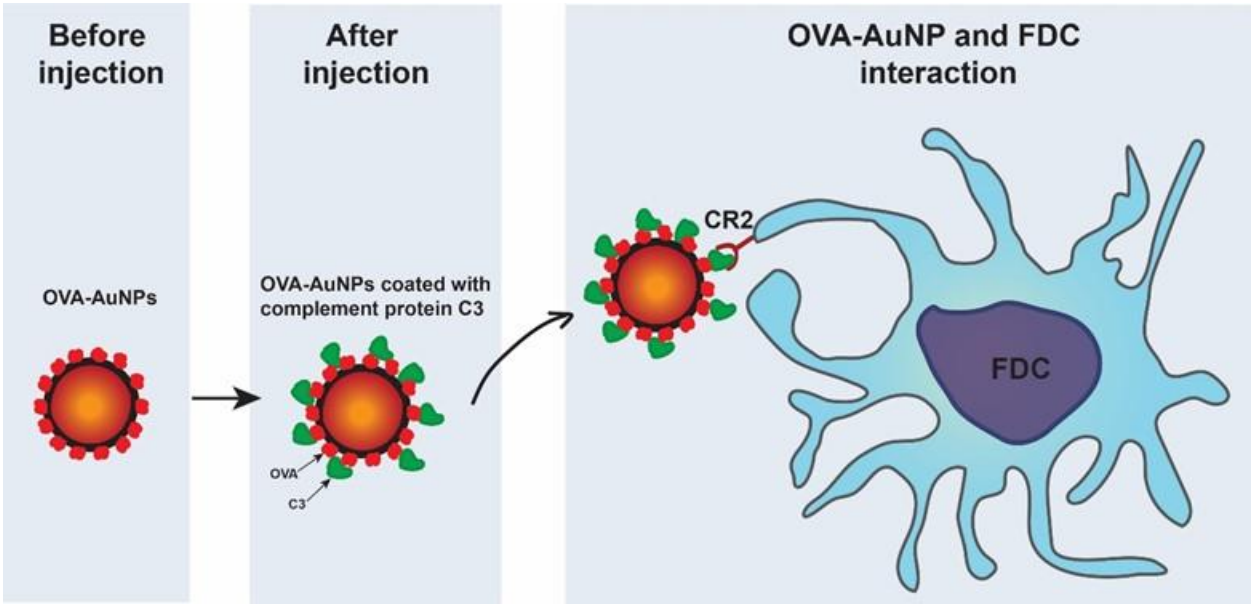

Fig. 2S. 7. Complement protein C3 opsonized on the OVA-AuNP surface mediating the interaction with the FDC through complement receptor 2 (Cr2).

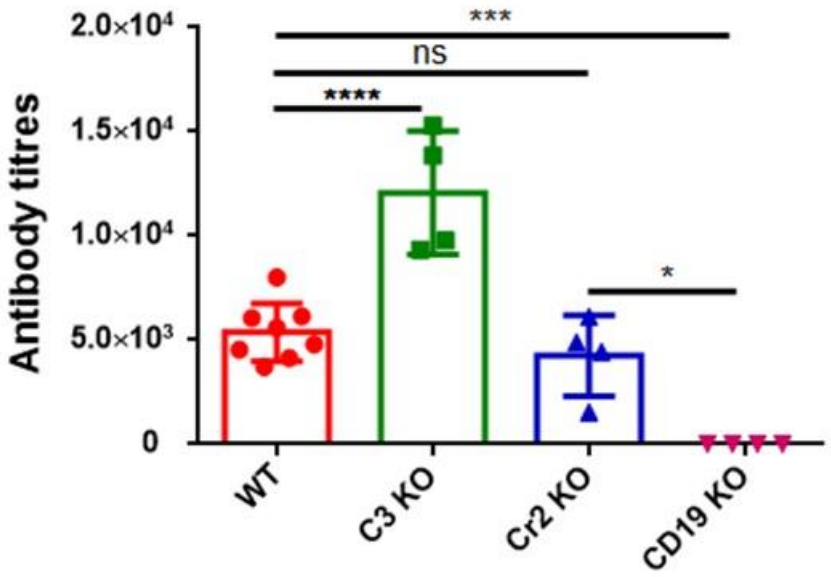

Fig. 2S. 8. Antigen-specific antibody production in sera are assessed after injection into wild type or knockout mice at 5 weeks. 50 nm OVA-AuNPs were injected into wild type, and C3, Cr2 and CD19 receptor knockout mice and mice were sacrificed after 5 weeks (n = 4-8/group of mice in C57BL/6 genetic background).

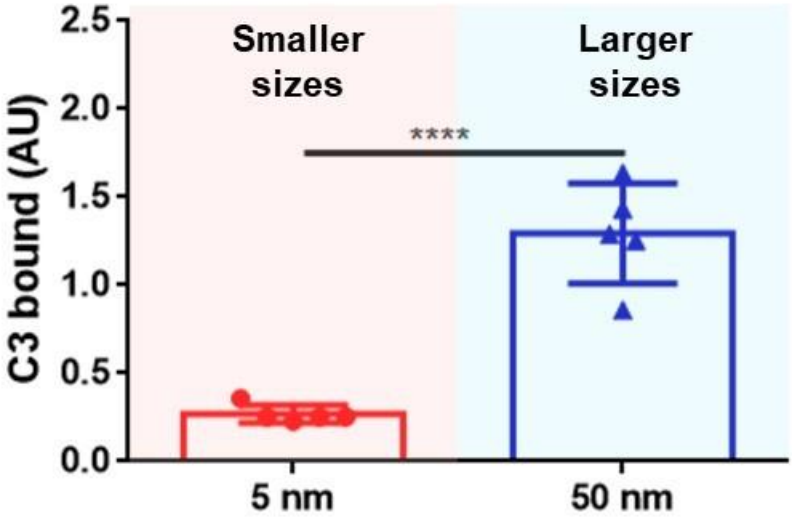

Fig. 2S. 9. Larger nanoparticles induce greater complement opsonization than smaller ones. Wild type mice serum was added to OVA-AuNP vaccine pre-coated plate in vitro. C3 deposition was tested using ELISA. Graphs represent mean ± SD; ****P < 0.0001. All data was analyzed using an unpaired t test.

Chapter 3 - Nanoparticle size influences antigen retention and presentation in lymph node follicles for humoral immunity

Introduction

Successful vaccinations require antigen delivery into lymph node follicles to generate efficient antibody-mediated humoral immune responses[5,8–10,34,46,90,91]. Lymphatic endothelial cells (LECs) form the subcapsular sinus (SCS) floor that only allow smaller sized antigens (<15 nm) to enter lymph node follicles[22–24]. Macrophages in the SCS capture larger sized nanoparticles (>50 nm), viruses, and bacteria and actively transport them to cross the layer of LECs into follicles[10,27–32]. This principle has been used to target the SCS macrophages for effective vaccination[10,51,52]. Recent studies showed that removing the SCS macrophages did not reduce humoral immune responses[47,92–96]. These contradictory findings raise a question: do SCS macrophages promote or prevent nanovaccine transport to lymph node follicles for humoral immune responses? We assessed the role of SCS macrophages and their contribution to delivery of nanovaccines to lymph node follicles and to production of antibodies.

Materials and methods

Synthesis of gold nanoparticles

15 nm gold nanoparticles (AuNPs) were synthesized using method adapted from Frens[78]. Briefly, 1 mL of 3% (w/v) sodium citrate tribasic (Sigma-Aldrich S4641) was prepared in 100 mL deionized water and boiled. Under vigorous stirring, 100 μL of 10% (w/v) aqueous HAuCl4 was added and allowed to react for 10 minutes. The reaction was then immediately cooled on ice to room temperature. These 15 nm AuNPs were then used for the preparation of 100 nm AuNPs as described previously by our group[79]. Molar equivalents of sodium citrate tribasic (1.5×10^{-2} M), aqueous HAuCl4 (2.5×10^{-2} M), and 15 nm AuNPs ($2\text{-}4 \times 10^{-9}$ M) were added to 95-97 mL

deionized H_2O to make 100 mL total. The molar equivalent of hydroquinone (Sigma-Aldrich H17902) (2.5×10^{-2} M) was then added to the solution under vigorous stirring. The reaction was maintained overnight. Tween-20 (final concentration of 0.05% w/v) was added to the solution and stirred for 10 minutes. 100 nm AuNPs were then washed two times by centrifugation at 750 g, resuspending the pellet in 0.02% sodium citrate tribasic and 0.05% Tween-20. AuNPs were stored at 4°C for future use.

Synthesis of nanoparticle conjugated vaccines

A model nanoparticle conjugated vaccine was composed of different sizes (15 nm and 100 nm) of spherical AuNPs conjugated to ovalbumin (OVA) (Sigma-Aldrich A5503) antigen. AuNP stocks were washed once using 0.02% sodium citrate tribasic buffer for 35 minutes before OVA protein conjugation. 100 mM sodium citrate tribasic solution and HCl in deionized water was prepared and pH was adjusted to 2.3. This solution was diluted to 20 mM of sodium citrate tribasic with approximately pH 3 and mixed with OVA into the final concentration of 10 mg/mL. OVA protein in 20 mM of sodium citrate tribasic was mixed on rotator for 2 hours and filtered using 0.22 µm PES filter. 250 µL OVA solution was added in to the AuNP solution with 1.6×10^{16} nm^2 total surface area. The mixed solution was then incubated in a 1.5 mL Eppendorf tube at 37ºC for 1 hour. After conjugation, the mixed solution was topped up with 1× PBS + 0.05% Tween-20. The OVA conjugated AuNPs (OVA-AuNPs) was then wash with 1× PBS + 0.05% Tween-20 and purified with centrifugation speeds of 5000 g for 15 nm AuNPs and 200 g for 100 nm AuNPs for 60 minutes. OVA-AuNPs were purified three times and resuspended in sterile PBS. OVA-AuNP nanovaccine was filtered using a 0.22 µm PES filter to remove the possible aggregates. The OVA-AuNP nanovaccine concentration was justified before footpad intradermal injection.

Physicochemical characterization of gold nanoparticles and nanovaccines

The core size of AuNPs and OVA-AuNPs were characterized by transmission electron microscopy (TEM) (Fig. 3S3 and Table. 3S1). TEM copper grids (Ted Pella 01813-F) was plasma treated. 5 µL of AuNP or OVA-AuNP stocks was added on the treated TEM grids. The samples were blotted after 3 minutes using Kimwipes. The samples were left on grids for another 10 minutes to be completely air dried. To visualize the protein layer conjugated on the AuNP, OVA-AuNP samples on the EM grid were washed one more time with 5 µL deionized water and blotted using Kimwipes. The samples were negatively stained with 3 µL of 1% uranyl acetate (Ted Pella 19481). The stained samples were blotted using Kimwipes after 1 min of staining and air dried for 10 more minutes. All samples were visualized using TEM at 120 kV (Tecnai 20, FEI, Hillsboro, OR, USA) with an AMT 16000 camera. The AuNP core sizes were determined by measuring over 100 nanoparticles using ImageJ (NIH, Maryland)[80]. The hydrodynamic diameters were characterized using dynamic light scattering (DLS) (Malvern Instruments Ltd., Worcestershire, UK) and absorbance was measured using UV-visible absorbance spectroscopy (Shimadzu Scientific Instruments). The surface charge was measured using Zetasizer Nano-ZS (Malvern Instruments Ltd.) in 150 mM HEPES, pH 7.5. The concentrations of AuNPs and OVA-AuNP were measured using UV-visible absorbance spectroscopy. The amount of OVA protein conjugated on AuNP were measured by bicinchoninic acid (BCA) assay (ThermoFisher Scientific 23235).

Extraction and quantification of OVA protein using bicinchoninic acid assay

OVA-AuNP solution with 2 x 10^{14} nm^2 total surface area was resuspended in 25 µL PBS in a 1.5 mL Eppendorf tube. 8 µL of 4% NuPAGE LDS buffer (ThermoFisher Scientific NP0007) and 4 µL of 500 mM dithiothreitol (DTT) (BioShop DTT001.5) were mixed in the Eppendorf. This solution was then incubated at 70°C for 1 hour. The Eppendorf was centrifuged at 18,000 g for 15

minutes. The supernatant was collected and mixed with 25 µL of 2% (w/v) sodium dodecyl sulfate (SDS) (ThermoFisher Scientific NP0001). To eliminate the SDS and DTT from the isolated OVA protein, 950 µL of 10% (w/v) trichloroacetic acid (TCA) (Sigma-Aldrich T6399) in acetone was added into the Eppendorf tube and incubated at -80˚C for 12 hours. The Eppendorf tube was centrifuged at 18,000 g at 4˚C for 15 minutes. The supernatant was removed, and the OVA protein was resuspended in 500 µL of 0.03% (w/v) deoxycholate (Sigma-Aldrich 30970) and vortexed thoroughly. 100 µL of 72% (w/v) TCA was mixed into the Eppendorf and incubated on ice for 30 minutes. The protein was centrifuged at 18,000 g at 4˚C for 15 minutes. 950 µl of acetone (-30˚C) was mixed into the Eppendorf tube and vortexed thoroughly. The tube was in incubated at -80˚C for 1 hour. The isolated OVA protein was pelleted at the bottom after centrifugation at 18,000 g at 4˚C for 15 minutes. The supernatant was removed, and the isolated protein was air dried for 30 minutes. The purified protein was dissolved into a 2% (w/v) SDS solution in PBS. To establish the standard curve, OVA protein was dissolved into a 2% (w/v) SDS solution in PBS and diluted stepwise. The purified protein and standards were incubated at 70˚C for 1 hour. 200 µL of the bicinchoninic acid (BCA) (Thermo Fisher Scientific 23235) reagent I from the kit was added to all samples and standards. These samples and standards were incubated at 60˚C for 30 minutes until a purple colour developed. All samples and standards were cooled to room temperature and analyzed on an absorbance plate reader at 562 nm (Tecan Sunrise). The protein amount was calculated based on the standard curve. The injected OVA-AuNP dose is normalized based on the injected OVA antigen amount (10 µg) (Fig. 3S4).

Animal care

All animal experiments were performed according to the protocols approved by the University of Toronto Division of Comparative Medicine and Animal Care Committee (protocol numbers:

20011620, 20011910, 20012102). 8 to 12-week old wild type C57BL/6 mice were purchased form Charles River Laboratories (Montreal, Canada). Mice were anesthetized using isoflurane (3%) carried with oxygen during intradermal footpad injection. OVA-AuNP nanovaccines were intradermally injected using a 29-gauge insulin needle. The injected dose was normalized to the OVA protein amount. The injected volume was 20 μL for each footpad and 4 footpads were injected in each mouse. The axillary, brachial, and popliteal sentinel lymph nodes were collected for further studies.

Administration of macrophage inhibitors

Clodronate or PBS liposomes (Liposoma BV CP-005-005) was used to eliminate subcapsular sinus (SCS) macrophages in lymph nodes (Fig. 3S1). Other macrophage inhibitors including gadolinium chloride ($GdCl_3$) (Sigma-Aldrich 203289), carrageenan (CGN) (Sigma-Aldrich C1138), and dextran sulfate 500 (DS500) (Sigma-Aldrich D6001), were used to inhibit SCS macrophage uptake function (Fig. 3S1). Free clodronate (Clodronic Acid Disodium Salt Hydrate) (TRC Canada C586875) and low molecular weight Dextran sulfate 9 (DS9) (average molecular weight 9,000 - 20,000 Da) (Sigma-Aldrich D6924) were used as negative controls, which cannot effectively physically or functionally eliminate macrophages. 20 μl of macrophage inhibitors were intradermally injected into the footpads of C57BL/6 mice using 29-gauge insulin syringes. Equivalently, the amount of injected macrophage inhibitors was 0.1 mg per footpad, in total 0.4 mg for four footpads. Macrophage inhibitors were intradermally injected into the mouse footpad (7, 3, 1, and 0 days (3 hours)) before or (3 and 7 days) after administration of 100 nm OVA-AuNP nanovaccine.

Histology, immunostaining, and imaging

The mice were sacrificed after different injection times (from 2 hours to 5 weeks). The axillary, brachial, and popliteal sentinel lymph nodes were collected for histological analysis. The collected sentinel lymph nodes were directly placed into frozen section compound (VWR® International, LLC 95057-838) in a plastic cryomold (Tissue-Tek® at VWR® 4565) and frozen with liquid nitrogen. This method can preserve the antigens on cell membrane for immunostaining. The frozen samples were taken to the Toronto Centre for Phenogenomics (TCP) on dry ice for further sample processing. 8 μm sample sections were cut on Cryostar NX70 and placed on charged slides. To visualize OVA-AuNP distribution, sample sections were stained using silver enhancement kits (Ted Pella, Inc. 15718) for enhancement of gold signal. Prior to the immunostaining, sample sections were post-fixed in 10% neutral buffered formalin, permeabilized in 0.5% Triton X-100. All sections were incubated in primary antibody overnight at 4 °C, rinsed in TBST then incubated in secondary antibody for 1 hour at room temperature. The subcapsular sinus (SCS) macrophages were stained using rat anti-sialoadhesin (CD169) antibody (Abcam ab53443; 1:600) followed by anti-rat secondary conjugated with Alexa Fluor 488 (Abcam ab150165; 1:200). Lymphatic endothelial cells were labeled using rabbit anti-Lyve1 antibody (Abcam ab14917; 1:500) followed by anti-rabbit secondary conjugated with Alexa Fluor 555 (Thermo Fisher A21428; 1:200), Syrian hamster anti-podoplanin antibody (BioXCell BE0236; 1:1000) followed by biotinylated anti-Syrian Hamster IgG (Abcam ab6891; 1:200) then Streptavidin-Alexa Fluor 594 (Thermo Fisher S11227; 1:1000), or rabbit anti-Prox1 antibody (BioLegend 925201; 1:1500) followed by anti-rabbit secondary conjugated with Alexa Fluor 555. Follicular dendritic cells (FDCs) were labeled using rabbit anti-CD21 antibody (Abcam ab75985; 1:1800) followed by anti-rabbit secondary conjugated with Alexa Fluor 555. B cells were detected using rat anti-B220 antibody (eBioscience 14-0452-82; 1:100) followed by anti-rat secondary conjugated with Alexa Fluor 674

(ThermoFisher A21247; 1:200), and germinal center formation was labeled using rat anti-GL7 antibody (FITC) (BioLegend 144604; 1:250). Nuclei were then counterstained with DAPI (Sigma-Aldrich D9542) on sample sections.

The sample sections were scanned using an Olympus VS-120 slide scanner and imaged using a Hamamatsu ORCA-R2 C10600 digital camera for all bright-field and fluorescent images. The images of silver stained OVA-AuNPs in lymph node follicles were quantified using ImageJ (NIH)[80]. The threshold of silver stained images was set up to the same value. The total area of silver stained area in lymph node follicles were analyzed. The space between lymphatic endothelial cells were measured using ImageJ (NIH)[80].

TEM study on lymph node tissues

SCS macrophage location, sinus structure, FDCs in lymph node follicles, and the location of OVA-AuNPs were studied using TEM at the subcellular level. The mice were sacrificed after different injection times (12 or 48 hours). The axillary, brachial, and popliteal sentinel lymph nodes were collected and directly fixed with 4% formaldehyde and 0.5% glutaraldehyde (Sigma-Aldrich 340855) in PBS at room temperature for 1 hour. The samples were stored at 4°C. The fixed samples were sent to the Nanoscale Biomedical Imaging Facility at The Hospital for Sick Children for further processing. The lymph node samples were mounted, sectioned and placed on copper grids (Ted Pella 01813-F). The sectioned samples were negative stained with 2% uranyl acetate (Ted Pella 19481) on copper grids. The images were taken using TEM at 120 kV. The space between lymphatic endothelial cells were measured using ImageJ (NIH)[80].The numbers of nanovaccines on FDC dendrites were quantified using TEM images. The area (um^2) of FDC dendrites were

measured using ImageJ (NIH)[80]. The total numbers of 100 nm OVA-AuNPs within the area of FDC dendrites were then calculated.

Lymph node disaggregation and cell staining and flow cytometry

Percentage of germinal center B cells (GL7+B220+) and numbers of germinal center B cells (GL7+B220+) were quantified using flow cytometry. The mice were immunized using different nanovaccine designs and sacrificed at 5 weeks. The axillary, brachial, and popliteal sentinel lymph nodes were collected and mechanically disaggregated using a razor blade. These lymph node samples were enzyme disaggregated into single cell suspension using 958 µL of Hanks' Balanced Salt Solution (HBSS) buffer (ThermoFisher Scientific 14185052) with 40 µL of 10 mg/ml collagenase IV (Sigma-Aldrich C5138) and 2 µL of 10 mg/mL of DNase (Roche 10104159001) in a 1.5 mL Eppendorf tube. Lymph node samples were incubated and rotated at 37°C for 30 minutes. The disaggregated lymph node cells were passed through a 70 µm cell strainer and centrifuged at 300 g at 4°C for 10 minutes in an Eppendorf tube. The supernatant was removed, and cell pellet was resuspended in HBSS blocking buffer supplemented with 0.5% (w/v) bovine serum albumin and 2 mM EDTA. Cell suspension was stained with fluorescent labelled antibodies. Anti-CD16/32 antibody (BioLegend 101302) was used for Fc receptor blocking. To determine the germinal center B cell formation. Zombie NIR Live/Dead stain (BioLegend 423106), BV510 anti-B220 (RA3-6B2) (BioLegend 103247), and Alexa Fluor® 647 anti-GL7 (BioLegend 144606) were used. Lymph node cells were stained on ice for 30 minutes and followed by 2 washes using HBSS blocking buffer. These cells were fixed using 1.6% paraformaldehyde (Thermo Fisher Scientific 28906) in HBSS on ice for 30 minutes. Cells were resuspended in blocking buffer for flow cytometry. The stained lymph node events were acquired using a 5-laser BD LSR FORTESSA X-20 flow cytometer. These events were then analyzed using FlowJo V10 software.

ELISA of OVA-specific antibody production

OVA-specific antibody production was measured in the blood sera using enzyme-linked immunosorbent assay (ELISA) after immunization of different nanovaccine formulation at 1 to 5 weeks. 100 µL of OVA with a concentration of 20 µg/mL in PBS was pre-coated on MaxiSorp 96-well plate (Thermo Fisher Scientific 442404) at 4°C overnight. The solution was removed. The wells were washed once with 400 µL of PBST. 200 µL of 1× casein buffer (Sigma-Aldrich B6429-500ML) was added to block the wells at room temperature for 2 hours. The wells were washed once with 400 µL of PBST. The blood serum samples were diluted 100 times with 0.5× Casein buffer and added into the 1st lane of the plate (200 µL). 100 µL of 0.5× casein buffer was added into the lanes except the 1st one to perform the serial dilution of the blood sera. The samples were serially diluted until the second final lane. The last lane was kept a base line. Samples were incubated at room temperature for 1 hour. The wells were washed two times using PBST (400 µL). Goat anti-mouse IgG secondary antibody, horseradish peroxidase (HRP) (Thermo Fisher Scientific 31430) was diluted 5000 times and added into the wells (100 µL). Samples were incubated at room temperature for 1 hour. The wells were washed two times using PBST (400 µL). TMB (3,3',5,5;-tetramethylbenzidine) chromogen solution (Thermo Fisher Scientific 002023) was added into wells (100 µL) and incubated at room temperature for 10 mins. The blue color was developed depending on the amount of detected OVA protein. The reaction was stopped by adding 1 M sulfuric acid (100 µL). The absorbance was measured using absorbance plate reader at 450 nm (Tecan Sunrise). The reference was setup at 570 nm. All titers reported are inverse dilutions where $A_{450\ nm}$ - $A_{570\ nm}$ equals 0.1.

Toxicity evaluation of macrophage inhibitors

Toxicology assessment of macrophage inhibitors were conducted using hematology and liver biochemistry assays. Macrophage inhibitors of clodronate liposomes, $GdCl_3$, CGN, and DS500 were intradermally injected into the mouse footpad. The amount of injected macrophage inhibitors was 0.1 mg per footpad, in total 0.4 mg for four footpads. Mice were sacrificed after 3 days of injection. Blood samples were collected through cardiac puncture using a 23-gauge needle and separated into two fractions. One fraction of blood was transferred to microfuge tubes containing dipotassium EDTA and kept on ice. These samples were taken to the DCM of Medical Science Building at the University of Toronto on ice for immune cell analysis and hematology analysis. Immune cell included white blood cells, lymphocytes, monocytes and neutrophils. Hematology analysis included red blood cell (RBC), hemoglobin (HGB), hematocrit (HCT), mean corpuscular volume (MCV), mean corpuscular hemoglobin (MCH), mean corpuscular hemoglobin concentration (MCHC), platelet (PLT), mean platelet volume (MPV), platelet hematocrit (%). The other blood fraction was centrifuged down at 500g for 10 minutes and the blood sera was collected. The sera samples were taken to the Toronto Centre for Phenogenomics (TCP) on dry ice for hepatotoxicity analysis of serum markers. Serum markers of liver parenchyma included alanine transaminase (ALT), aspartate aminotransferase (AST), alkaline phosphatase (ALP), and total bilirubin (TBIL). Liver and spleen sections were cut and fixed in 10% formalin for 1 day. The fixed tissue sections were taken to Toronto Centre for Phenogenomics (TCP) for further sample processing. Liver and spleen tissue sections were stained with hematoxylin and eosin to observe any systemic or gross inflammation. The sample sections were scanned using an Olympus VS-120 slide scanner and imaged using a Hamamatsu ORCA-R2 C10600 digital camera for all bright-field images.

Statistical analysis

Data was collected from 3-7 mice per group. All statistical analysis and graphing were performed using GraphPad Prism 6.0. Data were analyzed using one-way or two-way ANOVA followed by Tukey's multiple comparisons test or an unpaired t test. Data are shown as mean ± SD. $P < 0.05$ is defined as significant: $*P < 0.05$; $**P < 0.01$; $***P < 0.001$; $****P < 0.0001$.

Results and discussion

Depleting SCS macrophages allows more OVA-AuNP nanovaccines to access lymph node follicles

Our first set of experiments involved the complete removal of SCS macrophages. Clodronate liposomes have been shown to remove SCS macrophages without depleting other cell populations in lymph nodes (Fig. 3S1)[96–99]. We intradermally injected 20 μl of PBS or clodronate liposomes in the footpad of C57BL/6 mice. The amount of injected clodronate drug encapsulated in liposomes is 0.1 mg. We sacrificed the mice 7 days after PBS or clodronate liposome administration and collected the axillary, brachial, and popliteal as sentinel lymph nodes for histological analysis (Fig. 3.1A and 1B). We isolated sentinel lymph nodes and directly placed them into frozen solution in a plastic cryomold. We froze the sample by liquid nitrogen to preserve the antigens on the cell membrane for immunostaining. Tissue sections were sectioned with a thickness of 8 μm and placed on charged slides. Lymph node sections were stained using antibodies. Anti-CD169 (red color) was used to stain SCS macrophages. Anti-Lyve1 (green), anti-podoplanin (blue) and anti-Prox1 (green) were used to stain LECs. We found LECs form the lymph node subcapsular sinus with discontinuous cell connections at the sinus floor (Fig. 3.1A and 1B). White arrows show the space between LECs. The space size is about 1-10 μm (Fig. 3S2). There were no statistically significant differences in space size between PBS liposome and clodronate liposome treatments. SCS macrophages are resident cells located in the sinus or sitting at the inter-

endothelial space of the sinus floor. Some SCS macrophage can be located outside of the sinus and in the B cell follicles. PBS liposome treatment had no influence on macrophage populations, whereas clodronate liposomes depleted SCS macrophages. In both treatments, the sealed inter-endothelial cell space remained open. We conclude that clodronate liposome treatment eliminated SCS macrophages without disrupting the lymph node subcapsular sinus structure.

We next tested if SCS macrophage depletion would affect nanovaccine localization inside or outside of lymph node follicles (Fig. 3.1C and 1D). Our nanovaccine model is composed of ovalbumin (OVA) antigen conjugated to spherical gold nanoparticles (AuNPs). The full characterization of OVA-AuNP nanovaccine physicochemical properties is described in Figure 3S3 and Table 3S1. The rationale of choosing AuNPs is because they are easily synthesized with excellent size control, biocompatible and nonbiodegradable, and easily coated with multiple model antigens[100]. We previously determined that 100 nm OVA-AuNP nanovaccines have the highest follicle retention and OVA-specific antibody production[100]. In this study, we studied 100 nm OVA-AuNP nanovaccine location after PBS or clodronate liposome treatments. We injected 100 nm OVA-AuNP nanovaccines intradermally into the footpad 7 days post intradermal footpad injection of PBS or clodronate liposomes. The injected 100 nm OVA-AuNP nanovaccine dose is normalized based on the injected OVA antigen amount (10 μg) (Fig. 3S3-4, Table. 3S1). The sentinel lymph nodes were collected 12 hours after OVA-AuNP nanovaccine injection and directly fixed with 4% formaldehyde and 0.5% glutaraldehyde in PBS. The fixed samples were mounted and sectioned, then placed on copper grids. The tissue samples were negatively stained using 2% uranyl acetate. The morphology of the lymph node subcapsular sinus and OVA-AuNP location of tissue sections were imaged using transmission electron microscopy (TEM) at 120 kV. We pseudo-colored SCS

macrophages in green, LECs in brown, and OVA-AuNP nanovaccines in black for better visualization. TEM images revealed that SCS macrophages can reside (1) in the lymphatic sinus, (2) at the space between LECs, and (3) outside of the LEC floor and in the lymph node follicle (Fig. 3.1C). SCS macrophages are capable of sequestering OVA-AuNP nanovaccines in all locations. Clodronate liposome treatment eliminated SCS macrophages in the above-mentioned positions and allowed OVA-AuNP nanovaccines to cross the floor of LECs to access lymph node follicles (Fig. 3.1D). We illustrated a schematic to demonstrate this phenomenon (Fig. 3.1E). We conclude that SCS macrophages play a barrier role to prevent OVA-AuNP nanovaccines from accessing lymph node follicles.

Depleting SCS macrophages increases OVA-AuNP nanovaccine retention and presentation in lymph node follicles and induces greater humoral immune responses

We studied the effect of SCS macrophage depletion on OVA-AuNP nanovaccine follicle delivery and humoral immune responses. We determined the kinetics of 100 nm OVA-AuNP nanovaccine accumulation in lymph node follicles after various injection times (2 hours to 5 weeks). PBS or clodronate liposomes were injected intradermally into the footpad of mice 7 days before OVA-AuNP nanovaccine administration. Histological images of lymph node follicles revealed that CD21+ follicular dendritic cells (FDCs) (green color) remained intact in the B cell follicles after clodronate liposome administration indicating the treatment is specific for the depletion of CD169+ SCS macrophages (red color) (Fig. 3.2A). Gold nanoparticle signal was enhanced by silver staining. We observed a clear difference between clodronate liposome and PBS liposome pretreatments on OVA-AuNP accumulation in lymph node follicles (Fig. 3.2A). Clodronate liposome pretreatment led to faster follicle delivery at 12 hours, greater follicle accumulation at 48 hours to 2 weeks, and longer retention time of OVA-AuNPs in follicles compared to PBS

liposome pretreatment (Fig. 3.2B). From our previous study[100], we knew that FDCs in lymph node follicles determine OVA-AuNP nanovaccine retention and antigen presentation for B cell activation. TEM images revealed that there was an increase of 100 nm OVA-AuNP deposition and presentation on the FDC dendrites at 48 hours in clodronate liposome pretreatment than control condition (Fig. 3.2C and 2D). This indicated that more 100 nm OVA-AuNP nanovaccines can stimulate B cell activation after clodronate liposome treatment. We next tested if clodronate liposome pretreatment could induce greater humoral immune responses compared to PBS liposome pretreatment. We immunized the mice using 100 nm OVA-AuNP nanovaccines after PBS or clodronate liposome treatment and sacrificed the mice at 5 weeks. We performed histological analysis for germinal centers using an anti-GL7 stain. Our results showed that 100 nm OVA-AuNP nanovaccines could induce germinal centers (red color) that were attached to the FDC networks (green color) for both PBS and clodronate liposome pretreatments (Fig. 3.2E). We further quantified the percentage and total number of germinal center B cells ($GL7^{+}B220^{+}$) after disaggregation of sentinel lymph nodes into single cells for flow cytometry (Fig. 3.2F and 2G, and Fig. 3S5). We found that the clodronate liposome pretreatment generated 2 times more germinal center B cells than PBS liposomes pretreatment. Next, we quantified the amount of OVA-specific antibody production from the blood serum using enzyme-linked immunosorbent assay (ELISA) to determine if clodronate liposome pretreatment elicited greater antigen-specific antibody production. We determined that clodronate liposome pretreatment can induce 2 times more OVA-specific antibody than PBS liposome pretreatment (Fig. 3.2H). We conclude that SCS macrophage is a barrier to prevent OVA-AuNP nanovaccine retention and presentation in lymph node follicles that limits humoral immune responses.

Depleting SCS macrophages allows greater antigen-specific antibody production in various vaccine designs

We tested if this principle of eliminating SCS macrophage is applicable to various vaccine designs. We studied the effect of OVA-AuNP nanovaccine dose and size, and vaccine formulation on antigen-specific antibody production after elimination of SCS macrophages. We immunized the mice using different doses of 100 nm OVA-AuNP nanovaccine after PBS or clodronate liposome pretreatment and measured the antibody production from blood serum at 5 weeks (Fig. 3.3A). We found decreasing the 100 nm OVA-AuNP injection dose (normalized based on antigen OVA amount from 10 to 0.04 μg) led to linearly decreased OVA-specific antibody production after PBS liposome pretreatment. Surprisingly, lowering the 100 nm OVA-AuNP nanovaccine injection dose led to non-linearly decreased antibody production after clodronate liposome pretreatment. Antigen-specific antibody production was improved by 2-60 times after clodronate liposome pretreatment compared to PBS liposome pretreated condition at various 100 nm OVA-AuNP nanovaccine injection doses. After clodronate liposome pretreatment, we could achieve the same OVA-specific antibody production by reducing the injected dose of 100 nm OVA-AuNP by 16 times compared to the injected dose of 10 μg normalized OVA. We then tested another size of 15 nm OVA-AuNP nanovaccines and found they followed a similar dose-dependent behavior (Fig. 3.3B). OVA-specific antibody production was significantly higher in response to clodronate liposome than PBS liposome pretreatment. We further tested if this approach can be applied for other vaccine formulations. We tested different vaccine formulations including antigen alone (Fig. 3.3C) and antigen formulated with commercial adjuvant Alum (Fig. 3.3D). Pretreatment using clodronate liposomes with these vaccine formulations showed significantly higher OVA-specific antibody production than PBS liposome pretreatment. We conclude that eliminating SCS

macrophage is a universal approach to improving antigen-specific antibody production for a variety of vaccine designs.

Inhibition of macrophage uptake function improves nanovaccine delivery to lymph node follicles and induces robust humoral immune responses

We next determined if this phenomenon was clodronate liposome treatment-specific, or whether this phenomenon was related to the physical removal or functional removal of the SCS macrophages. SCS macrophages play key roles in innate immunity to protect the host against pathogens[96]. Repopulation of depleted SCS macrophages requires 2-6 months by monocytes[93]. It has been shown that chemical agents gadolinium chloride ($GdCl_3$), carrageenan (CGN), and dextran sulfate 500 (DS500) can inhibit macrophage uptake function (Fig. 3S1)[99,101–107]. We hypothesized that the pretreatment of the mice by these macrophage inhibitors can reduce the uptake capability of SCS macrophages without eliminating them. To tests this hypothesis, we sacrificed the mice 24 hours after intradermal footpad administration of various macrophage inhibitors and isolated sentinel lymph nodes for histological analysis, then compared to PBS control. The injection doses of macrophage inhibitors were standardized to be 0.1 mg in 20 μl volume. Histology revealed that SCS macrophages remained around the subcapsular sinus floor of lymph nodes 24 hours after macrophage inhibitor pretreatment (Fig. 3.4A), indicating SCS macrophages were not eliminated after the pretreatment with macrophage inhibitors. CD169 (red color) was used to stain for SCS macrophages and Prox1 (green color) was used to stain for LECs. We examined the TEM images with the enlarged panels focused on SCS macrophages after intradermal footpad injection of 100 nm OVA-AuNP nanovaccines after pretreatment of macrophage inhibitors (Fig. 3.4B). SCS macrophages were labelled in green and LECs were labelled in brown for better visualization. We found reduced amounts of 100 nm OVA-AuNP

nanovaccines in SCS macrophages after all types of macrophage inhibitor pretreatment compared to PBS control. We conclude that the inhibition of macrophage uptake function is sufficient to reduce the OVA-AuNP nanovaccine sequestration by SCS macrophages in lymph nodes.

We then determined if pretreatment with macrophage inhibitors (i.e., agents that alter the uptake function) led to the same phenomenon as clodronate liposome pretreatment in mice, resulting in enhanced OVA-AuNP nanovaccine delivery to lymph node follicles and induction of robust humoral immune responses (Fig. 4C-F). We sacrificed the mice 48 hours after 100 nm OVA-AuNP nanovaccine administration following macrophage inhibitor pretreatment. We achieved 2 times enhanced OVA-AuNP nanovaccine accumulation in lymph node follicles after inhibition of macrophage function compared to PBS control (Fig. 4C and 4E). Next, we immunized the mice using 100 nm OVA-AuNP nanovaccine (2.5 μg OVA amount) after 24 hours of macrophage inhibitor treatment and sacrificed the mice at 5 weeks. We achieved similar humoral immune responses across all macrophage inhibitor treatment groups (Fig. 4D and 4F). We can induce germinal centers (red color) after all types of macrophage inhibitor pretreatment, but not in PBS control mice (Fig. 4D). Mice pretreated with macrophage inhibitors had 10-13 times higher OVA-specific antibody production compared to PBS control (Fig. 4F). Here we explored the universality of macrophage inhibitors by disruption of SCS macrophage uptake, resulting in enhanced humoral immune responses.

Assessing the administration windows of macrophage inhibitors for efficient antibody production

We next assessed the administration time windows of macrophage inhibitors for efficient antibody production (Fig. 3.5A). Macrophage inhibitors can disrupt the SCS macrophage uptake function,

but it is unclear how long this effect can last for OVA-AuNP nanovaccines. We asked the question whether the administration time between the macrophage inhibitor and OVA-AuNP nanovaccines influences the antigen-specific antibody production. We addressed this question by testing different sequences of macrophage inhibitors and OVA-AuNP nanovaccine administration. Macrophage inhibitors (clodronate liposomes, $GdCl_3$, CGN, and DS500) were intradermally injected into the mouse footpad (7, 3, 1, and 0 days (3 hours)) before or (3 and 7 days) after administration of 100 nm OVA-AuNP nanovaccines and compared to PBS control (Fig. 3.5). We immunized the mice using 100 nm OVA-AuNP nanovaccines (2.5 μg OVA amount) and measured the OVA-specific antibody production from blood serum at 5 weeks. We found that the administration window to maximize antibody production is dependent on macrophage inhibitor type. They are highlighted using blue shaded area (Fig. 3.5). Clodronate liposomes deplete SCS macrophages and results in a broader window to induce efficient antibody production compared to PBS control. We failed to generate efficient antibody production when we administrated macrophage inhibitors 3-7 days after OVA-AuNP nanovaccine administration. We achieved efficient antibody production in all types of macrophage inhibitors when the macrophage inhibitors were administered 0-1 day prior to OVA-AuNP nanovaccines.

Macrophage inhibitors show great adjuvanticity when they were formulated with OVA-AuNP nanovaccines

Vaccine formulations are typically formulated with antigens and adjuvants that are co-administrated. Adjuvants are used to amplify antigen-specific immune responses. Designing novel adjuvants enable us to better engineer the immune system and develop successful vaccines[2,3,108–111]. We found pretreatment of macrophage inhibitor 0-1 day prior to OVA-AuNP nanovaccine administration resulted in enhanced antigen-specific antigen production (Fig. 3.5), we proposed to

formulate macrophage inhibitors with our 100 nm OVA-AuNP nanovaccines together to test the adjuvanticity of these macrophage inhibitors (Fig. 3.6). We pre-mixed the 100 nm OVA-AuNPs (2.5 μg OVA amount) with each macrophage inhibitor (0.1 mg) and injected them intradermally into the footpad of C57BL/6 mice. We measured the OVA-specific antibody production from blood serum at 1 to 5 weeks. We found OVA-AuNP nanovaccines formulated with macrophage inhibitors induced greater antibody production than OVA-AuNP nanovaccines alone after 2 weeks of immunization. We also achieved 34-39 times higher antibody production immunized by OVA-AuNP nanovaccines formulated with different types of macrophage inhibitors compared to OVA-AuNP nanovaccines alone at 5 weeks (Fig. 3.6). This finding is equivalent to the pretreatment of macrophage inhibitors (Fig. 3.4H and Fig. 3.5B-E). We conclude that macrophage inhibitors can act as adjuvants that can be easily pre-mixed with nanovaccines to induce greater humoral immune responses for more efficient vaccination.

Assessing the toxicity of macrophage inhibitors

We finally tested the toxicity of these macrophage inhibitors. Macrophage inhibitors disrupt the SCS macrophage function of local lymph nodes after intradermal footpad administration. We asked the question "what are the consequences of local innate immunity suppression on mice and could this induce systemic toxicity". We conducted a toxicology assessment using hematology and liver biochemistry assays. We injected the mice with 0.1 mg of these macrophage inhibitors and sacrificed the mice after 3 days. No significant difference in immune cell counts and hematological markers were determined across different macrophage inhibitors compared to PBS controls (Fig. 3S6 and S7). We did not see any increase in all of the tested liver function biomarkers alanine aminotransferase (ALT), aspartate aminotransferase (AST), alkaline phosphatase (ALP) and total bilirubin (TBIL) after macrophage inhibitor treatment compared to PBS controls (Fig. 3S8). All

biomarker concentrations are within the normal range for C57BL/6 mice[112]. We did not observe systemic or gross inflammation in the histological sections of C57BL/6 mice hepatic tissue and splenic tissues after macrophage inhibitor treatment (Fig. 3S9 and S10). Here, we conclude that this approach is safe because this approach only suppresses the SCS macrophage function and does not induce systemic toxicity.

Conclusions and outlook

SCS macrophages are the first layer of defense in lymph nodes against pathogen and infectious disease[25,26]. These SCS macrophages are highly involved in the sequestration and clearance of viruses and bacteria. SCS macrophages are considered professional antigen presenting cells that directly activate T cells and natural killer T cells[33,113,114]. Depletion of SCS macrophage limits cancer cell clearance and promote tumour growth[96]. SCS macrophages are important in capturing viruses, bacteria or immune complexes and promote antigen transport to B cell follicles to stimulate the humoral immune responses[10,27–32]. However, the importance of SCS macrophages in promoting B cell mediated humoral immunity has been recently challenged[10,47,92,94]. Here, we found that SCS macrophages play a barrier role to prevent OVA-AuNP nanovaccines from accessing lymph node follicles. Physical removal or functional impairment of SCS macrophages by chemical agents (clodronate liposomes, $GdCl_3$, CGN or DS500) allowed OVA-AuNP nanovaccines to more efficiently deliver to and retain in follicles and interact with FDCs. This led to enhancement of humoral immune responses and eventually elicited up to 60 times more antigen-specific antibody production depending on nanovaccine design and injection dose. We summarized this finding with a schematic (Fig. 3.7A). Our findings of greater B cell activation and antibody production after eliminating SCS macrophages using clodronate liposomes are supported by other groups[47,92–96].

We also tested other chemical agents and they were not sufficient to remove macrophages or disrupt their uptake function and failed to generate enhanced OVA-AuNP nanovaccine follicle delivery and humoral immune responses. For example, clodronate needs to be encapsulated into a liposome formulation to induce macrophage depletion, whereas free clodronate agent alone (0.1 mg) cannot remove SCS macrophages and induce robust humoral immunity (Fig. 3S11). Free clodronate formulated with OVA-AuNPs cannot induce effective vaccination compared to clodronate liposome formulated nanovaccines (Fig. 3S12). Dextran sulfate 9 (DS9) (0.1 mg) (average molecular weight 9,000 - 20,000 Da) is not sufficient to saturate macrophage scavenger receptors compared to DS500 (average molecular weight > 500,000 Da) and failed to inhibit macrophage uptake function[105] (Fig. 3S13). These results support the finding that inhibition of SCS macrophage uptake function is critical to allow more OVA-AuNP nanovaccines to enter lymph node follicles and mediate efficient humoral immune responses. The adjuvanticity of these macrophage inhibitor agents were determined by testing the neutralized antibody production of immunized mice. The nanovaccines formulated with macrophage inhibitor agents resulted in more than 30 times higher antibody production compared to nanovaccines alone. This category of adjuvant shows the reverse effects of reducing innate immunity and boosting humoral immunity. We term them “reverse adjuvants”. The mechanism of these adjuvants is different from any existing adjuvants used in vaccines[2,64,108,111,115–119]. The clinical applications of the “reverse adjuvants” need to be further explored in the future by combining with other commercially available adjuvants and vaccine formulations for specific infectious disease models. The potential adjuvanticity of other chemical agents for macrophages uptake inhibition including cell membrane, endocytosis, and cytoskeleton pathways need to be evaluated in the future. This study demonstrates

the role of SCS macrophages in the transport of the delivery of nanovaccine to the lymph node follicle. Delivery to the final target in the lymph node is critical to the vaccines' ability to generate neutralizing antibodies.

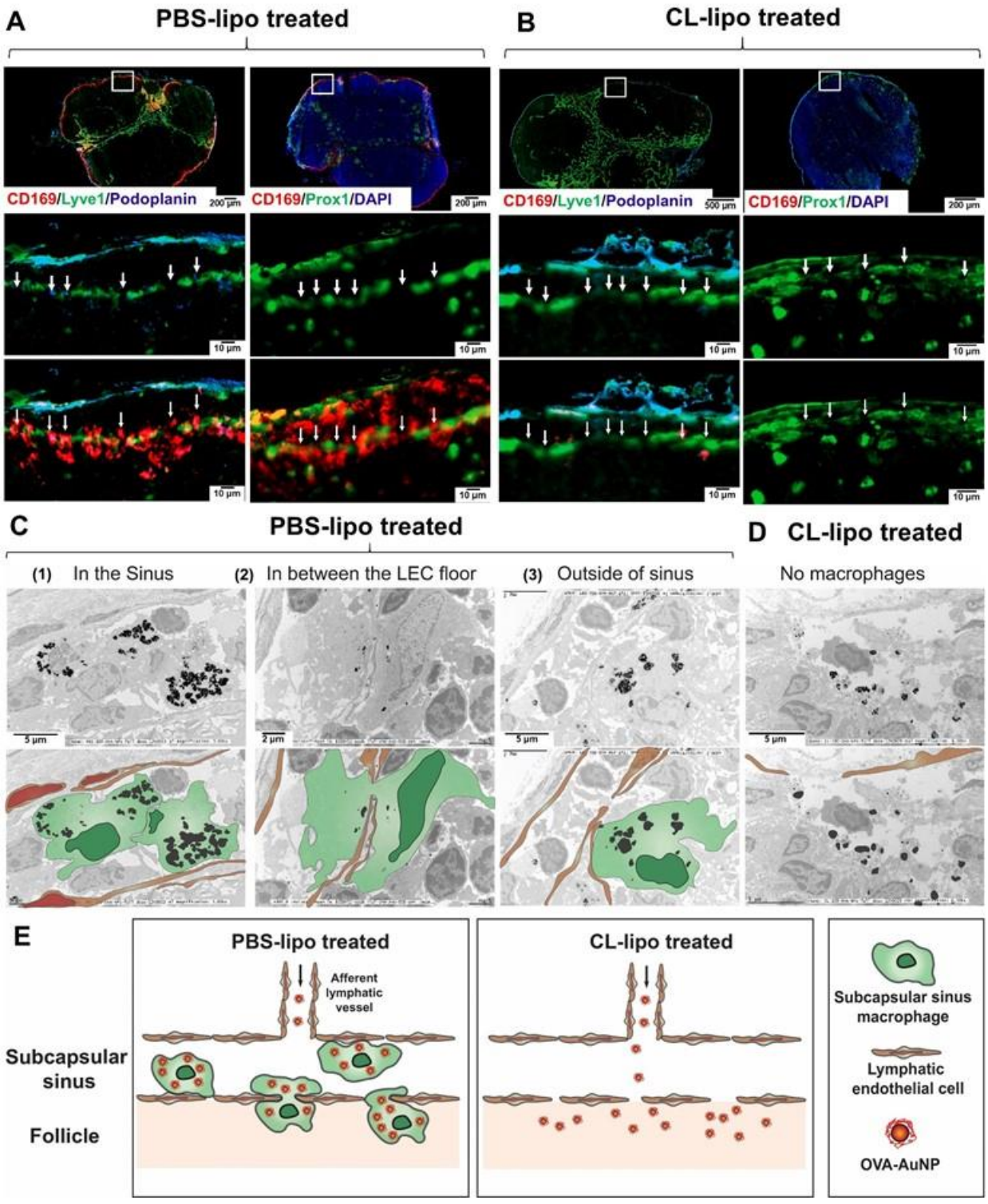

Fig. 3. 1. Depleting subcapsular sinus (SCS) macrophages allowed OVA-AuNP nanovaccines to access lymph node follicles. (A) Immunostaining images of the SCS macrophages (CD169, red), lymphatic endothelial cells (Lyve1, green; Podoplanin, blue; and Prox1, green). White arrows present the space between LECs. (B) SCS macrophages were depleted with clodronate liposomes in the lymph node, as demonstrated by the lack of CD169 red stain. (C) Representative TEM

images of lymph node subcapsular sinus after intradermal footpad injection of 100 nm OVA-AuNP nanovaccines at 12 hours. Corresponding schematics were demonstrated for better visualization of SCS macrophages (green), LECs (brown), OVA-AuNP nanovaccines (black). SCS macrophages can sequester nanovaccines when they resided (1) in the lymphatic sinus, (2) at the space between LECs, (3) out of the LEC floor and in lymph node follicles. (D) Clodronate liposome treatment depletes SCS macrophages and allows nanovaccines to cross the floor of LECs to access lymph node follicles. (E) Schematic of nanovaccine transport with and without SCS macrophage. PBS-lipo represents PBS liposome and CL-lipo represents clodronate liposome in the figure.

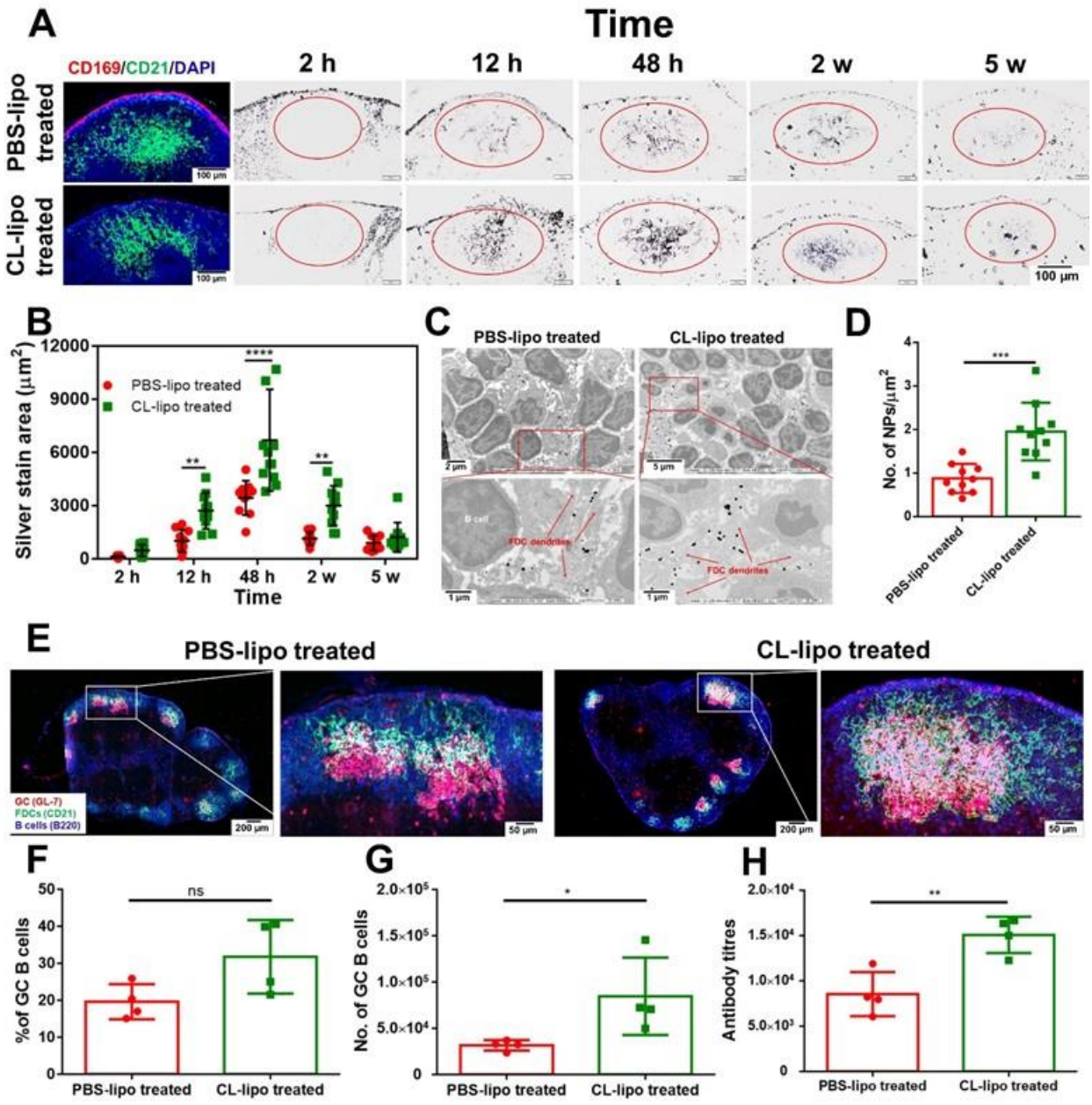

Fig. 3. 2. Depleting SCS macrophages increases OVA-AuNP nanovaccine retention and presentation in lymph node follicles and induced greater humoral immune responses. (A) Histological images of lymph node follicles after 7 days post intradermal footpad injection of PBS or clodronate liposome treatment. SCS macrophages (red) were depleted after clodronate liposome administration whereas follicular dendritic cells (FDCs, green color) in B cell follicles remained intact. Representative TEM images show that the retention of 100 nm OVA-AuNP nanovaccines in lymph node follicles varied between lymph nodes with and without SCS macrophage depletion. (B) Quantification of 100 nm OVA-AuNP nanovaccine accumulation in follicles at 2 hours to 5 weeks after 7 days of PBS or clodronate liposome administration. (C) TEM images of 100 nm OVA-AuNP nanovaccine deposition and presentation on the dendrites of follicular dendritic cells (FDCs) at 48 hours post intradermal footpad injection after 7 days of PBS and clodronate liposome administration. Red arrows point to the dendrites of FDCs. (D) Quantifying numbers of 100 nm

OVA-AuNP nanovaccines on FDC dendrites at 48 hours. Assessment of humoral immune responses including (E) germinal center formation (GL7 red; CD21 green; B220 blue), (F) percentage of germinal center B cells ($GL7^+B220^+$), (G) numbers of germinal center B cells ($GL7^+B220^+$), and (H) antigen-specific antibody production from blood serum after intradermal footpad injection of PBS and clodronate liposomes 7 days prior to 100 nm OVA-AuNP nanovaccine injection at 5 weeks (n = 4 mice/group). PBS-lipo represents PBS liposome and CL-lipo represents clodronate liposome in the figure. Data shown as mean ± SD; *P < 0.05; **P < 0.01; ***P < 0.001; ****P < 0.0001. All P values are from two-way ANOVA or followed by Tukey's multiple comparisons tests or an unpaired t test.

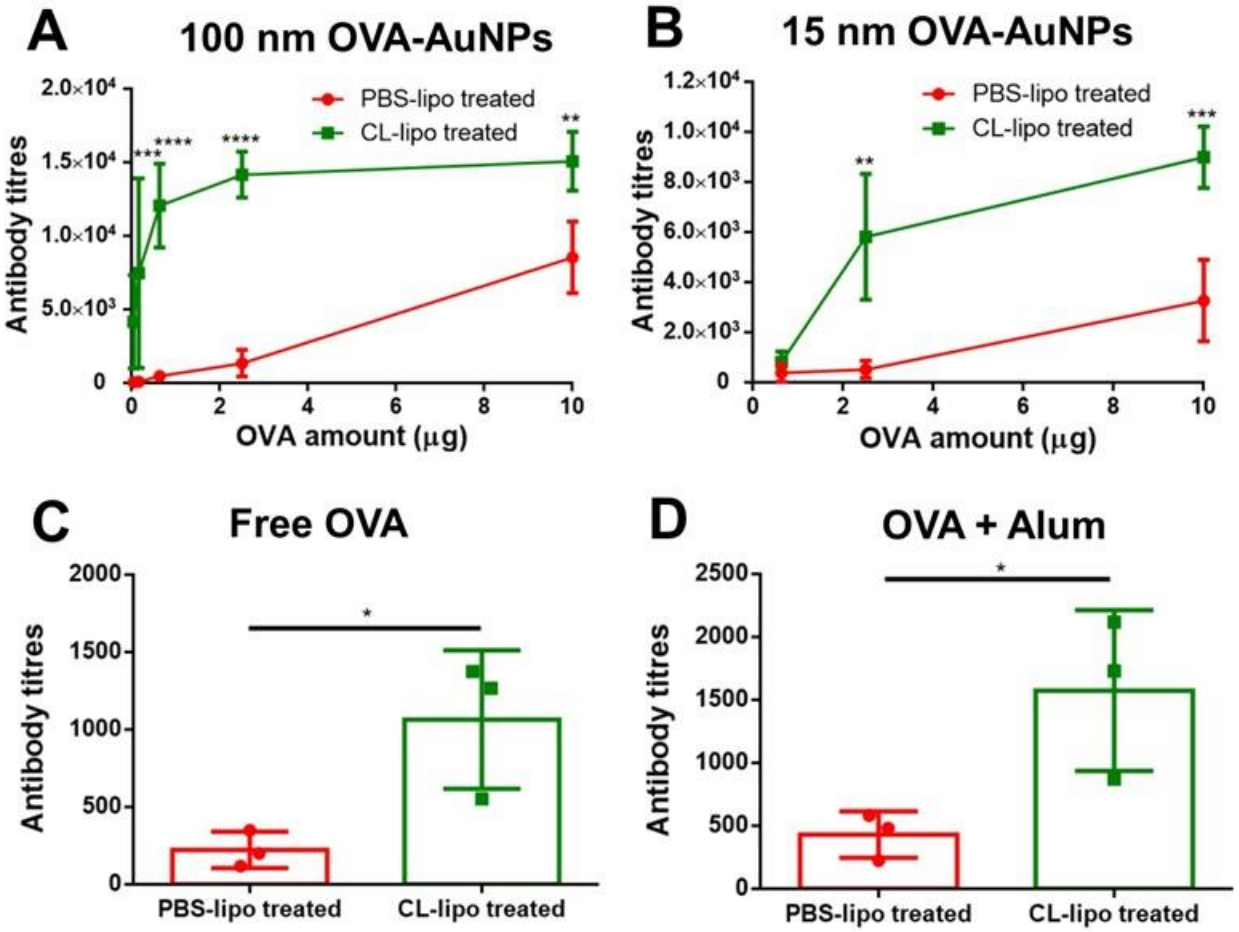

Fig. 3. 3. Depleting SCS macrophage allowed greater antigen-specific antibody production in various vaccine designs. Measurements of OVA-specific antibody production after administration of (A) 100 nm and (B) 15 nm OVA-AuNP nanovaccine with (PBS-lipo treated) and without (CL-lipo treated) SCS macrophages. (C) The antibody production was also examined for (C) free antigen and (D) antigen formulated with commercial adjuvant Alum with wild-type and depleted SCS macrophages (n = 3-6 mice/group). PBS-lipo represents PBS liposome and CL-lipo represents clodronate liposome in the figure. Data shown as mean ± SD; *P < 0.05; **P < 0.01; ***P < 0.001; ****P < 0.0001. All P values are from two-way ANOVA followed by Tukey's multiple comparisons tests or an unpaired t test.

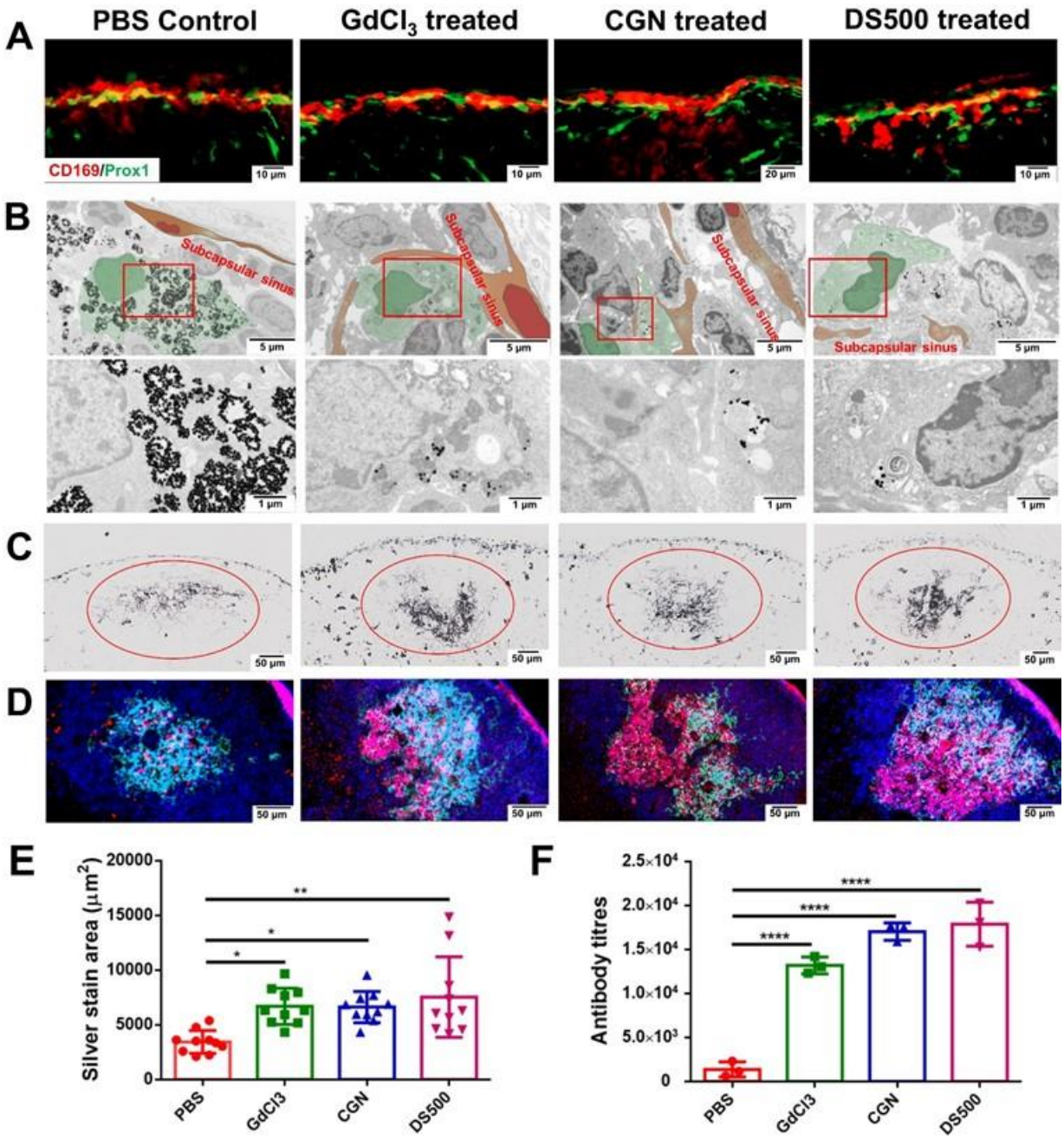

Fig. 3. 4. Inhibition of macrophage uptake function improved nanovaccine delivery to lymph node follicles and robust humoral immune responses. (A) SCS macrophages remain intact in the subcapsular sinus of lymph nodes after administration of macrophage inhibitors using GdCl3, carrageenan (CGN) or Dextran sulfate 500. CD169 (red color) stains for SCS macrophages and Prox1 (green color) stains for LECs. (B) Representative TEM images and the enlarged images on SCS macrophages were examined after intradermal footpad injection of 100 nm OVA-AuNP nanovaccines after 24 hours of macrophage inhibition administration. SCS macrophages labeled green and LECs labeled brown. Pretreatment of macrophage inhibitors induce greater 100 nm OVA-AuNP nanovaccine accumulation in lymph node follicles and humoral immune responses (C-F). (C) Histological images of 100 nm OVA-AuNP nanovaccines accumulation in lymph node

follicles were analyzed after 48 hours post nanovaccine intradermal footpad injection. Macrophage inhibitors were administered 24 hours prior to nanovaccine injection (n = 4 mice/group). Data were collected from 10 lymph node follicles for each condition. (E) Quantification of 100 nm OVA-AuNP nanovaccine accumulation in follicles at 48 hours after macrophage inhibitor administration. Assessment of (D) germinal center formation (GL7 red; CD21 green; B220 blue), and (F) antigen-specific antibody production in blood serum after administration of 100 nm OVA-AuNP nanovaccine at 5 weeks, macrophage inhibitors were prior to nanovaccine injection (n = 3 mice/group). The injected dose of 100 nm OVA-AuNP nanovaccine was normalized based on the inject OVA antigen amount (2.5 μg). Data shown as mean ± SD; *P < 0.05; **P < 0.01; ****P < 0.0001. All P values are from one-way ANOVA followed by Tukey's multiple comparisons tests.

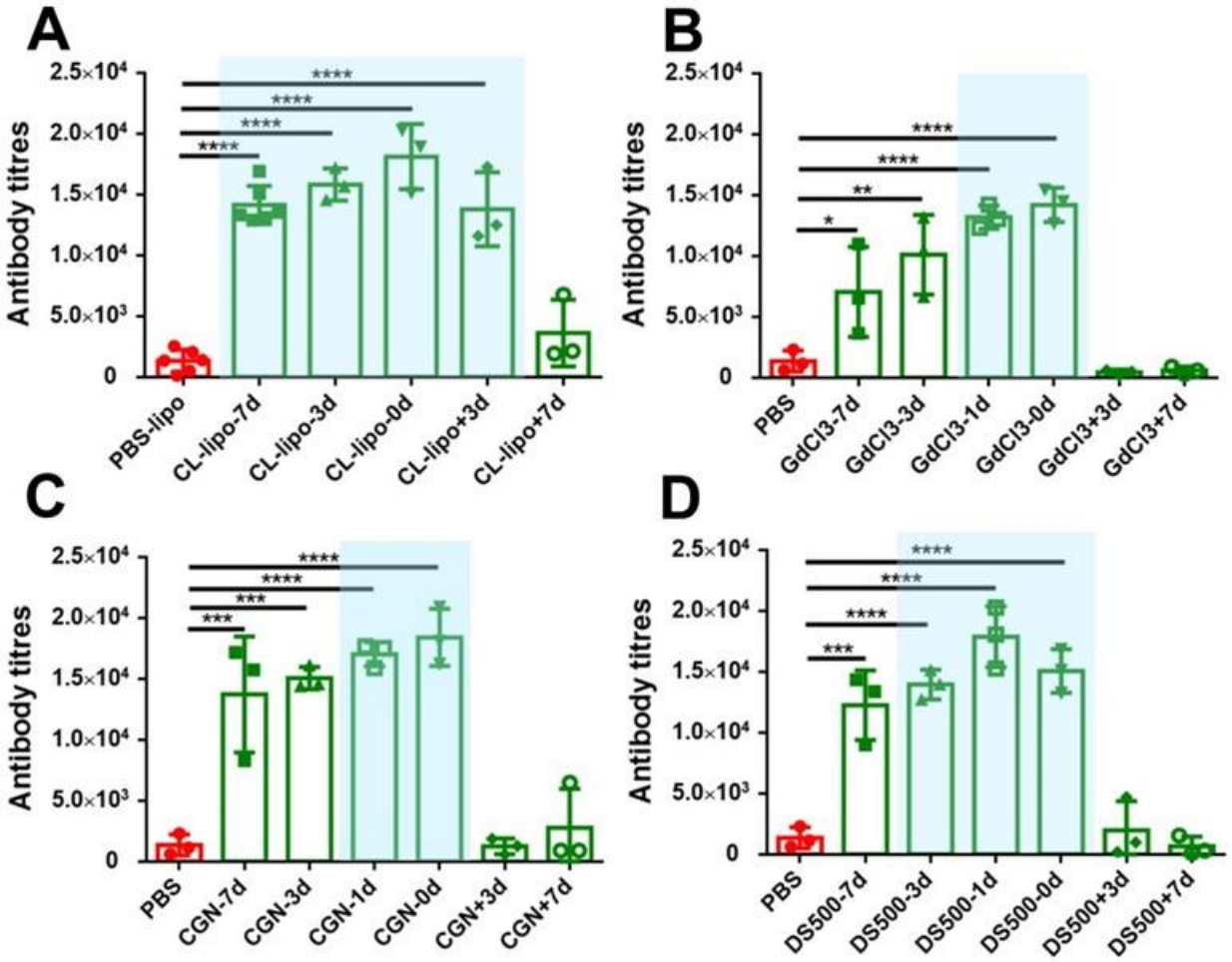

Fig. 3. 5. Assessing the administration windows of macrophage inhibitors for efficient antibody production. Antibody production at 5 weeks after (B) Clodronate liposomes, (C) $GdCl_3$, (D) CGN, and (E) DS500 were intradermally footpad injected before (7, 3, 1, and 0 days (3 hours)) or after (3 and 7 days) administration of 100 nm OVA-AuNP nanovaccine (n = 3-6 mice/group). The best administration windows were obtained for each macrophage inhibitors (blue shaded area) as determined by statistical comparison to control PBS condition. Data shown as mean ± SD; *P < 0.05; **P < 0.01; ***P < 0.001; ****P < 0.0001. All P values are from one-way ANOVA followed by Tukey's multiple comparisons tests.

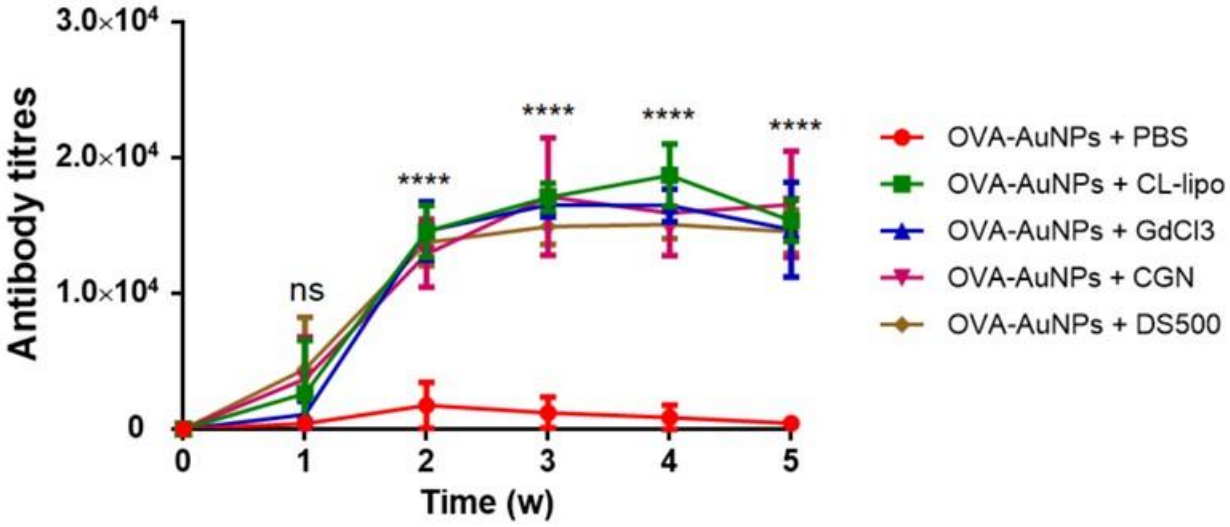

Fig. 3. 6. Macrophage inhibitors showed great adjuvanticity when they were formulated with OVA-AuNP nanovaccines. Antibody production after administration of OVA-AuNP nanovaccine and agents that inhibit macrophage uptake or deplete macrophages (n = 7 mice/group). The data were collected from two separate experiments. Data shown as mean ± SD; ***P < 0.001; ****P < 0.0001. All P values are from two-way ANOVA followed by Tukey's multiple comparisons tests.

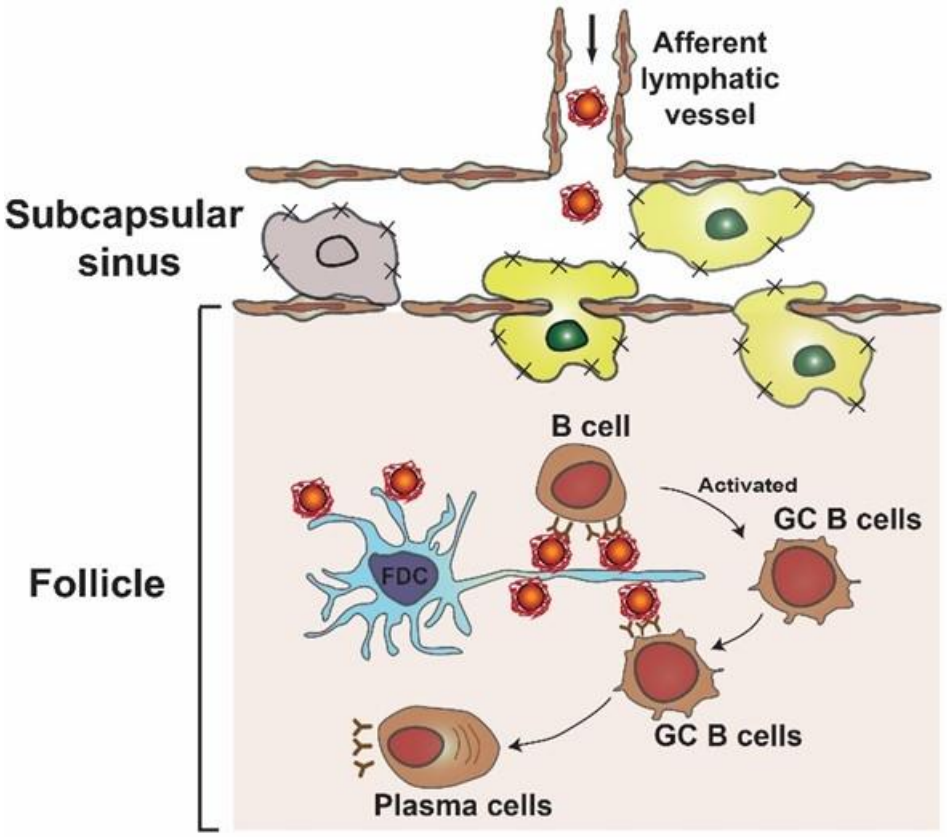

Fig. 3. 7. Schematic of transport of OVA-AuNP nanovaccines to the follicular dendritic cells in lymph node follicles for robust humoral immune responses.

Supplementary figures and table

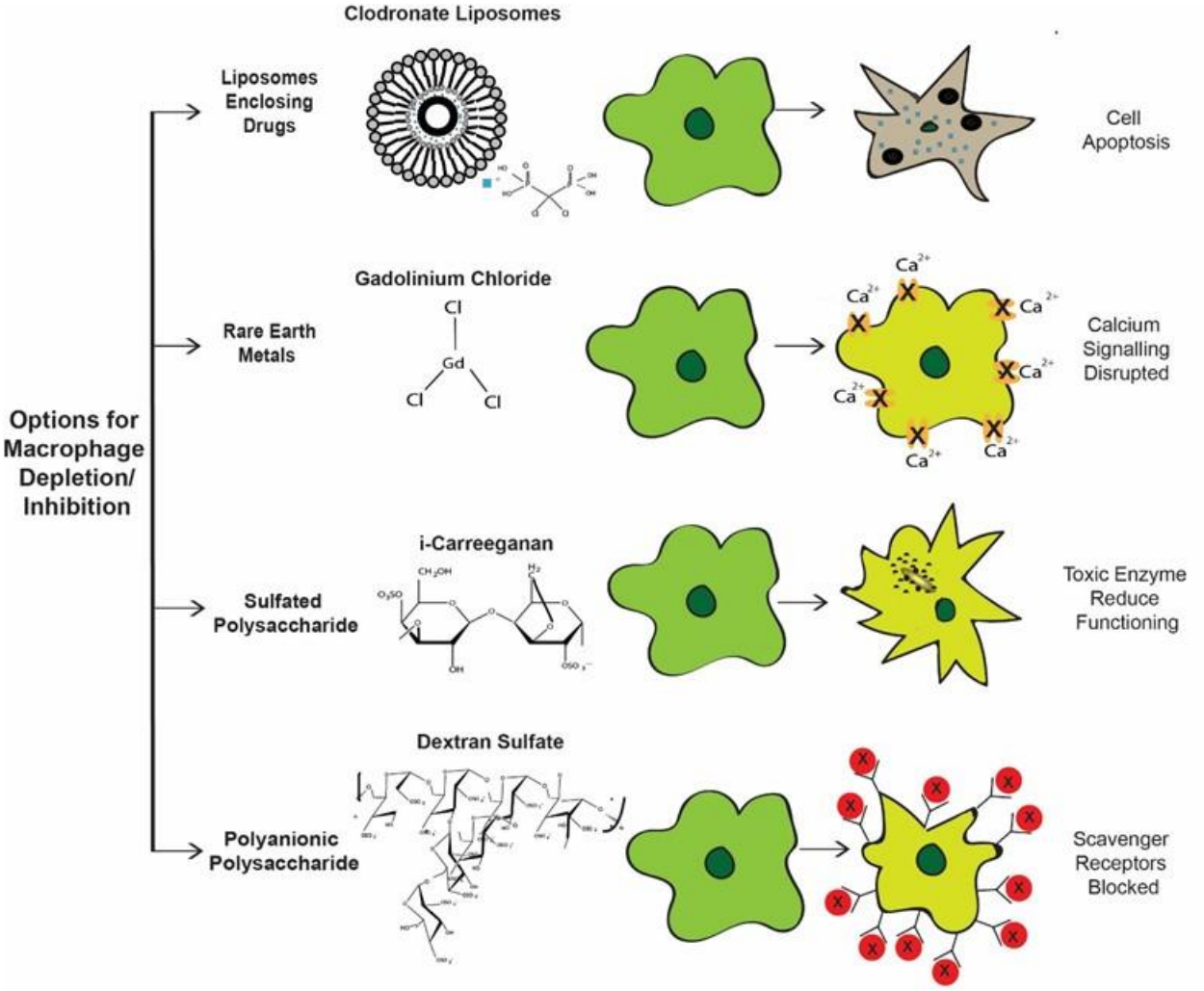

Fig. 3S. 1. Mechanism of macrophage inhibitors. Clodronate liposomes were used to deplete SCS macrophages in lymph nodes. Other macrophage inhibitors including gadolinium chloride ($GdCl_3$), carrageenan (CGN), or dextran sulfate 500 (DS500) were used to inhibit SCS macrophage uptake function

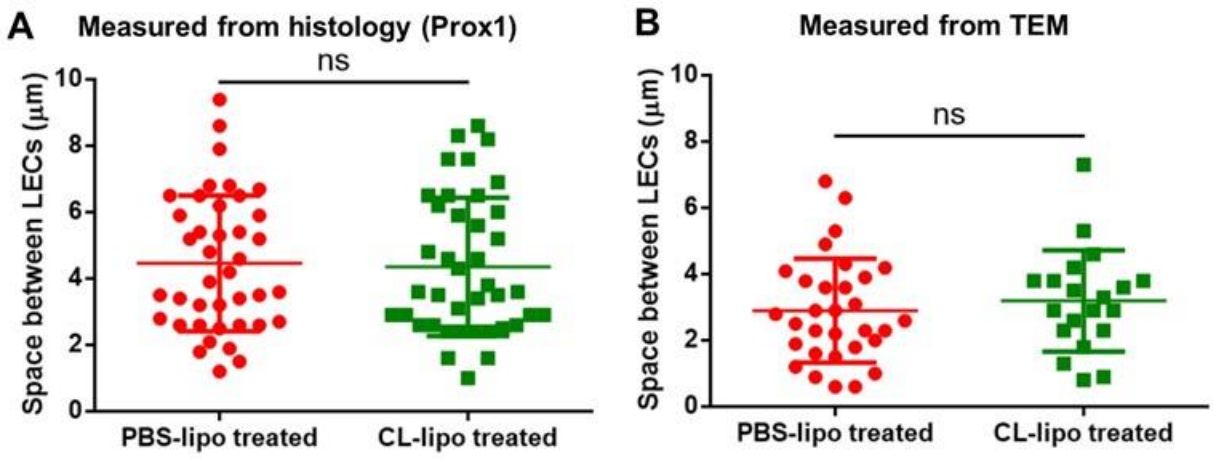

Fig. 3S. 2. Quantification of space between lymphatic endothelial cells (LECs). (A) Spaces between LECs were measured based on Prox1 antibody stain (n = 40). (B) Spaces between LECs were measured based on TEM (n > 20). Spaces between LECs was measured after PBS liposome and clodronate liposome treatment. PBS-lipo represents PBS liposome and CL-lipo represents clodronate liposome in the figure. Data shown as mean ± SD. The statistical analysis was studied by an unpaired t test.

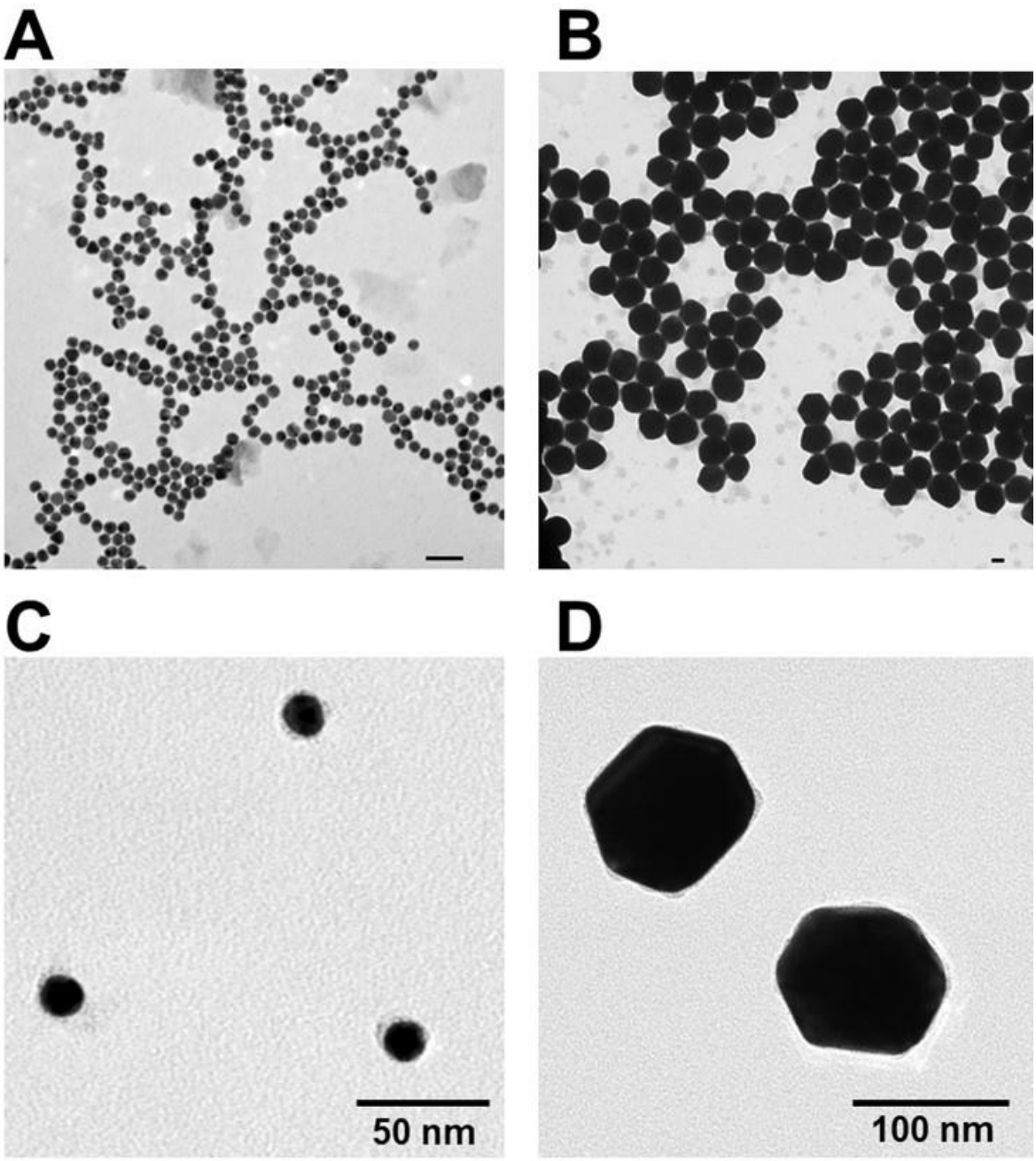

Fig. 3S. 3. Characterization of nanoparticles and nanovaccines. TEM images of (A) 15 and (B) 100 nm citrate-coated gold nanoparticles (citrate-AuNPs). Scale = 50nm. TEM images of ovalbumin-coated gold nanoparticles (OVA-AuNPs) with core sizes of (C) 15 and (D) 100 nm.

Table 3S.1. Physiochemical properties of nanoparticles and nanovaccines

Nanoparticle		Physicochemical Properties			
Size	Surface Ligands	Inorganic Diameter (nm)	Hydrodynamic Diameter (nm)	ξ Potential (mV)	λ_{LSPR} (nm)
15	Citrate	15.3 ± 1.2	19.2 ± 0.5	-9.7 ± 1.6	521
	OVA		79.6 ± 5.5	-21.5 ± 1.2	528
100	Citrate	109.0 ± 5.9	107.1 ± 2.9	-24.8 ± 1.1	575
	OVA		165.7 ± 6.5	-22.5 ± 1.3	587

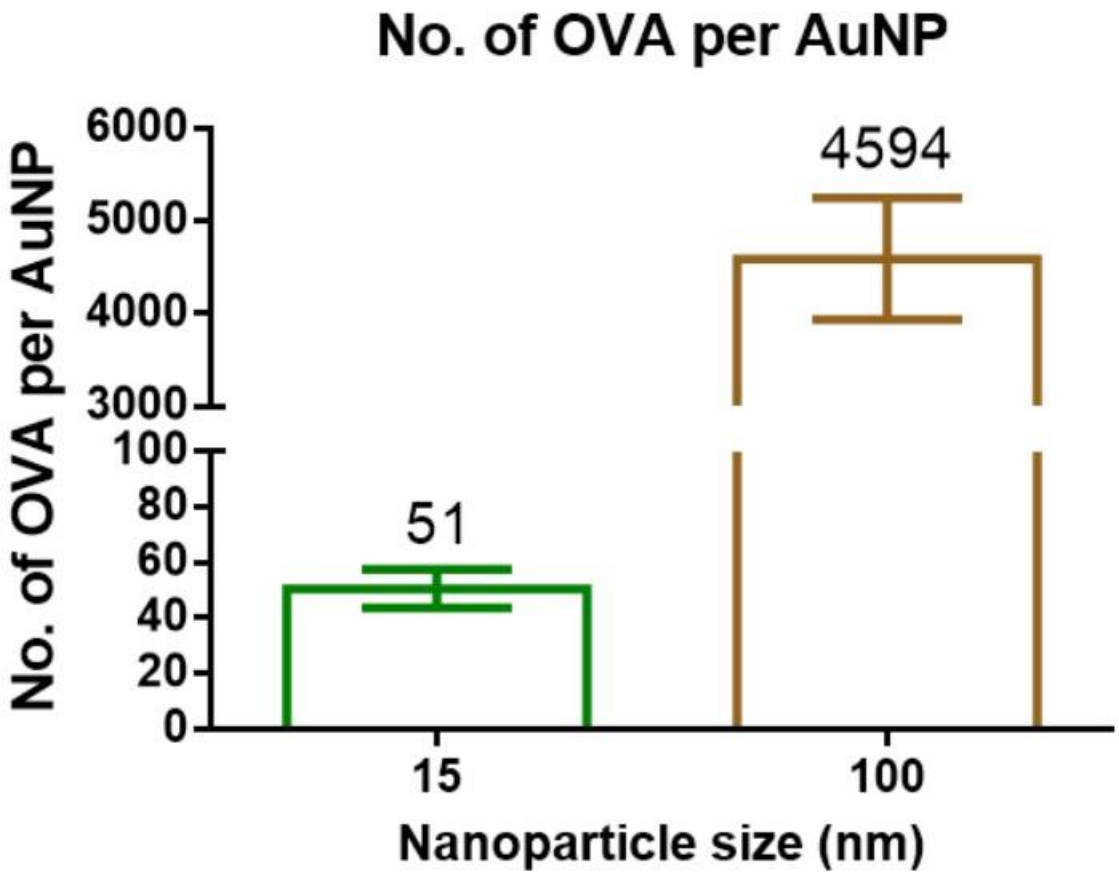

Fig. 3S. 4. Quantification of OVA protein amount AuNPs using bicinchoninic acid (BCA) assay. The OVA-AuNP injection dose is normalized based on the same total amount of OVA antigen.

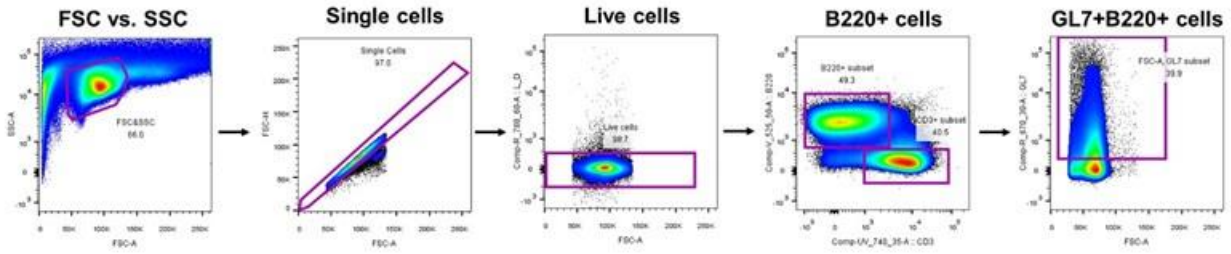

Fig. 3S. 5. Gating strategy for analyzing germinal center B cells after 5 weeks of immunization using 100 nm OVA-AuNPs.

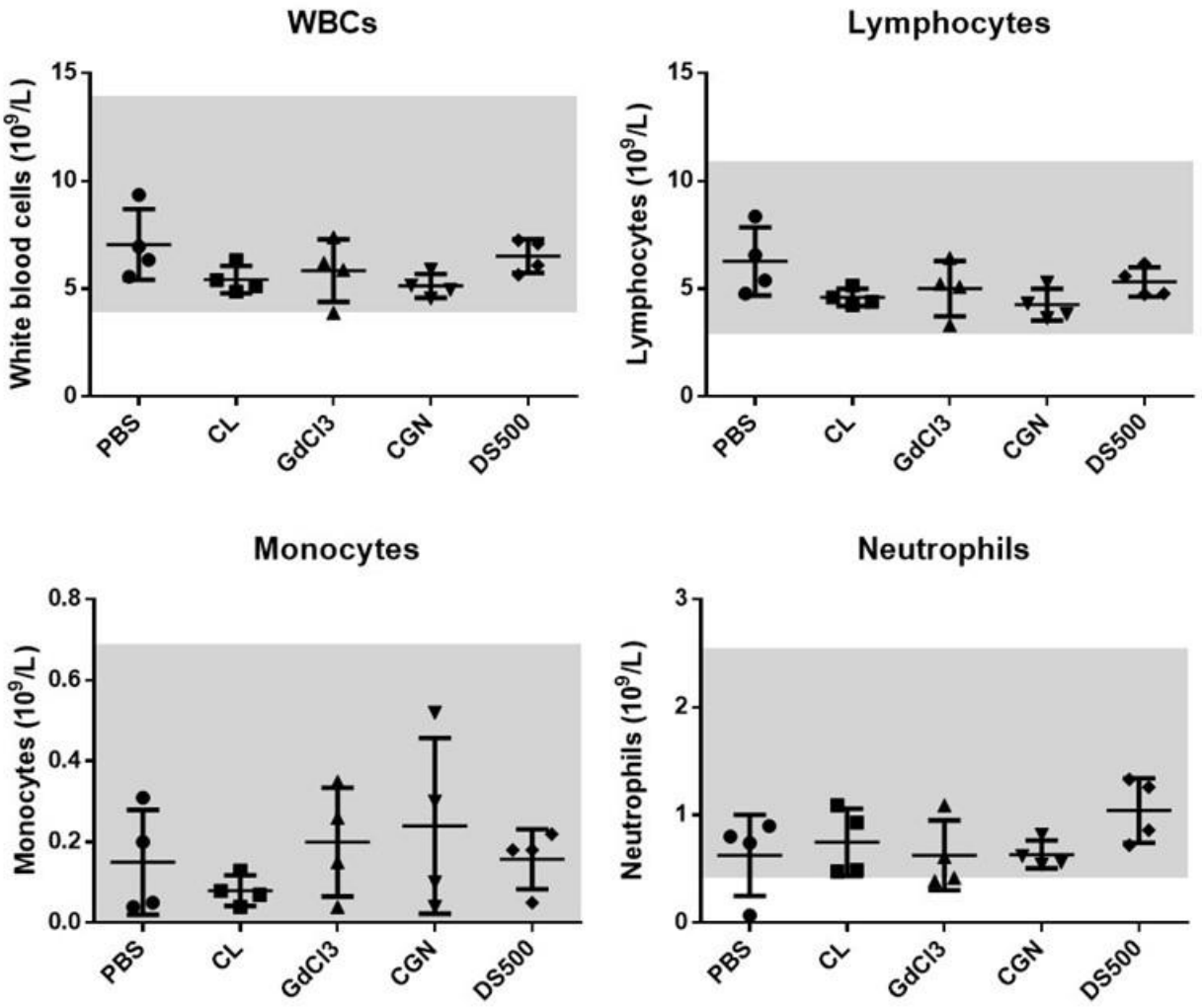

Fig. 3S. 6. Analysis of immune cells. Immune cell counts from blood of C57BL/6 mice 3 days after intradermal injection of macrophage inhibitors (0.1 mg per footpad, in total 0.4 mg for four footpads) and PBS controls (n = 4 mice/group). WBC represents white blood cells. Grey shaded area represents normal range of cell counts for C57BL/6 mice.

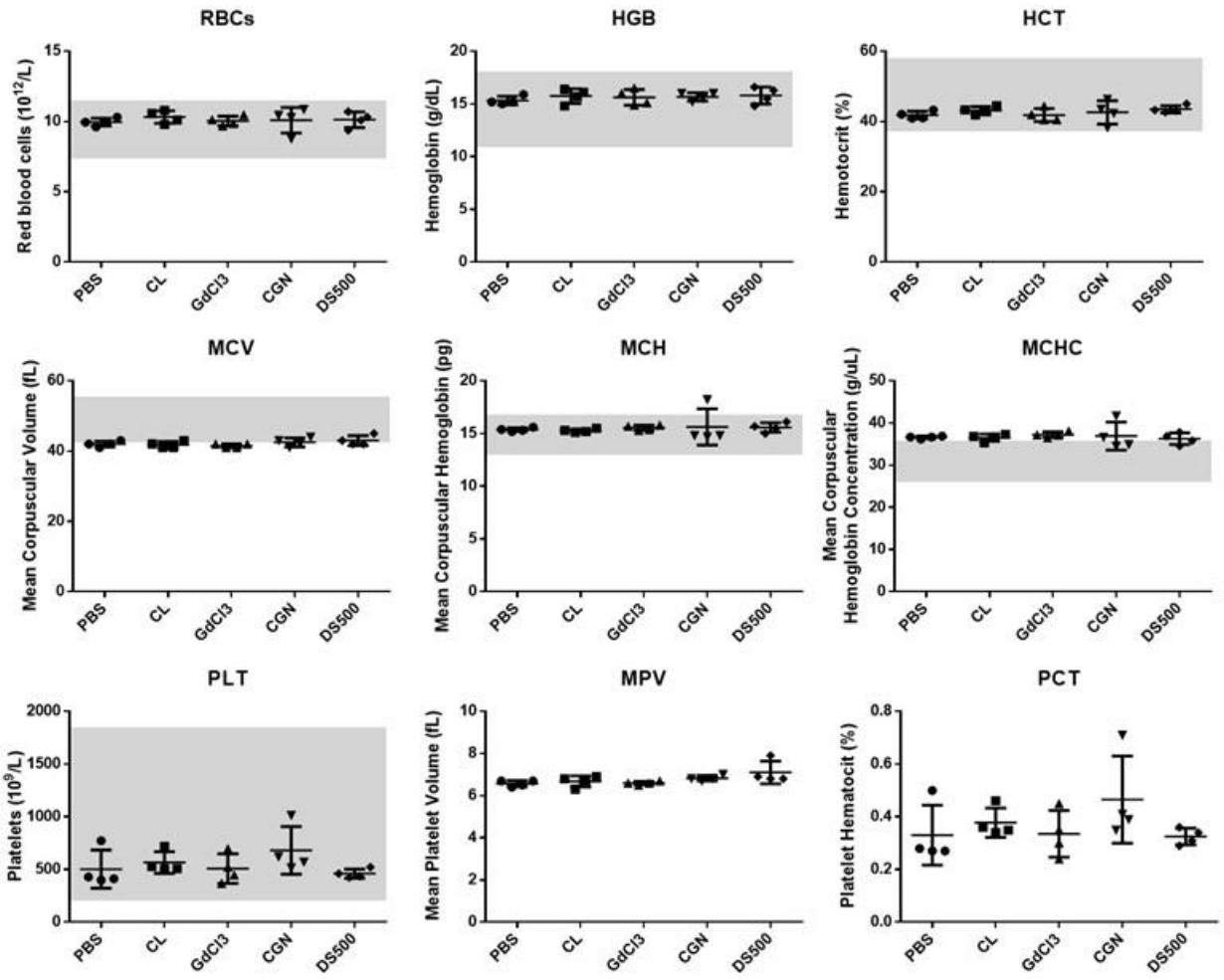

Fig. 3S. 7. Hematology study. Hematology analysis of C57BL/6 mice 3 days after intradermal injection of macrophage inhibitors (0.1 mg per footpad, in total 0.4 mg for four footpads) and PBS controls (n = 4 mice/group). Parameters shown include red blood cell count (RBC), hemoglobin (HGB), hematocrit (HCT), mean corpuscular volume (MCV), mean corpuscular hemoglobin (MCH), mean corpuscular hemoglobin concentration (MCHC), platelet count (PLT), mean platelet volume (MPV), and procalcitonin (PCT). Grey shaded area represents normal range for C57BL/6 mice.

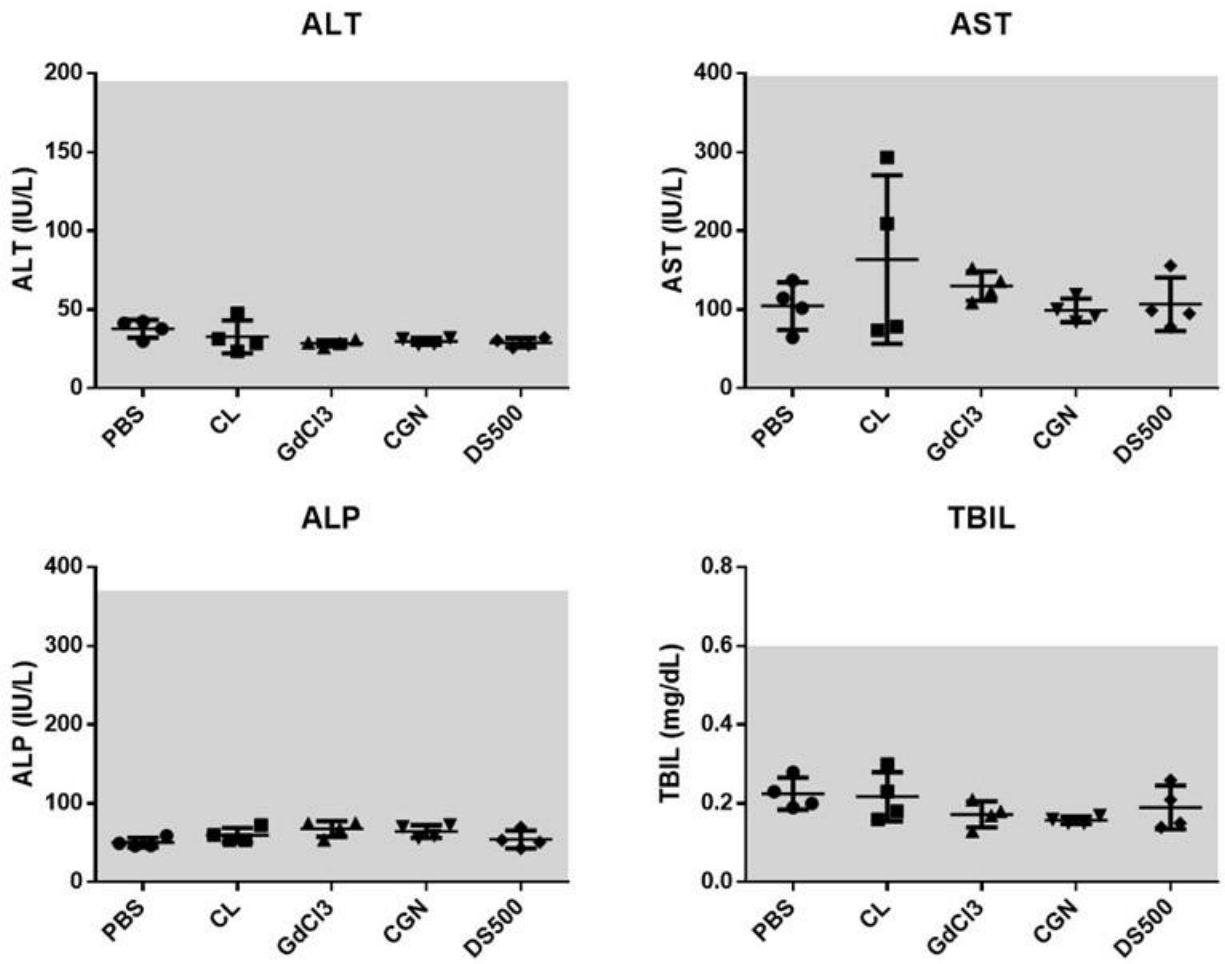

Fig. 3S. 8. Hepatotoxicity study. Hepatotoxicity analysis of serum markers alanine transaminase (ALT), aspartate aminotransferase (AST), alkaline phosphatase (ALP), and total bilirubin (TBIL) 3 days after intradermal injection of macrophage inhibitors (0.1 mg per footpad, in total 0.4 mg for four footpads) and PBS controls (n = 4 mice/group). Grey shaded area represents normal range for C57BL/6 mice.

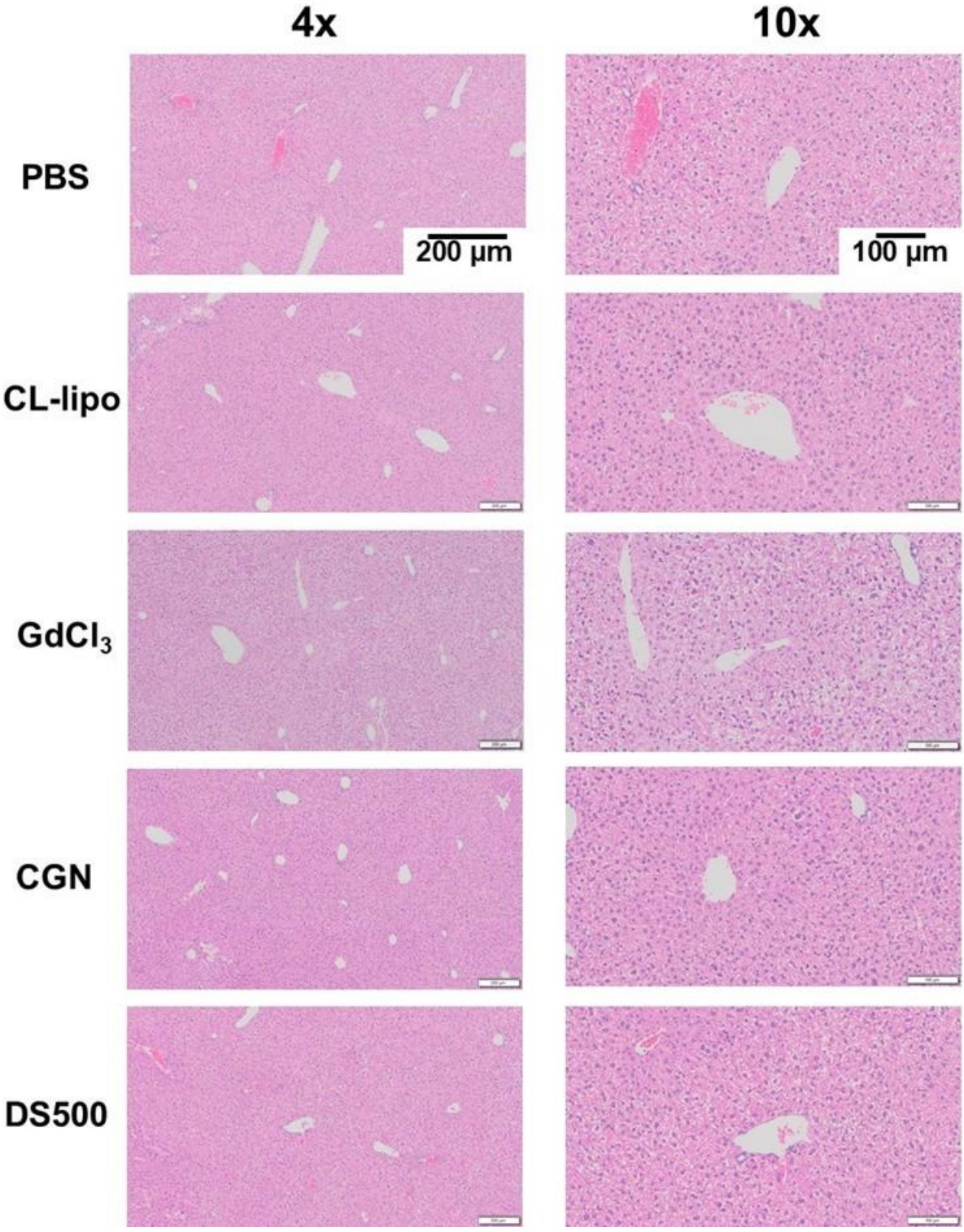

Fig. 3S. 9. Liver histology study. No inflammation was observed in the hepatic histological sections of C57BL/6 mice after treatment of PBS, clodronate liposomes, $GdCl_3$, CGN and DS500 macrophage inhibitors (0.1 mg per footpad, in total 0.4 mg for four footpads) at day 3 (n = 4 mice/group).

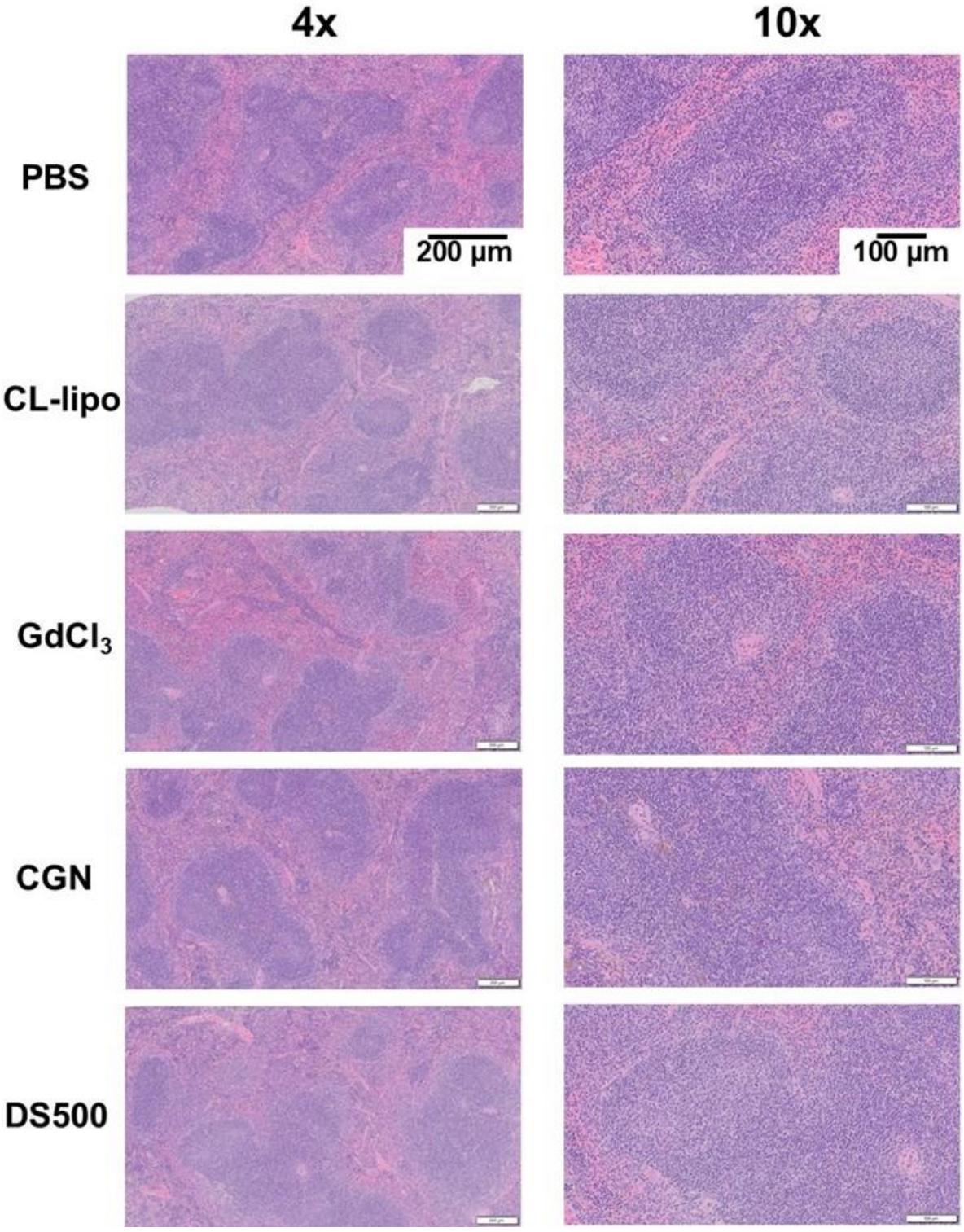

Fig. 3S. 10. Spleen pathology study. No inflammation was observed in the splenic histological sections of C57BL/6 mice after treatment of PBS, clodronate liposomes, $GdCl_3$, CGN and DS500 macrophage inhibitors (0.1 mg per footpad, in total 0.4 mg for four footpads) at day 3 (n = 4 mice/group).

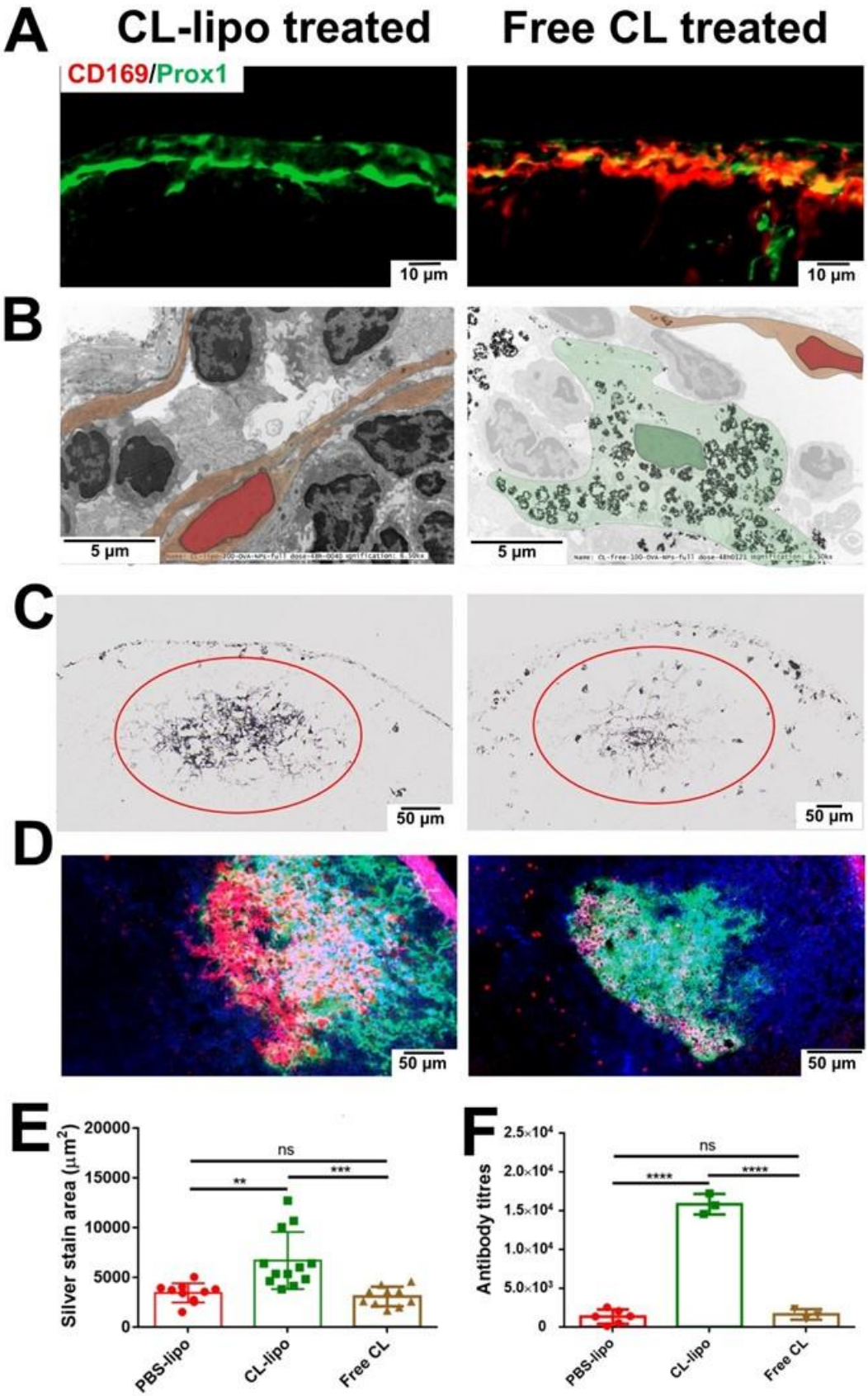
A
CL-lipo treated
Free CL treated
CD169/Prox1
10 μm
10 μm
B
5 μm
5 μm
C
50 μm
50 μm
D
50 μm
50 μm
E
Silver stain area (μm²)
20000
15000
10000
5000
0
ns
**
***
PBS-lipo
CL-lipo
Free CL
F
Antibody titres
2.5×10⁴
2.0×10⁴
1.5×10⁴
1.0×10⁴
5.0×10³
0
ns
****
****
PBS-lipo
CL-lipo
Free CL

Fig. 3S. 11. Free clodronate treatment cannot efficiently remove SCS macrophage and induce robust humoral immune responses. (A) SCS macrophages remained intact in the subcapsular sinus of lymph nodes after administration of free clodronate whereas clodronate liposome treatment removed SCS macrophages. The injection doses of clodronate amount are 0.1 mg in 20 μl volume. CD169 (red color) stains for SCS macrophages and Prox1 (green color) stains for LECs. (B) Representative TEM images and the enlarged images on SCS macrophages were examined after intradermal footpad injection of 100 nm OVA-AuNP nanovaccines after macrophage treatment using free clodronate or clodronate liposomes. The injected 100 nm OVA-AuNP nanovaccines were normalized based on the injected OVA antigen amount (10 μg). 100 nm OVA-AuNP nanovaccines were observed in the SCS macrophages after free clodronate treatment compared to clodronate liposome treatment. Pretreatment of clodronate liposomes induced greater 100 nm OVA-AuNP nanovaccine accumulation in lymph node follicles and humoral immune responses compared to free clodronate (C-F). (C) Histological images of 100 nm OVA-AuNP nanovaccines accumulation in lymph node follicles were analyzed after 48 hours post nanovaccines intradermal footpad injection. The injected 100 nm OVA-AuNP nanovaccine was normalized based on the injected OVA antigen amount (10 μg). Clodronate liposomes or free clodronate were administered 72 hours prior to nanovaccine injection (n = 4 mice/group). (E) Quantification of 100 nm OVA-AuNP nanovaccine accumulation in follicles at 48 hours after macrophage inhibitor administration. Assessment of (D) germinal center formation (GL7 red; CD21 green; B220 blue), and (F) antigen-specific antibody production in blood serum after administration of 100 nm OVA-AuNP nanovaccines at 5 weeks, Clodronate liposomes or free clodronate were administered prior to nanovaccine injection (n = 3 mice/group). The inject 100 nm OVA-AuNP nanovaccines were normalized based on the injected OVA antigen amount (2.5 μg). Data shown as mean ± SD; $^{**}P < 0.01$; $^{***}P < 0.001$. All P values are from one-way ANOVA followed by Tukey's multiple comparisons tests.

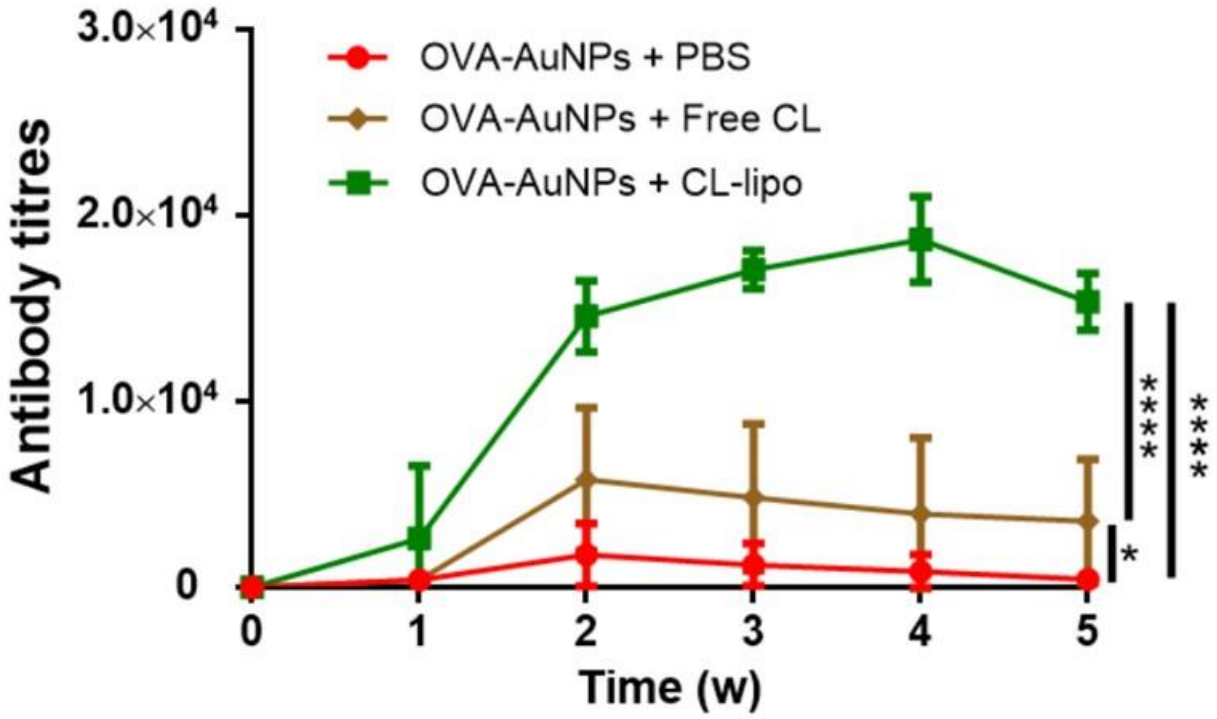

Fig. 3S. 12. Pre-mixing free clodronate with OVA-AuNPs cannot induce efficient adjuvant effects compared to clodronate liposome formulated with OVA-AuNP nanovaccines. Vaccine formulations that are composed of 100 nm OVA-AuNPs and free clodronate or clodronate liposomes were pre-mixed and injected through intradermal footpad into C57BL/6 mice (n = 4-7). Antigen OVA-specific antibody production from blood serum was measured weekly. The injected 100 nm OVA-AuNP nanovaccines were normalized based on the injected OVA antigen amount (2.5 μg). The clodronate amount is 0.1 mg. Data shown as mean ± SD; *P < 0.05; ****P < 0.0001. All P values are from two-way ANOVA followed by Tukey's multiple comparisons tests.

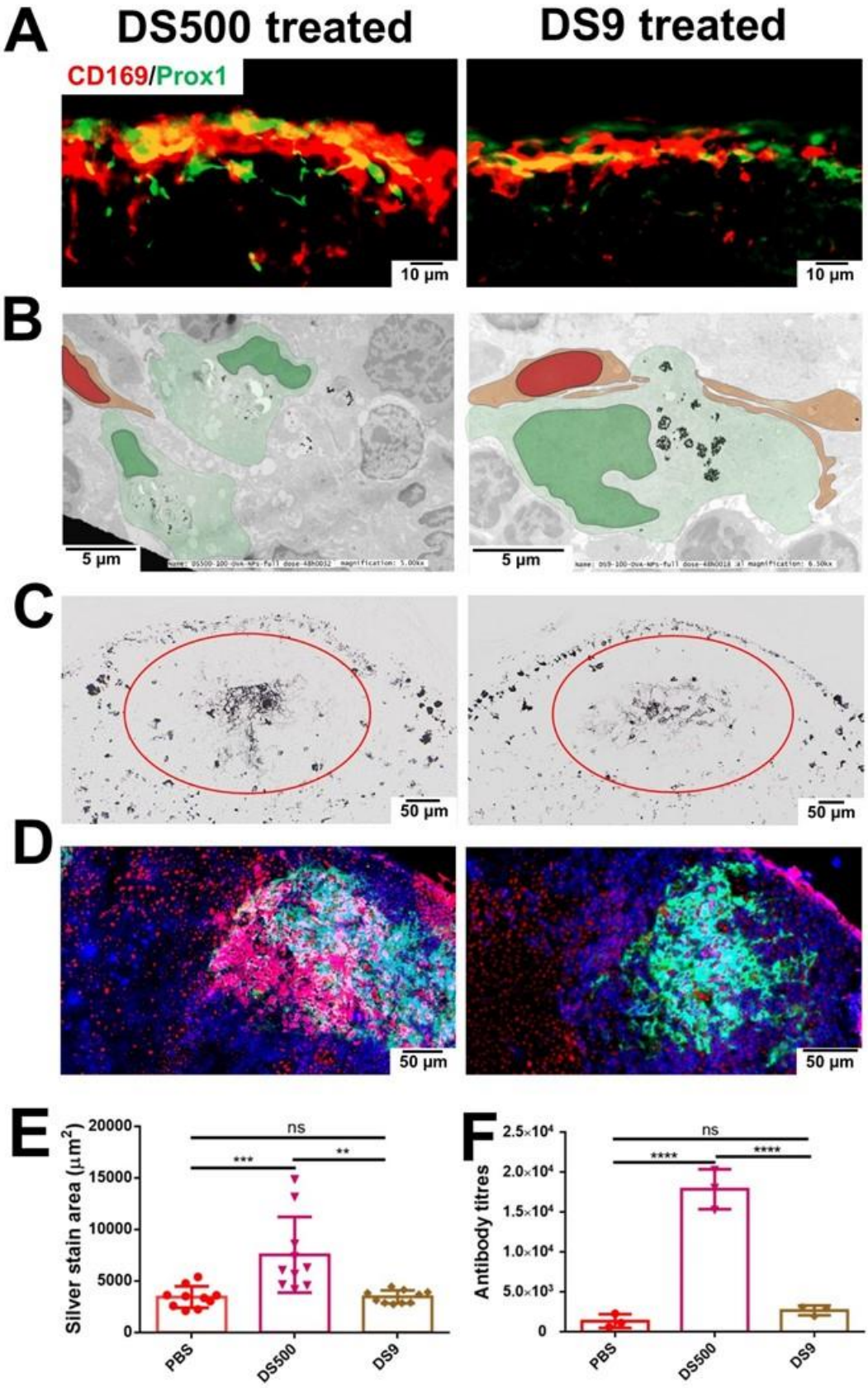
A
DS500 treated
DS9 treated
CD169/Prox1
10 µm
10 µm
B
5 µm
5 µm
C
50 µm
50 µm
D
50 µm
50 µm
E
Silver stain area (µm²)
20000
15000
10000
5000
0
ns
***
**
PBS
DS500
DS9
F
Antibody titres
2.5×10⁴
2.0×10⁴
1.5×10⁴
1.0×10⁴
5.0×10³
0
ns
****
****
PBS
DS500
DS9

Fig. 3S. 13. Low molecular weight dextran sulfate is not sufficient to inhibit macrophage and induce robust humoral immune responses. (A) SCS macrophages remained intact in the subcapsular sinus of lymph nodes after administration of both high molecular weight DS500 (average molecular weight > 500,000 Da) and low molecular weight DS9 (average molecular weight 9,000 - 20,000 Da). The injection amounts are 0.1 mg in 20 μl volume. CD169 (red color) stains for SCS macrophages and Prox1 (green color) stains for LECs. (B) Representative TEM images and the enlarged images on SCS macrophages were examined after intradermal footpad injection of 100 nm OVA-AuNP nanovaccines after macrophage treatment using DS500 or DS9. The injected 100 nm OVA-AuNP nanovaccines were normalized based on the inject OVA antigen amount (10 μg). Significantly less amount of 100-OVA-AuNP nanovaccines were observed in the SCS macrophages after DS500 compared to DS9 treatment. Pretreatment of DS500 induce greater 100 nm OVA-AuNP nanovaccine accumulation in lymph node follicles and humoral immune responses compared to DS9 (C-F). (C) Histological images of 100 nm OVA-AuNP nanovaccine accumulation in lymph node follicles were analyzed after 48 hours post nanovaccine intradermal footpad injection. The injected 100 nm OVA-AuNP nanovaccine were normalized based on the injected OVA antigen amount (10 μg). DS500 or DS9 were administered 24 hours prior to nanovaccine injection (n = 4 mice/group). (E) Quantification of 100 nm OVA-AuNP nanovaccine accumulation in follicles at 48 hours after macrophage inhibitor administration. Assessment of (D) germinal center formation (GL7 red; CD21 green; B220 blue), and (F) antigen-specific antibody production in blood serum after administration of 100 nm OVA-AuNP nanovaccine at 5 weeks, DS500 or DS9 were prior to nanovaccine injection (n = 3 mice/group). The injected 100 nm OVA-AuNP nanovaccine was normalized based on the inject OVA antigen amount (2.5 μg). Data shown as mean ± SD; *P < 0.05; **P < 0.01; ***P < 0.001. All P values are from one-way ANOVA followed by Tukey's multiple comparisons tests.

Chapter 4 - The effect of removing Kupffer cells on nanoparticle tumour delivery

Introduction

Nanomaterials are designed as drug carriers for the treatment of cancer but few nanomedicines have advanced to clinical use. A recent meta-analysis showed that less than 0.7% (median) of administered nanoparticles are delivered into solid tumours[120]. This low delivery efficiency can be attributed to phagocytic cells of the mononuclear phagocytic system sequestering nanomaterials due a combination of cellular and physical characteristics. For example, Tsoi and co-workers showed that when nanomaterials enter the liver, the flow rate of the nanomaterials slow by 1000 times in the liver sinusoid to enable interaction and uptake by hepatic Kupffer cells, B cells, and endothelial cells[121]. The most common strategies to prevent phagocytic uptake by the liver is by coating the nanoparticle surface with neutrally-charged anti-fouling polymers, such as polyethylene glycol, or by manipulating size and shape[122,123]. Even though this strategy has led to an increased blood-half life and tumour accumulation, these strategies do not allow us to determine the contribution of phagocytic cells in mediating the delivery process and have not advanced nanomedicine formulations to the clinic. This begs us to ask the question, "what is the impact on nanoparticle delivery to tumours after removing some or all of the main cells in the liver that sequesters them?" This allows us to determine the contribution of these cell types to the delivery process quantitatively and allows us to systematically focus on the "culprit" biological system to increase delivery in future studies. Improving delivery efficiency to tumours is likely a balancing act between different organs. To figure this out, we must analyze one organ at a time.

After we completed the meta-analysis, we were searching for strategies to improve the delivery efficiency of administered nanoparticles. In our analysis of the literature, there has been a number

of studies that have characterized different agents that can deplete macrophages. Examples include gadolinium chloride[102,124], methyl palmitate[125,126], dextran sulfate (500 kDa)[127], carrageenan[103,128], and clodronate liposomes[129]. Ohara and co-workers went a step further in their analysis and demonstrated the impact of depleting liver Kupffer cells in mediating the therapeutic effectiveness of Doxil by measuring tumour volume. It was difficult to determine the impact of the Kupffer cell depletion on nanoparticle delivery because Doxil can serve as "chemotherapeutic agent as well as a macrophage inhibitor". However, the results of these studied provided a chemical tool (e.g., clodronate-liposome for Kupffer cell depletion) that allowed us to elucidate how liver macrophages impact the nanoparticle delivery process. This enabled the probing of the influence of nanoparticle formulations and tumour types in mediating the delivery process. Furthermore, by carefully selecting the proper nanoparticle type, we quantified the delivery process to allow our results to be fully compared in future studies. As the field of nanomedicine start to database these quantitative results, analysis of a large dataset will lead to rational engineering strategies to overcome the delivery problem. In this study, we fully determined the impact of dose-dependent removal of Kupffer cells on nanoparticle tumour delivery and evaluated the toxicity to the animal after removal of these cells. We showed that removing all or a portion of Kupffer cells can increase delivery of nanoparticles to the tumour up to 150 times. These enhancements were dependent on nanoparticle size, material composition, and tumour type. Our data shows that strategies to tune inherent biology can improve nanoparticle delivery efficiency to solid tumours.

Materials and methods

Mammalian Cell Culture

Ovarian adenocarcinoma (SKOV3), breast adenocarcinoma (MDA-MB-231), melanoma (MDA-MB-435S), and non-small cell lungs carcinoma (A549) cell lines were cultured for inoculation of tumour xenografts. The SKOV3, MDA-MB-231, and A549 cell cultures were maintained in DMEM supplemented with 10% FBS and 1% penicillin/streptomycin in T-175 tissue culture flasks (Nest Biotechnology Co., Ltd. Wuxi, China) and kept at 37 °C in a 5% CO_2 humid environment. Cells were passaged at 85% confluence and subdivided in 1/4 to 1/6 in fresh T-175 flasks. MDA-MB-435S cells were cultured identically except RPMI supplemented with 10% FBS and 1% penicillin/streptomycin was used in place of DMEM.

Preparation of Human Tumour Xenograft Models

All animal procedures and husbandry were conducted in accordance with the guidelines from the animal ethics committee from the Division of Comparative Medicine at the University of Toronto (animal protocol numbers: 20010886 and 20011813). Six-week-old female CD1 *nu/*nu mice were purchased from Charles River Laboratories. Animals were acclimatized for one week following delivery. T-175 culture flasks at 85-90% confluence containing a given cell line were harvested using 0.25% w/v trypsin for 10 min at 37°C in 5% CO_2. The cell suspensions were centrifuged at 500g for 5 min and the supernatant was discarded. The cell pellets were suspended in 1 mL of DMEM or RPMI and the cell aliquot was counted with a hemacytometer. A 500 µL aliquot of the stock was mixed with 500 µL of Matrigel™ and kept on ice. To inoculate tumours, mice were subject to anesthesia initially at, 5% v/v isoflurane in oxygen and later maintained using 3% v/v isoflurane in oxygen. Using a 1 mL syringe equipped with a 25g needle, 200 µL of the stock cell-Matrigel™ mixture was injected subcutaneously in the animal's right hind flank (SKOV3, A549, and MDA-MB-435S). For MDA-MB-231 orthotopic xenografts, the cell suspension was

inoculated between the inguinal fourth and fifth mammary fat pad on either the right or left side. For SKOV3, A549, and MDA-MB-435S xenografts, between 4-6 × 10^6 cells were injected, while for MDA-MB-231, 6-8 × 10^6 cells were inoculated. Animals were then removed from anesthesia and allowed to recover under ambient conditions for 10 min before being placed back in their respective housing. Tumour growth was monitored by the Division of Comparative Medicine for ulceration. Mice were selected for experiments after tumour volume reached 1 cm^3; MDA-MB-231 xenografts were selected when the tumour volume was 0.8 cm^3. The PC3 orthotopic tumour xenografts were a gift from Dr. Gang Zheng at Toronto General Hospital. Tumour volume was monitored using MRI and animals were selected when the diameter reached 7 mm.

Administration of Clodronate, PBS Liposomes and Gold Nanoparticles

Mice were tail vein injected with 200 µL of clodronate liposomes suspension (0.05 $mg \cdot mL^{-1}$) or 200 µL of saline (PBS) liposomes (control) using a 29g insulin needle. For an average mouse of 20g of body weight, this injected dose resulted in both hepatic and splenic macrophage depletion as stated by the manufacturer. For experiments investigating dose dependent macrophage depletion, the stock clodronate liposomes were diluted to 0.017, 0.01, 0.005, and 0.0025 $mg \cdot mL^{-1}$ with sterile 1× PBS. After 48h, A750-AuNPs were suspended in sterile PBS and injected into the animal *via* the tail vein. A fixed injection volume of 150 µL was used in the administration of all AuNPs. The injected dose was normalized to the total nanoparticle surface area across the different sized AuNPs investigated. The surface area of a single AuNP with radius, *r* was assumed as a sphere. For AuNPs with average diameters of 50, 100, and 200 nm, the surface areas were assumed to be 7854 nm^2, 31416 nm^2, and 125664 nm^2, respectively. For a standardized total injected surface area of 3.18 × 10^{15} nm^2, the concentrations of 50, 100, and 200 nm AuNPs administered were 4.0 nM, 1.12 nM, and 0.28 nM, respectively.

In Vivo Fluorescence Imaging of Gold Nanoparticle Biodistribution

Following administration of A750-AuNPs, animals were imaged using a Kodak *in vivo* multispectral imaging system (Bruker Corporation, Billerica, MA) at 2h, 6h, 12h and 24h post injection. Mice were initially placed under 4% (v/v) isoflurane in oxygen and the anesthesia was maintained at 3% (v/v) during the course of the image. Excitation and Emission bandpass filters at 750 nm and 830 nm (Carestream Health, Inc., Rochester, NY), respectively were used in the acquisition of A750-AuNP fluorescence from whole body animal images. The bandpass of each filter was *ca.* 35 nm at full-width-half-maximum. Images were acquired with an exposure and integration time of 10 min. Fluorescence images were modified using Image J software to enhance contrast and clarity, a fixed contrast setting was used to present fluorescence images from both experimental and control animals. To qualitatively assess AuNP biodistribution at the organ level, *ex vivo* images of extracted organs were also taken in petri dishes. Identical organs from clodronate treated and PBS treated animals were also paired and imaged in groups for qualitative comparison.

Quantitative Blood and Organ Distribution of Gold Nanoparticles using ICP-MS

To quantitatively determine the AuNP blood and tumour pharmacokinetic profiles, mice were euthanized at 2h, 6h, 12h and 24h post nanoparticle injection. Blood was collected *via* cardiac puncture using a 1 mL syringe equipped with a 25g needle. The harvested organs included: lungs, heart, liver, spleen, stomach, intestines, kidneys, axillary lymph nodes, brachial lymph nodes, inguinal lymph nodes and the tumour. A skin sample was also taken from the animal's posterior thoracic cavity. Average mass of the tumours resected from each mouse tumour model can be found in Supporting Information, Table 4S.2. Organs and blood samples were weighed and placed into glass culture tubes. In addition to organ samples, a portion of or the total administered AuNP dose was also added to a separate tube. To the samples, 800 µL of concentrated nitric acid (69%

w/v) was added. For regional lymph nodes, this volume was reduced to 200 µL of nitric acid. An acid control sample containing solely nitric acid was also prepared in triplicate. The samples were placed on a heat bath at 70°C and allowed to digest overnight. The following day, 200 µL of concentrated hydrochloric acid (37% w/v) was added to each tube. To lymph node samples, the volume was reduced to 50 µL, as to maintain a 4:1 volume ratio between HNO_3 and HCl. The organ digestate was maintained at 70°C for an additional 3h. The digested samples were transferred into 50 ml conical vials and diluted to a final volume of 40 mL with deionized water, samples containing lymph nodes were diluted to a total volume of 10 mL. The final acid concentration in each sample was 2% (v/v) HNO_3 and 0.5% (v/v) HCl. Diluted samples were then passed through a 0.22 µm PES syringe filter (EMD Millipore - Merck KGaA, Darmstadt, Germany). A calibration curve ranging from 1×10^{-3} - 1×10^{2} $\mu g \cdot mL^{-1}$ of elemental gold (High-Purity Standards, Charleston, SC) prepared in 2% (v/v) HNO_3 and 0.5% (v/v) HCl was used to determine the quantity of gold in each sample. Quantitative gold concentrations were determined using a NexION 350X inductively coupled plasma mass spectrometer (ICP-MS) (PerkinElmer, Billerica, MA). A 500 µL injection loop was used and sample solution was mixed with carrier (2% (v/v) HNO_3 and 0.5% (v/v) HCl) and internal standard (Ir 1000 $mg \cdot L^{-1}$) prior to aspiration; several rinses were added between samples to minimize cross contamination. The mass analyzer was set to Au 197 and Ir 192 for all measurements. Prior to analysis, the instrument was calibrated using a setup solution containing 1 $\mu g \cdot L^{-1}$ of Be, Ce, Fe, In, Li, Mg, Pb, and U in 1% HNO_3 using the SmartTune method as indicated by the manufacturer. Quantitative analysis of total gold content in organs is presented as a normalized percentage of the injected dose (% I.D.). Since several AuNP ensembles were used over the course of this study, the data have been normalized to the average injected dose value of AuNPs determined from each measured replicate across the dosages of clodronate investigated.

The blood half-life of AuNPs was determined as a % I.D. weighted against the amount of blood retrieved from the animal and normalized to 1.8 g; the average total blood content of a 20 g mouse. The decay curves were fit as single exponential decays using GraphPad Prism 6 software. To determine the % I.D. of the AuNPs that were delivered to the tumour, the area-under-the-curve (AUC) of the pharmacokinetic profile was determined using the trapezoidal approximation bounded by a time frame of 22h.

Analysis of Silver Nanoparticle Biodistribution using ICP-MS

Quantitative determination of silver nanoparticle biodistribution using ICP-MS was done similarly as described for gold nanoparticles with the following modifications. SKOV3 xenograft mice were euthanized 3h post injection and blood was collected *via* cardiac puncture. The organs analyzed included: liver, spleen, blood, and the tumour. Organ samples were digested overnight using concentrated HNO_3 and diluted to a final volume of 2% v/v prior to aspiration in the ICP. The mass analyzer was set to Ag 107 where Ir 192 was used as an internal standard. The quantity of silver in each organ was determined using a silver standard curve and the quantitative organ biodistribution was normalized as a % I.D. to the quantity of silver measured in the injected aliquot.

Analysis of the Biodistribution of Liposomes and Silica Nanoparticles

The quantitative determination of liposome and silica nanoparticle organ biodistribution was done using fluorimetric analysis of organs imaged *ex vivo*. SKOV3 xenograft mice were injected with liposomes or silica nanoparticles 48h after initial administration of clodronate liposomes (0.017 $mg \cdot g^{-1}$) or PBS liposomes. Animals were then euthanized 3h post injection of liposomes or silica nanoparticles and blood was removed *via* cardiac puncture and extracted organs were washed with copious amounts of distilled water. Organs analyzed included: livers, spleens, and tumours. Organs were grouped into clodronate treated or control (PBS liposomes) and imaged adjacently in the same field using a Kodak in vivo multispectral imager. Organs were imaged using 650 nm excitation and fluorescence emission was collected using a 700 nm bandpass filter with FWHM *ca.* 35 nm and exposure time of 1 min. Both liposomes and silica nanoparticles contained dye analogues of Cy5. Analysis of *ex vivo* fluorescence images of organs was done using ImageJ software (National Institutes of Health, Bethesda, MD). The background signal of each image was determined by averaging three independent measurements of image area. Peripheries of organs were traced and the average integrated fluorescence density was calculated for each organ. The integrated fluorescence intensities were averaged for each organ in the clodronate or control treated animals and were used to quantitatively compare organ biodistribution of liposomes or silica nanoparticles.

Immunohistochemistry and Histological Tissue Analysis

Sections of liver, spleen and tumour tissues were fixed in 10% formalin for one week. The fixed tissues were then sent to the University Health Network Pathology Research Program at Toronto General Hospital or Toronto Centre for Phenogenomics for the remaining histological preparation. Tissue sections were stained with hematoxylin and eosin to observe any gross inflammation in

hepatic and splenic tissue due to clodronate or AuNPs. Histology tissues were also treated with silver nitrate to observe AuNP distribution and immunohistochemically treated with F4/80 antibody and Ki67 to stain macrophages and cancer cells, respectively. The stained slices were imaged using an IX51 light microscope. For semi-quantitative analysis of Kupffer cell populations in liver tissue, histological slides were sent to the Advanced Bioimaging Centre at Mount Sinai Hospital for full slide scans. The full images of the hepatic tissue sections were expanded to identical magnifications using Adobe Photoshop. A 20 cm × 20 cm frame was drawn centered on a hepatic central vein or portal triad from three independent positions in the tissue. In these areas Kupffer cells were identified using the brownish-red staining of horseradish peroxidase and the presence of a nucleus as the tissues were also counterstained with hematoxylin. From sequential counts in triplicate, an average Kupffer cell quantity was determined for each dose of clodronate investigated.

Hematology and Liver Biochemistry of Clodronate Treated C57BL/6 Mice

C57BL/6 mice at 7-9 weeks were injected with PBS or clodronate liposomes at dosages of, 0.005, 0.017, 0.05 $mg \cdot g^{-1}$ to create four groups of 4 animals per group (n=4). At 48h post injection, animals were anesthetized with 4% v/v isoflurane in oxygen and anesthesia was maintained at 3%. The thoracic cavity of the animal was exposed and blood was collected through cardiac puncture using a 23g needle. For hematology samples, blood was transferred to microfuge tubes containing di potassium EDTA at a final concentration of 5-10 mM and kept on ice. For liver biochemistry analysis, serum was isolated from whole blood by centrifugation at 500g for 10 min. The serum was transferred to a fresh microfuge tube and kept on ice. Both blood and serum samples were sent for analysis at Toronto Centre for Phenogenomics immediately after collection and were analyzed within one day. Serum biochemistry markers of liver parenchyma included: alanine

aminotransferase, alkaline phosphatase, aspartate transaminase, and bilirubin. Hematology markers: red blood cell (RBC), hemoglobin (HGB), hematocrit (HCT), mean corpuscular volume (MCV), mean corpuscular hemoglobin (MCH), mean corpuscular hemoglobin concentration (MCHC), red blood cell distribution with (RDW), platelet (PLT), mean platelet volume (MPV), white blood cells (WBC), neutrophils (NE), lymphocytes (LY), monocytes (MO), basophils (BA), and eosinophils (EO).

Cecal Ligation and Puncture Sepsis Model in C57BL/6 Mice

C57BL/6 mice at 7-9 weeks were used in the induction of the CLP model of polymicrobial sepsis. Mice were injected 48h prior to the CLP procedure with PBS liposomes or clodronate liposomes at dosages of, 0.005, 0.017, 0.05 $mg \cdot g^{-1}$ to create four groups each containing ten animals (n=10). It is noteworthy that animals in clodronate groups were blinded to the surgeons and all surgeries were conducted in a biosafety cabinet. Animals were anesthetized through inhalation of isoflurane at 4% v/v in oxygen, the maintenance concentration of isoflurane was 2.5% v/v throughout the duration of the procedure and the animal was kept on a heat pad at 38°C to maintain body temperature. The abdomen of the mouse was shaved and twice sterilized with 70% ethanol and betadine. Buprenorphine 0.15 $mg \cdot kg^{-1}$ was administered subcutaneously as pre-operative analgesia. Mice were covered with slotted sterile drapes exposing only the sterile portion of the abdomen. A 1-1.5 cm skin incision was made along the midline exposing the abdominal muscle. A 1 cm incision was then made in the muscle layer to expose the peritoneum. The cecum was isolated, placed on gauze and hydrated with sterile saline. A 6.0 absorbable silk suture was used to ligate the cecum 1 cm from the distal end. This accounted for a cecal ligation point that was *ca.* 25% of the animal's entire cecum. A single perforation was made midway in the ligated portion using a 21g needle. A pin-head amount of fecal material was extruded using forceps and the large intestine

was returned to the peritoneal cavity. The incisions in the abdominal muscle and skin were closed using 3.0-5.0 absorbable silk suture. Animals were kept under a heat lamp for 15 min during recovery with access to food and water. Postoperative analgesia (buprenorphine, 0.15 $mg \cdot kg^{-1}$) was given every 10-12h to ease pain and discomfort. Animals were monitored every 4-6h for a total of 48h following completion of the surgical procedure. Rectal body temperature was taken as hypothermia was used as an indirect indicator of sepsis. The endpoint in this study was defined by a rectal body temperature below 32°C. Animals having body temperatures below this threshold were euthanized in accordance with ethics approval as established by the Animal Care Committee at the University of Toronto. To confirm induction of sepsis, blood was collected from euthanized septic animals (n=4) through cardiac puncture. Whole blood was diluted with sterile PBS, plated on LB agar plates (BD Biosciences, Mississauga, Ontario, Canada) and incubated at 37°C overnight. Agar plates were imaged using a standard smartphone camera. Control blood was collected through tail vein puncture of sterile animals (n=4).

Statistical Analyses

Data was analyzed by unpaired t-tests or one-way or two-way ANOVA methods using GraphPad Prism 6 with Bonferroni correction. The Holm-Sidak approach was taken for multiple comparisons. Survival curves were analyzed by log-rank (Mantel-Cox) test. Data is presented as average values of three to four replicates and precision reported is the sample standard deviation unless stated otherwise. Statistical significance between different experimental groups was measured at ($*p < 0.05$, $**p < 0.01$, $***p < 0.001$ and $****p < 0.0001$).

Results

We designed a series of experiments to allow us to determine the impact of the liver Kupffer cells in mediating the tumour delivery process. These experiments involved the (1) dose-dependent removal of macrophages using dicholoromethylenediphosphonic acid-liposomes (clodronate liposomes) and then (2) administration of therapeutic nanoparticles (gold nanoparticles, silica, and liposomes) in different tumour mouse models (ovarian, breast, skin, prostate, and lung cancer). At the beginning of this project, we focused on gold nanoparticles because of their versatility in different sizes and surface chemistries and ease of quantification using both optical imaging (*via* fluorescent labeling) and elemental analysis with inductively-coupled plasma-mass spectrometry.

Gold Nanoparticle Functionalization

We first designed a library of gold nanoparticles (AuNPs) for assessment. AuNPs were synthesized, surface modified, and tagged with AlexaFluor750 (A750) as described previously by our group[77,79]. The surfaces of the nanoparticles were first functionalized with a mixed ligand film comprised of 5 kDa methoxy-terminated poly(ethylene glycol) (5KmPEG) and 10 kDa amino terminated poly(ethylene glycol) (10KamPEG) at a 4:1 ratio. The mixed PEG ligands were grafted to the nanoparticle surface at a density of 5 PEG·nm^{-2} to passivate the surface against the adsorption of serum proteins[123]. The AuNPs were characterized using transmission electron microscopy, absorbance and fluorescence spectroscopy, and dynamic light scattering (see Fig. 4S1-S2) and the results are summarized in Table 4S.1 prior to animal studies.

Characterization of depletion of phagocytes in the liver and spleen.

Clodronate-liposomes were effective in killing phagocytic cells. Mice injected with clodronate liposomes (0-0.05 mg·g^{-1}) were euthanized at 48h post injection. Clodronate liposomes depleted F4/80+ hepatic and splenic macrophages proportionally to dose (Fig. 4.2A-C and Fig. 4S3). The

liver histological sections suggested that the more phagocytic Kupffer cells near the portal triads were depleted to a greater extent in comparison to the Kupffer cells near the central vein (Fig. 4. 2A-C). It has been shown that 43% of Kupffer cells are located between adjacent portal triads. The number decreases successively to 25% toward the central vein. Blood flows from numerous portal triads into a single central vein (black arrow in Fig. 4.2A) and therefore cells located near the portal triads are the first to interact with the nanoparticles. The relative number of KCs compared to controls decreased to 25% and to 10% when 0.017 mg/g, and 0.050 mg/g of clodronate liposomes was administered respectively (Fig. 4.2). The annotations shown in Fig. 4.1D-F are representative of the above histological sections. In panel E, clear Kupffer cell depletion zones can be seen between adjacent portal triads. Furthermore, dosimetric depletion influenced the repopulation of Kupffer cells (Fig. 4.2H) in Balb/C mice. Our data suggests that when only a portion of Kupffer cells are depleted, the livers of these animals repopulate to normal levels in 5 vs 10 days. It is noteworthy that Balb/C mice were seen to have less Kupffer cells than CD1 *nu/nu* mice in comparison of hepatic histology (Supporting information Fig. 4S4).

Clodronate Liposomes Improve the Pharmacokinetics and Delivery of Nanoparticles to Tumours

We first asked, if both the liver and spleen were completely depleted of phagocytic macrophages, what is the maximum increase in nanoparticle tumour delivery? Mice were injected with clodronate liposomes or PBS liposomes 48h prior to administration of 100 nm AuNPs to deplete the liver and splenic macrophages [130]. There was a re-distribution of the AuNPs after administration of clodronate liposomes (Fig. 4.2). We also found that after 48h, gold nanoparticle uptake in the liver was minimized to less than 10% I.D. (Supporting Information, Fig. 4S5). Since fluorescence is a semi-quantitative method, we further quantified the distribution of the AuNPs by

using Inductively-Coupled Plasma–Mass Spectrometry (ICP-MS) (Fig. 4.2 C and D). Clodronate liposomes increased the blood half-life of 100 nm AuNPs 13 times, from 0.64 h^{-1} to 8.00 $h^{-1}$and increased their delivery to the tumour from 0.03 %I.D. to 0.5 %I.D. The full biodistribution analysis is shown in the supporting information Fig. 4S6. The removal of phagocytic cells re-distributed the administered nanoparticles and led to an increase in tumour accumulation of 13 times; 6 times higher than previously reported.

How Does Macrophage Depletion Relate to Nanoparticle Size?

We next evaluated the impact of nanoparticle size in mediating the improvement in delivery efficiency. Macrophages are well-known to have a size-dependent interaction with nanoparticles[122]. A range of AuNP size (50-200 nm) was selected. Fig. 4.3A and B show 24h *in vivo* whole animal fluorescence images and *ex vivo* fluorescence images of organs from animals that were administered 50 nm and 200 nm AuNPs, respectively. In Fig. 4.3A, the whole animal fluorescence images in Fig. 4.3AI and 3AIII appear similar, albeit the *ex vivo* organ fluorescence images in II and IV differ significantly. A similar redistributive trend was seen for 50 nm AuNPs that was displayed previously for 100 nm AuNPs in (Supporting information, Fig. 4S5). A four times reduction in nanoparticle accumulation in the liver liberated an excess of 250 times more nanoparticles in the blood after administration of clodronate liposomes (Fig. 4.3D). For these 50 nm AuNPs, we observed an increase in delivery efficiency to the tumour from 0.12% to 2.15% ID at 24h. For 200 nm AuNPs, clear differences can be seen from the *in vivo* animal fluorescence images shown in Fig. 4.3BI and 3BIII resembling the biodistribution pattern for 100 nm AuNPs. The data in Fig. 4.3A shows substantially improved pharmacokinetics for 200 nm AuNPs in comparison to the 50 nm AuNPs (Fig. 4.4B). Quantitative analysis of the 200 nm AuNP biodistribution using ICP-MS (Fig. 4.3D) highlighted an improvement of 150 times in the delivery

efficiency of AuNPs to the tumour from 0.0057% to 0.8500% ID at 24h. There was a direct relationship between nanoparticle size and delivery efficiency (Fig. 4.4) and the relationship is defined by Equation 1.

$$\frac{[I.D.T_{CL}]}{[I.D.T_{PB}]} = 0.0033{d_{AuNP}}^2 + 0.053d_{AuNP} \quad (1)$$

Our data suggests that the relative increase in nanoparticle tumour delivery is exponentially proportional to the diameter of the nanoparticle when macrophages are depleted. The most substantial increase (150-times) was seen for 200 nm AuNPs. It is noteworthy that 50 nm AuNPs had the highest accumulation in the tumour at 24h (2.15 %I.D.) across all three nanoparticle sizes investigated and represents a 20-times increase relative to control animals (0.12% I.D.). Mathematical modeling of these data provides insight into the relative delivery efficiency that could be expected for a specific nanomaterial size. These results suggest that this two-step delivery strategy can improve the delivery of larger nanomaterials to tumours.

Gold Nanoparticle Tumour Delivery Efficiency is Dependent on Clodronate Dose and Cancer Type

In the previous experiment, we used a dose of clodronate liposomes to completely remove all hepatic and splenic macrophages. However, if such a high dose (0.05 mg/g of animal body weight) is required to improve AuNP delivery, this approach may not be viable for use in patients as Kupffer cells are an integral component of the innate immune system. This level of macrophage depletion may compromise patient immunity to an extent that may require sterile quarantine. Thus, we opted to evaluate if improvements in nanoparticle delivery efficiency could be realized at lower doses of clodronate liposomes leaving the host with some intact innate macrophages. Four additional doses of clodronate liposomes were investigated in the range of 0.0025 $mg \cdot g^{-1}$ to 0.017 $mg \cdot g^{-1}$ of animal body weight and each dose was injected into the animal 48h prior to AuNP

administration. Analysis of the total gold content in the AuNP organ biodistribution also displayed a dose dependent decrease in the amount of gold in the liver, with incremental increases in accumulation in the spleen as shown in Fig. 4.6A. The total amount of AuNPs in the liver decreased successively from 58 ± 6% I.D (control) to 10 ± 3% I.D. Depleting 50% of Kupffer cells resulted in a 10-times increase in delivery of AuNPs to the tumour at 0.0025 $mg \cdot g^{-1}$ of clodronate liposomes (Fig. 4.6B). Interestingly, no statistically significant improvements were seen in AuNP tumour accumulation beyond 0.005 $mg \cdot g^{-1}$ dose of clodronate liposomes. This data suggests that complete hepatic and splenic depletion is not required to maximize the enhancement in tumour delivery of subsequently administered nanoparticles using this two-step delivery strategy. We next determined whether the improved AuNP delivery efficiency after clodronate liposome administration occurs in tumors beyond the SKOV3 ovarian cancer xenograft model. We investigated the delivery efficiency of AuNPs after administering a lower dose of clodronate liposomes (0.017 mg/g) in a subcutaneous xenograft of non-small cell lung cancer (A549), and in orthotopic xenografts of breast cancer (MDA-MB-231), skin cancer (MDA-MB-435) and prostate cancer (PC3). We observed improvements of 20-fold relative to control animals for SKOV3, A549 and MDA-MB-231 tumour, while almost a 100-fold increase was seen in animals with PC3 orthotopic xenografts for the delivery of 100 nm AuNPs 48 hrs after administration of clodronate liposomes (Fig. 4.6C). Interestingly, no significant improvement in tumour delivery efficiency was seen for the MDA-MB-435 tumour model. This suggests that tumours present unique intrinsic barriers to nanoparticle accumulation. Of all the tumour models investigated, PC3 tumours had some of the largest masses (0.7700 ± 0.4109 g) while MDA-MB-231 tumours grown on the mammary fat pad had the smallest masses (0.0078 ± 0.0065 g) (see Supporting Information Table 4S.2). The results showed the highest and lowest AuNP accumulation of 1.923 %ID and 0.006 %ID, respectively. This data is

consistent with a previously reported study suggesting that tumour pathophysiology influences nanoparticle uptake[131]. PC3 tumours also displayed the highest mass normalized AuNP accumulation of 2.091 %ID/g at 24h, see supporting information Fig. 4S7. We saw no depletion of tumour associated macrophages in SKOV3 tumours after administration of clodronate liposomes (Supporting Information, Fig. 4S8).

Macrophage Depletion Enhances the Tumour Delivery of Various Nanomaterials

We evaluated whether macrophage depletion could improve the delivery of different nanoparticle types. To encompass a broad classification of materials, we selected silica, silver, and liposomal nanoparticles at a fixed diameter of 100 nm and surface modified with PEG ligands (see Supporting Information, Fig. 4S9, S10 and Table 4S.3). Fig. 4.7A-C shows the hepatic, splenic, and tumoural tissue distribution of SiNPs, nano-liposomes, and AgNPs at 3h post injection, respectively. The clodronate liposome dose used was 0.017 $mg \cdot g^{-1}$ and animals were injected with clodronate liposomes or PBS liposomes 48h prior to nanoparticle administration. Macrophage depletion increased the delivery of all particles to the tumour (Fig. 4.7A-C). Enhancements in tumour delivery were 2, 5 and 7 times for nano-liposomes, SiNPs and AgNPs, respectively. Collectively the data in Fig. 4.6 and Fig. 4.7 highlight the universality of this two-step delivery strategy to improve the tumour delivery of nanomedicines, both across various nanomaterials and types of cancer and using a dose that does not result in complete hepatic and splenic macrophage depletion.

Macrophage Depletion Causes No Systemic Toxicity but Increases Disease Onset in a Model of Polymicrobial Sepsis

The data regarding enhancements in nanoparticle tumour delivery after macrophage depletion with clodronate liposomes is promising, but arguably is a double-edged approach in comparison to

materials or drug design. Therefore, we asked: “what is the consequence of this immune suppression on the animal and could this impair their ability to combat infection?”

We first conducted a toxicology assessment using hematology and liver biochemistry assays on animals treated with a dosing scheme of clodronate liposomes from 0.00-0.05 $mg \cdot g^{-1}$ (Fig. 4.8A and Supporting Information, Fig. 4S.11, S.12 and Tables 4S4-S5). We saw an increased quantity of the parenchymal markers alanine aminotransferase (ALT), aspartate aminotransferase (AST), and alkaline phosphatase (ALP) after treatment with an increasing dose of clodronate liposomes, albeit the marker concentrations are still within the normal range for these animals. These observations have also been reported elsewhere when Kupffer cells were depleted with clodronate liposomes[132]. Histological sections of CD1 nu/nu mice hepatic tissue showed no systemic or gross inflammation relative to controls (Supporting Information, Fig. 4S13). A similar dose dependent depletion of Kupffer cells and splenic macrophages was seen in C57BL/6 mice (Supporting Information, Fig. 4S14 and Fig. 4S15). Furthermore, no statistically significant differences in hematological markers were seen across the doses of clodronate liposomes investigated against control animals (Supporting Information, Fig. 4S11 and S12).

We sought to gain insight in the consequence of the host acquiring a severe microbial infection when macrophages were at their lowest levels. We selected an animal model of polymicrobial sepsis to answer this question as this is a severe complication that could arise from an infection. Furthermore, sepsis is a common problem for many patients receiving chemotherapy[133] and Kupffer cells are integral towards combating sepsis[134]. The data in Fig. 4.8B shows total animal survival 48h after induction of sepsis intraoperatively through a cecal ligation and puncture

procedure. We confirmed induction of the sepsis animal model by bacterial culture of blood collected from septic animals (Supporting Information Fig. 4S16). Mice with body temperature below 32°C were euthanized according to ethics guidelines of the animal use protocol where the endpoint was considered as a morbid state. Animals in groups treated with clodronate liposomes from 0.005-0.050 $mg \cdot g^{-1}$ are shown by the red, blue and solid black lines in Fig. 4.8B. Clodronate liposomes increased the disease onset of sepsis where only 20% and 30% of animals exhibited mild hypothermia with body temperatures greater than 32°C for all three treatment groups. Interestingly, there was no statistically significant difference between the group treated with 0.017 $mg \cdot g^{-1}$ clodronate liposomes and the control (P=0.01932, Mantel-Cox Log rank test). However, the overall median survival for control animals was 38h. Those animals receiving clodronate liposomes at 0.05, 0.017, and 0.005 $mg \cdot g^{-1}$ decreased to 12h, 23h, and 10h, respectively. Our data shows that survival was not dependent on clodronate dose, rather any degree of depletion increased the onset of sepsis. This data suggests that if a patient were to acquire an acute infection that led to sepsis when their innate immunity was at peak suppression, their prognosis would be less favorable. Since depleting only a portion of Kupffer cells results in twice faster repopulation (Fig. 4.2H), this minimizes the duration of time between clodronate and nanoparticle injection cycles that a patient is left with a weakened innate immune system. This reduces the risk of infection without sacrifice to enhancement in nanoparticle tumour delivery.

Discussion

The purpose of designing long-circulating nanoparticles is to enable a high concentration of nanoparticles to accumulate in the tumour. Here, we focused on the removal of different amounts of these nanoparticle sequestration cell types in the liver to determine their contribution to the

delivery process. While our results show drastic improvements in the delivery efficiency of nanoparticles to tumours when these cells were removed, we were surprised that the increase was not more dramatic. By removing the contribution of these cells to the delivery process, we show that they are likely to contribute only 2% (maximum) to the delivery problem. This begs the issue of what are the contributions from the other organs, especially tumour (and how their pathophysiology mediates this process).

When the nanoparticles are available for accumulation in the tumour, they must either (a) reside in the tumour vessel, or (b) enter into tumour stroma. The calculation of tumour delivery efficiency assumes they are resident in the tumour over a period of time. In our strategy, we removed the liver cells that take them up, but if they are not able to accumulate in the target diseased tissue, they can stay in circulation or be taken up by other cell types in the liver and potentially other organs. If they circulate long-enough, they may be taken up by re-populated Kupffer cells. Hence, a high delivery efficiency to the tumour is a balancing act between the tissue kinetics between the different organs that are involved in the process. This study shows the liver Kupffer cells may only contribute 2% to the delivery efficiency.

A next step to addressing the "delivery problem" would be to evaluate how each organ contributes to the delivery process. This may involve analysis of the spleen, lymph nodes, skin, and other organs that have been reported to sequester nanoparticles, as well as the tumour system. A full understanding of the contribution of each organ, from the organ-, cellular-, and molecular-level, would help us to develop rational strategies to overcome the poor delivery efficiency. These results would allow us to consider how to design a multi-functional nanosystem that can avoid biological

barriers, or how to use combinatory strategies to alter biological systems for effective nanoparticle delivery to the tumour. These basic studies are important to solving the “delivery problem”.

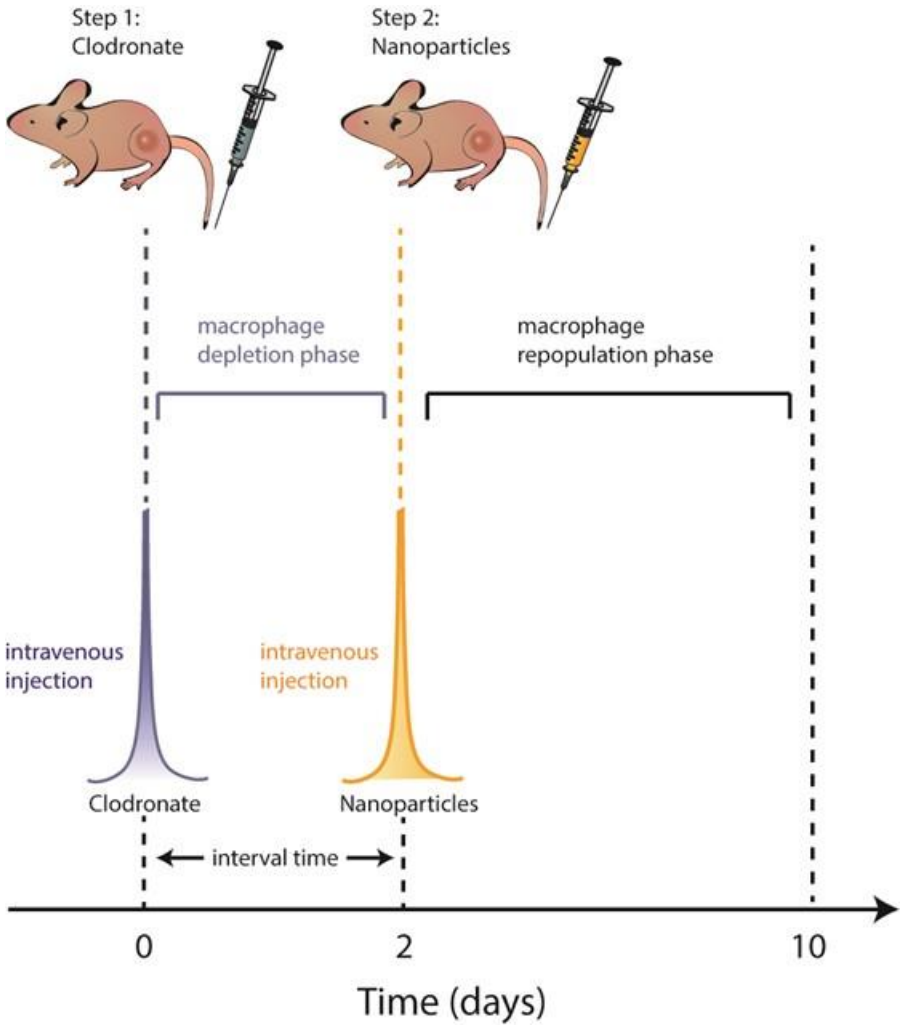

Fig. 4. 1. Two-step injection scheme to improve the delivery of nanoparticles to the tumour. Clodronate liposomes are intravenously injected into the mouse via the tail vein to remove a portion of Kupffer cells within 48h. Gold nanoparticles are then intravenously injected. Removal of a portion of Kupffer cells ensure host immune tolerance is not significantly suppressed and provides improved pharmacokinetics of gold nanoparticles by preventing off-target accumulation in the liver. Nanoparticle transport through the blood stream is enhanced and the subsequent delivery to the tumour is increased. Within 10 days from clodronate administration, Kupffer cells are repopulated from monocytes in the blood.

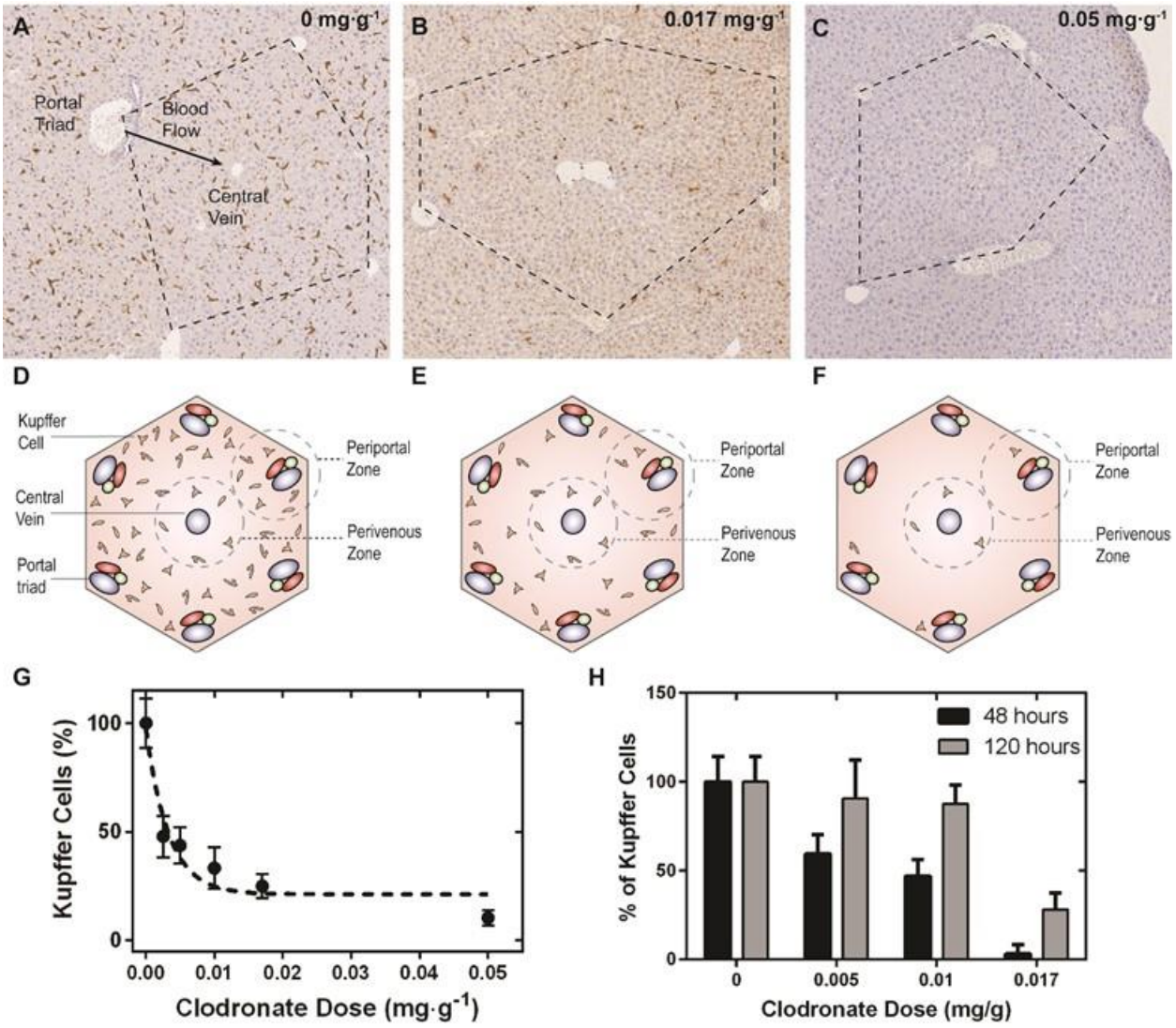

Fig. 4. 2. Histological sections of mouse liver tissue immunohistochemically stained with anti-F4/80-HRP 48h after administration of 0-0.05 mg·g^{-1} of clodronate liposomes (A-C). The histological sections are schematically represented in D-F. The liver contains a hexagonal microvascular repeating unit known as the hepatic lobule (black dashed lines). Blood flows from several portal triads (portal vein, hepatic artery, and bile ducts) and drains into a single central vein. At increasing doses of clodronate liposomes, clear depletion zones of Kupffer cells can be seen in periportal regions and between adjacent portal triads as compared to perivenous regions (panel B and E) relative to controls (A). At a dose of 0.05 mg·g^{-1}, near complete depletion of Kupffer cells can be seen in the hepatic lobule shown in C. G Normalized percentage of Kupffer cells counted from fixed areas of CD1 nu/nu hepatic tissue sections from animals treated with clodronate liposomes (0.00-0.05 mg·g^{-1}). H Depletion and repopulation of Kupffer cells in BALB/c mice. The number of Kupffer cells from fixed areas of tissue were quantified at 120h and were normalized to the initial amounts at 48h after adminstration of clodronate liposomes. It was found that 0.017 mg·g^{-1} was sufficient to completely deplete the livers in this strain of mice.

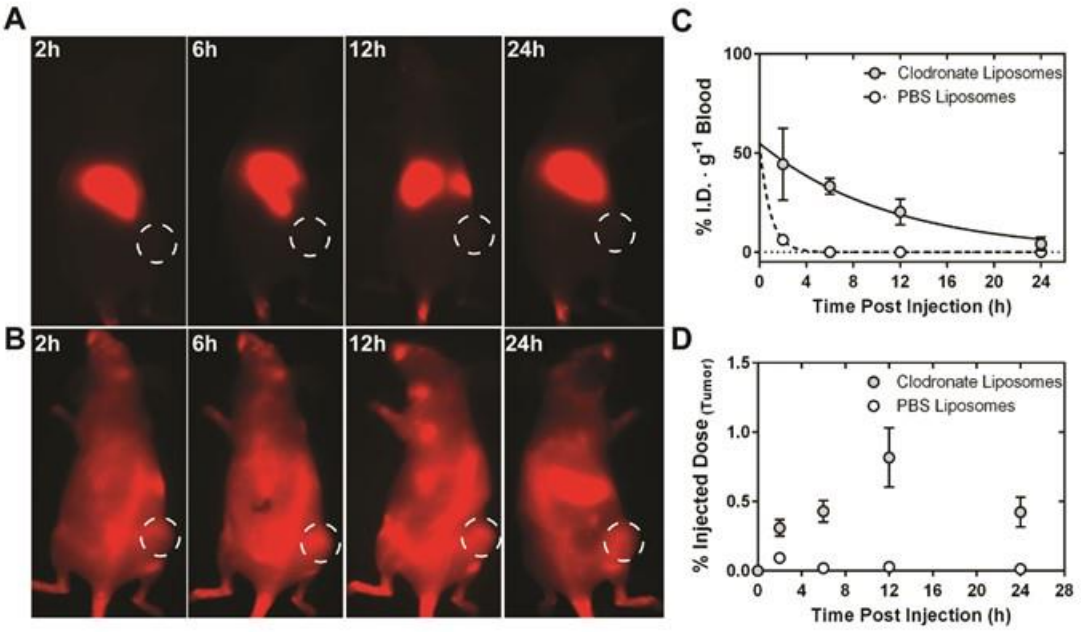

Fig. 4. 3. A In vivo fluorescence images of a single CD1 Nu/Nu SKOV3 xenograft at 2-24h, after the intravenous injection of AuNPs that was treated with PBS liposomes. B Analogous images of a single animal after administration of AuNPs, albeit this animal was injected with clodronate liposomes 48h prior. Improved circulation of the AuNPs can be visualized by a clearly resolved whole-body fluorescence image with fluorescence emerging from the position of the tumour xenograft (dashed white lines). C The normalized blood half-life of AuNPs as determined by ICP-MS in animals treated with clodronate liposomes (grey) and those with PBS liposomes (white). The curves were fit as single phase exponential decays, and the administration of clodronate liposomes improved the half-life of the AuNPs to $8 \cdot h^{-1}$ from $0.64 \cdot h^{-1}$. D The pharmacokinetic accumulation of AuNPs at the SKOV3 tumor from 2-24h after administration of clodronate (grey) and PBS liposomes (white). The integrated area-under-curve (AUC) as determined by ICP-MS was found to be 0.5 %I.D. in animals treated with clodronate where control showed 0.03 %I.D..

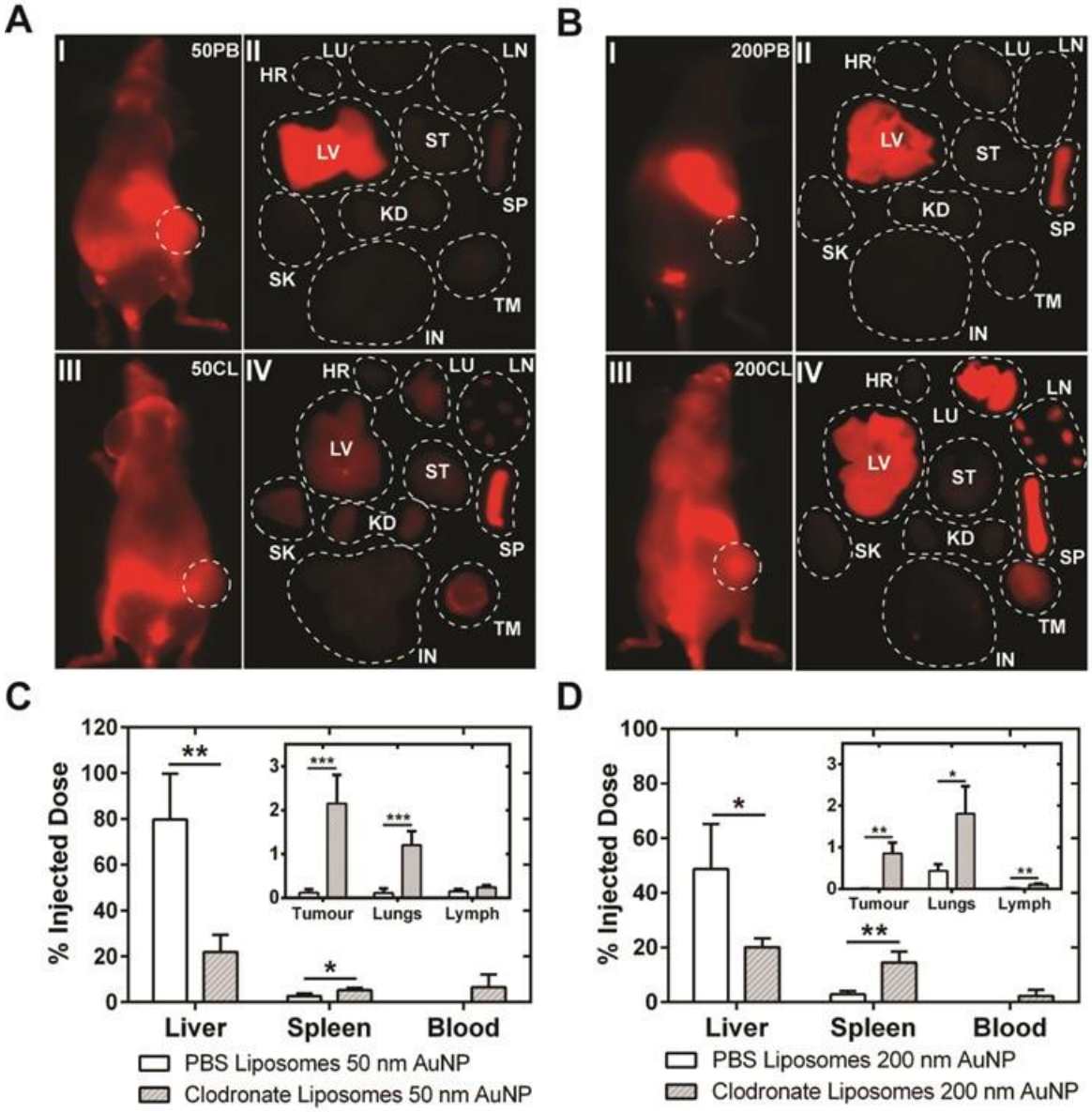

Fig. 4. 4. Biodistribution of 50 nm and 200 nm AuNPs 48h after clodronate administration. A In vivo animal (I + III) and ex vivo organ (II + IV) fluorescence images 24h after tail vein injection of 50 nm AuNPs in control (top) and clodronate (bottom) treated animals. Organ abbreviations: (HR) heart, lungs (LU), liver (LV), stomach (ST), spleen (SP), skin (SK), kidneys (KD), tumour (TM), and intestines (IN). The quantitative organ distribution as determined by ICP-MS is shown in panel C. A reduction in uptake of nanoparticles in the liver translated to a near 20-times increase in delivery of nanoparticles to the tumour. B In vivo animal (I+III) and ex vivo organ (II+IV) fluorescence images 24h after administration of 200 nm AuNPs in animal treated with PBS liposomes (top) and clodronate liposomes (bottom). The quantitative organ distribution is shown in panel D. A two-fold decrease in liver accumulation of 200 nm AuNPs translated to 142-times increase in the delivery of the nanoparticles to the tumour. *Statistical significance was considered as $p < 0.05$.

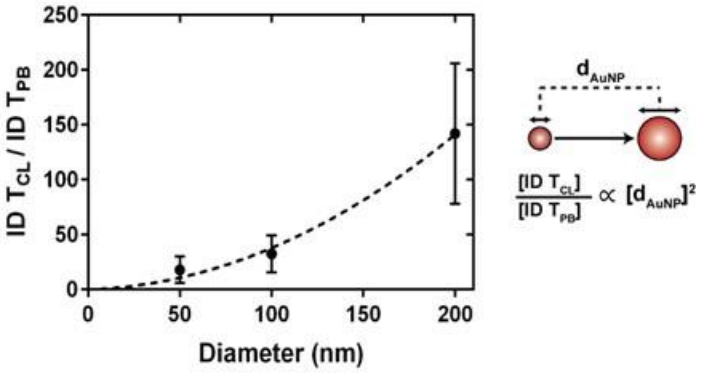

Fig. 4. 5. The delivery of AuNPs to SKOV3 tumors is improved exponentially as a function of nanoparticle diameter (d_{AuNP}) using clodronate liposomes 48h prior to AuNP administration. The relative increase in AuNP tumour delivery efficiency with clodronate liposomes (ID T_{CL}) compared to controls (ID T_{PB}) was 18, 32 and 150 times for nanoparticle diameters of 50, 100, and 200 nm respectively.

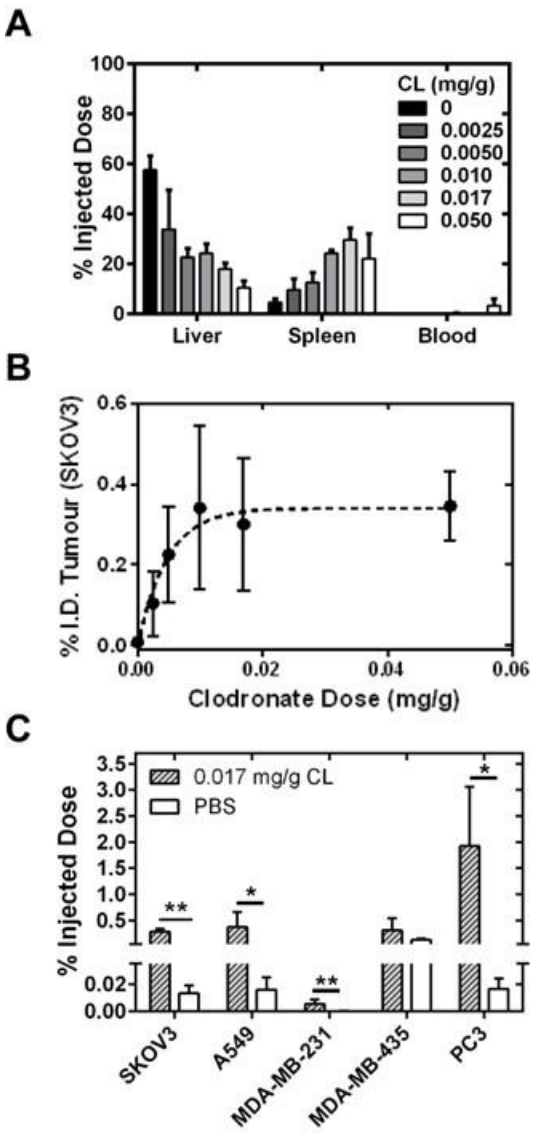

Fig. 4. 6. A Biodistribution at 24h of 100nm AuNPs as measured by ICP-MS in the liver, spleen, and blood at an increasing dosage of clodronate liposomes. A gradual decrease from 80% I.D. to less than 20% I.D. was seen for the liver, while the accumulation of AuNPs in the spleen increased from 10% to 40% I.D. It was found that less than 1% of AuNPs were seen circulating in blood at all other dosages of clodronate. B AuNP tumour accumulation as a %I.D. for increasing dosages of clodronate liposomes. C Administration of clodronate liposomes at a dose of 0.017 mg/g improved the global delivery of nanoparticles to four of five xenograft tumour models investigated. The increased accumulation of A750-AuNPs in SKOV3 and A549 subcutaneous xenografts and MDA-MB-231 and PC3 orthotopic xenografts was 20 to 100 times ($p < 0.05$).

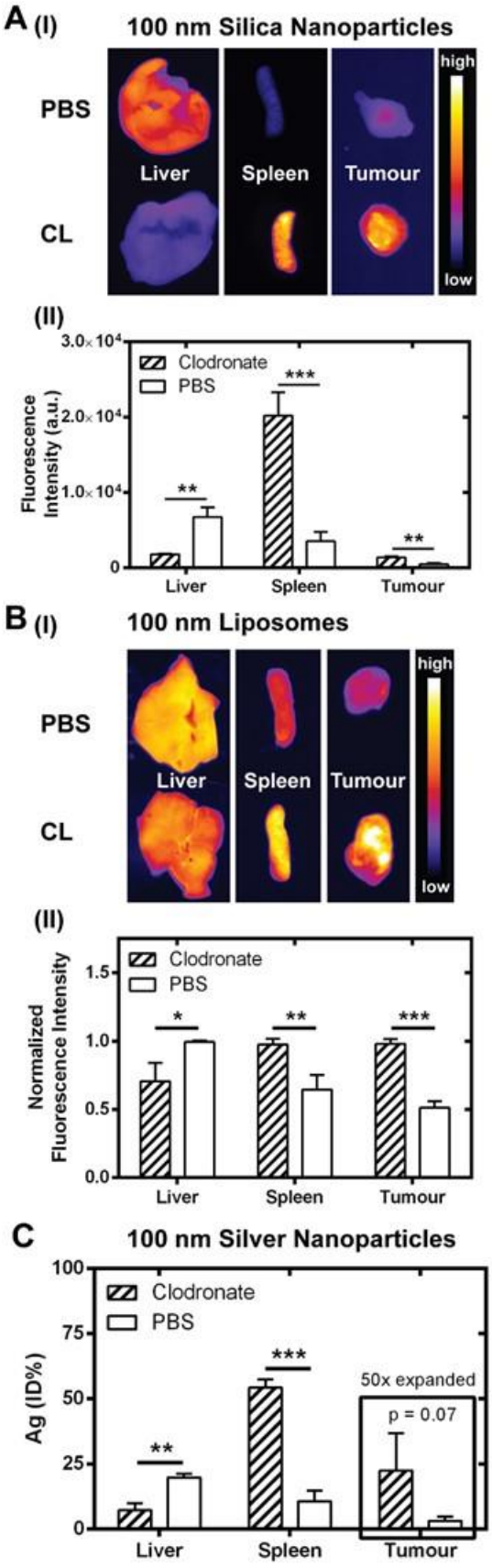
A (I)
100 nm Silica Nanoparticles
PBS
CL
Liver
Spleen
Tumour
high
low
(II)
Clodronate
PBS
Fluorescence Intensity (a.u.)
3.0×10⁴
2.0×10⁴
1.0×10⁴
0
**
***
**
Liver
Spleen
Tumour
B (I)
100 nm Liposomes
PBS
CL
Liver
Spleen
Tumour
high
low
(II)
Clodronate
PBS
Normalized Fluorescence Intensity
1.5
1.0
0.5
0.0
*
**
***
Liver
Spleen
Tumour
C
100 nm Silver Nanoparticles
Clodronate
PBS
Ag (ID%)
100
75
50
25
0
**
***
50x expanded
p = 0.07
Liver
Spleen
Tumour

Fig. 4. 7. A(I) Ex vivo fluorescence images showing the distribution of 100 nm SiNPs in livers, spleens, and tumours 48h hours after administration of clodronate liposomes (CL) or PBS liposomes (PBS). The average integrated fluorescence intensity of the corresponding tissues is shown in panel (II). B The distribution of 100 nm nano-liposomes in liver, spleen, and tumours are shown qualitatively by the ex vivo fluorescence images in (I) and the average integrated fluorescence intensity normalized on an organ basis is given in panel (II). C The organ distribution of 100 nm AgNPs was determined using ICP-MS. The silver signal from each tissue was normalized as a %I.D. The Ag signal in the tumours was expanded by 50-fold for illustration on the same axis scale. Macrophage depletion reduced the liver accumulation of all three types of nanoparticles with resultant increases to splenic and tumour tissue. Nanoparticle delivery to the tumour increased between 2-7 times and was dependent on the nanoparticle type. The dose of clodronate liposomes was 0.017 $mg \cdot g^{-1}$, mice were euthanized 3h after injection of nanoparticles. Animals used in these experiments were SKOV3 tumour xenografts in CD1 nu/nu mice (n = 3-4).

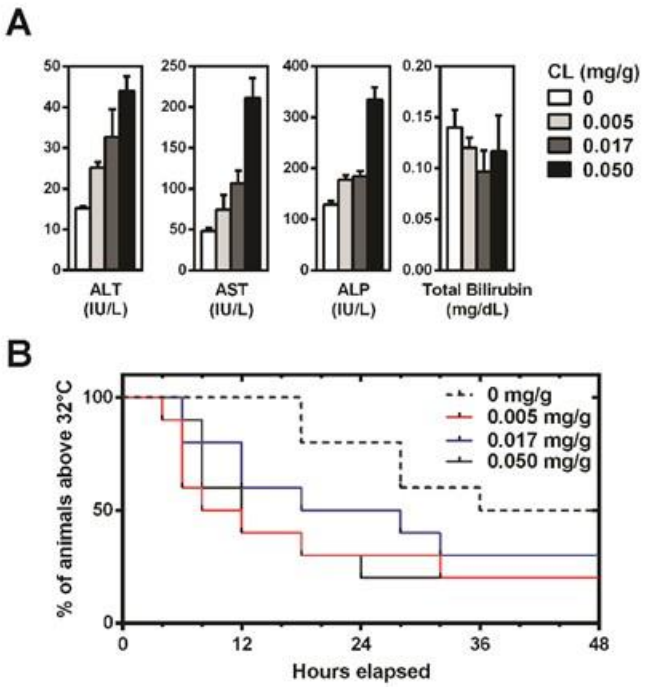

Fig. 4. 8. A Hepatotoxicity analysis of serum markers alanine transaminase (ALT), aspartate aminotransferase (AST), alkaline phosphatase (ALP) and total bilirubin after intravenous administration of clodronate liposomes (0-0.05 $mg \cdot g^{-1}$). Data are represented as an average of n = 3, where error bars illustrate the standard deviation of the measurement. B Survival curves of animals administered clodronate liposomes (0-0.05 $mg \cdot g^{-1}$) followed by induction of sepsis 48h through cecal ligation and puncture. Survival was defined by animals exhibiting hypothermia with a body temperature higher than 32°C. Macrophage depletion with clodronate liposomes increased the onset of sepsis and reduced median survival time by three-fold and overall survival by up to 30%. There was no statistical significance between animals receiving 0.017 $mg \cdot g^{-1}$ of clodronate liposomes and control animals (p = 0.1932 by Mantel-Cox Log rank test). Each group consisted of n = 10 animals.

Supplementary figures and table

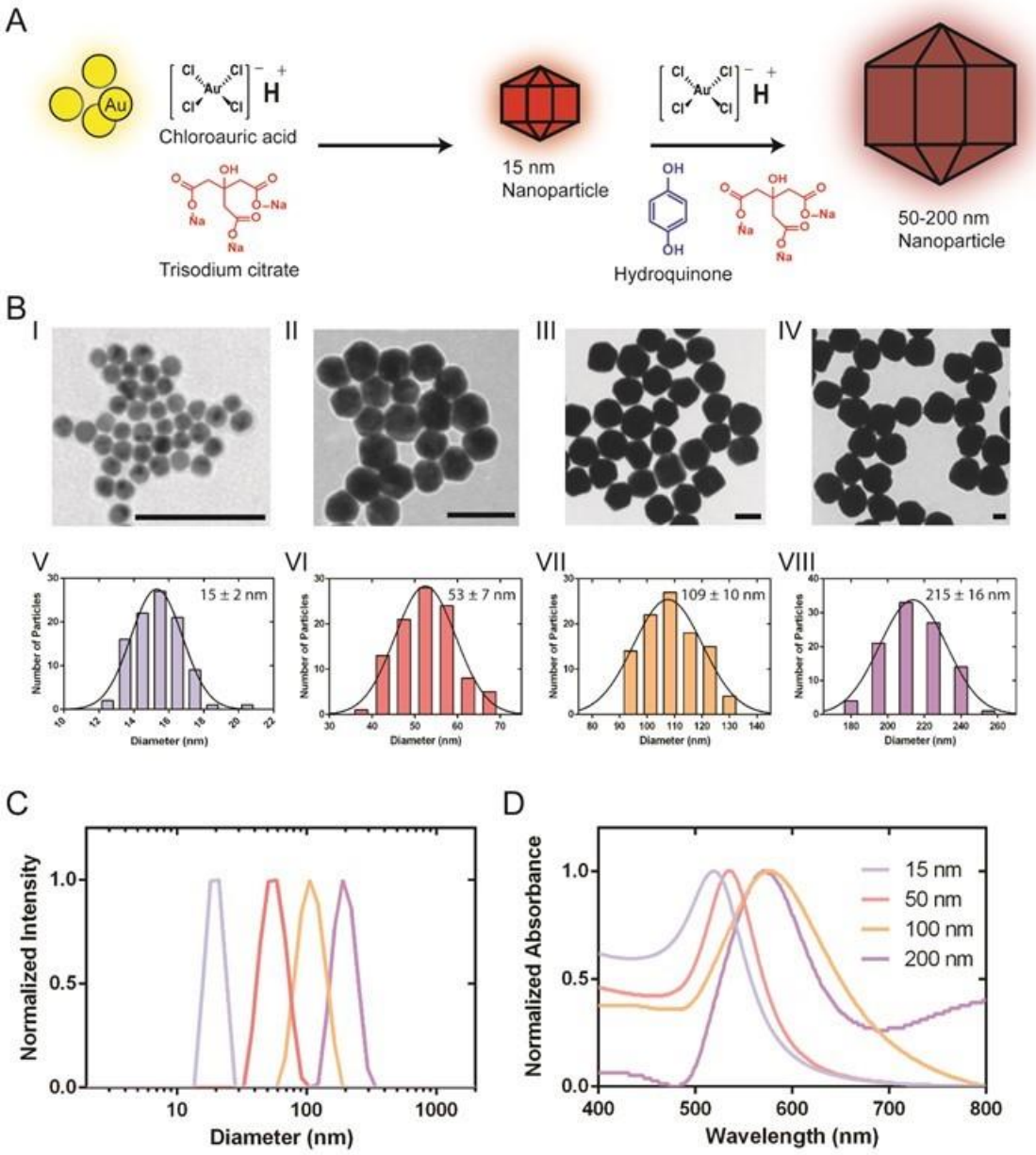

Fig. 4S. 1. A Scheme for the synthesis of 15 nm AuNPs that seed the growth of larger 50-200 nm AuNPs. Chloroauric acid is reduced by citrate at reflux to produce 15 nm AuNP seeds. The purified 15 nm AuNP seeds are further reduced to larger 50-200 nm AuNPs with hydroquinone at room termperature in the presence of additional citrate and chloroauric acid. B TEM images of (I) 15, (II) 50, (III) 100, and (IV) 200 nm AuNPs, the scale bar in each image is 100 nm. (V-VIII) Corresponding average diameters as determined by fitting a Gaussian to each measured nanoparticle distribution. Average NP diameter was determined by measuring 90-100 NPs from a single TEM frame. The scale bar in each figure is 100 nm The hydrodynamic diameter and the extinction spectra of the 15-200 nm AuNPs is given by C and D, respectively.

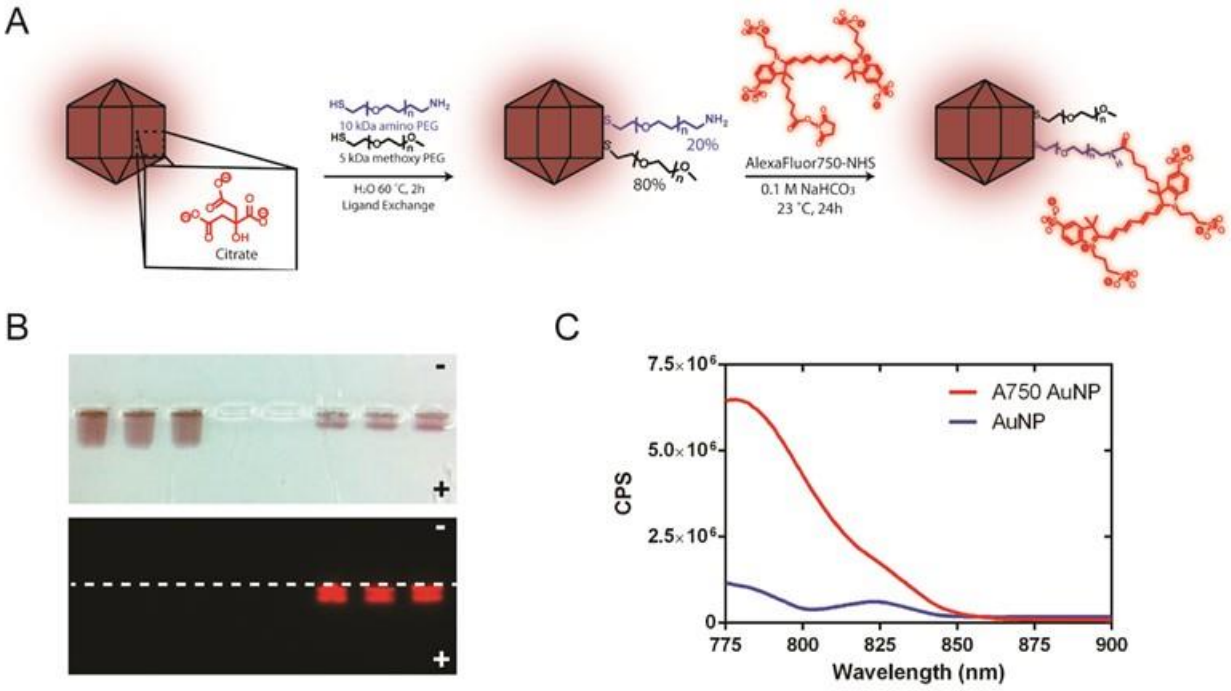

Fig. 4S. 2. A Surface modification of AuNPs. Citrate capped AuNPs are ligand exchanged with thiolated 5kDa mPEG and 10kDa amino-PEG at a 4:1 ratio. The free amine facilitated the covalent attachment of Alexa-750 to render the NPs fluorescent. B Agarose gel electrophoresis of 100 nm citrate capped (left) and A750 AuNPs (right). The panel below is the same agarose gel fluorescently imaged at 830 nm after excitation with 750 nm light. C Solution phase fluorescence measurements of 100 nm A750-AuNPs (red) and citrate AuNPs (blue).

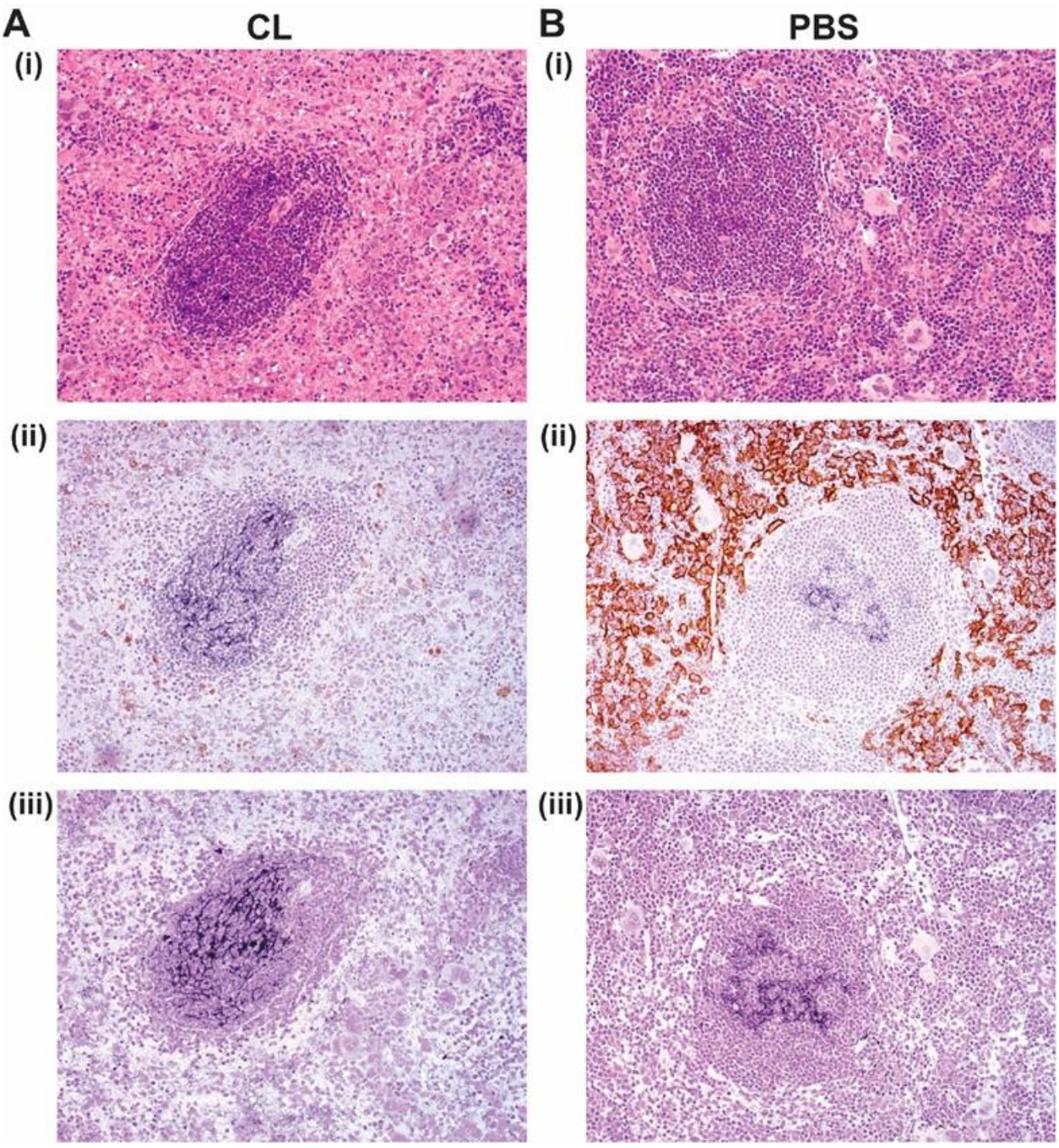

Fig. 4S. 3. Histopathology of CD1 nu/nu mice splenic tissue 48h after administration of clodronate liposomes A and PBS liposomes B. The panels shown in (i) are tissue slices (H&E) stained. The reduced hematoxylin staining in panel A (i) demonstrates a reduction of cells in the red-pulp space. The immunohistochemical staining of the same tissue slice with anti-F4/80-HRP (ii) illustrates the depletion of macrophages in the red-pulp space in A(ii) from B(ii). The tissue slices shown by A(iii) and B(iii) are stained with silver nitrate to show the location of AuNPs which appear in the white pulp region in both animals treated with clodronate liposomes and PBS liposomes. The dose of clodronate liposomes was 0.05 $mg \cdot g^{-1}$.

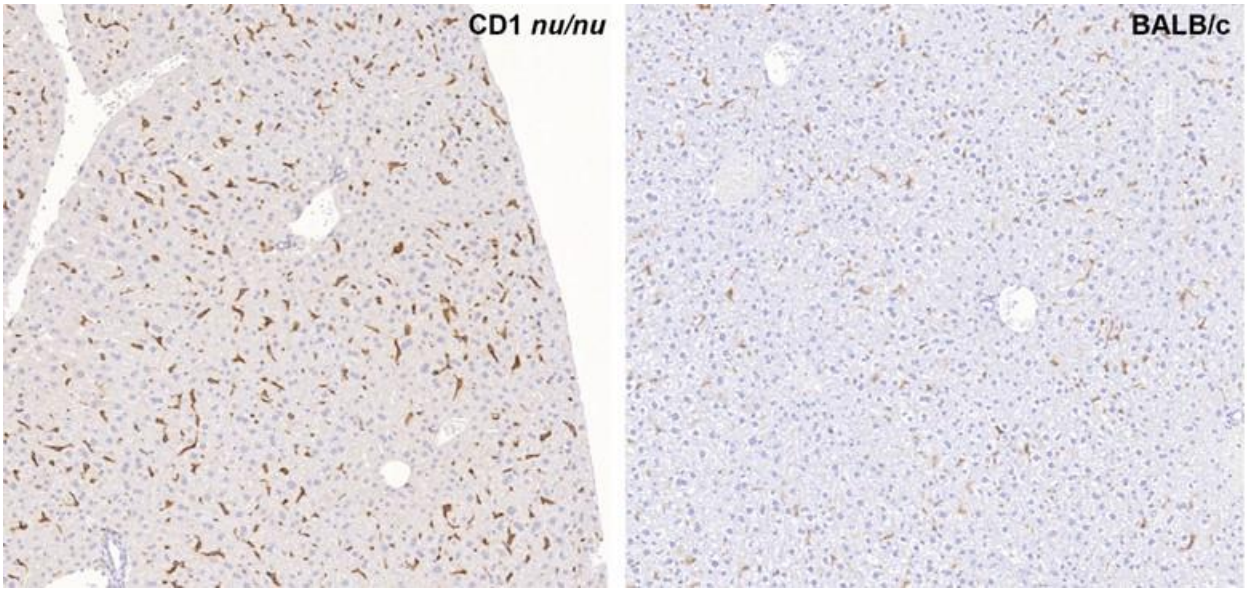

Fig. 4S. 4. Histology slices of liver tissue stained with anti-F4/80 HRP from CD1 nu/nu mice (left) and BALB/c mice (right). Animals were injected with PBS liposomes 48h prior to isolation and fixation of resected livers. The histological sections qualitatively illustrate a higher density Kupffer cells in CD1 nu/nu hepatic tissue as compared to BALB/c. The data is also consistent with the complete hepatic depletion seen of BALB/c livers when animals were injected with a clodronate liposomes dose of 0.017 $mg \cdot g^{-1}$.

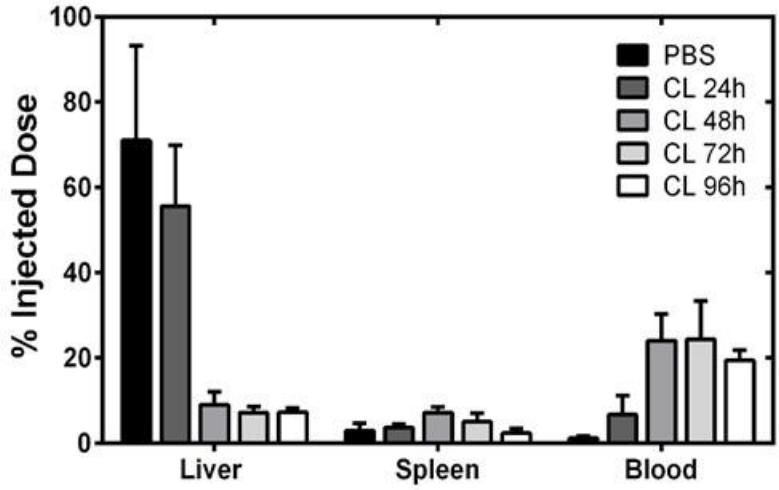

Fig. 4S. 5. Evaluation of the delay time between the injection of clodronate liposomes and AuNPs. The AuNP accumulation in the liver, spleen and that remaining in the blood was used assess the degree of macrophage depletion from clodronate liposomes. It was found that 48h after administration of 0.05 $mg \cdot g^{-1}$ clodronate liposomes, complete depletion of Kupffer cells and splenic macrophages minimized the accumulation of AuNPs in these organs and maximized the amount of available AuNPs in the blood.

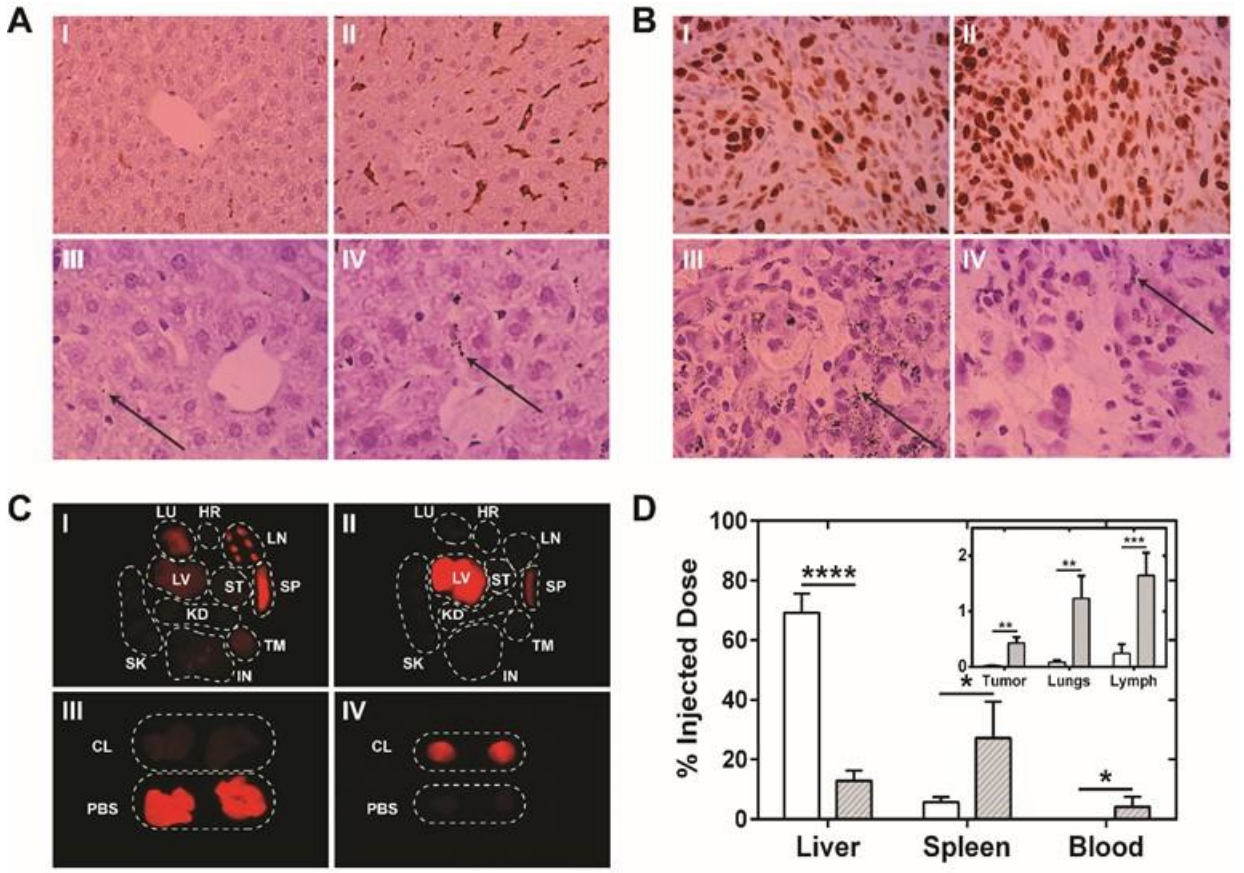

Fig. 4S. 6. A Histological sections of liver tissue from CD1 nu/nu SKOV3 xenografts after injection of AuNPs. Images (I+III) and (II+IV) are stained with hematoxylin/eosin and silver, respectively. The top two panels are tissue slices from an animal that was administered clodronate liposomes while those on the bottom are respective of pretreatment with PBS liposomes. Increased liver tissue distribution of AuNPs are seen in (IV) as qualitatively illustrated by black clusters characteristic of silver reduction. **B** Histological sections of tumor tissues that were stained with anti-Ki-67/HRP and counter stained with hematoxylin (I+III) to illustrate cancer cells while (II+IV) are stained with silver nitrate to visualize AuNPs. Panels (I+II) were tissues taken from an animal that received clodronate liposomes + AuNPs; clusters of AuNPs are visualized as dark smudges (arrows) in the tumor tissue on the contrary to the slice shown in (IV) where no silver reduction is visible. **C** Ex vivo fluorescence images of the 24h biodistribution of AuNPs in an animal treated with (I) and without (II) clodronate liposomes. The animal organs: heart (HR), lungs (LU), liver (LV), stomach (ST), spleen (SP), skin (SK), kidneys (KD), tumor (TM), and intestines (IN) are organized similar to their intrinsic anatomical arrangement. Panels (III) and (IV) show the livers and tumors from pretreatment with clodronate (top) and PBS (bottom) liposomes. The qualitative redistribution of the AuNPs from liver sequestration improves the delivery to the solid tumor. **D** The total organ distribution after 24h as measured by ICP-MS with (grey) and without (white) injection of clodronate liposomes. All organs harvested were analyzed, only organs showing statistically significant (p-value < 0.05) differences in quantitative accumulation are shown. The liver signals were reduced 4-times in animals that were administrated clodronate liposomes an increase in accumulation was seen to the spleen, lungs, and axillary, brachial and inguinal lymph nodes (lymph); AuNPs were still in circulation after 24h. Clodronate liposomes administration

enabled a 32-times increase in AuNP delivery to the tumor. Statistical significance was measured at *p-value < 0.05, **p-value < 0.01, ***p-value < 0.001, and ****p-value < 0.0001.

Table 4S. 1. Average tumor masses resected from each cancer type.

Tumor Model	Average mass (g)
SKOV3	0.51 ± 0.26
MDA-MD-231	0.0078 ± 0.0065
MDA-MB-435	0.43 ± 0.34
PC3	0.77 ± 0.41
A549	0.17 ± 0.21

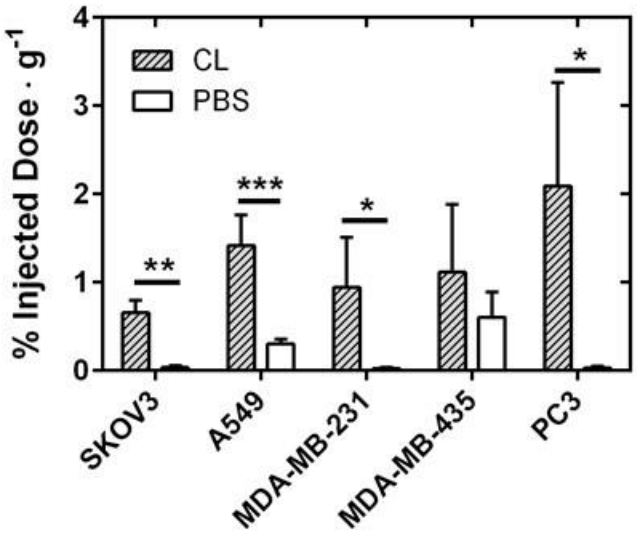

Fig. 4S. 7. Mass normalized tumor delivery of 100 nm AuNPs (%I.D.·g^{-1}) to various cancer types. The increased accumulation of AuNPs in SKOV3 and A549 subcutaneous xenografts and MDA-MB-231 and PC3 orthotopic xenografts was 20 to 60 times. *p-value < 0.05, **p-value < 0.01, and ***p-value < 0.001.

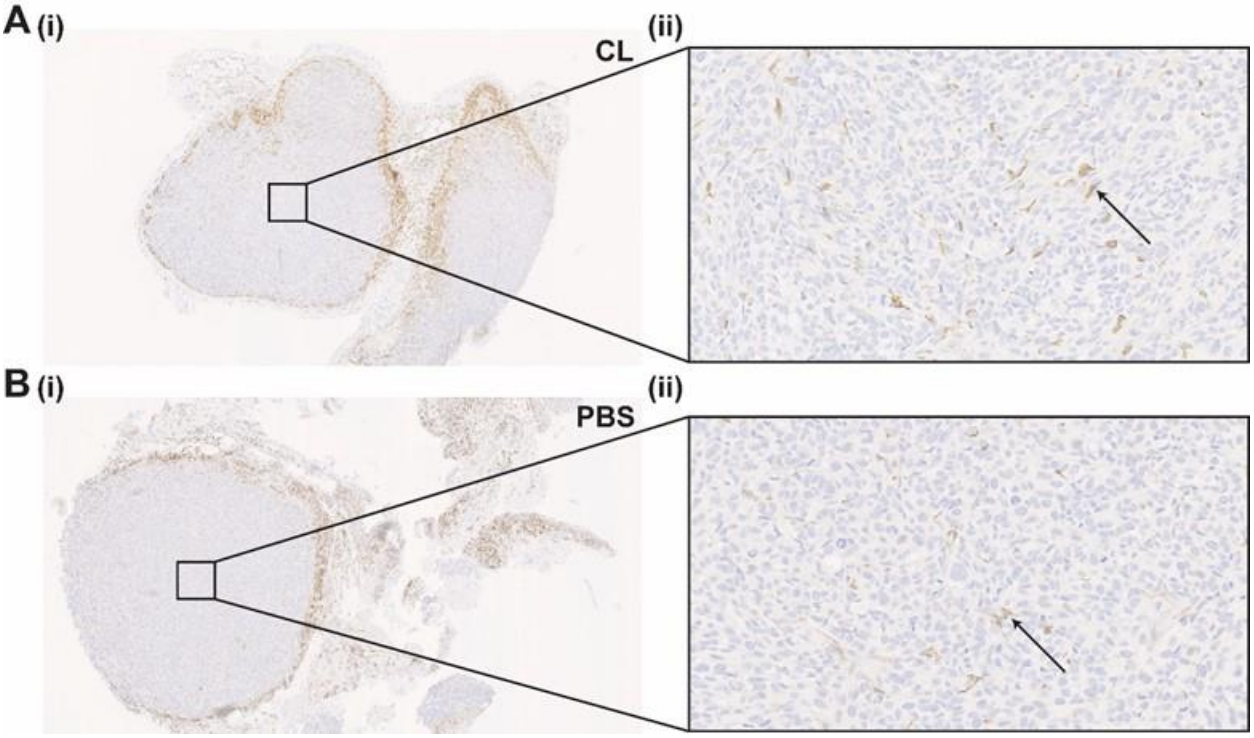

Fig. 4S. 8. SKOV3 tumor tissue stained with anti-F4/80 HRP to illustrate tumor associated macrophages. Panels A (i) and (ii) are images at of a tissue slice at 2.5× and 20× from an animal 48h after injection with clodronate liposomes. Analagous images are shown in B (i) and (ii) from a control animal treated 48h prior with PBS liposomes. Qualitatively, the tumor associated macrophages that are illustrated by the the brownish-colour (arrows) do not differ in the two tissues. This suggests tumor associated macrophages in the SKOV3 tumor were not depleted with clodronate liposomes at a dose of 0.05 $mg \cdot g^{-1}$.

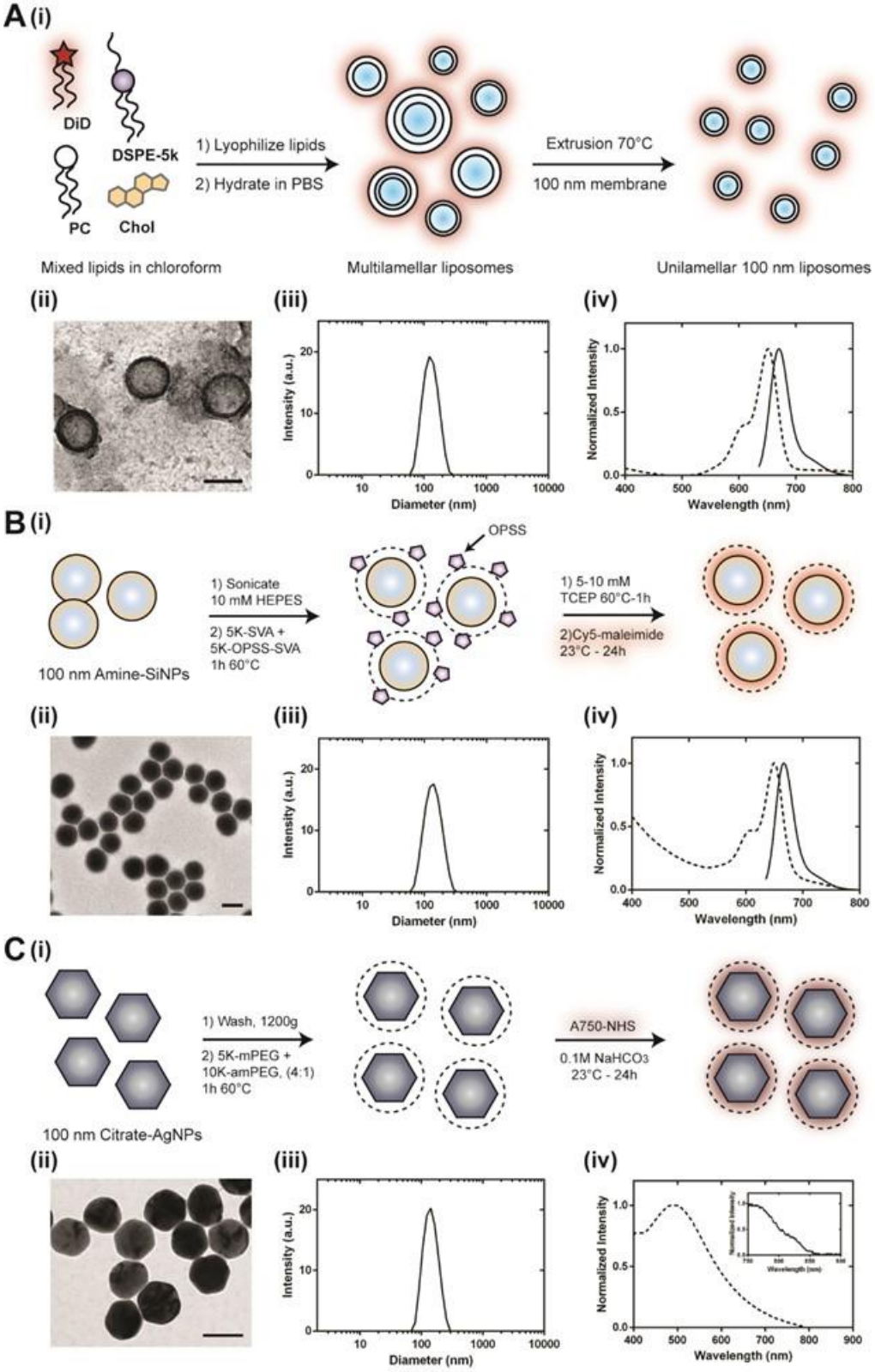

Fig. 4S. 9. A Synthesis and characterization of nano-liposomes. The synthetic scheme is shown by (i) where mixed lipid films are lyophilized from organic solvents, hydrated in PBS buffer and then

crude liposomes are sized and homogenized by extrusion through a 0.1 µm nucleopore membrane. Analysis of nano-liposomes was done by TEM (ii), DLS (iii) and absorbance/fluorescence spectroscopy (iv). B Surface modification of amine terminated SiNPs (i) scheme for derivatization: SiNPs were conjugated with a mixed film of OPSS and methoxy terminated 5kDa PEG ligands. TCEP was used to reduce the OPSS disulfide to a free thiol to conjugate with sulfo-Cy5 maleimide to render the NPs fluorescent. A TEM image, DLS spectrum and absorbance and fluorescence spectra of the modified SiNPs are shown by (ii-iv), respectively. C (i) Scheme for the ligand exchange of citrate stabilized AgNPs with methoxy and amine terminated PEG ligands. The terminal amine was used to couple the fluorophore A750-NHS. SiNPs were characterized by TEM (ii), DLS (iii), and absorbance/fluorescence spectroscopy (iv). AgNPs exhibited weak fluorescence, inset in panel C (iv). The scale bar in each TEM image from panels A-C is 100 nm.

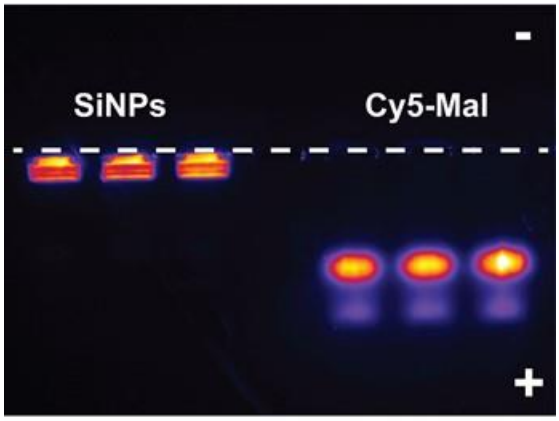

Fig. 4S. 10. To confirm the removal of excess Sulfo-Cy5 maleimide, the SiNPs were interrogated against free sulfo-Cy5 maleimide using a 0.7% w/v agarose gel. Samples were run in triplicate, where both displayed anodic migration and confirmed the absence of unconjugated sufo-Cy5 maleimide in the SiNPs samples.

Table 4S. 2. Physico-chemical properties of lipsomes, AgNPs, and SiNPs.

Nanoparticle	**Inorganic diameter (nm)**	**Hydrodynamic diameter (nm)**	**Zeta potential (mV)**
DiD-Liposome	-	109.0 ± 8.5	-5.56 ± 0.86
A750-AgNP	96.0 ± 10.0	142.1 ± 9.5	-14.7 ± 0.4
A647-SiNP	101.1 ± 6.2	139.1 ± 9.6	-8.04 ± 0.33

Table 4S. 3. Liver biochemistry panel from C57BL/6 mice treated with clodronate liposomes.

	Clodronate liposome dose (mg·g^{-1})				Reference (mean ± SD)*
	0	**0.005**	**0.017**	**0.05**	
ALT (u/L)	15.2 ± 0.5	25.2 ± 1.32	32.6 ± 6.88	44.0 ± 3.49	50.53 ± 37.15
AST (u/L)	48.3 ± 3.27	74.0 ± 18.6	106.5 ± 15.6	211.3 ± 23.9	126.54 ± 133.29
ALP (u/L)	128.4 ± 7.65	177.2 ± 9.42	184.8 ± 9.68	334.5 ± 24.1	234.51 ± 93.36
TBIL (mg/dL)	0.14 ± 0.02	0.12 ± 0.01	0.10 ± 0.02	0.12 ± 0.04	0.28 ± 0.1

*__Reference from:__ http://www.criver.com/files/pdfs/rms/c57bl6/rm_rm_d_c57bl6n_mouse.aspx

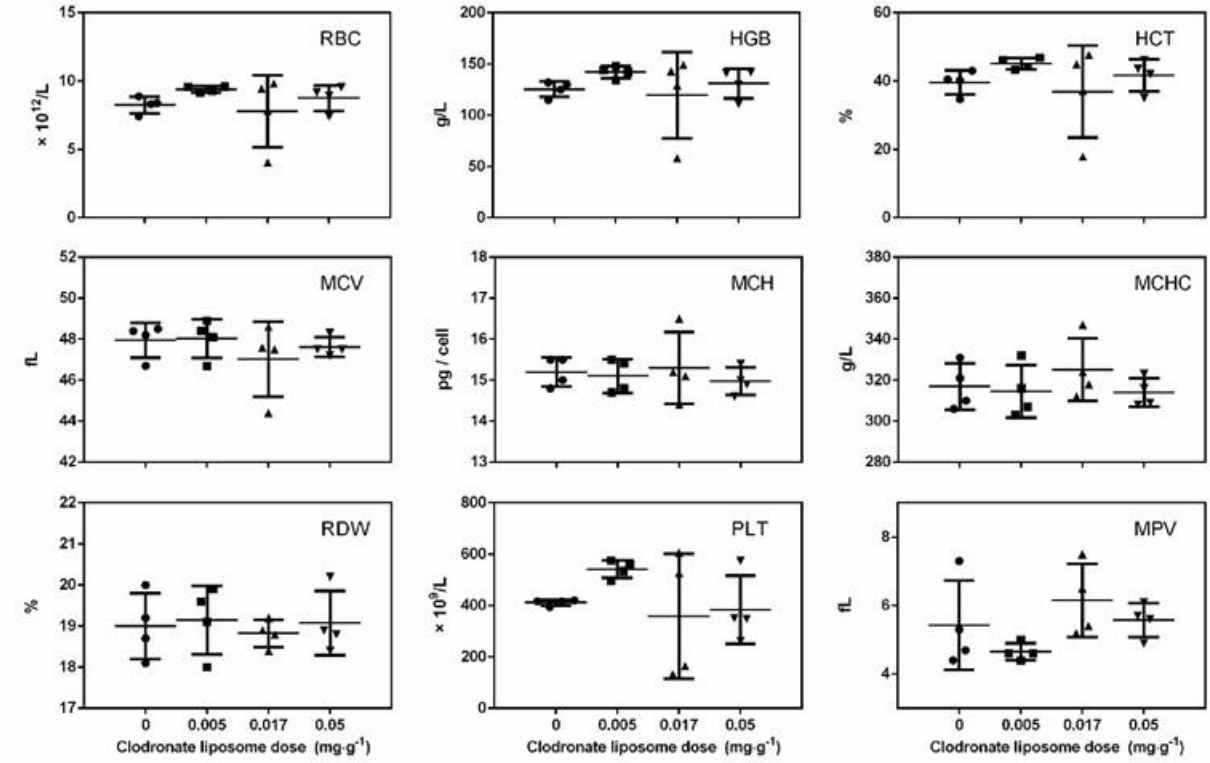

Fig. 4S. 11. Hematology analysis of C57BL/6 mice 48h after intravenous injection of clodronate liposomes from 0-0.05mg·g^{-1}. Error bars represent standard deviation calculated from four animals. Parameters shown include red blood cell count (RBC), hemoglobin (HGB), hematocrit (HCT), mean corpuscular volume (MCV), mean corpuscular hemoglobin (MCH), mean corpuscular hemoglobin concentration (MCHC), red blood cell distribution width (RDW), platelet count (PLT), and mean platelet volume (MPV). No statistical significance was observed between treatment groups for all parameters as analyzed by one-way ANOVA with Bonferroni correction ($\alpha = 0.05$).

Table 4S. 4. Hematology analysis from C57BL/6 mice treated with clodronate liposomes.

	Clodronate liposome dose (mg·g^{-1})				Reference (mean ± SD)*
	0	**0.005**	**0.017**	**0.05**	
RBC (M/µL)	8.26 ± 0.61	9.40 ± 0.23	7.79 ± 2.64	8.76 ± 0.95	9.17 ± 1.05
HGB (g/dL)	12.55 ± 0.76	14.20 ± 0.59	11.98 ± 4.20	13.10 ± 1.44	13.72 ± 1.59
HCT (%)	39.6 ± 3.5	45.1 ± 1.6	36.9 ± 13.4	41.7 ± 4.7	45.32 ± 6.27
MCV (fL)	47.95 ± 0.84	48.03 ± 0.94	47.03 ± 1.82	47.63 ± 0.47	49.46 ± 3.88
MCH (pg/cell)	15.20 ± 0.36	15.10 ± 0.41	15.30 ± 0.88	14.98 ± 0.33	15.02 ± 1.11
MCHC (g/dL)	31.70 ± 1.13	31.45 ± 1.29	32.53 ± 1.53	31.4 ± 0.70	30.54 ± 3.19
RDW (%)	19.00 ± 0.80	19.15 ± 0.84	18.83 ± 0.33	19.08 ± 0.78	17.90 ± 1.24
PLT (K/µL)	412 .00 ± 11.46	542.25 ± 34.46	357.50 ± 243.31	384.00 ± 133.85	1167.12 ± 306.96
MPV (fL)	5.43 ± 1.31	4.65 ± 0.25	6.15 ± 1.07	5.58 ± 0.50	4.90 ± 0.33

*__Reference from:__ http://www.criver.com/files/pdfs/rms/c57bl6/rm_rm_d_c57bl6n_mouse.aspx

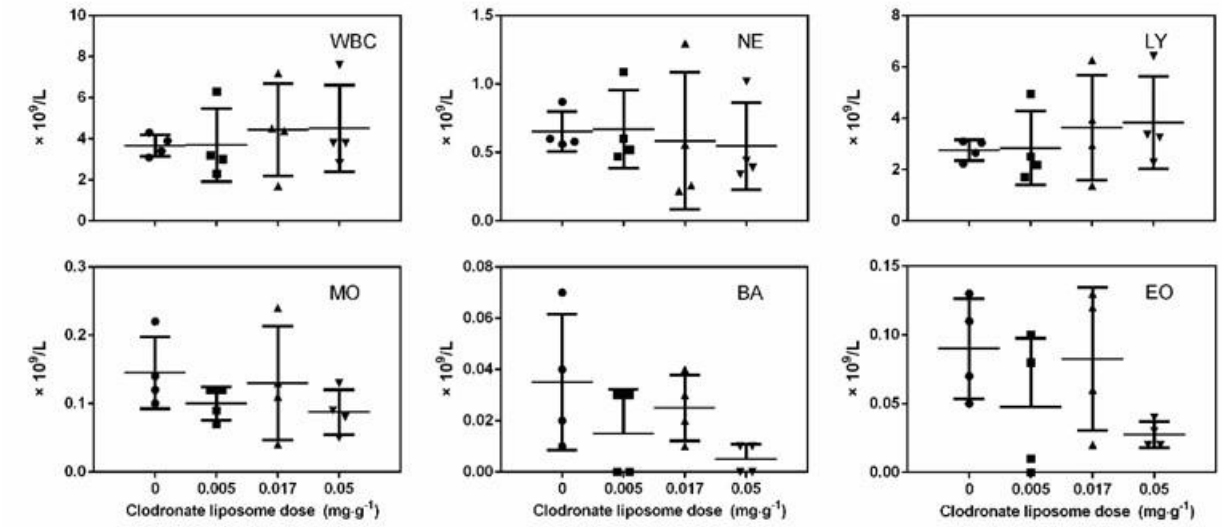

Fig. 4S. 12. Analysis of immune cells from blood of C57BL/6 mice 48h after intravenous injection of clodronate liposomes 0-0.05mg·g^{-1}. Error bars represent standard deviation calculated from four animals. Parameters shown include white blood cells (WBC), neutrophils (NE), lymphocytes (LY), monocytes (MO), basophils (BA), and eosinophils (EO). No statistical significance was observed between treatment groups for all parameters as analyzed by one-way ANOVA with Bonferroni correction ($\alpha = 0.05$).

Table 4S. 5. Immune cell counts from C57BL/6 mice treated with clodronate liposomes.

	Clodronate liposome dose ($mg \cdot g^{-1}$)				Reference (mean ± SD)*
	0	**0.005**	**0.017**	**0.05**	
WBC (K/µL)	3.68 ± 0.53	3.70 ± 1.78	4.45 ± 2.25	4.50 ± 2.12	8.69 ± 2.44
NE (K/µL)	0.65 ± 0.15	0.67 ± 0.29	0.59 ± 0.50	0.55 ± 0.32	1.22 ± 0.51
LY (K/µL)	2.76 ± 0.41	2.84 ± 1.44	3.63 ± 2.05	3.83 ± 1.79	6.92 ± 1.92
MO (K/µL)	0.15 ± 0.05	0.10 ± 0.02	0.13 ± 0.08	0.09 ± 0.03	0.37 ± 0.15
BA (K/µL)	0.04 ± 0.03	0.02 ± 0.02	0.03 ± 0.01	0.01 ± 0.01	0.03 ± 0.04
EO (K/µL)	0.09 ± 0.04	0.05 ± 0.05	0.08 ± 0.05	0.03 ± 0.01	0.16 ± 0.13

*__Reference from:__ http://www.criver.com/files/pdfs/rms/c57bl6/rm_rm_d_c57bl6n_mouse.aspx

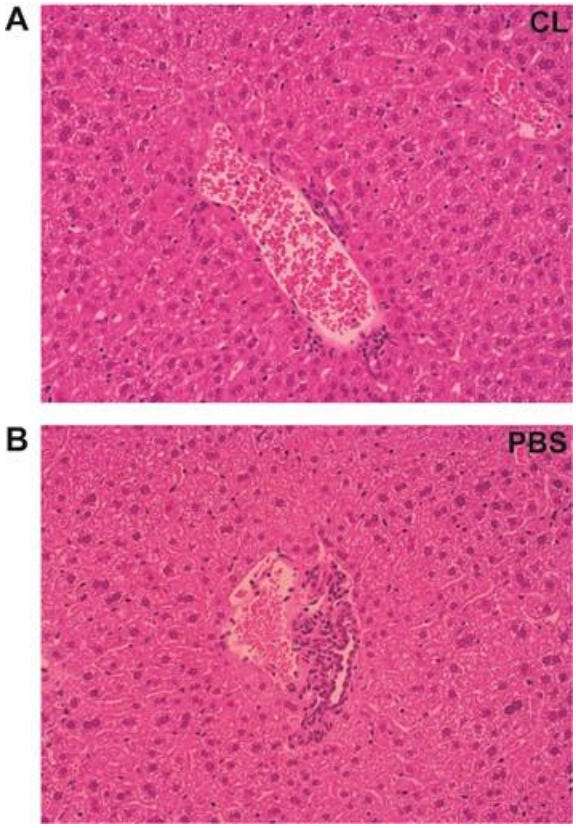

Fig. 4S. 13. CD1 nu/nu hepatic tissue stained with hematoxylin and eosin (H&E) from an animal treated with clodronate liposomes A and control PBS liposomes B after 48h. Clodronate liposomes were not seen to cause any gross inflammation to hepatic tissue in comparison to controls.

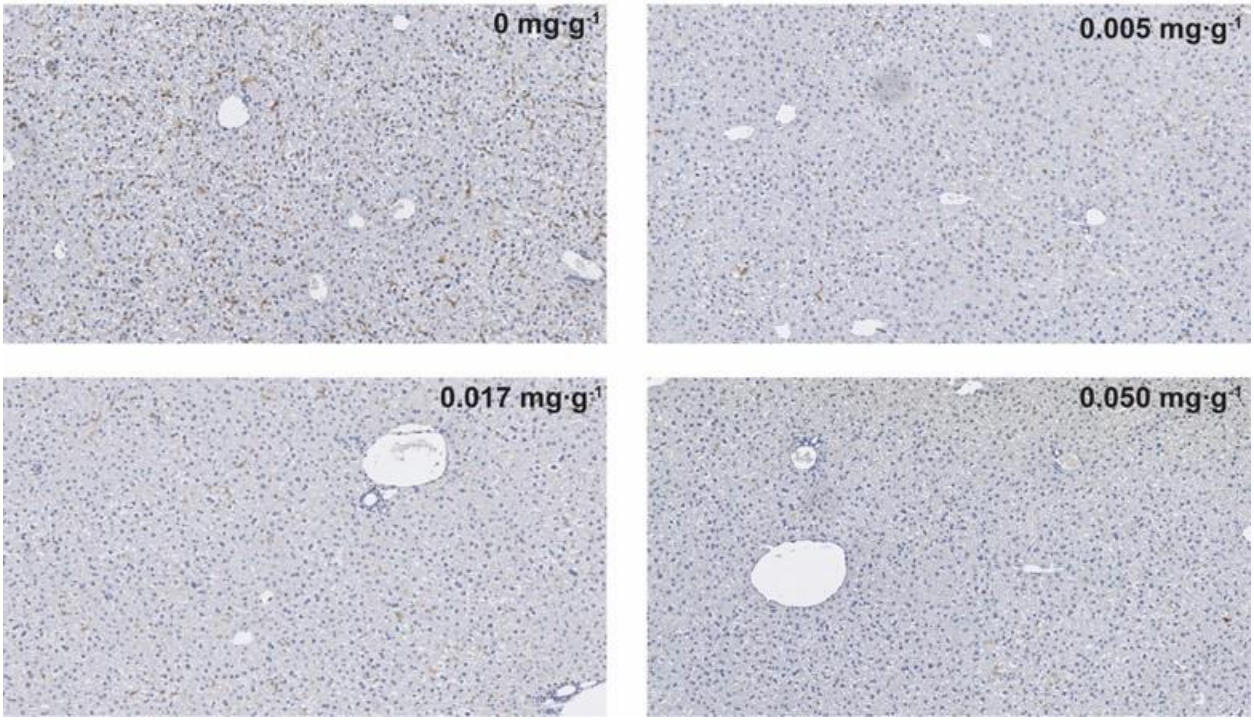

Fig. 4S. 14. Immunohistochemically stained tissue sections with anti-F4/80-HRP and counterstained with hematoxylin from livers of C57BL/6 mice treated with clodonate liposomes 0-0.05mg·g^{-1}. The data show a similar dose-dependent depletion of Kupffer cells in hepatic tissue as seen for CD1 nu/nu mice.

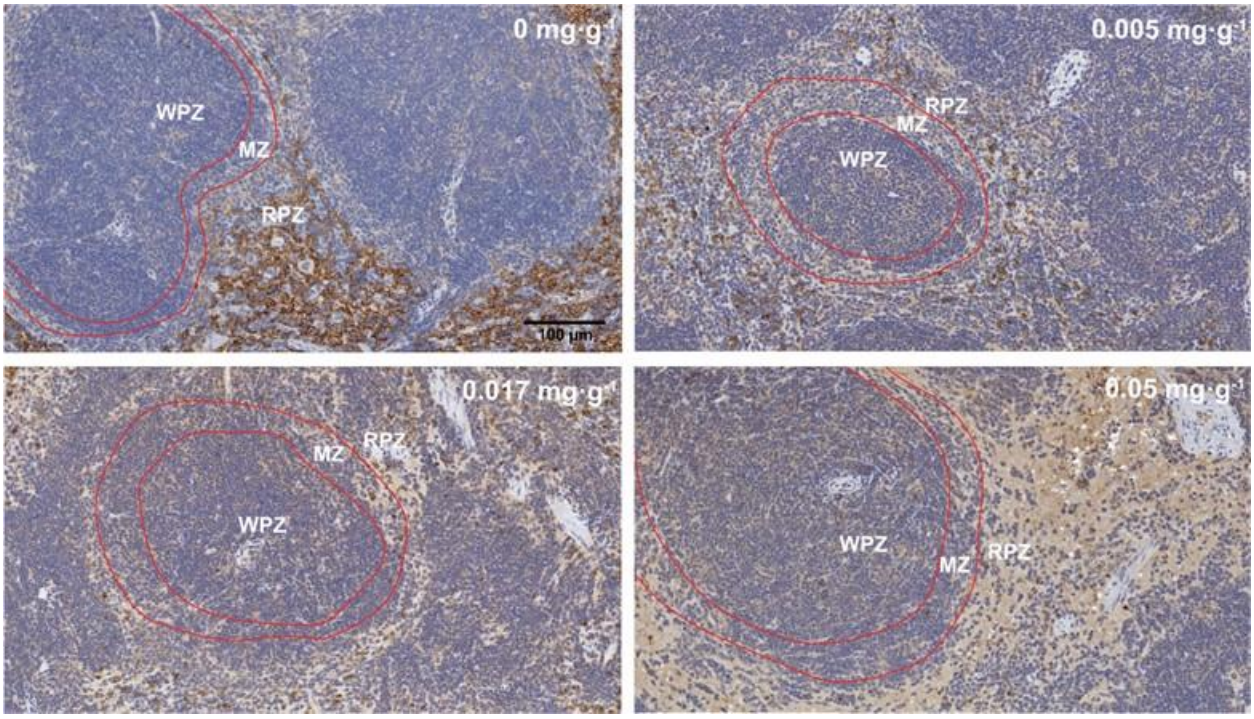

Fig. 4S. 15. Immunohistochemically stained splenic tissue sections with anti-F4/80-HRP and counter stained with hematoxylin from C57BL/6 mice treated with clodonate liposomes 0-0.05mg·g^{-1}. The white-pulp zone (WPZ), marginal zone (MZ) and red-pulp zone (RPZ) can be spatially resolved in the tissue sections. Panels A-D show a similar dose-dependent, successive decrease in the quantity of red-pulp macrophages. This dose-dependent depletion of red-pulp macrophages is consistent with what was seen for CD1 nu/nu mice.

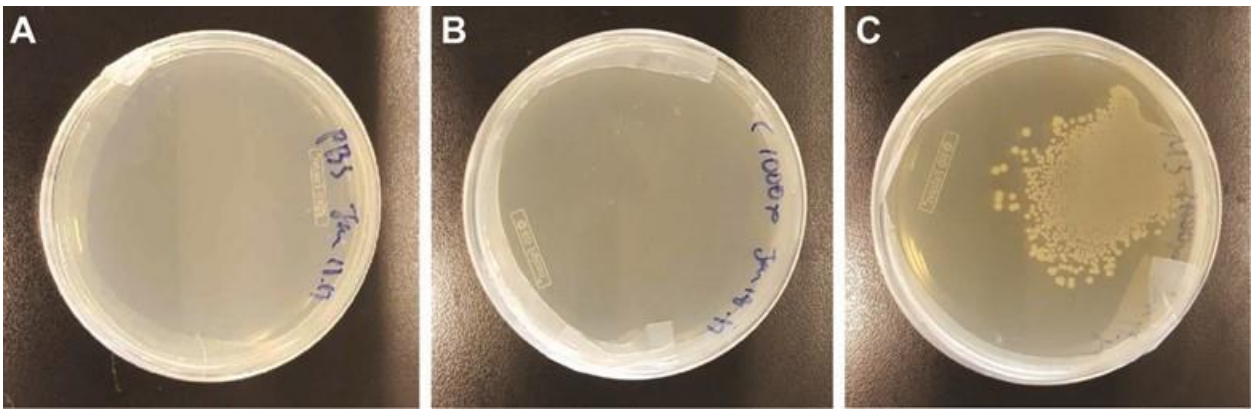

Fig. 4S. 16. To confirm induction of sepsis in C57BL/6 after the cecal ligation and puncture procedure, bacteria cultures were done by plating sterile PBS (A), blood from sterile animals (n=4) (B) and blood isolated from killed septic animals (n=4) and incubating at 37°C for 24h. (C) Bacterial colony growth can be seen in the agar plate in C, confirming induction of sepsis.

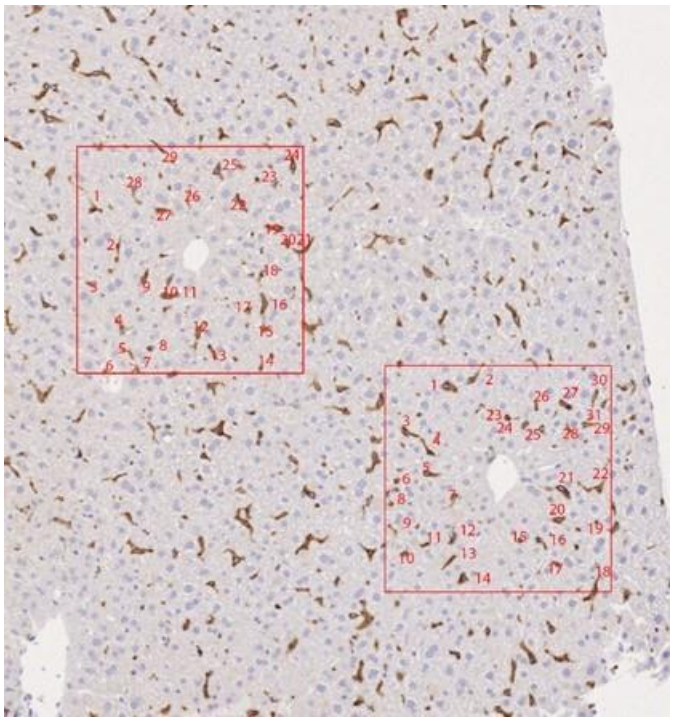

Fig. 4S. 17. CD1 nu/nu hepatic tissue immunohistochemically stained with anti-F4/80 HRP to display Kupffer cells (brownish-red features). The average number of Kupffer cells in hepatic tissue was used to provide a semi-quantitative assessment on the degree of macrophage for a given dose of clodronate liposomes. The number of Kupffer cells in fixed areas centered on either a portal triad or central vein (red box) were counted. The average was computed from three independent areas of each tissue slice.

Chapter 5 - Conclusions and future directions

Summary

Efficient vaccination requires long-lived germinal center reactions to drive antibody-mediated humoral immunity. Antigens must be retained and presented to B cells in lymph node follicles to generate an effective humoral immune response. A proposed strategy is to use engineered nanoparticles to deliver antigens into follicles. However, our understanding of how lymph nodes direct nanoparticle transport and retention is limited. A better understanding of nanoparticle designs and their interactions with lymph nodes can guide the rational/optimal engineering of nanoparticles for optimal immune responses. In my PhD thesis, I divided my objective into three aims: (1) understand how nanoparticle design influences antigen retention and presentation in lymph node follicles, (2) alter the immune cell populations in lymph nodes to enhance nanoparticle delivery, (3) manipulate the immune cell populations in the liver to enhance the systemic delivery into lymph nodes.

In chapter 2, we found that follicular dendritic cell (FDC) networks determine the intra-lymph node follicle fate of these nanoparticles by clearing smaller ones (5-15 nm) within 48 h and retaining larger ones (50-100 nm) for over 5 weeks. The 50-100 nm-sized nanoparticles had 175-fold more delivery of antigen at the FDC dendrites, 5-fold enhanced humoral immune responses of germinal center B cell formation, and 5-fold more antigen specific antibody production over 5-15 nm nanoparticles. Our results show that we can tune humoral immunity by simply changing the antigen delivery carrier size to produce effectiveness of vaccines.

In chapter 3, we assessed the role of type of immune cells called the resident macrophages in the subcapsular sinus on nanovaccine delivery to lymph node follicles. We discovered that SCS

macrophages play a barrier role to prevent nanovaccines from accessing lymph node follicles. This is illustrated by measuring the humoral immune responses after removing or functionally altering these cells in the nanovaccine transport process. We observed up to 60 times more antigen-specific antibody production after suppressing SCS macrophages. The degree of the enhanced antibody production is dependent on the nanovaccine dose and size, formulation, and administration time. These findings suggest that altering transport barriers to enable more nanovaccine delivery to the lymph node follicles for neutralized antibody production is an effective strategy to boost vaccination.

In Chapter 4, we evaluated the role of the resident macrophages in the liver on nanoparticle delivery to lymph nodes and tumours after systemic administration of nanoparticles. After complete removal of liver macrophages, we achieved up to 10 times enhanced lymph node delivery and 50 times improved tumour accumulation in multiple nanoparticle designs and tumour models. We further reduced the dose of macrophage depleting chemicals to precisely remove the macrophages in periportal area of the liver that sequesters most of injected nanoparticles. This strategy allowed us to remove the partial liver macrophage populations but keep an intact immune system that enables to mediate the risk of infection in a sepsis model.

The significance of these researches reveals the mechanism of how our immune systems, especially lymph node physiology mediates nanoparticle vaccine retention and presentation in follicles. This fundamental knowledge provides us critical insights towards engineering design of nanoparticle vaccines and development of strategies to alter lymph node physiology to generate robust vaccination responses.

Future directions

Physicochemical property of nanoparticle impacts in vivo behavior

Nanoparticle physicochemical design mediates biological interaction in vivo. My PhD study highlights the complement system as immune recognition mediators to bridge nanoparticle-conjugated vaccines and long-term humoral immunity. Future work will explore a better understanding of synthetic materials and biological agents (immune complexes, viruses, and bacteria) behaviors in lymph nodes. This provides more detailed guidance of rational nanoparticle design (Fig. 5.1). Future work should focus on building up the correlations among physicochemical design (materials types, sizes, shapes and surface chemistries) of synthetic materials, complement activation, lymph node delivery and follicle retention, germinal center reactions and neutralized antibody production. This will allow us to determine the optimized nanoparticle physicochemical properties to maximize the interaction with complements and lymph node retention that will elicit longer and great humoral immune responses.

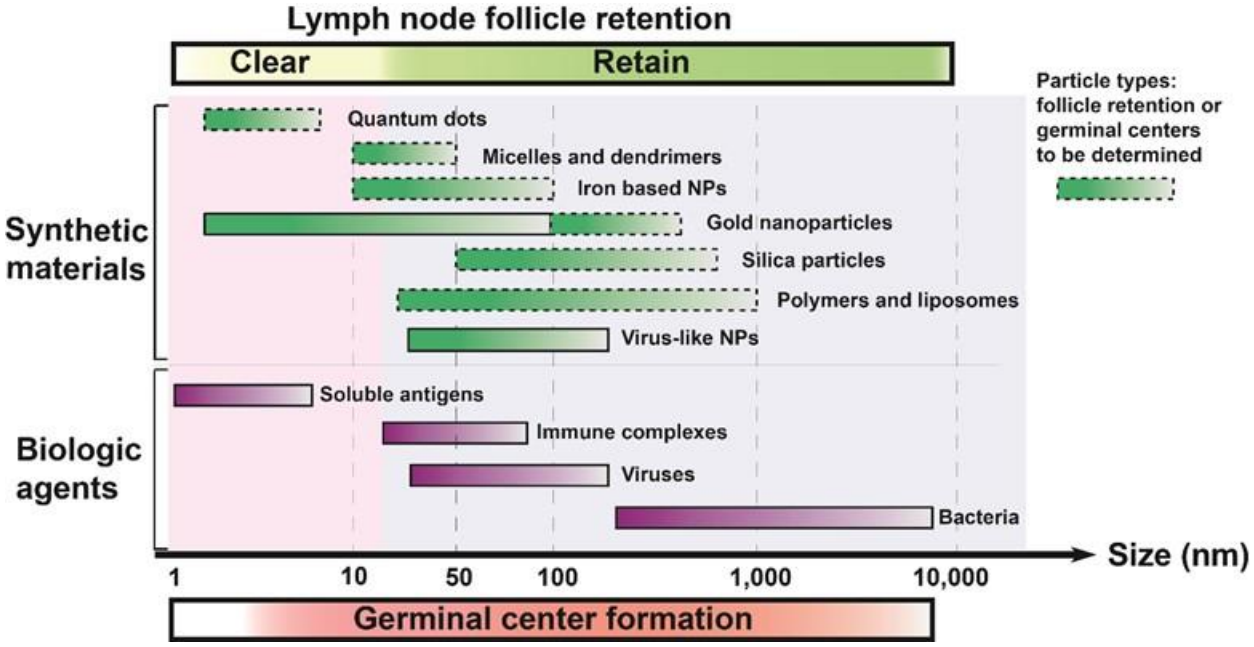

Fig. 5. 1. Physicochemical properties of synthetic materials and biologic agents determine lymph node follicle retention and germinal center reaction for effective vaccine development.

Antigen structure display on nanoparticles

Antigen arrangement and display is essential for clustering B cell receptors and stimulate B cell activation. Structural antigen design can be incorporated into a nanoparticle platform to mimic the pathogen surface pattern and engage with B cell receptor recognition for efficient humoral immune responses. The structural of virus protein antigen can first be determined using X-ray crystallography and cryo-electron microscopy. Computational protein structural design principle can then be utilized to rationally design the antigen system. The computational approach has been demonstrated the capability of designing nanoparticle scaffolds for multivalent presentation of viral glycoprotein antigens with atomic-level accuracy[135]. The advances of nanoparticle-based antigen design is summarized in Fig. 5.2.[136]. These self-assembling protein nanoparticles successfully displayed intact native-like HIV Env trimer, influenza hemagglutinin or prefusion RSV trimers in the predicted structure[57,135,137]. With this level of precisely antigen structure display, we will be able to address the following questions in the future: (1) Does the antigen structure display on a nanoparticle show the same presentation and accessibility compared to antigen structure without a nanoparticle?; (2) What is the optimal antigen density on a nanoparticle to induce the optimized crosslinking of B cell receptors?; and (3) Can we incorporate multiple antigen structures on a single nanoparticle to fully mimic the virus, such as influenza? Addressing the above-mentioned questions will allow us to integrate antigen structure design into the development of the next generation nanoparticle vaccines to against infectious diseases.

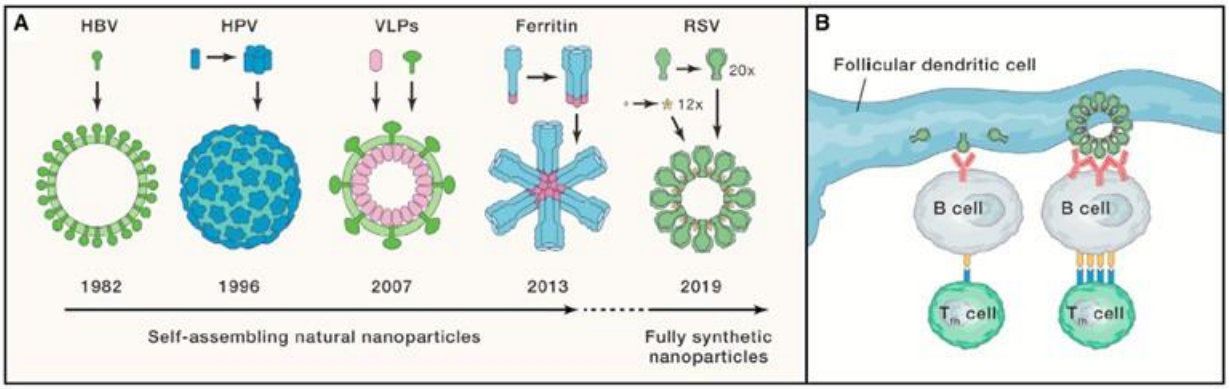

Fig. 5. 2. Antigen structure display on nanoparticle platform for vaccine development[136].

Potential projects:

Project 1: Designing nanoparticle core materials for vaccines

Objective: Identify an optimal nanoparticle core material that demonstrates the highest antigen integration and humoral immune responses.

Rationale: Nanoparticle core materials induce different immunogenicity. It is unclear clear how the different materials impact antigen integration and humoral immune responses.

Significance: Rational nanoparticle core design is essential for development of nanoparticle vaccines.

In this project, I will design and synthesize multiple material types. These will include gold nanoparticles, silica nanoparticles, poly(lactic-co-glycolic acid) (PLGA) polymer nanoparticles, and liposomes. The nanoparticles (1) can be easily synthesized with precise size; (2) are biocompatible, which allows us to track them at the tissue and cellular levels; and (3) can be coated with multiple molecules, which enable them to be combined with antigens and adjuvants. I will then conjugate a model antigen OVA onto these nanoparticle surfaces through chemical reactions. The coating of OVA on the nanoparticle surface is coordinated by a combination of electrostatic adsorption and coordinate bonding. I will characterize their physicochemical properties (e.g.,

hydrodynamic diameters and surface changes) using electron microscopy, dynamic light scattering, and Zetasizer Nano-ZS. I will quantify the amount of OVA antigen integration into the nanoparticle using a protein quantification assay. I will perform the in vitro immunogenicity test with B cells. B cells will be isolated from both male and female mouse lymph nodes (6-8 weeks old mouse) and cultured with nanoparticles in vitro. I hypothesize that the optimal designed nanoparticle should activate the B cells. The activated B cells will be quantified using flow cytometry and the antibody production will be quantified using enzyme-linked immunosorbent assay. In the end I will identify an optimal nanoparticle chemical composition that demonstrates the highest antigen integration and B cell activation that can generate greatest antibody production.

Project 2: Engineering nanoparticles incorporated with toll-like receptor adjuvants

Objective: Identify an optimal surface toll-like receptor (TLR) ligand conjugation that demonstrates the highest humoral immune responses.

Rationale: TLR ligands are efficient adjuvants to be incorporated on nanoparticle surface to induce efficient humoral immune responses.

Significance: Rational nanoparticle surface design with adjuvants is important for development of nanoparticle vaccines.

TLR play central roles in the recognition of pathogen-associated molecular patterns and initiation of B cell immune responses. TLR ligands have become a key component of efficient vaccination due to their adjuvant properties. TLRs in B cells can be divided into two groups: (1) cell surface receptors (such as TLR4) and (2) receptors localized in the endosome of a cell (such as TLR9). In this project, I will be focused on implementing the TLR ligands as adjuvants onto nanoparticles to maximize B cell activation and antibody production. I will conjugate a TLR4 ligand

(monophosphoryl lipid A) or/and a TLR9 ligand (CpG oligodeoxynucleotide) on the nanoparticle surface. The amount of TLR ligands will be quantified by a DNA assay. The antigen OVA will be further conjugated on the nanoparticle. I will test the immunogenicity of these engineered nanoparticles. These studies will identify the dominant pathway (either activation through the cell surface receptors or through the endosome inside the cell) or if it is necessary to incorporate both pathways in nanoparticle design to maximize B cell activation, proliferation, and antibody production. This project will identify the optimal surface adjuvant ligand integration on nanoparticle that demonstrates the highest B cell activation and antibody production.

Project 3: Engineering antigen structure using computational protein design.

Objective: use computational protein structural design principles to rationally design the antigen system.

Rationale: Structural antigen design can be incorporated into a nanoparticle to mimic the pathogen surface pattern.

Significance: Rational antigen structural design can maximize B cell recognition for efficient vaccination.

In this project, I will consider the structure of HIV as a virus model for this proof of concept study. Since envelope glycoprotein gp120 expressed on every surface of HIV viral envelope, I will incorporate the HIV-1 gp120 protein structure on a nanoparticle and determine its structure using X-ray crystallography and cryoelectron microscopy. I will use a computational structure-based design to modify the sequence of the HIV-1 gp120 protein. I will then engineer disulfide bridges onto them and conjugate modified gp120 proteins onto nanoparticles. I expect this synthetic nanoparticle will expose 20-50 copies of modified HIV-1 gp120 protein aligned on the surface.

This engineered surface structure will be designed to maximize antigen density with the repetitive HIV-1 gp120 protein pattern for optimal B cell recognition and activation. I will test the stability of this engineered nanoparticle using mouse serum. I expect that this structural antigen designed nanoparticles will generate B cell activation and antibody production in vitro. I expect this nanoparticle system to be successfully delivered to the lymph node follicles for robust antibody production. This computational approach can be widely used to design and engineer the structural antigen nanoparticles for other pathogens. The result of these studies will be computing designs and engineering antigen structures on nanoparticle cores that demonstrate the maximize B cell recognition and antibody production.

Conclusion & Outlook

Vaccines have protected people for hundreds of years against pathogens and infectious diseases. We do not understand the mechanism how vaccines work nor how our humoral immunity generates specific antibody to neutralize pathogens until 50 years ago. Thanks to recent advances of biology and immunology fields, we can evaluate the role of immune cell populations and test their functions for acquired immune responses that enables us to development more effective vaccines.

A vaccine is made of antigens and adjuvants. Anything that can induce greater immune response in addition to antigen is considered as an adjuvant (from Latin, meaning “to help”). In the equation of vaccine development, greater value of x represents the superior help or adjuvanticity to amplify the antigen-specific immune responses. Designing novel adjuvants with greater values of x enable us to better engineer our immune system and develop successful vaccines for infectious diseases. However, the mechanism of how adjuvant works is still a black box.

$$Vaccine = antigen + adjuvant$$

$$adjuvant = x$$

$$antigen\ + x > antigen\ alone$$

In my thesis, we developed two types of adjuvants: (1) nanoparticles that serve as adjuvants to improve antigen integration and display, and antigen retention and presentation in lymph node follicles for humoral immunity, and (2) pharmacological agents that disrupted the macrophage uptake function can be considered as adjuvants to improve antigen delivery to lymph node follicles. The latter shows the reverse effects of reducing innate immunity and boosting humoral immunity. We term them "reverse adjuvants". The clinical applications of these adjuvants need to be further explored in the future by combining with other commercially available adjuvants and vaccine formulations for specific infectious disease models.

We need vaccines to help us boost our immune system. Vaccines also need help.

References

(1) Rappuoli, R. Vaccines: science, health, longevity, and wealth. *Proceedings of the National Academy of Sciences of the United States of America* **2014**, *111*, 12282.

(2) Rappuoli, R. Rino Rappuoli. *Nat Rev Drug Discov* **2007**, *6*, 694.

(3) Rappuoli, R.; Aderem, A. A 2020 vision for vaccines against HIV, tuberculosis and malaria. *Nature* **2011**, *473*, 463–469.

(4) Rappuoli, R.; Pizza, M.; Del Giudice, G.; Gregorio, E. de. Vaccines, new opportunities for a new society. *Proceedings of the National Academy of Sciences of the United States of America* **2014**, *111*, 12288–12293.

(5) Allen, C. D. C.; Okada, T.; Cyster, J. G. Germinal-center organization and cellular dynamics. *Immunity* **2007**, *27*, 190–202.

(6) Mesin, L.; Ersching, J.; Victora, G. D. Germinal Center B Cell Dynamics. *Immunity* **2016**, *45*, 471–482.

(7) Ols, S.; Yang, L.; Thompson, E. A.; Pushparaj, P.; Tran, K.; Liang, F.; Lin, A.; Eriksson, B.; Karlsson Hedestam, G. B.; Wyatt, R. T.*; et al.* Route of Vaccine Administration Alters Antigen Trafficking but Not Innate or Adaptive Immunity. *Cell Reports* **2020**, *30*, 3964-3971.e7.

(8) Rappuoli, R. Glycoconjugate vaccines: Principles and mechanisms. *Science translational medicine* **2018**, *10*.

(9) Cyster, J. G.; Allen, C. D. C. B Cell Responses: Cell Interaction Dynamics and Decisions. *Cell* **2019**, *177*, 524–540.

(10) Cyster, J. G. B cell follicles and antigen encounters of the third kind. *Nature immunology* **2010**, *11*, 989–996.

(11) Batista, F. D.; Harwood, N. E. The who, how and where of antigen presentation to B cells. *Nature reviews. Immunology* **2009**, *9*, 15–27.

(12) Moore, J. E.; Bertram, C. D. Lymphatic System Flows. *Annual review of fluid mechanics* **2018**, *50*, 459–482.

(13) Ruddle, N. H. Lymphatic vessels and tertiary lymphoid organs. *The Journal of clinical investigation* **2014**, *124*, 953–959.

(14) Wang, Y.; Oliver, G. Current views on the function of the lymphatic vasculature in health and disease. *Genes & development* **2010**, *24*, 2115–2126.

(15) Hawley, A. E.; Davis, S. S.; Illum, L. Targeting of colloids to lymph nodes: influence of lymphatic physiology and colloidal characteristics. *Advanced drug delivery reviews* **1995**, *17*, 129–148.

(16) Maisel, K.; Sasso, M. S.; Potin, L.; Swartz, M. A. Exploiting lymphatic vessels for immunomodulation: Rationale, opportunities, and challenges. *Advanced drug delivery reviews* **2017**, *114*, 43–59.

(17) Willard-Mack, C. L. Normal structure, function, and histology of lymph nodes. *Toxicologic pathology* **2006**, *34*, 409–424.

(18) Osamu Ohtani and Yuko Ohtani. Structure and function of rat lymph nodes. *Arch Histo Cytol* **2008**, *71*, 69–76.

(19) Thierry, G. R.; Gentek, R.; Bajenoff, M. Remodeling of reactive lymph nodes: Dynamics of stromal cells and underlying chemokine signaling. *Immunological Reviews* **2019**, *289*, 42–61.

(20) Swartz, M.A., Hirosue, S., Hubbell, J.A. Engineering Approaches to Immunotherapy. *Science translational medicine* **2012**, *4*, 148rv9.

(21) Hunter, M. C.; Teijeira, A.; Halin, C. T Cell Trafficking through Lymphatic Vessels. *Frontiers in immunology* **2016**, *7*, 613.

(22) Rantakari, P.; Auvinen, K.; Jäppinen, N.; Kapraali, M.; Valtonen, J.; Karikoski, M.; Gerke, H.; Iftakhar-E-Khuda, I.; Keuschnigg, J.; Umemoto, E.*; et al.* The endothelial protein PLVAP in lymphatics controls the entry of lymphocytes and antigens into lymph nodes. *Nature immunology* **2015**, *16*, 386–396.

(23) Hons, M.; Sixt, M. The lymph node filter revealed. *Nature immunology* **2015**, *16*, 338–340.

(24) Roozendaal, R.; Mempel, T. R.; Pitcher, L. A.; Gonzalez, S. F.; Verschoor, A.; Mebius, R. E.; Andrian, U. H. von; Carroll, M. C. Conduits mediate transport of low-molecular-weight antigen to lymph node follicles. *Immunity* **2009**, *30*, 264–276.

(25) Moran, I.; Grootveld, A. K.; Nguyen, A.; Phan, T. G. Subcapsular Sinus Macrophages: The Seat of Innate and Adaptive Memory in Murine Lymph Nodes. *TRENDS in Immunology* **2019**, *40*, 35–48.

(26) Louie, D. A. P.; Liao, S. Lymph Node Subcapsular Sinus Macrophages as the Frontline of Lymphatic Immune Defense. *Frontiers in immunology* **2019**, *10*, 347.

(27) Phan, T. G.; Green, J. A.; Gray, E. E.; Xu, Y.; Cyster, J. G. Immune complex relay by subcapsular sinus macrophages and noncognate B cells drives antibody affinity maturation. *Nature immunology* **2009**, *10*, 786–793.

(28) Phan, T. G.; Grigorova, I.; Okada, T.; Cyster, J. G. Subcapsular encounter and complement-dependent transport of immune complexes by lymph node B cells. *Nature immunology* **2007**, *8*, 992–1000.

(29) Junt, T.; Moseman, E. A.; Iannacone, M.; Massberg, S.; Lang, P. A.; Boes, M.; Fink, K.; Henrickson, S. E.; Shayakhmetov, D. M.; Di Paolo, N. C.*; et al.* Subcapsular sinus macrophages in lymph nodes clear lymph-borne viruses and present them to antiviral B cells. *Nature* **2007**, *450*, 110–114.

(30) Gonzalez, S. F.; Degn, S. E.; Pitcher, L. A.; Woodruff, M.; Heesters, B. A.; Carroll, M. C. Trafficking of B cell antigen in lymph nodes. *Annual review of immunology* **2011**, *29*, 215–233.

(31) Kuka, M.; Iannacone, M. Viral subversion of B cell responses within secondary lymphoid organs. *Nature reviews. Immunology* **2018**, *18*, 255–265.

(32) Carrasco, Y. R.; Batista, F. D. B cells acquire particulate antigen in a macrophage-rich area at the boundary between the follicle and the subcapsular sinus of the lymph node. *Immunity* **2007**, *27*, 160–171.

(33) Bernhard, C. A.; Ried, C.; Kochanek, S.; Brocker, T. CD169+ macrophages are sufficient for priming of CTLs with specificities left out by cross-priming dendritic cells. *Proceedings of the National Academy of Sciences of the United States of America* **2015**, *112*, 5461–5466.

(34) Heesters, B. A.; van der Poel, C. E.; Das, A.; Carroll, M. C. Antigen Presentation to B Cells. *TRENDS in Immunology* **2016**, *37*, 844–854.

(35) Heesters, B. A.; Myers, R. C.; Carroll, M. C. Follicular dendritic cells: dynamic antigen libraries. *Nature reviews. Immunology* **2014**, *14*, 495–504.

(36) Bachmann, M. F.; Jennings, G. T. Vaccine delivery: a matter of size, geometry, kinetics and molecular patterns. *Nature reviews. Immunology* **2010**, *10*, 787–796.

(37) Allen, C. D. C.; Cyster, J. G. Follicular dendritic cell networks of primary follicles and germinal centers: phenotype and function. *Seminars in immunology* **2008**, *20*, 14–25.

(38) Mitchell, J.; Abbot, A. Ultrastructure of the antigen-retaining reticulum of lymph node follicles as shown by high-resolution autoradiography. *Nature* **1965**, *208*, 500–502.

(39) Roozendall, R.; Carroll, M. C. Complement receptors CD21 and CD35 in humoral immunity. *Immunological Reviews* **2007**, *2019*, 157–166.

(40) Kosco-Vilbois, M. H. Are follicular dendritic cells really good for nothing? *Nature reviews. Immunology* **2003**, *3*, 764–769.

(41) Szakal, A. K.; Kosco, M. H.; Tew, J. G. Microanatomy of Lymphoid Tissue During Humoral Immune Responses: Structure Function Relationships. *Ann. Rev. lmmunol.* **1989**, *7*, 91–109.

(42) Rodda, L. B.; Lu, E.; Bennett, M. L.; Sokol, C. L.; Wang, X.; Luther, S. A.; Barres, B. A.; Luster, A. D.; Ye, C. J.; Cyster, J. G. Single-Cell RNA Sequencing of Lymph Node Stromal Cells Reveals Niche-Associated Heterogeneity. *Immunity* **2018**, *48*, 1014-1028.e6.

(43) Wang, X.; Cho, B.; Suzuki, K.; Xu, Y.; Green, J. A.; An, J.; Cyster, J. G. Follicular dendritic cells help establish follicle identity and promote B cell retention in germinal centers. *The Journal of experimental medicine* **2011**, *208*, 2497–2510.

(44) Tew, J. G.; Wu, J.; Fakher, M.; Szakal, A. K.; Qin, D. Follicular dendritic cells, beyond the necessity of T-cell help. *TRENDS in Immunology* **2001**, *22*, 361–367.

(45) Tew, J. G.; Wu; Jiuhua; Qin, D.; Helm, S.; Burton, G. F.; Szakal, A. K. Follicular dendritic cells and presentation of antigen and costimulatory signals to B cells. *Immunological Reviews* **1997**, *156*.

(46) Victora, G. D.; Nussenzweig, M. C. Germinal centers. *Annual review of immunology* **2012**, *30*, 429–457.

(47) Gonzalez, S. F.; Lukacs-Kornek, V.; Kuligowski, M. P.; Pitcher, L. A.; Degn, S. E.; Kim, Y.-A.; Cloninger, M. J.; Martinez-Pomares, L.; Gordon, S.; Turley, S. J.*; et al.* Capture of influenza by medullary dendritic cells via SIGN-R1 is essential for humoral immunity in draining lymph nodes. *Nature immunology* **2010**, *11*, 427–434.

(48) Heinen, E.; Braun, M.; Coulie, P. G.; van Snick, J.; Moeremans, M.; Cormann, N.; Kinet-Denoël, C.; Simar, L. J. Transfer of immune complexes from lymphocytes to follicular dendritic cells. *European journal of immunology* **1986**, *16*, 167–172.

(49) Mueller, S. N.; Tian, S.; DeSimone, J. M. Rapid and Persistent Delivery of Antigen by Lymph Node Targeting PRINT Nanoparticle Vaccine Carrier To Promote Humoral Immunity. *Molecular pharmaceutics* **2015**, *12*, 1356–1365.

(50) van den Elsen, J. M. H.; Isenman, D. E. A crystal structure of the complex between human complement receptor 2 and its ligand C3d. *Science* **2011**, *332*, 608–611.

(51) Kratzer, R.; Mauvais, F.-X.; Burgevin, A.; Barilleau, É.; van Endert, P. Fusion proteins for versatile antigen responses differential capacity to prime immune targeting to cell surface receptors reveal differential capacity to prime immune responses. *J. Immunol* **2010**, *184*, 6855–6864.

(52) Taylor, P. R.; Zamze, S.; Stillion, R. J.; Wong, S.Y.C.; Gordon; S.; Martinez-Pomares, L. Development of a specific system for targeting protein to metallophilic macrophages. *Proceedings of the National Academy of Sciences of the United States of America* **2004**, *101*, 1963–1968.

(53) Heesters, B. A.; Chatterjee, P.; Kim, Y.-A.; Gonzalez, S. F.; Kuligowski, M. P.; Kirchhausen, T.; Carroll, M. C. Endocytosis and recycling of immune complexes by follicular dendritic cells enhances B cell antigen binding and activation. *Immunity* **2013**, *38*, 1164–1175.

(54) Rappuoli, R.; Gregorio, E. de; Costantino, P. On the mechanism of conjugate vaccines. *Proceedings of the National Academy of Sciences of the United States of America* **2019**, *116*, 193–198.

(55) Tokatlian, T.; Read, B. J.; Jones, C. A.; Kulp, D. W.; Menis, S.; Chang, J. Y. H.; Steichen, J. M.; Kumari, S.; Allen, J. D.; Dane, E. L.*; et al.* Innate immune recognition of glycans targets HIV nanoparticle immunogens to germinal centers. *Science (New York, N.Y.)* [Online early access]. DOI: 10.1126/science.aat9120.

(56) Wilson, J. T. A sweeter approach to vaccine design. *Science (New York, N.Y.)* **2019**, *363*, 584–585.

(57) Marcandalli, J.; Fiala, B.; Ols, S.; Perotti, M.; van der Schueren, W. de; Snijder, J.; Hodge, E.; Benhaim, M.; Ravichandran, R.; Carter, L.*; et al.* Induction of Potent Neutralizing Antibody Responses by a Designed Protein Nanoparticle Vaccine for Respiratory Syncytial Virus. *Cell* **2019**, *176*, 1420-1431.e17.

(58) Irvine, D. J.; Hanson, M. C.; Rakhra, K.; Tokatlian, T. Synthetic Nanoparticles for Vaccines and Immunotherapy. *Chemical reviews* **2015**, *115*, 11109–11146.

(59) Irvine, D. J.; Read, B. J. Shaping humoral immunity to vaccines through antigen-displaying nanoparticles. *Current opinion in immunology* **2020**, *65*, 1–6.

(60) Hotaling, N. A.; Tang, L.; Irvine, D. J.; Babensee, J. E. Biomaterial Strategies for Immunomodulation. *Annual review of biomedical engineering* **2015**, *17*, 317–349.

(61) Moon, J. J.; Huang, B.; Irvine, D. J. Engineering nano- and microparticles to tune immunity. *Advanced materials (Deerfield Beach, Fla.)* **2012**, *24*, 3724–3746.

(62) Reddy, S. T.; Rehor, A.; Schmoekel, H. G.; Hubbell, J. A.; Swartz, M. A. In vivo targeting of dendritic cells in lymph nodes with poly(propylene sulfide) nanoparticles. *Journal of controlled release : official journal of the Controlled Release Society* **2006**, *112*, 26–34.

(63) Reynoso, G. V.; Weisberg, A. S.; Shannon, J. P.; McManus, D. T.; Shores, L.; Americo, J. L.; Stan, R. V.; Yewdell, J. W.; Hickman, H. D. Lymph node conduits transport virions for rapid T cell activation. *Nat. Immunol.* **2019**, *20*, 602–612.

(64) Irvine, D. J.; Swartz, M. A.; Szeto, G. L. Engineering synthetic vaccines using cues from natural immunity. *Nature materials* **2013**, *12*, 978–990.

(65) Reddy, S. T.; Swartz, M. A.; Hubbell, J. A. Targeting dendritic cells with biomaterials: developing the next generation of vaccines. *TRENDS in Immunology* **2006**, *27*, 573–579.

(66) Carroll, M. C. The role of complement and complement receptors in induction and regulation of immunity. *Annual review of immunology* **1998**, *16*, 545–568.

(67) Dempsey, P.W.; Allison, M.E.D.; Akkaraju, S.; Goodnow, C.C.; Fearon, D.T. C3d of complement as a molecular adjuvant, bridging innate and acquired immunity. *Science (New York, N.Y.)* **1996**.

(68) Mattsson, J.; Yrlid, U.; Stensson, A.; Schön, K.; Karlsson, M. C. I.; Ravetch, J. V.; Lycke, N. Y. Complement activation and complement receptors on follicular dendritic cells are critical for the function of a targeted adjuvant. *Journal of immunology (Baltimore, Md. : 1950)* **2011**, *187*, 3641–3652.

(69) Reddy, S. T.; van der Vlies, A. J.; Simeoni, E.; Angeli, V.; Randolph, G. J.; O'Neil, C. P.; Lee, L. K.; Swartz, M. A.; Hubbell, J. A. Exploiting lymphatic transport and complement activation in nanoparticle vaccines. *Nature biotechnology* **2007**, *25*, 1159–1164.

(70) Shen, L.; Tenzer, S.; Storck, W.; Hobernik, D.; Raker, V. K.; Fischer, K.; Decker, S.; Dzionek, A.; Krauthäuser, S.; Diken, M.*; et al.* Protein corona-mediated targeting of nanocarriers to B cells allows redirection of allergic immune responses. *The Journal of allergy and clinical immunology* [Online early access]. DOI: 10.1016/j.jaci.2017.08.049.

(71) Quach, Q. H.; Ang, S. K.; Chu, J.-H. J.; Kah, J. C. Y. Size-dependent neutralizing activity of gold nanoparticle-based subunit vaccine against dengue virus. *Acta biomaterialia* **2018**, *78*, 224–235.

(72) Cantisani, R.; Pezzicoli, A.; Cioncada, R.; Malzone, C.; Gregorio, E. de; D'Oro, U.; Piccioli, D. Vaccine adjuvant MF59 promotes retention of unprocessed antigen in lymph node macrophage compartments and follicular dendritic cells. *Journal of immunology (Baltimore, Md. : 1950)* **2015**, *194*, 1717–1725.

(73) Quach, Q. H.; Kah, J. C. Complement activation by gold nanoparticles passivated with polyelectrolyte ligands. *RSC Adv.* **2018**, *8*, 6616–6619.

(74) Lazarovits, J.; Sindhwani, S.; Tavares, A. J.; Zhang, Y.; Song, F.; Audet, J.; Krieger, J. R.; Syed, A. M.; Stordy, B.; Chan, W. C. W. Supervised Learning and Mass Spectrometry Predicts the in Vivo Fate of Nanomaterials. *ACS nano* **2019**, *13*, 8023–8034.

(75) Kasturi, S. P.; Skountzou, I.; Albrecht, R. A.; Koutsonanos, D.; Hua, T.; Nakaya, H. I.; Ravindran, R.; Stewart, S.; Alam, M.; Kwissa, M.*; et al.* Programming the magnitude and persistence of antibody responses with innate immunity. *Nature* **2011**, *470*, 543–547.

(76) McHeyzer-Williams, M.; Okitsu, S.; Wang, N.; McHeyzer-Williams, L. Molecular programming of B cell memory. *Nat Rev Immunol* **2012**, *12*, 24–34.

(77) Chou, L. Y. T.; Zagorovsky, K.; Chan, W. C. W. DNA assembly of nanoparticle superstructures for controlled biological delivery and elimination. *Nature nanotechnology* **2014**, *9*, 148–155.

(78) Frens, G. Controlled nucleation for the regulation of the particle sie in monodisperse gold suspensions. *Nature Physical Science* **1972**, *241*.

(79) Perrault, S. D.; Chan, W. C. W. Synthesis and surface modification of highly monodispersed, spherical gold nanoparticles of 50-200 nm. *Journal of the American Chemical Society* **2009**, *131*, 17042–17043.

(80) Schneider, C. A.; Rasband, W. S.; Eliceiri, K. W. NIH Image to ImageJ: 25 years of image analysis. *Nat Methods* **2012**, *9*, 671–675.

(81) Syed, A. M.; Sindhwani, S.; Wilhelm, S.; Kingston, B. R.; Lee, D. S. W.; Gommerman, J. L.; Chan, W. C. W. Three-Dimensional Imaging of Transparent Tissues via Metal Nanoparticle Labeling. *Journal of the American Chemical Society* **2017**, *139*, 9961–9971.

(82) Sindhwani, S.; Syed, A. M.; Wilhelm, S.; Glancy, D. R.; Chen, Y. Y.; Dobosz, M.; Chan, W. C. W. Three-Dimensional Optical Mapping of Nanoparticle Distribution in Intact Tissues. *ACS nano* **2016**, *10*, 5468–5478.

(83) Lee, I.-H.; Kwon, H.-K.; An, S.; Kim, D.; Kim, S.; Yu, M. K.; Lee, J.-H.; Lee, T.-S.; Im, S.-H.; Jon, S. Imageable antigen-presenting gold nanoparticle vaccines for effective cancer immunotherapy in vivo. *Angewandte Chemie (International ed. in English)* **2012**, *51*, 8800–8805.

(84) Niikura, K.; Matsunaga, T.; Suzuki, T.; Kobayashi, S.; Yamaguchi, H.; Orba, Y.; Kawaguchi, A.; Hasegawa, H.; Kajino, K.; Ninomiya, T.*; et al.* Gold nanoparticles as a vaccine platform: influence of size and shape on immunological responses in vitro and in vivo. *ACS nano* **2013**, *7*, 3926–3938.

(85) Wei, M.; Chen, N.; Li, J.; Yin, M.; Le Liang; He, Y.; Song, H.; Fan, C.; Huang, Q. Polyvalent immunostimulatory nanoagents with self-assembled CpG oligonucleotide-conjugated gold nanoparticles. *Angewandte Chemie (International ed. in English)* **2012**, *51*, 1202–1206.

(86) Lazarovits, J.; Chen, Y. Y.; Song, F.; Ngo, W.; Tavares, A. J.; Zhang, Y.-N.; Audet, J.; Tang, B.; Lin, Q.; Cruz Tleugabulova, M.*; et al.* Synthesis of Patient-Specific Nanomaterials. *Nano letters* [Online early access]. DOI: 10.1021/acs.nanolett.8b03434.

(87) Li, X.; Wang, X.; Ito, A. Tailoring inorganic nanoadjuvants towards next-generation vaccines. *Chemical Society reviews* **2018**, *47*, 4954–4980.

(88) Rickert, R.C.; Rajewsky, K.; Roes, J. Impairment of T-cell-dependent B-cell responses and B-l cell development in CD19-deficient mice development in CD19-deficient mice. *Nature* **1995**, 352–355.

(89) Carroll, M. C. CD21/CD35 in B cell activation. *Seminars in immunology* **1998**, *10*, 279–286.

(90) Sun, X.; Stefanetti, G.; Berti, F.; Kasper, D. L. Polysaccharide structure dictates mechanism of adaptive immune response to glycoconjugate vaccines. *Proceedings of the National Academy of Sciences of the United States of America* **2019**, *116*, 193–198.

(91) Silva, N. S. de; Klein, U. Dynamics of B cells in germinal centres. *Nature reviews. Immunology* **2015**, *15*, 137–148.

(92) Iannacone, M.; Moseman, E. A.; Tonti, E.; Bosurgi, L.; Junt, T.; Henrickson, S. E.; Whelan, S. P.; Guidotti, L. G.; Andrian, U. H. von. Subcapsular sinus macrophages prevent CNS invasion on peripheral infection with a neurotropic virus. *Nature* **2010**, *465*.

(93) Delemarre, F. G.A.; Kors, N.; van Rooijen, N. The in situ immune response in popliteal lymph nodes of mice after macrophage depletion. Differential effects of macrophages on thymus-dependent and thymus-independent Immune responses. *Immunobiology* **1990**, *180*, 395–404.

(94) Tonti, E.; Jiménez de Oya, N.; Galliverti, G.; Moseman, E. A.; Di Lucia, P.; Amabile, A.; Sammicheli, S.; Giovanni, M. de; Sironi, L.; Chevrier, N.*; et al.* Bisphosphonates target B cells to enhance humoral immune responses. *Cell Reports* **2013**, *5*, 323–330.

(95) Farrell, H. E.; Davis-Poynter, N.; Bruce, K.; Lawler, C.; Dolken, L.; Mach, M.; Stevenson, P. G. Lymph node macrophages restrict murine cytomegalovirus dissemination. *Journal of Virology* **2015**, *89*.

(96) Pucci, F.; Garris, C.; Lai, C. P.; Newton, A.; Pfirschke, C.; Engblom, C.; Alvarez, D.; Sprachman, M.; Evavold, C.; Magnuson, A.*; et al.* SCS macrophages suppress melanoma by restricting tumor-derived vesicle-B cell interactions. *Science (New York, N.Y.)* **2016**, *352*, 242–246.

(97) Delemarre, F.G.A.; Kors, N.; Kraal, G.; van Rooijen, N. Repopulation of macrophages in popliteal lymph nodes of mice after liposome-mediated depletion. *Journal of Leukocyte Biology* **1990**, *47*.

(98) Oussoren, C.; Velinova, M.; Scherphof, G.; van der Want, J. J.; van Rooijen, N.; Storm, G. Lymphatic uptake and biodistribution of liposomes after subcutaneous injection IV. Fate of liposomes in regional lymph nodes. *Biochimica et Biophysica Acta* **1998**, *1370*, 259–272.

(99) van Rooijen, N.; Sanders, A. Elimination, blocking, and activation of macrophages: three of a kind? *Journal of Leukocyte Biology* **1997**, *62*, 702–709.

(100) Zhang, Y.-N.; Lazarovits, J.; Poon, W.; Ouyang, B.; Nguyen, L. N. M.; Kingston, B. R.; Chan, W. C. W. Nanoparticle Size Influences Antigen Retention and Presentation in Lymph Node Follicles for Humoral Immunity. *Nano letters* **2019**, *19*, 7226–7235.

(101) Zhang, Y.-N.; Poon, W.; Tavares, A. J.; McGilvray, I. D.; Chan, W. C. W. Nanoparticle-liver interactions: Cellular uptake and hepatobiliary elimination. *Journal of controlled release : official journal of the Controlled Release Society* **2016**, *240*, 332–348.

(102) Diagaradjane, P.; Deorukhkar, A.; Gelovani, J. G.; Maru, D. M.; Krishnan, S. Gadolinium chloride augments tumor-specific imaging of targeted quantum dots in vivo. *ACS nano* **2010**, *4*, 4131–4141.

(103) Fowler, E. F.; Thomson, A. W. Effect of carrageenan on activity of the mononuclear phagocyte system in the mouse. *Br. J. Exp. Path.* **1978**, *59*, 213–219.

(104) Nicklin, S.; Atkinson, H.; Miller, K. Iota-carrageenan induced reaginic antibody production in the rat-I. Characterisation and kinetics of the response. *Int J Immunopharmacol.* **1985**, *7*, 677–685.

(105) Bradfield, J.W.B.; Souhami, R. L.; Addison, I. E. The Mechanism of the Adjuvant Effect of Dextran Sulphate. *Immunology* **1974**, *26*, 383–392.

(106) Kamochi, M.; Ogata, M.; Yoshida, S.; Matsumoto, T.; Kubota, E.; Mizuguchi, Y.; Shigematsu, A. Dextran sulphate enhancement of lipopolysaccharide-induced tumour necrosis factor-α production by murine peritoneal macrophages: Correlation with macrophage blockade. *FEMS Immunol Med Microbiol.* **1993**, *7*, 153–160.

(107) Rüttinger, D.; Vollmar, B.; Wanner, G. A.; Messmer, K. In vivo assessment of hepatic alterations following gadolinium chloride-induced Kupffer cell blockade. *Journal of Hepatology* **1996**, *25*, 960–967.

(108) Rappuoli, R. Bridging the knowledge gaps in vaccine design. *Nature biotechnology* **2007**, *25*, 1361–1366.

(109) Delany, I.; Rappuoli, R.; Gregorio, E. de. Vaccines for the 21st century. *EMBO molecular medicine* **2014**, *6*, 708–720.

(110) Del Giudice, G.; Podda, A.; Rappuoli, R. What are the limits of adjuvanticity? *Vaccine* **2001**, *20*, S38-41.

(111) Reed, S. G.; Orr, M. T.; Fox, C. B. Key roles of adjuvants in modern vaccines. *Nature medicine* **2013**, *19*, 1597–1608.

(112) Charles River. Research models: C57BL/6 mice. Available at www.criver.com **2012**.

(113) Asano, K.; Nabeyama, A.; Miyake, Y.; Qiu, C.-H.; Kurita, A.; Tomura, M.; Kanagawa, O.; Fujii, S.-i.; Tanaka, M. CD169-positive macrophages dominate antitumor immunity by crosspresenting dead cell-associated antigens. *Immunity* **2011**, *34*, 85–95.

(114) Barral, P.; Polzella, P.; Bruckbauer, A.; van Rooijen, N.; Besra, G. S.; Cerundolo, V.; Batista, F. D. CD169(+) macrophages present lipid antigens to mediate early activation of iNKT cells in lymph nodes. *Nature immunology* **2010**, *11*, 303–312.

(115) Moyer, T. J.; Zmolek, A. C.; Irvine, D. J. Beyond antigens and adjuvants: formulating future vaccines. *The Journal of clinical investigation* **2016**, *126*, 799–808.

(116) Pulendran, B.; Ahmed, R. Immunological mechanisms of vaccination. *Nature immunology* **2011**, *12*, 509–517.

(117) Coffman, R. L.; Sher, A.; Seder, R. A. Vaccine adjuvants: putting innate immunity to work. *Immunity* **2010**, *33*, 492–503.

(118) Mbow, M. L.; Gregorio, E. de; Valiante, N. M.; Rappuoli, R. New adjuvants for human vaccines. *Current opinion in immunology* **2010**, *22*, 411–416.

(119) Moyer, T. J.; Kato, Y.; Abraham, W.; Chang, J. Y. H.; Kulp, D. W.; Watson, N.; Turner, H. L.; Menis, S.; Abbott, R. K.; Bhiman, J. N.*; et al.* Engineered immunogen binding to alum adjuvant enhances humoral immunity. *Nature medicine* [Online early access]. DOI: 10.1038/s41591-020-0753-3.

(120) Wilhelm, S.; Tavares, A. J.; Dai, Q.; Ohta, S.; Audet, J.; Dvorak, H. F.; Chan, W.C.W. Analysis of nanoparticle delivery to tumours. *Nature Reviews Materials* **2006**, *1*, 1–12.

(121) Tsoi, K. M.; MacParland, S. A.; Ma, X.-Z.; Spetzler, V. N.; Echeverri, J.; Ouyang, B.; Fadel, S. M.; Sykes, E. A.; Goldaracena, N.; Kaths, J. M.*; et al.* Mechanism of hard-nanomaterial clearance by the liver. *Nature materials* **2016**, *15*, 1212–1221.

(122) Walkey, C. D.; Olsen, J. B.; Guo, H.; Emili, A.; Chan, W. C. W. Nanoparticle size and surface chemistry determine serum protein adsorption and macrophage uptake. *Journal of the American Chemical Society* **2012**, *134*, 2139–2147.

(123) Dai, Q.; Walkey, C.; Chan, W. C. W. Polyethylene glycol backfilling mitigates the negative impact of the protein corona on nanoparticle cell targeting. *Angewandte Chemie (International ed. in English)* **2014**, *53*, 5093–5096.

(124) Renaud, G.; Hamilton, R. L.; Havel, R. J. Hepatic metabolism of colloidal gold-low-density lipoprotein complexes in the rat: evidence for bulk excretion of lysosomal contents into bile. *Hepatology* **1989**, *9*, 380–392.

(125) Sarkar, S.; Khan, M. F.; Kaphalia, B. S.; Ansari, G. A. Methyl Palmitate Inhibits Lipopolysaccharide-Stimulated Phagocytic Activity of Rat Peritoneal Macrophages. *J Biochem Mol Toxicol* **2006**, *20*, 302–308.

(126) Cai, P.; Kaphalia, B. S.; Ansari, G. A. S. Methyl palmitate: inhibitor of phagocytosis in primary rat Kupffer cells. *Toxicology* **2005**, *210*, 197–204.

(127) Gemsa; D.; Seitz, M.; Kramer, W.; Til, l. G.; Resch, K. The effects of phagocytosis, dextran sulfate, and cell damage on PGE1 sensitivity and PGE1 production of macrophages. *J Immunol.* **1978**, *120*, 1187–1194.

(128) Magaña, I. B.; Yendluri, R. B.; Adhikari, P.; Goodrich, G. P.; Schwartz, J. A.; Sherer, E. A.; O'Neal, D. P. Suppression of the reticuloendothelial system using λ-carrageenan to prolong the circulation of gold nanoparticles. *Therapeutic delivery* **2015**, *6*, 777–783.

(129) Ohara, Y.; Oda, T.; Yamada, K.; Hashimoto, S.; Akashi, Y.; Miyamoto, R.; Kobayashi, A.; Fukunaga, K.; Sasaki, R.; Ohkohchi, N. Effective delivery of chemotherapeutic nanoparticles by depleting host Kupffer cells. *International journal of cancer* **2012**, *131*, 2402–2410.

(130) van Rooijen, N.; Hendrikx, E. Liposomes for Specific Depletion of Macrophages from Organs and Tissues. *Methods Mol. Biol.* **2010**, *605*, 189–203.

(131) Sykes, E. A.; Dai, Q.; Sarsons, C. D.; Chen, J.; Rocheleau, J. V.; Hwang, D. M.; Zheng, G.; Cramb, D. T.; Rinker, K. D.; Chan, W. C. W. Tailoring nanoparticle designs to target cancer based on tumor pathophysiology. *Proceedings of the National Academy of Sciences of the United States of America* **2016**, *113*, E1142-51.

(132) Radi, Z. A.; Koza-Taylor, P. H.; Bell, R. R.; Obert, L. A.; Runnels, H. A.; Beebe, J. S.; Lawton, M. P.; Sadis, S. Increased serum enzyme levels associated with kupffer cell reduction with no signs of hepatic or skeletal muscle injury. *The American journal of pathology* **2011**, *179*, 240–247.

(133) Williams, M. D.; Braun, L. A.; Cooper, L. M.; Johnston, J.; Weiss, R. V.; Qualy, R. L.; Linde-Zwirble, W. Hospitalized cancer patients with severe sepsis: analysis of incidence, mortality, and associated costs of care. *Crit Care.* **2004**, *8*, R291-8.

(134) Callery, M. P.; Kamei, T.; Flye, M. W. Callery, 1990, Arch. Surg., Kupffer cell blockade increases mortality during intra-abdominal sepsis despite improving systemic immunity. *Arch Surg.* **1990**, *125*, 36–40.

(135) Antanasijevic, A.; Ueda, G.; Brouwer, P. J. M.; Copps, J.; Huang, D.; Allen, J. D.; Cottrell, C. A.; Yasmeen, A.; Sewall, L. M.; Bontjer, I.*; et al. Structural and functional evaluation of de novo- designed, two-component nanoparticle carriers for HIV Env trimer immunogens* 10; bioRxiv, 2020.

(136) Rappuoli, R.; Serruto, D. Self-Assembling Nanoparticles Usher in a New Era of Vaccine Design. *Cell* **2019**, *176*, 1245–1247.

(137) He, L.; Val, N. de; Morris, C. D.; Vora, N.; Thinnes, T. C.; Kong, L.; Azadnia, P.; Sok, D.; Zhou, B.; Burton, D. R.*; et al.* Presenting native-like trimeric HIV-1 antigens with self-assembling nanoparticles. *Nature communications* **2016**, *7*, 12041.

Chapter 6 - Curriculum Vitae

Yinan Zhang

Email: yinanzhang.zhang@mail.utoronto.ca
Tel: 647-985-0120
Address: 116 Granby St. Toronto, ON, M5B 1J1, Canada

Education

- **09/2014 - 7/2020:** Ph.D candidate, Institute of Biomaterials and Biomedical Engineering, University of Toronto, Toronto, Ontario, Canada. Thesis title: "Towards understanding nanoparticle interaction with lymph node for humoral immunity"
  Supervisor: Prof. W.C.W. Chan
- **01/2008 - 12/2010:** MASc., Mechanical Engineering, Concordia University, Montreal, Quebec, Canada. Thesis title: "Investigation of the equilibrium Mg-Zn-Ca system using diffusion couples and key alloys"
  Supervisors: Profs. M. Medraj and P. Chartrand
- **09/2003 - 07/2007:** BSc. (highest thesis honor), Material Science and Engineering, Beijing University of Technology, Beijing, China. Thesis title: "Effects of the addition of Nd element in the Mg-6Al-xSr alloys on the microstructures and mechanical properties"
  Supervisors: Profs. Y.F. Wu and W.B. Du
- **09/2000 - 07/2003:** High School Diploma, High School Affiliated to Renmin University of China, Beijing, China

Research Experience

- **Nanotechnology, biomedical science and immunoengineering**
  - **09/2014 - 7/2020:** Research Assistant (RA), Project: "Towards understanding how lymph nodes process nanoparticle vaccines for humoral immunity"
    Integrated Nanotechnology & Biomedical Sciences Laboratory
    Institute of Biomaterials and Biomedical Engineering, University of Toronto, Toronto, ON, Canada
    Supervisors: Prof. W.C.W. Chan
- **Biomaterials and tissue engineering**
  - **02/2014 - 08/2014:** RA., Project: "Development of an elastic and adhesive blood-resistance material for surgical sealant"
    RA., Project: "Development of the rapid photopolymer elastin like peptides for tissue engineering application"
    Center for Biomedical Engineering, Department of Medicine, Brigham and Women's Hospital, Harvard Medical School
    Harvard-MIT Division of Health Sciences and Technology, MIT
    Program Sponsor: Massachusetts General Hospital, Cambridge, MA, USA
    Supervisor: Profs. N. Annabi and A. Khademhosseini
  - **01/2011 - 01/2014:** RA., Project: "Development of Mg-based matallic glassy material for biocompatible implants"
    Concordia University and McGill University, Montreal, QC, Canada
    Supervisors: Profs. M. Medraj and Z. Altounian

- **Aerospace**
  - **04/2010 - 02/2014**: RA., Project: "Develop direct laser deposition (DLD) process parameters and perform evaluation of mechanical properties for a repair of engine components manufactured from Inconel 718 and Waspaloy"
    RA., Project: "Friction stir manufacturing of Al-based metal matrix composites"
    National Research Council Canada - Aerospace, Montreal, QC, Canada
    Supervisor: Dr. X. Cao
- **Structural Materials**
  - **01/2011 - 02/2014**: RA., Project: "Development of the advanced Mg- and Al-based alloys for automotive applications"
    Supported by General Motors and NSERC. Collaboration with Ecole Polytechnique Montreal
    Mechanical Engineering, Concordia University, Montreal, QC, Canada
    Supervisor: Prof. M. Medraj
  - **01/2008 - 12/2010**: RA., Project: "Investigation of the equilibrium Mg-Zn-Ca system using diffusion couples and key alloys"
    Supported by General Motors and NSERC. Mechanical Engineering, Concordia University, Montreal, QC, Canada
    Supervisors: Profs. M. Medraj and P. Chartrand
  - **09/2006 - 12/2007**: RA., Project: "Effects of the addition of Nd element in the Mg-6Al-xSr alloys on the microstructures and mechanical properties"
    Material Science and Engineering, Beijing University of Technology, Beijing, China
    Supervisors: Profs. Y.F. Wu and W.B. Du
  - **02/2006 - 07/2006**: RA., Project: "Investigation of nano-grained materials and microstructures using spark plasma sintering technique and transmission electron microscope"
    Material Science and Engineering, Beijing University of Technology, Beijing, China
    Supervisor: Prof. X.Y. Song

Honors and Awards

- **2019-2020:** Doctoral Completion Awards at the Institute of Biomaterials and Biomedical Engineering (IBBME) of University of Toronto, ON, Canada ($3,300)
- **2019:** The UofT most understandable scientist as the First Place, University of Toronto, ON, Canada ($800 iPad Air)
- **2016:** Paul and Sally Wang Distinguished Graduate Scholarship at IBBME of University of Toronto, ON, Canada [Only one scholarship is awarded annually] ($6,000)
- **2015:** Paul and Sally Wang Distinguished Graduate Scholarship at the Institute of IBBME of University of Toronto, ON, Canada [Only one scholarship is awarded annually] ($6,422)
- **2015-2018:** Alexander Graham Bell Canada Graduate Scholarship by Natural Sciences and Engineering Research Council of Canada (NSERC) ($35,000/yr for 3 years, $105,000 in total)**.**
- **2014-2015:** Wildcat Graduate Scholarship at the Institute of Biomaterials and Biomedical Engineering (IBBME) of University of Toronto, ON, Canada [Only one scholarship is awarded annually for domestic student] ($11,666/yr)
- **2014:**Ontario Graduate Scholarship at the University of Toronto, ON, Canada ($15,000/yr)
- **2014:** Ph.D offer from University of Toronto with annual stipend of the Institute ($16,000/yr) + the cost of tuition and fees, ON, Canada
- **2014:** Our project of Sticking Together - An Elastic Surgical Glue on the $100,000, BRIght Futures Prize (Brigham and Women's Hospital) was nominated.
- **2013:** Micro- and Nanotechnologies in Medicine Travel Scholarship, supported by Harvard Medical School, Brigham and Women's Hospital and the National Science Foundation, Cambridge, MA, USA
- **2013-2015:** Administrator and editor, Website of the Canadian Biomaterials Society
- **2012-2014:** Vice President, The Montreal Chapter of the Canadian Biomaterials Society
- **2012:** Excellence presentation prize, 1st student seminar by advanced study committee FOCHAPEE
- **2012:** Junior Engineer, ordre des ingénieurs du Québec
- **2011:** Nominated for NSERC Innovation Challenge Award, Concordia University
- **2010:** CALPHAD-STT scholarship, CalphadXXXIX international conference
- **2009:** Golden Key International Honour Society, (top 15% of the class and interested in service and leadership development), Concordia University, Canada.
- **2008 - 2009:** Partial tuition fee remission award, Concordia University
- **2007:** Best bachelor thesis, Material Science and Engineering Department, Beijing University of Technology
- **2006:** Group 1st prize, personal 1st prize, material mechanical properties speech competition, Beijing University of Technology
- **2005:** Group 2nd prize, personal 1st prize, university English drama competition, Beijing University of Technology

Contributions

Journal Articles: (*equal contribution)

• Biomedical engineering (immunology, nanotechnology, tissue engineering)

1. Y.N. Zhang, W. Poon, E. Sefton, W.C.W. Chan, "Suppressing subcapsular sinus macrophages enhance transport of nanovaccines to lymph node follicles for robust humoral immunity", *ACS Nano,* (2020).
2. B. Ouyang, *W. Poon, *Y.N. Zhang, P.Z. Lin, B.R. Kingston, A.M. Syed, A.J. Tavares, J. Chen, M.S. Valic, J. Couture-Senécal, G. Zheng, W.C.W. Chan, "Trillion nanoparticles overwhelm liver clearance and enhance tumour delivery". *Nature Materials,* (Accepted, 2020).
3. Y.N. Zhang, *J. Lazarovits, *W. Poon, *B. Ouyang, L.N.M. Nguyen, B.R. Kingston, W.C.W. Chan, "Nanoparticle size influences antigen retention and presentation in lymph node follicles for humoral immunity", *Nano Letters*, Vol. 19, 7226−7235 (2019).
4. W. Poon, *Y.N. Zhang, *B. Ouyang, B.R. Kingston, J.L. Wu, S. Wilhelm, W.C.W. Chan, "Elimination pathways of nanoparticles", *ACS Nano,* Vol. 13, 5785-5798 (2019).
5. J. Lazarovits, Y.Y. Chen, F. Song, W. Ngo, A.J. Tavares, Y.N. Zhang, J. Audet, B. Tang, Q. Lin, M.C. Tleugabulova, S. Wilhelm, J.R. Krieger, T. Mallevaey, W.C.W. Chan, "Synthesis of patient-specific nanomaterials", *Nano Letters*, Vol. 19, 116-123 (2019).
6. *A.J. Tavares, *W. Poon, *Y.N. Zhang, Q. Dai, R. Besla, D. Ding, B. Ouyang, A. Li, J. Chen, G. Zheng, C. Robbins, W.C.W. Chan, "Effect of removing Kupffer cells on nanoparticle tumor delivery", *Proceedings of the National Academy of Sciences*, Vol. 114, E10871-E10880 (2017).
7. N. Annabi, Y.N. Zhang, A. Assmann, A. Vegh, G. Cheng, B. Dehghani, S. Gangadharan, A. Khademhosseini, A. Weiss, "Engineering a highly elastic human protein-based sealant for surgical applications", *Science Translational Medicine,* Vol. 9, eaai7466 (2017).
8. Y.S. Zhang, Y.N. Zhang, W. Zhang, "Cancer-on-a-chip systems at the frontier of nanomedicine", *Drug Discovery Today,* Vol. 22, 1392-1399 (2017).
9. *Y.N Zhang, *W. Poon, A.J. Tavares, I.D. McGilvray, W.C.W. Chan, "Nanoparticle–liver interactions: Cellular uptake and hepatobiliary elimination", Special issue: Drug Delivery Research in North America, *Journal of Controlled Release*, Vol. 240, 332-348 (2016).
10. *Y.N. Zhang, *R. Avery, *Q.V. Martín, A. Assmann, B.D. Olsen, N. Annabi and A. Khademhosseini, "Rapid photopolymer elastin like peptides for tissue engineering application", *Advanced Functional Materials,* Vol. 25, 4814-4826 (2015).

• Material science and mechanical engineering

1. J. Wang, Z. Zhang, Y.N. Zhang, D. Han, L. Jin, L. Sheng, P. Chartrand, M. Medraj, "Investigation on metallic glass formation in Mg-Zn-Sr ternary system by the CALPHAD method", *Materials Letters*, Vol. 256, 126628 (2019).
2. X. Zhang, Y.N. Zhang, D. Kevorkov, M. Medraj, "Experimental investigation of the Mg-Zn-Zr ternary system at 450°C", *Journal of Alloys and Compounds*, Vol. 680, 212-225 (2016).
3. J. Wang, Y.N. Zhang, P. Hudon, P. Chartrand, I.H. Jung and M. Medraj, "Experimental determination of the phase equilibria in the Mg-Zn-Sr ternary system", *Journal of Materials Science*, Vol. 50, 7636-7646 (2015).
4. J. Wang, Y.N. Zhang, P. Hudon, I.H. Jung, P. Chartrand and M.Medraj, "Experimental study of the crystal structure of the $Mg_{15-x}Zn_xSr_3$ ternary solid solution in the Mg-Zn-Sr system at 300 °C", *Journal of Materials and Design*, Vol. 86, 305-312 (2015).
5. J. Wang, Y.N. Zhang, P. Hudon, I.H. Jung, M.Medraj and P. Chartrand, "Experimental study

of the phase equilibria in the Mg-Zn-Ag ternary system at 300 ℃", *Journal of Alloys and Compounds*, Vol. 639, 593-601 (2015).

6. Y.N. Zhang, X. Cao, P. Wanjara and M. Medraj, "Tensile properties of laser additive manufactured Inconel 718 using filler wire", Special issue: The Materials Science of Additive Manufacturing, *Journal of Materials Research*, Vol. 29, 2006-2020 (2014).
7. M. Mezbahul-Islam, Y.N. Zhang, C. Shekhar and M. Medraj, "Critical assessment and thermodynamic modeling of Mg-Ca-Zn system supported by key experiments", *CALPHAD: Computer Coupling of Phase Diagrams and Thermochemistry*, Vol. 46, 134-147 (2014).
8. Y.N. Zhang, X. Cao, P. Wanjara and M. Medraj, "Oxide films in laser additive manufactured Inconel 718", *Acta Materialia*, Vol. 61, 6562-6576 (2013).
9. Y.N. Zhang, X. Cao, P. Wanjara, "Fiber laser deposition of Inconel 718 using filler wire", *Journal of Advanced Manufacturing Technology*, Vol. 69, 2569-2581 (2013).
10. Y.N. Zhang, X.D. Liu, Z. Altounian and M. Medraj, "Coherent nano-scale ternary precipitates in crystallized $Ca_4Mg_{72}Zn_{24}$ metallic glass", *Scripta Materialia*, Vol. 68, 647-650 (2013).
11. Y.N. Zhang, G.J. Rocher, B. Briccoli, D. Kevorkov, X.B. Liu, Z. Altounian and M. Medraj, "The crystallization characteristics of the Mg-rich metallic glasses in the Ca-Mg-Zn system", *Journal of Alloys and Compounds*, Vol. 552, 88-97 (2013).
12. D. Kevorkov, Y.N. Zhang, K. Shabnam, P. Chartrand, M. Medraj, "Experimental study of the Al-Ca-Zn system at 350ºC", *Journal of Alloys and Compounds*, Vol. 539, 97-102 (2012).
13. Y.N. Zhang, X. Cao, S. Larose and P. Wanjara, "Review of the tools for friction stir welding and processing", special issue on Advances in High Temperature Joining of Materials, *Canadian Metallurgical Quarterly*, Vol. 51, No. 3, 250-261 (2012).
14. Y.N. Zhang, D. Kevorkov, X.D. Liu, F. Bridier, P. Chartrand and M. Medraj, "Homogeneity range and crystal structure of the $Ca_2Mg_5Zn_{13}$ compound", *Journal of Alloys and Compounds*, Vol. 523, 75-82 (2012).
15. Y.N. Zhang, D. Kevorkov, F. Bridier and M. Medraj, "Experimental investigation of the Ca-Mg-Zn system using diffusion couples and key alloys", *Journal of Science and Technology of Advanced Materials*, Vol. 12, No. 8, rec.No. 025003 (2011).
16. Y.N. Zhang, D. Kevorkov, J. Li, E. Essadiqi and M. Medraj, "Determination of the solubility range and crystal structure of the Mg-rich ternary compound in the Ca-Mg-Zn system", *Intermetallics*, Vol. 18, No. 12, 2402-2411 (2010).
17. Y.F. Wu, W.B. Du, Y.N. Zhang, Z.H. Wang, "Creep mechanism of as-cast Mg-6Al-6Nd alloy", *Rare Metals*, Vol. 29, No. 5, 538-541 (2010).

Oral and Poster Presentations (Selected):

1. Y.N. Zhang, Nanovaccine induces robust humoral immunity for vaccination, The UofT most understandable scientist (UTMUST) 2019 event, University of Toronto, November 22, 2019, Toronto, ON, Canada. (Oral) [First place award]
2. Y.N. Zhang, J. Lazarovits, W. Poon, B. Ouyang, L.N.M. Nguyen, B.R. Kingston, W.C.W. Chan, Nanoparticle size influences antigen retention and presentation in lymph node follicles for humoral immunity, Donnelly Centre Graduate Student Association, November 4, 2019, Toronto, ON, Canada. (Oral)
3. W. Poon, A.J. Tavares, Y.N. Zhang, B. Ouyang, B.R. Kingston, J.L.Y. Wu, R. Besla, D. Ding, A. Li, J. Chen, S. Wilhelm, G. Zheng, C. Robbins, W.C.W. Chan, Removing Kupffer cells improves nanoparticle tumour delivery and elimination, Vancouver Nanomedicine Day, September 12-14, 2019, Vancouver, BC, Canada. (Oral)
4. B. Ouyang, W. Poon, Y.N. Zhang, P.Z. Lin, B.R. Kingston, A.M. Syed, A.J. Tavares, J. Chen, M.S. Valic, J. Couture-Senécal, G. Zheng, W.C.W. Chan, Nanoparticle delivery depends on

dose, Gordon Research Conference/Seminar for Cancer Nanomedicine, June 23-28, 2019, West Dover, VT, USA. (Poster). [Best Poster award]

5. Y.N. Zhang, Towards understanding how lymph node processes nanoparticles, College of Veterinary Medicine, China Agricultural University, June 11, 2019, Beijing, China. (Oral)
6. N. Annabi, Y.N. Zhang, A. Assmann, A. Vegh, G. Cheng, B. Dehghani, S. Gangadharan, A. Khademhosseini, A. Weiss, Engineering a Highly Elastic Protein-based Surgical Sealant, European Chapter Meeting of the Tissue Engineering and Regenerative Medicine International Society (TERMIS), June 26-30, 2017, Davos, Switzerland. (Oral)
7. Y.N. Zhang, R. Avery, Q.V. Martín, A. Assmann, A. Vegh, A. Memic, B.D. Olsen, N. Annabi, and A. Khademhosseini, A highly elastic and rapidly crosslinkable hydrogel for biomedical applications, Materials research society (MRS) fall meeting, November 29-December 4, 2015, Boston, Massachusetts, USA. (Poster)
8. Y.N. Zhang, X. Cao, P. Wanjara and M. Medraj, Fiber Laser Deposition of Superalloys Using Filler Wire or Powder, ASME Turbo Expo, June 15th to 19th, 2015, Montreal, Canada. (Oral)
9. Y.N. Zhang, G.J. Rocher, B. Briccoli, X.D. Liu, X.B. Liu, Z. Altounian and M. Medraj, Crystallization studies of the Mg-rich metallic glasses in the Ca-Mg-Zn system, *American Society of Metals (ASM) Montreal Chapter*, February 2013, École Polytechnique de Montréal, Montreal, Canada. (Poster)
10. Y.N. Zhang, X. Cao, M. Guerin, S. Larose, P. Wanjara, Tools for friction stir welding and processing: a review, Innovations in Joining of Advanced Materials, *COM*, 2011, Montreal, Canada. (Oral)
11. Y.N. Zhang, D. Kevorkov, J. Li, E. Essadiqi, M. Medraj, Experimental investigation of the Ca-Mg-Zn system via diffusion couples and key experiments, *CalphadXXXIX*, 2010, Jeju, Korea. (Oral)